Design, characterization and structuring of Pt based catalysts for Water Gas Shift reaction

Miriam González Castaño

Ph.D. Thesis

Directors

Svetlana Ivanova
Jose Antonio Odriozola Gordon

Contents

General introduction and objectives

Actual energetic system

The growth of the environmental concern, in view of the global warming produced by the greenhouse gas emissions, and the predicted depletion of the energetic sources stimulated the scientific interest to search for new energy-friendly sources. The 20th century was characterized by a socio-economic enlargement being reflected on the increase of the total economic demand. The evolution of the energetic sources utilization through the years shows the total fossil fuels dependency (Figure 1) [1].

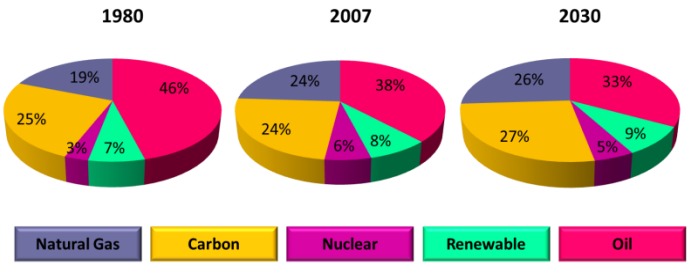

Figure 1. Worldwide Energetic Mixture. Adapted from [1]

The fossil fuels based economic model demonstrates two main disadvantages: one is the geographical availability limitation derived from the unequal distribution of the sources, which are placed just in a few countries. The other important drawback concerns to the environmental consequences derived from their continuous use.

Therefore, it is mandatory to develop alternative energy models, as for example those based on H_2 as a fuel. H_2 technology is one of the most promising energy vectors to its sustainability and environmental responsibility [2]. On the other hand, H_2 demand continuously increases in recent years mainly due to its application in petroleum refining processes, such as hydrotreating and hydrocracking [3], production of methanol [4], methanol-to-gasoline technology (MTG) [5], ammonia and hydrocarbon synthesis via Fischer-Tropsch processes [6].

However, H_2 does not exist by itself in the nature and it must be produced. H_2 containing streams can be achieved by using nuclear energy, water electrolysis or chemical methods. The most popular chemical H_2 production routes are:

- Gasification or partial oxidation (POX): It is defined as the reaction between a hydrocarbon or alcohol with sub-stoichiometric amount of oxygen that is needed for its complete oxidation (Equation 1.1). The tendency to total hydrocarbon' oxidation must be controlled in order to obtain higher selectivity towards H_2. Although the exothermicity of this reaction presents an advantage and no external energy sources are needed, the temperature reactor gradient and the catalyst hot spots formation should be controlled. In addition, the used oxygen usually is previously separated from air, which requires the use of expensive technologies.

$$C_nH_mO_z + \frac{1}{2}(n-z)O_2 \rightarrow nCO + \frac{m}{2}H_2 \qquad \textit{(Equation 1)}$$

- Steam reforming (STR): Generally, it can be assumed as the reaction between hydrocarbon or alcohol and water to produce CO and H_2 (Equation 1.2). Industrially, methane steam reforming is the most employed process to produce synthesis gas from natural gas. This reaction is highly endothermic being favored at higher temperatures and pressures. At industrial scale, it is normally carried out at 15-30 pressure bars and at 850-950 ºC employing a steam/carbon ratio around 3.

$$C_nH_mO_z + (n-z)H_2O \rightarrow nCO + \left(n + \frac{m}{2} - z\right)H_2 \qquad \textit{(Equation 2)}$$

- Dry reforming: In a general way, describes the reaction between a carbonaceous molecule and CO_2 to obtain synthesis gas (Equation 1.3). This process has the advantage to transform CO_2, a greenhouse gas, in other mixture with higher added value. Actually, methane dry reforming is considered as an option to profit the biogas. The negative aspect comes from reaction's strong endothermic character requiring large amounts of energy, optimized installations and high operational costs.

$$aC_nH_m + bCO_2 \leftrightarrow c\,CO + \left(a \cdot \frac{m}{2}\right)H_2 \qquad \textit{(Equation 3)}$$

- Autothermal reforming (ATR): It is defined as a combination of partial oxidation (POX) and steam reforming (STR) reaction. When both reactions are combined (Equation 1.4) the heat released from the oxidation reaction is used to assure the steam reforming. The correct tuning of the reaction conditions leads to an auto-sustainable process. Moreover, the H_2/CO ratio obtained in this process can be modulated by varying the gas compositions introduced in the reactor.

$$C_nH_mO_z + aO_2 + bH_2O \leftrightarrow cCO + dH_2 + eCO_2 \qquad \textit{(Equation 4)}$$

- Pyrolysis: It is described as thermochemical decomposition process carried out in absence of oxygen. The thermal cracking produces gaseous products (CO_2, CH_4, CO, H_2O) and carbon as solid product. Others liquid byproducts could be also obtained, depending on the pyrolized molecule.

In all chemical processes described above, the produced H_2 is accompanied by H_2O, CO and CO_2. Among the gases, the CO presence must be especially considered because it supposes an inconvenient for the correct performance of the fuel cells, the devices used to convert the H_2 chemical energy into electric energy. Among the variety of existing fuel cells, the Polymer Electrolite Membrane (PEM) fuel cell seems to be the most promising candidate for the next generation power sources for transportation, stationary and portable applications, because of its noteworthy features including low operating temperature (around 90ºC), high power density and easy scale-up [7].

The PEM fuel cell use hydrogen fuel and oxygen from the air to produce electricity. The H_2 fuel is channeled to the anode while the oxygen is directed to the cathode. On anode the Pt catalysts caused the hydrogen splitting into protons and electrons. The existing membrane conducts only protons and forces the electrons to travel an external circuit thus creating an electrical current. As a final step the reaction of both with oxygen on the cathode results in water which is evacuated from the cell (Figure 2).

The most sensible element of this technology is the anode catalyst which is easily poisoned in contact with CO molecules if present in the H_2 stream. At the PEM fuel cell operating temperatures, the CO molecules irreversibly adsorb on the anode surface inhibiting its activity. It is then mandatory to use H_2 stream with insignificant CO concentration, typically < 50 ppm for Pt-Ru based anodes and < 10 ppm for Pt based one.

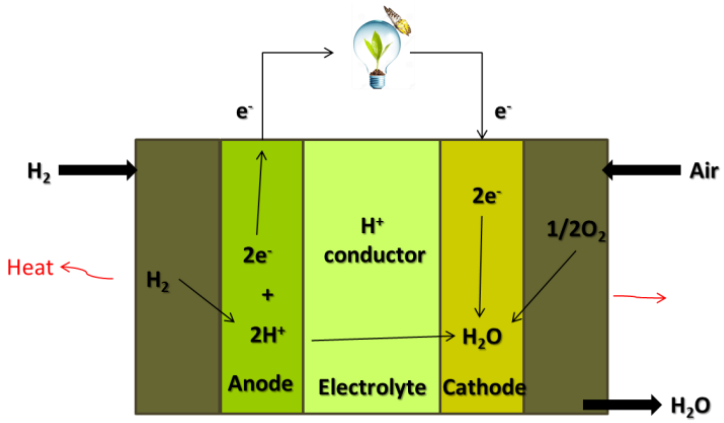

Figure 2. PEM fuel cells operation

All the H_2 producing processes described above, results in CO concentration much higher than the necessary trace levels and therefore, purification processes must be applied.

Typically the first cleaning step is the water gas shift (WGS) reaction followed by either preferential oxidation (PrOx) and/or methanation reaction. Although the step sequence of a complete process, including the H_2 production and the subsequent clean steps, will depend on the H_2 sources, the H_2 production reaction and the process application, a possible schematic sequence to converts liquid hydrocarbons into CO-free H_2-rich stream is shown in Figure 3.

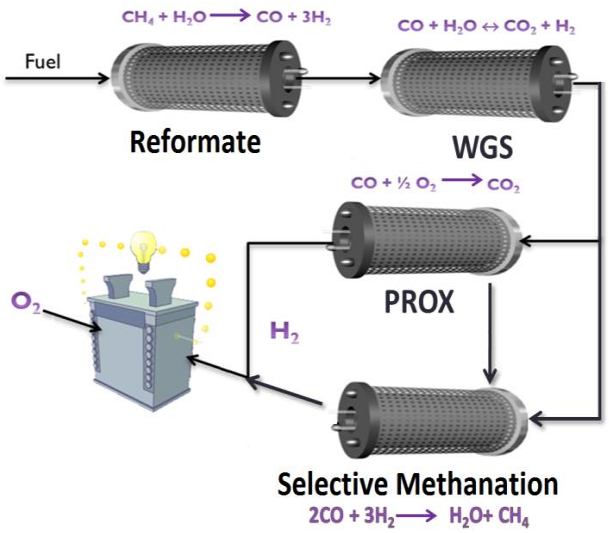

Figure 3. Clean hydrogen production via fuel processing steps

Water Gas Shift (WGS) reaction

The WGS reaction was discovered by the Italian physicist Felice Fontana in 1780 and it was industrially applied for the first time in the Haber-Bosh process for ammonia production. In this process, the WGS reaction is combined with gasification of coal or natural gas reforming to produce the H_2 needed for the ammonia synthesis. The WGS *(Equation 1.5)* process consists in the reaction of CO and H_2O molecules to produce CO_2 and H_2. So, the WGS possesses the advantage to increase the hydrogen yield at the same time that reduces the CO content. The WGS reaction is an exothermic equilibrium reaction and the equilibrium conversion decreases with the temperature [8]. Therefore, better performances are achieved by operating at relatively high temperatures and exploiting the reaction kinetics when the gas composition is far from the equilibrium. However, at these temperatures the CO conversions are thermodynamically limited [9]. Hence, the lowest temperature at which maximum CO conversions can be achieved is determined by the kinetics of the catalyst [10].

$$CO + H_2O \leftrightarrow H_2 + CO_2 \qquad \Delta H° = -41.2\ kJ \cdot mol^{-1} \quad \textit{(Equation 5)}$$

Industrially, the WGS reaction is usually carried out in two separated units: High Temperature Shift (HTS) and Low Temperature Shift (LTS). A high temperature catalyst is used in a HTS reactor to maximize the reaction rate, and a low temperature catalyst is subsequently used in a LTS reactor to maximize the conversion [11]. Pointing to fuel cell application the best

solution will be a low temperature WGS catalyst, ideal for maximizing the CO conversion and safer operational conditions [12].

The main high temperature WGS catalyst is based on iron usually promoted with chromium oxide for stability [13]. Chromium oxide prevents the sintering of iron crystals and preserves their activity at high temperatures [14]. These catalysts work extremely well in the 450-600ºC temperatures range being the outlet CO concentration around 3-5%. However, catalyst poor performance at lower temperatures, the toxicity of the water-soluble Cr^{6+} ions causing health hazards during catalyst manufacture and handling and the low volumetric catalytic activity (10000 - 15000h^{-1}), especially at low temperatures, when CO conversion is favored thermodynamically motivates further investigations.

The second, low temperature stage consists of gas reaction at temperatures near 200 ºC where the CO concentration is reduced to less than 0.6% [13]. Low temperature catalysts for the WGS reaction are based on Cu supported on alumina, which promoted with ZnO presents longer life [15].

Although the industrial WGS process is very well-known and will remain unchanged while the application of this technology is needed to produce clean hydrogen, the new challenge is to develop catalysts able to implement the fuel cell on portable applications motivating a renewed interest on the WGS process. Thereby, other catalyst features become fundamental for the successful implementation of WGS processors in mobile units. In this context,

the WGS catalyst must not require controlled and elaborated pre-reduction procedures (such in the case of the Cu-based LTS catalysts), must be non-pyrophoric and oxidation-tolerant on exposure to air. For example, Cu based catalysts are extremely pyrophoric when activated (reduced) and, therefore, safety from runaway heat generation and fire cannot be ensured upon air exposure.

Another very important requisite for the WGS unit for mobile application is the volume reduction exigency which is not an easier task because of the high contact times needed to achieve acceptable CO conversions in the WGS reaction units.

In response to these needs, noble metal based WGS catalysts are under intense development worldwide for fuel cell applications. Several systems based on noble metals have been reported in the literature being gold and platinum ones described as the most promising systems. Both metals present satisfactory results but recently, the balance tilts towards the platinum based systems which clearly demonstrate a superior activity, ascribed often to mechanistic differences through which the reaction happens [16–18].

Pt based catalysts

The increased interest on platinum based catalysts for WGS reaction is reflected on the large number of papers published in the last two decades, Figure 1.4.

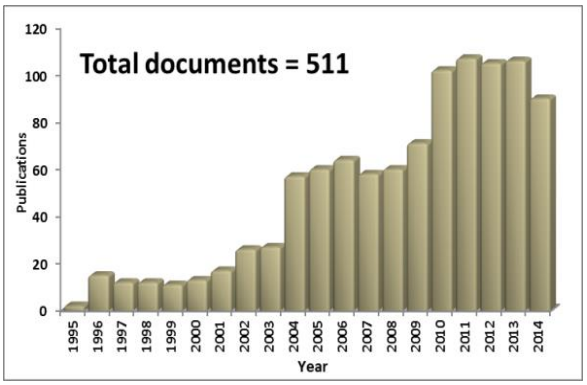

Figure 4. Number of publications, in Scopus database using "WGS" and "Platinum", as search strings for the 1995-2014 period

In general, the publications focused either on the WGS activity influence of the synthesis method, support modification, structural effects, oxidation state of the noble metal during the reaction or to the predominant mechanisms and reaction intermediates through which the reaction occurs. Several supports, classified as "reducible" and "non-reducible" oxides, have been studied for the Pt WGS catalysts. Olympiou et al. [19] studied the WGS reaction over Pt, Pd and Rh supported on irreducible alumina correlating the WGS activity exhibited to the surface concentration and binding energy of CO on the metal. The Pt > Rh > Pd order of activity was found and the WGS mechanism matches the one proposed by Grenoble et al. [20] for supports such alumina. In this mechanism, it was proposed that the water dissociation happens onto the support and the activated species migrates from the support to the noble metal to complete the reaction. However, none of these works consider the capacity of platinum itself to dissociate water [21].

Support importance: ceria modifications

Pt based catalysts and also other noble metals, exhibit an important enhancement of the catalytic activity exhibited when supported on reducible oxides [22–25]. The reducible oxides are not simply spectators in the WGS reaction but, in turn, play an important role [18,26–28]. Within the reducible oxides used as a supports the most studied are titania [8,26,29,30] and ceria [22,24,31–36]. Phatak et al. [37] reported for Pt supported on ceria WGS turnover rate 30 times higher than that of Pt alumina supported catalyst. In particular, Pt/CeO_2 raised the scientific interest for WGS reaction, since in the early 1980s, during the development of the three-way catalysts (TWC), it was discovered that ceria is the best non-noble metal oxide promoter for a typical Pt–Pd–Rh/alumina TWC because it enhances the water-gas shift reaction [38]. The strong interaction between Pt and ceria, exemplified by the ceria surface oxygen reducibility upon metal addition, was recognized as indication of the electronic effect exercised by the oxidized Pt-Ox-Ce sites, the active sites in the TWC redox chemistry. Accordingly to Flytzani, this effect was even more evident after aging, leading to metal separation in two groups: large platinum particles (presumably inert) and non-metallic part, which are presumably atomic or subnanometric oxidized $Pt\text{-}O_x$ clusters strongly bound to the ceria surface [39].

In this line, Tauster el al. [40] introduced the term strong-metal support interaction in order to describe the contribution of the reducible oxide support

to the catalytic site formation. It was discovered that some Pt supported on a reducible oxide catalysts the hydrogenation activity of the noble metal is decreased by structural effects: decoration or partial coverage of the active metal sites by reduced M-O_x species. Raman studies reported by Murrel et al. [41,42] showed that Pt form surface metal oxide structures (M-O) interacting strongly with ceria surface, being the latter present in bulk form or within an alumina host structure.

Commonly, it is established that both, noble metal and support, play essential roles for the WGS reactions. It is also accepted that the catalytic activity of the supported metal particles is highly influenced by particle size, shape and metal oxidation state, as well as by the nature and reduction degree of the support and by the metal/oxide interaction.

Initially, the main role of the support is to disperse the active phase. The support must be able to interact with the active phase in order to obtain highly dispersed and stable noble metal based catalysts. Typically, support modifications are undertaken to enhance the catalytic performance of the catalyst through changing its structural or electronic properties [18,43–46]. The synergy between the ceria and the modifier can be achieved in three different ways: solid solution formation [47,48], interaction between segregated oxides [49,50] or by metallic particles deposition on the ceria surface [51,52].

Several studies have demonstrated that doping ceria with elements with different ionic radii or oxidation states induces effects on the ceria' properties: reducibility, oxygen storage capacity and resistance to sintering [53,54]. Considering that partial reduction of ceria support is convenient for oxygen vacancies formation and activation of water during WGS reaction, the improvement of the latter should result in catalyst' promotion and increased CO oxidation rate. The redox capacity of the samples should markedly determine the catalytic activity being the capacity to exchange oxygen species with the media, depending on the reaction atmosphere and the formation of Ce^{3+}- $O_v^{\cdot}$ sites, a feature closely related with the catalytic performance.

Numerous studies regarding the doping agents' introduction with unique purpose to increase the ceria redox properties and catalytic performance after metal addition could be found in the literature [26,45,50,55,56] with contradictory conclusions. For example, it was reported that the introduction of Zr (IV) to the ceria lattice, for gold based catalysts, worsens the WGS activity, an effect explained by the stabilization of cubic and tetragonal polymorphic ZrO_2 forms in respect to the monoclinic one, the active to dissociate water [57]. On the contrary, the zirconia addition has been reported beneficial for ceria based catalysts specially when forming solid solution resulting in improved reducibilities and easier oxygen exchange with the media [56].

In addition to the good redox properties, suitable ceria based support should also lower the barrier for ceria to metal oxygen transfer facilitating the oxidation of adsorbed CO. This influence of the ceria cations on the adsorption state of CO is related to its back-bonding possibility from the metal to the CO adsorbate. So, by varying the acidic properties of the catalyst and the CO-support interaction one can modulate the easiness of the system to react with the neighboring activated intermediate species.

Duarte de Farias et *al* [58] reported that ceria-zirconia mixed oxide presents higher basic character than the pure ceria but are also more acid if Lewis sites are considered. They suggest that CO adsorbs preferably at Zr- defective center located at the metal- support interface which interacts with the O^{2-} and OH^- to form reaction intermediates. Similar results has been published for other transition metals employed as doping agents [59,60] being the catalytic performances more frequently related to the redox properties modification.

Deactivation of the catalysts

The use of noble metal catalysts, more expensive than conventional LTS catalysts based on transition metal oxides, could be considered economically viable if they present a higher resistance to deactivation.

Different catalytic behavior as a function of the particle size of the noble metal has been reported being more active the more dispersed noble metal because of their higher surface/volume ratio and/or metal-support interaction.

Indeed the noble metal sintering has been reported as one of the main causes of deactivation for platinum based catalysts [61–63]. This phenomenon could be avoided either by support modifications in order to achieve higher noble metal-support interactions and as a consequence higher platinum dispersion [31,64] or by changes in the method of preparation [65].

Moreover, in the case of ceria supported catalysts, support overreduction and carbonaceous species active sites blocking are also reported as important deactivation causes. The overreduction phenomena imply that the major proportion of the cerium oxide is completely reduced and therefore, the pair redox Ce^{4+}/Ce^{3+} is not available for the catalytic process. The impossibility of the ceria to be reoxidized by the reactant water reduces drastically the catalytic activity [66]. On the other hand, the carbonaceous species can be also formed from the reaction intermediates hindering the WGS reaction active sites.

From, the introduction of ceria provided catalysts with much better properties than the original Pt/Al_2O_3 systems. The strong interaction of Pt/Ceria, exemplified by the enhanced reducibility of the surface oxygen of ceria upon the metal addition was recognized as an indication of an electronic effect displayed by oxidized sites ($Pt\text{-}O_x\text{-}Ce$) which are probably responsible of the redox chemistry.

Besides, further advances were achieved through the addition of promoters able to diminish the platinum sintering that provokes the catalyst deactivation.

The described features characteristic of platinum based systems converted the proper catalyst design in a tremendously interesting approach.

Metal-support interactions: WGS mechanism and active species

In principle, the structural and electronic properties of the catalysts and the WGS reaction mechanism should be connected. The structural and electronic properties of the active sites are usually affected by the chemical environment and do affect the creation and transformation of the formed species through a reaction mechanism [67–70]. Therefore, the design and optimization of metal-oxide supported WGS catalyst requires further knowledge about how the reactants, intermediates and products interact with the active phase.

The importance of the noble metal-support interactions and its essential role for the catalytic activity has received much attention reflected in the development of numerous mechanistic and kinetics studies. To date, some disagreement remains about the nature of the reaction intermediates and the role of the support. Indeed, the chemical nature of the intermediates and their true localization, e. g. support, metal-support interface, or metal surface still remain controversial.

Concerning the mechanism of the WGS reaction, two main reaction pathways has been generally proposed in the literature. In the proposed redox mechanism [71], CO adsorbs on the metal surface and then diffuses to the metal-support interface and reacts with the lattice oxygen of the support to

form CO_2. Water adsorbs and dissociates mainly on the reduced support sites, thus re-oxidizing them and subsequently producing H_2. For the redox pathway, the successive oxidation and reduction steps occur as follows:

$$CO + {}^{*} \leftrightarrow {}^{*}CO \qquad \textit{(Equation 6)}$$

$$H_2O + {}^{*} \leftrightarrow H_2O^{*} \qquad \textit{(Equation 7)}$$

$$H_2O^{*} + {}^{*} \leftrightarrow OH^{*} + H^{*} \qquad \textit{(Equation 8)}$$

$$2\,HO^{*} + {}^{*} \leftrightarrow H_2O^{*} + O^{*} \qquad \textit{(Equation 9)}$$

$$HO^{*} + {}^{*} \leftrightarrow O^{*} + H^{*} \qquad \textit{(Equation 10)}$$

$$CO^{*} + {}^{*}O \leftrightarrow CO_2{}^{*} + 2^{*} \qquad \textit{(Equation 11)}$$

$$2H^{*} \leftrightarrow H_2 + 2^{*} \qquad \textit{(Equation 12)}$$

Where "*" represents a surface site, and therefore, "X^{*}" stands for adsorbate bonded to this site.

Within the associative mechanism, H_2O and CO adsorbs on catalyst active sites to form surface "carbon-containing" intermediates which react or decompose to form CO_2 and H_2. The associative mechanism proposed by Iwasawa and Shido [72] happens as follows and it involves the reaction through adsorbed intermediate species such as formate, carbonate or carboxyl:

$$CO + {}^{*} \leftrightarrow {}^{*}CO \qquad \textit{(Equation 6)}$$

$$H_2O + 2\,{}^{*} \leftrightarrow OH^{*} + H^{*} \qquad \textit{(Equation 13)}$$

$$OH^{*} + {}^{*}CO \leftrightarrow HOOC^{**} \qquad \textit{(Equation14a)}$$

$$OH^{*} + {}^{*}CO \leftrightarrow OCOH^{*} + {}^{*} \qquad \textit{(Equation 14b)}$$

Which eventually dissociates

$$HOOC^{**} \leftrightarrow CO_2 + H^* + {}^* \qquad \textit{(Equation 15a)}$$

$$OCOH^* \leftrightarrow CO_2 + H^* \qquad \textit{(Equation 15b)}$$

Or reacts with OH^*

$$HOOC^{**} + {}^*OH \leftrightarrow CO_2 + H_2O^* + 2^* \qquad \textit{(Equation 16a)}$$

$$OCOH^* + {}^*OH \leftrightarrow CO_2 + H_2O^* + {}^* \qquad \textit{(Equation 16b)}$$

Mechanism and active species for Pt catalysts

In literature, discussion for and against both mechanisms could be found. For example, Kalamaras et *al.* [73] concluded that the WGS reaction on Pt/CeO_2 catalyst at 300ºC occurs mainly through redox mechanism with a minor contribution of the associative via formate mechanism.

On the contrary, Jacobs et *al.* [33] proposed an associative formate pathway, using IR spectroscopy suggesting as catalytically active sites the Type II bridging OH groups on partially reduced ceria which reacts with CO and generates surface formate. The formates decomposition is then promoted by water molecules and platinum metal, caused by the higher oxygen vacancies concentration around platinum able to dissociate water and decompose the formates.

Solid arguments against the formate, as main reaction intermediates, were reported by Rodriguez et *al.* [74]. In this study by DRIFTS spectroscopy, it was observed that the temperature of maximum formate concentration (250ºC) do not correlate with the highest activity temperature found for Pt/CeO_2. Actually, the maximum CO conversion was found at 300-350 ºC when the amount of detected formates was negligible. In concordance, Burch [75] affirmed that the formate species appear to be mere spectators not involved in the reaction on the basis of the differences observed between formate decomposition and WGS reaction rates.

Gabrow et *al.*[76] reported after DFT calculations, as a possible reaction pathway for Pt (111) surface, the associative mechanism through carboxyl intermediate species, under the basis of more favorable energetic formation. The intermediates decomposition as described above was reported to be encouraged by OH species. In the Figure 5, all possible reaction pathways are presented. The E_a indicates the forward activation energy barrier and the ΔE, both in eV. The path involving the smallest activation energy barriers is highlighted.

The difficulty to establish an unequivocal mechanism was analyzed by Burch et al. [75] in an interesting study, in which the large amount of published ambiguous results and the limitations is discussed.

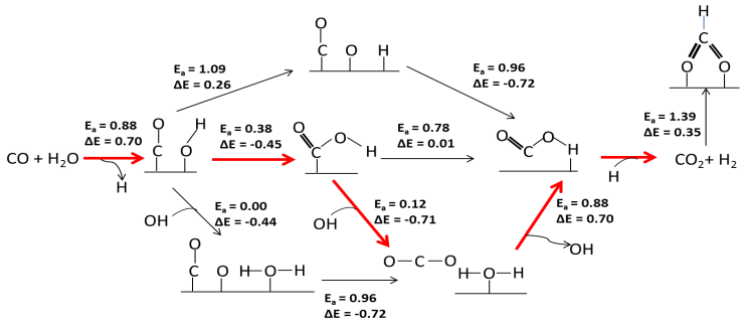

Figure 5. Possible reaction pathways on Pt(111). Adapted from reference [76]

Under reaction conditions the catalyst can undergo chemical transformations that drastically modify its composition with respect to the initial one [77]. Nowadays, the highly dispersed (even atomic) supported metal catalyst field is continuously growing. The supported metal catalysts consist on clusters or metal particles agglomerations characterized by the particle size itself and by the exposed active metal surface area. As the size of the metal structure is often reduced to nanometer size clusters, which properties obey the quantic principles, the catalytic activity is frequently related to the particle size and shape of the metal species.

On one other hand, considering that the electron transfer between adjacent oxygen (from the support) and platinum is expected and required, the reactivity of the oxygen atoms of the support should be also influenced by the platinum particle size [78]. However, Panagiotopoulou et al. [79] reported in Pt/TiO_2 catalyst similar turnover frequency for a wide range of platinum particle sizes. Similar results were obtained by Grenoble et al. [20] who

reported constant turnover frequencies for noble metal supported on Al_2O_3 catalysts over a wide range of particle size. For Pt/ceria, catalysts Kalamaras et *al.* [73] also calculated turnover frequencies rather insensitive to the platinum particle size. Nevertheless, this study reports a specific kinetic rate dependence on the particle size in such a way that, higher the particles size higher the rate. The enhanced catalytic performance observed for bigger particle size was ascribed to a different electron density on the Pt-support interface leading to an increased number of water dissociation sites. In agreement, Jacobs et al. [33] reported that bigger platinum particle sizes enhance the reducibility of the sample by the easier accommodation of hydrogen dissociated species on its surface. As a result, large platinum particles are easily reducible because of facilitated H_2 dissociation, being weaker its interaction with the support.

On the other hand, differences on the metal sizes lead to varied metal/support interactions which hardly influences the reduction behavior. Stronger metal/support interactions hinder platinum oxide reduction being the PtO_x species not fully converted to Pt^0 even at 300 ºC [80].

The oxidation state of active platinum species during the WGS reaction is still subject of continuous debate. Actually, the recent technical developments have allowed important advances on the determination of the active species responsible of the WGS activity. For low temperature WGS, Fu el al. [81] claimed that the WGS mechanism involves mainly cationic platinum species

within the Pt-O_x-Ce sites. Pt(II) and Pt(IV) but not Pt^0 were identified by XPS spectroscopy. Cationic clusters as major active species in WGS have been proposed for similar gold and palladium catalysts supported on ceria [39]. From *operando* studies, the opposite conclusions were stablished by Xu et al. [78] reporting that at the temperatures (300ºC) at which the catalyst exhibits maximum conversion, most of the platinum oxide is transformed into metallic platinum.

Micromonolithic structures

Along to the catalytic activity and stability, others intrinsic disadvantages should be solved for an efficient implementation of WGS units on portable devices. Commonly, a major requisite for WGS catalysts for reaching acceptable CO conversions is to work efficiently and at lower contact times which becomes a key drawback to overpass, for example, in the case of vehicle devices. Compared to the stationary applications, the volume of a portable fuel processor is strongly constrained by the need for compaction and fast response. Considering the conventional industrial WGS units the volume reduction of the mobile reactor should attain at least two orders of magnitude before the fuel cells successfully compete techno-economically with other modes of electricity production. The diminishing of the catalyst bed volume and higher catalytic efficiency could be achieved only by the use of structured reactors, as for example, monoliths.

The benefits of the noble metal based catalysts structured on micromonolithic reactors were already stablished by Wagner et al. [8] reporting a catalytic system able to reach the equilibrium conversions at 20000 h^{-1}. It should be noted that, in such space velocities, a conventional Cu-ZnO LTS catalyst will not give equilibrium conversions. Indeed, particulate (extrudate or sphere) catalysts will give rise to a very high pressure drop at these space velocities.

As a solution, the HTS and LTS units could be replaced by one single medium temperature shift, MTS, structured reactor. Even for stationary processors, the replace concept is appealing due to the immense volume/weight savings. Consequently, the micromonolithic catalysts become interesting approaches although possessing lower efficiencies (around 5%) for almost 90% bed catalyst volume reductions. Examples of some metallic and ceramic monolithic structures are presented in Figure 6.

In general, the usually applied ceramic honeycomb micromonoliths, present several disadvantages, such as, i) non-uniform flow distribution due to the monoliths' unidirectional channels and closed structures between channels, ii) slow diffusion rate of reactants to the catalysts and iii) lower mechanical resistance. In addition, its low thermal conductivities suppose an obstacle to dissipate the heat generated during the exothermic reactions such as WGS, where any local increase of the temperature could influence the activity.

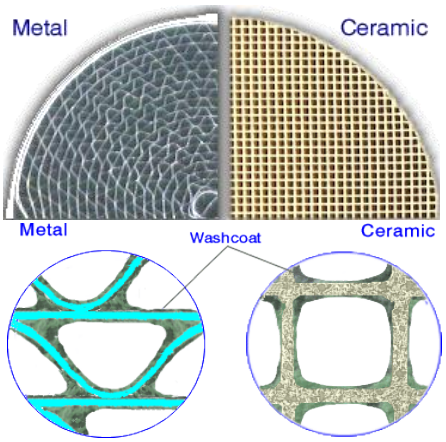

Figure 6. Comparison between metallic and ceramic monolithic structures: a) front section and b) channels shape

An excellent candidate to substitute the ceramic monoliths is its metallic homologue. The metallic micromonoliths present higher thermal conductivities, higher geometric surface area per volume unit and easier manufacture. Normally, the metallic micromonoliths are prepared by rolling a flat and corrugate metal sheet leading to cylindrically-shaped body composed by longitudinal flow gas channels.

Technically, monolithic reactors can be classified as micromonoliths when one of their dimensions is lower to 1 mm. Furthermore, the use of this kind of metallic structures allows a cheaper and quicker evaluation of the catalysts for their posterior scale up to microreactors.

The surface area can range from 200 to 1200 square inches (compared to about 400 of the ceramic micromonoliths). Indeed, greater cell per in^2 (cpsi) allows to deposit higher catalysts amounts maintaining appropriated layer

thickness and hence, maintaining the good mass and heat transfers capacitites provided by micromonolithic structures. For example, geometrical studies about the optimal cpsi range in metallic micromonoliths indicates that 600 and 900 cpsi exhibited similar and better performances compared to the ceramic micromonolithic structures with lower cpsi, around 225 cpsi.

However, the main disadvantage of the metallic substrates is the lower adherence between the catalysts and the micromonolithic channels and its stability in the reaction conditions. Therefore, the selection of the metallic alloy is a key step for solve those problems. Among the different metals and alloys that can be used as substrates, the aluminum and steels are the most employed. The aluminum conducts better the heat and it is much easily covered with Al_2O_3 because of its higher chemical compatibility. However, it is important to consider the corrosion phenomena that can occur in the extremely reductive conditions in which the WGS reaction is carried out.

Among the stainless steel, ferritic alloys as FeCrAlloy ones accomplish good stabilities regarding the carburization corrosion phenomena. Moreover, the low adherence initially presented by metallic systems can be overpassed through generating as α-Al_2O_3 layer when calcined among 875ºC and 925ºC during a long period of time (> 12 h). This layer increases the surface rugosity of the micromonolithic wall favoring the anchorage of the catalyst because of its ceramic nature.

Actually, the performance and durability of the micromonolithic catalysts strongly depend on the layer quality. Several methods through which a catalyst layer can be deposited over the monolithic walls as sol-gel, electrophoretic deposition (EPD), electrochemical deposition and electroless plating, etc [82]. Among them, the coating from a slurry (or suspension) has been the most employed and it is commonly labeled washcoating method. It is usually carried out with a slurry of particles of a comparable size to that of the macropores of the support [83].

Indeed, a proper performed washcoating method, and this implies a careful control of the suspension properties, allows achieving uniform catalyst layers. Apart of the catalysts, there are numerous other materials which can act as an additive, binder or adhesive to the washcoat slurry. Key steps in slurry preparation are particle size reduction and addition of appropriate acid/sol to adjust the pH, viscosity and homogeneity of the slurry in water.

The above described skins make the metallic micromonoliths, in particular the FeCrAlloy based ones, more convenient than the ceramic ones for design of the structured WGS catalysts.

For all described above, this PhD thesis will be focused on the development of a highly active catalyst with real potential applicability for a portable WGS process. For this purpose, the catalyst design should passes through attaining improved redox properties, platinum dispersions, water activation capacities,

all together within the general aim of reaching enhanced catalytic performances for long-term stabilities.

The realization of the proposed goal has been approached from two different perspectives. By one hand, the physicochemical properties of the Pt ceria based catalysts were modified, and the resulted solids characterized and tested in WGS reactions conditions in order to discern the catalyst composition influence on its WGS activity. On the other hand, the necessity of structured WGS catalyst for portable fuel processor application is considered and several structured platinum ceria systems were investigated.

This thesis is organized in 6 chapters. Along the first one, the techniques as well as the instrumentation employed to perform the experiments are presented on the Chapter 1. The Chapter 2, the physicochemical properties of platinum based catalysts supported on Al_2O_3 and CeO_2/Al_2O_3 commercial supports are evaluated through general characterization and catalytic tests. The catalysts supported on "home-made" CeO_2/Al_2O_3 support are also studied. In the Chapter 3, starting from a chosen platinum ceria based sample, the effect of support modifications is analyzed. Different doping agents on the ceria lattice are introduced with purpose to enhance catalyst's activity and stability. In chapter 4, the suitability of structured Pt based catalysts is evaluated. A new concept is also introduced in this chapter e.g. the presence of pre-catalyst layer- buffer layer. The better catalytic performances exhibited

by the bi-layer micromonolith systems motivates the studies described in Chapter 5.

Finally, in the chapter 6, it is presented an interesting comparison among Pt and Au based catalysts being mainly focused on the noble metal nature features depending on the conditions in which those are tested. For further understanding above the different catalytic features between Au and Pt, those were extensively studied by EXAFS and XANES techniques providing fundamental knowledge above the platinum and support structures in WGS conditions.

It should be mentioned that this Thesis is developed under the International PhD normative. According to it, a brief summary containing some introduction, the objectives, the main results and the conclusions will be also presented in Spanish. Simultaneously, some parallel studies were performed under industrial contract supported by "Técnicas Reunidas" which results are not presented on this Thesis because of confidentiality.

Finally, the experimental section and the already published papers and patent in ISI indexed journals are included in annexes at the end of the present PhD Thesis.

References

[1] M.J. Economides, D.A. Wood, J. Nat. Gas Sci. Eng. 1 (2009) 1.

[2] I.H. Son, A.M. Lane, Catal. Letters 76 (2001) 151.

[3] D.C. Elliott, Energy and Fuels 21 (2007) 1792.

[4] C.N. Hamelinck, A.P.C. Faaij, J. Power Sources 111 (2002) 1.

[5] M. Stöcker, Microporous Mesoporous Mater. 29 (1999) 3.

[6] M.E. Dry, Catal. Today 71 (2002) 227.

[7] Y. Wang, K.S. Chen, J. Mishler, S.C. Cho, X.C. Adroher, Appl. Energy 88 (2011) 981.

[8] C. Ratnasamy, J.P. Wagner, Catal. Rev. 51 (2009) 325.

[9] A.R. Dubrovskiy, E. V. Rebrov, S.A. Kuznetsov, J.C. Schouten, Catal. Today 147 (2009) 198.

[10] T. Giroux, S. Hwang, Y. Liu, W. Ruettinger, L. Shore, Appl. Catal. B Environ. 56 (2005) 95.

[11] S.M. Opalka, T.H. Vanderspurt, R. Radhakrishnan, Y. She, R.R. Willigan, J. Phys. Condens. Matter 20 (2008) 064237.

[12] D.L. Trimm, Appl. Catal. A Gen. 296 (2005) 1.

[13] M.A. Edwards, D.M. Whittle, C. Rhodes, A.M. Ward, D. Rohan, M.D. Shannon, G.J. Hutchings, C.J. Kiely, Phys. Chem. Chem. Phys. 4 (2002) 3902.

[14] C. Rhodes, G.J. Hutchings, A.M. Ward, Catal. Today 23 (1995) 43.

[15] M.S. Spencer, Top. Catal. 8 (1999) 259.

[16] G. Jacobs, S. Ricote, P.M. Patterson, U.M. Graham, A. Dozier, S. Khalid, E. Rhodus, B.H. Davis, Appl. Catal. A Gen. 292 (2005) 229.

[17] G. Jacobs, S. Ricote, B.H. Davis, Appl. Catal. A Gen. 302 (2006) 14.

[18] M. Gonzalez Castaño, T.R. Reina, S. Ivanova, M.A. Centeno, J.A. Odriozola, J. Catal. 314 (2014) 1.

[19] G.G. Olympiou, C.M. Kalamaras, C.D. Zeinalipour-Yazdi, A.M. Efstathiou, Catal. Today 127 (2007) 304.

[20] D.C. Grenoble, M.M. Estadt, D.F. Ollis, J. Catal. 67 (1981) 90.

[21] S. Seong, A.B. Anderson, 3654 (1996) 11744.

[22] A. Martinez-Arias, J.M. Coronado, R. Cataluna, J.C. Conesa, J. Soria, J. Phys. Chem. B 102 (1998) 4357.

[23] S. Damyanova, J.M.C. Bueno, Appl. Catal. A Gen. 253 (2003) 135.

[24] A.P. Ferreira, J.C.S. Araújo, J.W.C. Liberatoria, S. Damyanova, D. Zanchetc, F.B. Noronha, J.M.C. Bueno, Stud. Surf. Sci. Catal. 167 (2007) 433.

[25] J.Z. Shyu, K. Otto, J. Catal. 115 (1989) 16.

[26] G. Dutta, U. V. Waghmare, T. Baidya, M.S. Hegde, K.R. Priolkar, P.R. Sarode, Chem. Mater. 18 (2006) 3249.

[27] C.I. Vignatti, M.S. Avila, C.R. Apesteguía, T.F. Garetto, Catal. Today 171 (2011) 297.

[28] G. Jacobs, S. Ricote, U.M. Graham, B.H. Davis, (2014).

[29] V. Idakiev, Z.-Y. Yuan, T. Tabakova, B.-L. Su, Appl. Catal. A Gen. 281 (2005) 149.

[30] J.A. Rodriguez, S. Ma, P. Liu, J. Hrbek, J. Evans, M. Pérez, Science 318 (2007) 1757.

[31] P. Panagiotopoulou, J. Papavasiliou, G. Avgouropoulos, T. Ioannides, D.I. Kondarides, Chem. Eng. J. 134 (2007) 16.

[32] K.R. Hwang, S.K. Ihm, J.S. Park, Fuel Process. Technol. 91 (2010) 729.

[33] G. Jacobs, U.M. Graham, E. Chenu, P.M. Patterson, A. Dozier, B.H. Davis, J. Catal. 229 (2005) 499.

[34] G. Jacobs, L. Williams, U. Graham, D. Sparks, B.H. Davis, J. Phys. Chem. B 107 (2003) 10398.

[35] G. Jacobs, E. Chenu, P.M. Patterson, L. Williams, D. Sparks, G. Thomas, B.H. Davis, Appl. Catal. A Gen. 258 (2004) 203.

[36] G. Jacobs, P.M. Patterson, L. Williams, E. Chenu, D. Sparks, G. Thomas, B.H. Davis, Appl. Catal. A Gen. 262 (2004) 177.

[37] A.A. Phatak, N. Koryabkina, S. Rai, J.L. Ratts, W. Ruettinger, R.J. Farrauto, G.E. Blau, W.N. Delgass, F.H. Ribeiro, Catal. Today 123 (2007) 224.

[38] G. Kim, Ind. Eng. Chem. Prod. Res. Dev. 21 (1982) 267.

[39] M. Flytzani-Stephanopoulos, B.C. Gates, Annu. Rev. Chem. Biomol. Eng. 3 (2012) 545.

[40] S.J. Tauster, S.C. Fung, R.L. Garten, J. Am. Chem. Soc. 100 (1978) 170.

[41] L.L. Murrell, S.J. Tauster, D.R. Anderson, e 10th International Congress on Catalysis Budapest (1993), pp. 19–24.

[42] L.L. Murrel, S. J. Tauster, D. R. Anderson Catal. Automot. Pollut. Control II (1991) 275.

[43] J. Kugai, J.T. Miller, N. Guo, C. Song, J. Catal. 277 (2011) 46.

[44] P.C.A. Brito, D.A.A. Santos, J.G.S. Duque, M.A. Macêdo, Phys. B Condens. Matter 405 (2010) 1821.

[45] C.T. Campbell, C.H.F. Peden, Science 309 (2005) 713.

[46] N. Acerbi, S. Golunski, S.C. Tsang, H. Daly, C. Hardacre, R. Smith, P. Collier, J. Phys. Chem. C 116 (2012) 13569.

[47] F.J. Pérez-Alonso, M. Lopez Granados, M. Ojeda, P. Terreros, S. Rojas, T. Herranz, J.L.G. Fierro, Chem. Mater. 17 (2005) 2329.

[48] G. Xiao, S. Li, H. Li, L. Chen, Microporous Mesoporous Mater. 120 (2009) 426.

[49] G. Avgouropoulos, T. Ioannides, J. Mol. Catal. A Chem. 296 (2008) 47.

[50] A.S. Reddy, C.Y. Chen, C.C. Chen, S.H. Chien, C.J. Lin, K.H. Lin, C.L. Chen, S.C. Chang, J. Mol. Catal. A Chem. 318 (2010) 60.

[51] T. Tabakova, L. Ilieva, I. Ivanov, R. Zanella, J.W. Sobczak, W. Lisowski, Z. Kaszkur, D. Andreeva, Appl. Catal. B Environ. 136-137 (2013) 70.

[52] T. Tabakova, V. Idakiev, D. Andreeva, I. Mitov, Appl. Catal. A Gen. 202 (2000) 91.

[53] T.R. Reina, S. Ivanova, J.J. Delgado, I. Ivanov, V. Idakiev, T. Tabakova, M.A. Centeno, J.A. Odriozola, ChemCatChem 6 (2014) 1401.

[54] O.H. Laguna, M.A. Centeno, M. Boutonnet, J.A. Odriozola, Appl. Catal. B Environ. 106 (2011) 621.

[55] B.M. Reddy, A. Khan, Catal. Surv. from Asia 9 (2005) 155.

[56] S. Damyanova, B. Pawelec, K. Arishtirova, M.V.M. Huerta, J.L.G. Fierro, Appl. Catal. A Gen. 337 (2008) 86.

[57] J. Li, J. Chen, W. Song, J. Liu, W. Shen, Appl. Catal. A Gen. 334 (2008) 321.

[58] A.M. Duarte de Farias, D. Nguyen-Thanh, M. a. Fraga, Appl. Catal. B Environ. 93 (2010) 250.

[59] G. Lafaye, J. Barbier, D. Duprez, Catal. Today (2015) 1.

[60] Y. Peng, W. Yu, W. Su, X. Huang, J. Li, Catal. Today 242 (2015) 300.

[61] S.Y. Choung, M. Ferrandon, T. Krause, 99 (2005) 257.

[62] W. Ruettinger, O. Ilinich, R.J. Farrauto, J. Power Sources 118 (2003) 61.

[63] X. Wang, R.J. Gorte, J.P. Wagner, J. Catal. 212 (2002) 225.

[64] Y. Nagai, K. Dohmae, Y. Ikeda, N. Takagi, T. Tanabe, N. Hara, G. Guilera, S. Pascarelli, M.A. Newton, O. Kuno, H. Jiang, (2008) 9303.

[65] M. El Doukkali, A. Iriondo, P.L. Arias, J. Requies, I. Gandarías, L. Jalowiecki-Duhamel, F. Dumeignil, Appl. Catal. B Environ. 125 (2012) 516.

[66] T.R. Reina, S. Ivanova, V. Idakiev, J.J. Delgado, I. Ivanov, T. Tabakova, M.A. Centeno, J.A. Odriozola, Catal. Sci. Technol. 3 (2013) 779.

[67] F.F. Tao, M. Salmeron, Science 331 (2011) 171.

[68] C.T. Campbell, Top. Catal. 1 (1994) 353.

[69] G.A. Somorjai, Langmuir 7 (1991) 3176.

[70] J.K. Nørskov, T. Bligaard, B. Hvolbaek, F. Abild-Pedersen, I. Chorkendorff, C.H. Christensen, Chem. Soc. Rev. 37 (2008) 2163.

[71] P. Liu, J.A. Rodriguez, J. Chem. Phys. 126 (2007) 164705.

[72] T. Shido, Y. Iwasawa, J. Catal. 141 (1993) 71.

[73] C.M. Kalamaras, S. Americanou, A.M. Efstathiou, J. Catal. 279 (2011) 287.

[74] W. Xu, R. Si, S.D. Senanayake, J. Llorca, H. Idriss, D. Stacchiola, J.C. Hanson, J.A. Rodriguez, J. Catal. 291 (2012) 117.

[75] R. Burch, A. Goguet, F.C. Meunier, Appl. Catal. A Gen. 409-410 (2011) 3.

[76] L.C. Grabow, A.A. Gokhale, S.T. Evans, J.A. Dumesic, M. Mavrikakis, J. Phys. Chem. C 112 (2008) 4608.

[77] J.A. Rodriguez, J.C. Hanson, P.J. Chupas, In Situ Characterization of Heterogeneous Catalysts, wiley, 2013.

[78] A. Bourane, O. Dulaurent, D. Bianchi, J. Catal. 196 (2000) 115.

[79] D.I. Panagiotopoulou, P. Kondarides, J. Catal. 225 (2004) 327.

[80] K. Shyu, J Z, Otto, Appl. Surf. Sci. 32 (1988) 246.

[81] Q. Fu, H. Saltsburg, M. Flytzani-Stephanopoulos, Science 301 (2003) 935.

[82] V. Meille, Appl. Catal. A Gen. 315 (2006) 1.

[83] P. Avila, M. Montes, E.E. Miró, Chem. Eng. J. 109 (2005) 11.

Chapter 1

Experimental techniques for characterization and catalytic activity

Summary

The main aim of the catalyst characterization is to acquire valuable understanding above the catalyst characteristics being it enough deeper to be connected to the differences on the catalytic behavior. The resulted information should provide the needed information for future catalytic improvements. In the present chapter, the principles and/or conditions employed on the physicochemical characterization are briefly described. Besides, the technique specifications of the methods used for the study of the different materials reported on the thesis are also included. Additionally, the operation features chosen for the catalytic activity evaluation of the samples are presented.

1.1. Physicochemical characterization

1.1.1. X-Ray microfluorescence (μXRF)

X-Ray fluorescence (XRF) is the emission characteristic "secondary" (or fluorescence) X-Rays from a material when it is excited by bombarding with high energy X-Rays. Those primary photons penetrate into the sample, it are able to extract electrons from the internal layers of the atoms. The resulted energetic states empties are occupied by electrons which were on others superior energetic states. The relaxing process releases certain energy as photons, X fluorescence radiation or secondary which its long wave is characteristic of each element. Moreover, the μXRF exhibit an intensity which is proportional to the element concentration. Those features make the μXRF technique a suitable one to analyze the chemical composition of the prepared samples.

In this study, the chemical composition of the prepared samples was determined in an EDAX Eagle III spectrophotometer with a rhodium source of radiation working at 40 KV. For the measurements, the samples were dispersed in boric acid pellets and covered by thin wax film.

1.1.2. Textural properties: specific surface area, pore volume and pore size.

The solid materials present a determined surface though which interacts with the media. This surface can be composed by pores which nature will depend

on the material synthesis [1]. The commented pores can be classified as a function of its size (Table 1.1)

Table 1.1. Pores classification depending of the size

Pores type	Size range (nm)
Ultramicropores	$\phi < 0.7$ nm
Micropores	$\phi < 2$ nm
Mesopores	$2 \text{ nm} < \phi < 50$ nm
Macropores	$\phi < 50$ nm

Among the techniques developed for surface studies, the N_2 adsorption at its boiling temperature (196.2 ºC) is one of the most employed and provides an adsorption isotherm which relates the adsorbed N_2 volume with its partial pressure. The isotherm profile allows stablishing the surface area and pore volume and shape of the studied material.

The surface area, which is expressed in m^2/g, represents the accessible surface of the material where a determined adsorbate can be adsorbed by gram of sample. The specific surface is determined by the BET method and corresponds to the sum of the internal surface of the pores and the external surface of the grains.

The pore volume, expressed in cm^3/g represents the inner and outer granular volume.

Moreover the average pore size (Å) can estimated as the ratio of the pore volume and the specific surface area normalized using a coefficient that depends on the pore shape.

The N_2 adsorption experiments were carried out on a Micromeritics ASAP 2010 instrument. Prior the analysis, the samples were degassed for 2 h at 150 ^{o}C in vacuum. The BJH method was employed for determining the pore size distributions.

1.1.3. X-Ray diffraction (XRD)

The X-Ray diffraction is a characterization technique no destructive which provides structural information of crystalline materials. The XRD technique provides information of the crystalline phases constituting the material and, with some refining, provides a quantification of those phases.

In the diffraction phenomena, it happens a coherent and elastic dispersion (Rayleigh diffusion) which is produced when the X radiation interacts to the electrons that constitute the crystallographic planes. The diffracted waves are produced by the constructive and destructive interferences of the dispersed waves of each atom. Considering that either the position as the properties influence the dispersion, each solid diffracts depending on its structure.

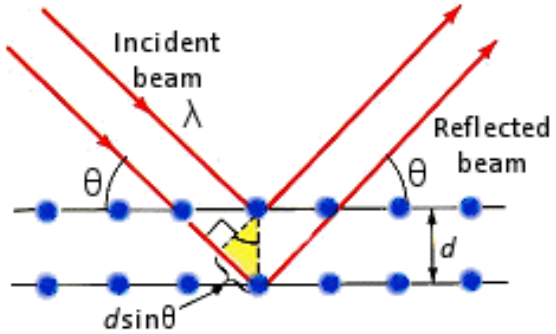

Figure 1.1. Bragg's reflection from the crystallographic layers

The interaction of the incident X rays with the sample diffracts when the conditions satisfy the Bragg's Law (Eq. 1.1) This law relates the wavelength of electromagnetic radiation to the diffraction angle and the lattice spacing in the crystalline sample. The diffracted X-rays are then detected processed and counted. By scanning the sample along a range of 2θ angles, all possible diffraction directions of the lattice should be attained due to the random orientation pf the powered material.

$$n\lambda = 2d\sin\theta \qquad \textit{Equation 1.1}$$

From XRD, the crystalline domain of the sample can be also calculated through the Scherrer's equation (Equation 1.2) where t represents the crystallite size; K is a constant which depends on the shape factor of each material (typically 0.9); λ is the long wave of the indicident radiation and β is the half-height width.

$$t = \frac{K\lambda}{\beta Cos\theta} \qquad \textit{Equation 1.2}$$

In this Thesis, the XRD measurements were performed on an X'Pert Pro PANalytical employing the Cu K_α radiation (40mA, 45 kV) over a range of 10 to 95º using a step size of 0.05 and step time of 240 s.

1.1.4. Transmission and Scanning Electron Microscopy: TEM and SEM.

Contrary to the optic microscopies, the electron microscopy employs as lighting source an electronic beam possessing a very short long wave which interacts to the sample. In the TEM microscopy, the electron beam passes through an ultra-thin sample. The image is formed from the interaction of the transmitted electrons through the system; the image is magnified and focused onto an imaging device, such fluorescent screen, a photographic film or to be detected by a sensor such as CCD camera. This technique allows the evaluation of the micromorphology of the catalysts as well as the presence of different crystalline phases. This technique permits the analysis of nanomaterials from some nanometers (low resolution TEM) up to angstroms (high resolution TEM).

For the SEM microscopy the electron beam instead to pass through the sample, the surface of the sample is scanned generating secondary electrons from the sample allowing the image generation. This technique also provides morphological information of the surface but its resolution limit is lower (in the best case, above 1 nm) than that offered by the TEM microscopy.

Additionally, both techniques allow the study of the chemical composition through Energy dispersive X-Ray spectroscopy (EDX) from the radiation emitted by the sample when it is excited with electromagnetic radiation.

The High-Resolution Transmission Electron Microscopy (HRTEM) and High Angle Annular Dark Field-Scanning Transmission Electron Microscopy (HAADF-STEM) images presented on this Thesis were recorded on a JEOL2010F instrument. The spatial resolution at Scherzer defocus conditions in HRTEM mode is 0.19 nm meanwhile the HAADF-STEM studies were performed using an electron probe of 0.5 nm of diameter and diffraction camera length of 10 cm. The employed EDX instrument was Oxford Instrument, Inca Energy-200. Loose power samples were supported on a holey carbon-coated copper grid without using any solvents. The excess of the sample was removed with N_2. This approach allows obtaining electron transparent ultrathin regions.

On the other hand, the SEM microscopies presented in this memory were obtained in Hitachi® S-4800 SEM-FEG provided with secondary and retrodispersed electron detectors.

1.1.5. Raman and Infrared (IR) spectroscopies

The energy of the molecules can be associated mainly to three components: i) the electron movement, ii) the vibration of the constituent atoms and iii) the rotation of the molecule. This classification obeys to the different time scales

in which the each kind of vibration happens being the electronic vibration significantly faster than the rotational ones.

The vibrational transitions observed in Raman or Infrared spectroscopy can be obtained after the excitation of a molecule with an adequate radiation source in a long wave range (λ) comprised between 10^{-2} and 10^{-4}. The observed vibrational transitions proceed from the atomic cores which constitute the molecules. However, no all the transitions are allowed but for each molecule the transition number depends on its symmetry and on the selection rules.

Despite of the different physical origin of Raman and IR spectroscopies, both techniques provide structural information of the studied sample because of the relation between the observed bands in the respective spectra and their molecular symmetry. The IR adsorption spectra are produced by photons in the IR region which are absorbed by two vibrational levels of the molecule in its energetic basal state. On the other hand, Raman spectra are originated because of the polarization caused after the sample irradiation with energies (ultraviolet, visible or near-infrared).

So, the Raman experiment were carried out in a dispersive microscopy Horiva Jobin Yvon® (HR800) with a confocal aperture of 1000 μm, using an objective 50x and a green laser (λ = 532.14 nm). The laser potency was reduced to 5 mW through an optical density filter D0.6.

The IR spectroscopies were performed in transmission mode being the IR radiation passed through the sample. The samples were pilled without any

diluent presenting a diameter of 15 mm. FTIR spectra were recorded using THERMO NICOLET Avatar 380 FT-IR Spectrophotometer, equipped with a DTGS/ KBr detector, and accumulating 128 scans at a spectral resolution of 4 cm^{-1}. The experiments were performed in situ using a purpose-made IR cell connected to a conventional vacuum adsorption apparatus with a residual pressure lower than 10−5 mbar.

1.1.6. UV-Vis spectroscopy (UV-Vis)

Ultraviolet-visible spectroscopy (UV-Vis) refers to absorption or reflectance spectroscopy in the ultraviolet-visible spectral range corresponding to electronic transitions in the measures samples. This implies, that r uses light in the visible and adjacent regions, near-UV and near-infrared (NIR).

The absorption or reflectance in the visible range directly affects the perceived color of the samples. This technique is complementary to the fluorescence spectroscopy. Meanwhile fluorescence deals with the transitions from the excited to the ground state, the absorption measurements transitions from the ground to the excited state. There three main transitions that can be considered:

- *d-d transitions:* They are typical of transition metals ions. These electronic transitions principally give rise to adsorption in the visible range and are therefore responsible for the color of transition metal complexes.

- *Charge-transfer transitions:* They involve an electronic transfer from the occupied orbital towards empty ones.
- $\pi - n^*$ *and* $n - \pi^*$ *transitions:* They normally occur on organic molecules due to the electronic transitions between *n* and π orbitals.

The UV-Vis spectra were recorder on a Varian spectrometer model Cary 100, equipped with integrating sphere and using $BaSO_4$ as reference. All the spectra were recorded in a diffuse reflectance mode and transformed to a magnitude proportional to the extinction coefficient through the Kubelka-Munk function $F_{(R\infty)}$[2].

$$F_{(R\infty)} = \frac{(1-R_\infty)^2}{2\,R_\infty} \propto \frac{\kappa}{\sigma} \qquad \textit{Equation 1.3}$$

In practice, R_∞, is the reflectance of a layer so thick that further increase of the thickness does not change the reflectance. κ is the absorbance in cm^{-1} and σ is the dispersion factor that it is assumed to be independent of the wavelength for the particles with grain size higher than the light wavelength.

1.1.7. Temperature programmed techniques: TPR, TPD and TPO

TPD studies are very useful in catalysts characterization providing useful information above the surface properties which will depend on the gas composition employed and the operative conditions. For the sample analysis, the sample is exposed to certain as stream and the temperature is increased following a temperature program. The TPD experiments were carried out in a PID Eng &Tech using a conventional quartz reactor.

The Temperature Programed Reduction (TPR) experiments provide information about the reducibility of the species [3] and they were performed using 5 % H_2 in Ar and the temperature was increased at 10 ºC/min. The feed stream is bifurcated in two lines; one of them is passed through the sample contrary to the other one which is employed as reference. The difference between the H_2 inlet and the outlet is the measured as a function of the temperature by using a thermal conductivity detector (TCD). A molecular sieve 13X was used to retain the H_2O produced during the reduction. For the quantitative analysis the TCD signal was calibrated with a CuO pattern (Strem Chemicals 99.999%).

The Temperature Programmed Desorption/Oxidation (TPD/TPO) allows obtain information related to the nature of the adsorbed species [4]. TPD /TPO measurements were carried out at atmospheric pressure in a conventional U-shape quartz reactor. The gas composition was analyzed at the exit of the reactor by a mass spectrometer PFEIFFER Vacuum PrismaPlus controlled by the program Quadera®. For the TPD experiments, the reactive gas stream employed flushed through the sample was Argon 99.999 (Air Liquid) meanwhile a 5 % O_2 (Air Liquid) balanced in Ar was used for the TPO tests.

1.1.8. Oxygen storage complete capacity (OSSC) and oxygen storage capacity (OSC)

Surface migration of oxygen can be of utmost importance in oxidation processes in which the catalysis are submitted to repeated changes in the gas composition [5]. In this sense, the Oxygen storage complete capacity (OSSC) and the Oxygen storage capacity (OSC) provide very useful information about the redox properties of the samples.

For the OSCC 100 mg of catalysts was loaded and firstly oxidized into a U-shaped quartz reactor using a 5% O_2/Ar flow until 350 ºC. Then, the sampled is set to the desired temperature and submitted to ten equivalent CO pulses. The OSCC is obtained from the total CO_2 produced in all CO pulses. The samples are degassed in Ar flow and subjected to a new series of oxidizing (ten O_2 pulses).

For the OSC experiment, the sample is exposed to 5 alternating pulses (O_2-CO-O_2-CO-O_2-CO). The OSC is determined by the average amount of CO_2 per pulse formed after the first CO pulse of the alternated ones. This method is based on the one presented by Duprez et al [5,6]. The gas composition was analyzed by a mass spectrometer PFEIFFER Vacuum PrismaPlus controlled by Quadera® software.

1.2. Catalytic activity

The Water Gas Shift reaction was performed using the home-made equipment shown in the Figure 1.2. The temperature range was raised in the 180-350 ºC range using two reaction conditions labeled model or ideal and realistic conditions. For the model WGS reaction just water and CO diluted in N_2 were used while for the realistic WGS reaction a reformate gas surrogate containing H_2 and CO_2. The later conditions were chosen in order to simulate the outlet of a typical ethanol reformer and they are also known as CO clean-up conditions.

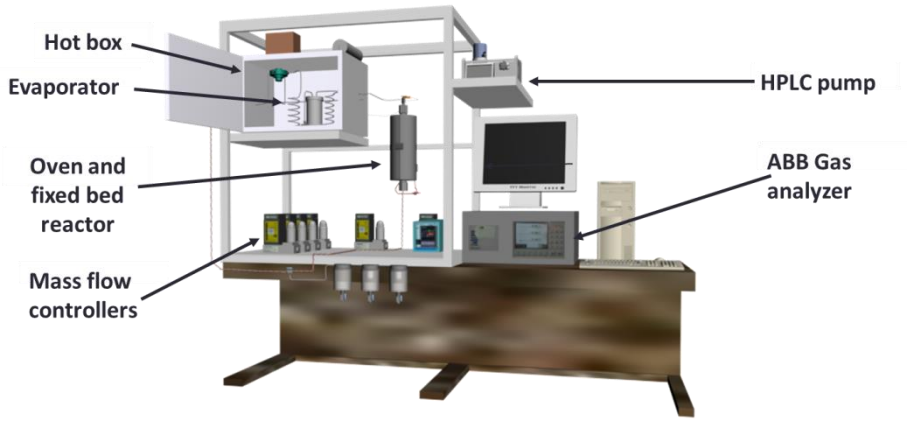

Figure 1.2. Experimental set-up for the WGS reaction

For the entire catalytic test, the solids were sieved and the 600-800 μm fraction retained. The GHSV was estimated as the ratio feed flow to catalyst bed volume and expressed in h^{-1}. The CO and CO_2 content was analyzed with

an ABB gas analyzer and the activity expressed in terms of CO conversion. The CO conversion was estimated according to the equation 1.4.

$$CO\ conversion\ (\%) = \frac{CO_{in} - CO_{out}}{CO_{in}}\ x\ 100 \qquad \textit{Equation 1. 4}$$

References

[1] G. Leofanti, M. Padovan, G. Tozzola, B. Venturelli, Catal. Today 41 (1998) 207.

[2] H.G. Völz, 13 (1985) 153.

[3] S.D. Robertson, B.D. McNicol, J.H. De Baas, S.C. Kloet, J.W. Jenkins, J. Catal. 37 (1975) 424.

[4] D.P. Woodruff, T.A. Delchar, (1986).

[5] S. Kacimi, J.B. Jr, R. Taha, D. Duprez, Catal. Letters 22 (1993) 343.

[6] S. Royer, D. Duprez, ChemCatChem 3 (2011) 24.

Chapter 2

Synthesis and characterization of Pt based catalysts: catalytic screening

Summary

In this chapter, the synthesis parameters are described, e.g. platinum deposition method and loadings and support nature. The goal was to select the features for the starting catalyst of the thesis. With that purpose, platinum was deposited on two different commercial supports: a high surface γ-Al_2O_3 and on a CeO_2/Al_2O_3 (Puralox) both supplied by Sasol. For each support, two platinum contents were chosen: 2wt. % and 4wt. %. A homemade CeO_2/Al_2O_3 support with its corresponding catalyst (4% platinum content) was also prepared. The catalysts were tested in WGS reaction and some general characterization techniques such as XRMF, S_{BET}, XRD and TPR were employed to comprehend the observed catalytic behavior and to relate it to the support nature and platinum content.

2.1. Introduction

Heterogeneous catalysts could be classified as complex systems considering both composition and structure. The catalysts generally are constituted by support and active phase. In WGS reaction, the support choice is an essential feature that must be carefully carried out in order to achieve highly active catalysts. An optimal support must possess several characteristics; for example, it should be a thermostable material with high mechanical resistance and high porosity. The main scope of the support is to achieve an excellent active components dispersion and to avoid its sintering, thus increasing the life time of the catalysts. However, for many catalytic processes, the support is not an inert material but plays a key role in the catalytic reaction [1].

The Al_2O_3 has been extensively studied and widely employed as catalytic support in industrial processes [2–5]. Among the possible Al_2O_3 phases, the γ-Al_2O_3 is one of the most used because of its high surface area, pore volume and thermal stability [6]. Despite of the variety of experimental and computational [6,7] studies, there is still a considerable debate about the structure of γ-Al_2O_3. The structure of γ- Al_2O_3 is traditionally considered as a cubic defect spinel type. The oxygen lattice is built up by a cubic close-packed stacking of oxygen layers, with Al atoms occupying the octahedral and tetrahedral sites. To satisfy the γ- Al_2O_3 stoichiometry some of the lattice

positions should remain empty (vacancies creation). Regarding the redox activity of the alumina, it is considered as "irreducible" support.

Contrary to the γ-Al_2O_3 support, the cerium oxide is a "reducible" oxide and it has also become a widespread support in heterogeneous catalysis [8–12]. The CeO_2 crystallize within a cubic fluorite type structure, forming a face centered cubic cell (fcc). In Figure 2.1, it can be observed that Ce^{4+} cations placed in the faces and in the corners of a cube formed the fcc packing, being each one surrounded by eight equivalent oxygen anions occupying the tetrahedral holes where tetrahedrally coordinated for four Ce^{4+} neighbors.

The relevance of cerium oxide is mainly based on its oxygen storage capacity resulting from oxygen mobility in its lattice. The oxidation state of the cerium oxide changes, through relaxing or catching oxygen atoms, in reductive or oxidant atmospheres. The oxygen absence in cerium oxide structure provokes a point defect, known as oxygen vacancy. The oxygen vacancies should migrate to stabilize the system due to the Gibbs energy minimization requirement [13,14] which occurs especially at the surface. The oxygen mobility of the ceria is then directly related to the creation, stabilization and diffusion of those oxygen vacancies, due to the reversible redox behavior of the Ce^{4+}/Ce^{3+} couple of CeO_2 and leading to the formation of non-stoichiometric oxides CeO_{2-x} ($0 < x < 0.5$).

The easier oxygen vacancies formation within the cerium oxide constitutes the key factor for its application in catalytic systems, inasmuch as the high ionic mobility converts it in an oxygen storage oxide. Pointing to its catalytic activity in the oxidation reactions and more particularly in the WGS reaction the ceria' oxygen storage capacity (OSC) has been demonstrated to participate in the reaction mechanism forming in its oxygen vacancies either reaction intermediates [15] or acting as centers for active phase nucleation leading to higher metal dispersions and higher overall activity per active site [16–21]. Moreover, the excellent catalytic properties of cerium oxide could be maintained also by supporting a thin ceria oxide layer on an irreducible oxide, such as alumina [22–25]. Referring to the latter, the noble metal (platinum) was deposited on two available commercial supports (Sasol): γ-Al_2O_3 and CeO_2/γ-Al_2O_3 containing 20 wt.% cerium oxide. For sake of comparison a "home-made" - CeO_2/Al_2O_3 support was also prepared mimicking the commercial support composition.

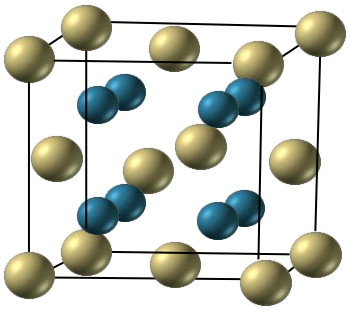

Figure 2.1. Cerium oxide unit cell

On the other hand, two different platinum contents were chosen for the commercial supports (2 and 4 wt.%) meanwhile only the 4 wt.% loading was selected for the "home-made" CeO_2/Al_2O_3 support.

2.2. Synthesis of the catalysts

CeO_2/Al_2O_3 support synthesis

The "home-made" CeO_2/Al_2O_3 support was prepared by wetness impregnation using $Ce(NO_3)_3 \cdot 6H_2O$ as ceria precursor. The latter was dissolved in ethanol and impregnated on high specific surface area γ-Al_2O_3. Once the solvent excess removed at reduced pressure and 50 ºC in a rotavapor, the resulting solid was dried at 120 ºC. Finally, the support was calcined 4h at 450ºC with 10ºC/min heating ramp. The "home-made" CeO_2/Al_2O_3 support was labeled CeAl HM.

Pt deposition

The nominal Pt contents were 2 and 4 wt.%. The corresponding support powder was sieved in order to obtain a fraction between $100 \leq \phi \leq 200$ μm. The Pt was deposited by wetness impregnation using Tetrammineplatinum (II) Nitrate Solution ($[Pt(NH_3)_4(NO_3)_2]$ as precursor. The Pt precursor solution was mixed with 1M acetic acid in 1:1,1 molar ratios. After impregnation, the solids were dried and calcined 8h at 350ºC using 5ºC/min as heating ramp.

The nomenclature for the catalysts based on alumina was Pt(2%)/Al_2O_3 and Pt(4%)/Al_2O_3. For the CeO_2-Al_2O_3 commercial support was denoted as Puralox and the catalysts prepared from it as Pt(2%)/Puralox and Pt(4%)/Puralox depending on the Pt content. Accordingly, the platinum based catalyst deposited on CeAl HM was named Pt(4%)/CeAl HM.

2.3. Physicochemical characterization of the samples

2.3.1. Textural properties and chemical composition

In the Figure 2.2, the N_2 adsorption-desorption isotherms for the obtained solids are shown. All of them exhibit type IV isotherms, which according to IUPAC [26] are typical for mesoporous solids. For this type of solids once a monolayer adsorbed, the adsorption proceeds to multilayer formation giving a significant adsorption volume increase.

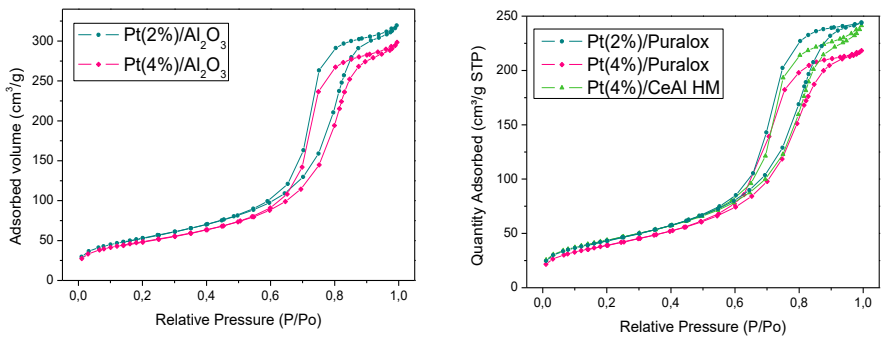

Figure 2.2: N_2 adsorption-desorption isotherms for the synthetized solids.

The following desorption process takes place at lower pressures than the capillary condensation and results in hysteresis. All the solids present H1 type

hysteresis, indicative of the presence of pores in a relatively uniform shape and size. Particles crossed by nearly cylindrical channels or spheroidal particles aggregates (consolidated or not) are associated with H1 hysteresis.

In Table 3.1 the textural properties of the studied systems are shown. Al_2O_3 support presents the highest specific surface area, which decrease with the ceria addition. Further, the platinum addition, no matter the support, leads to decrement in the specific surface area and pore diameter (d_{pore}) values. On the other hand, the pore volume (V_{pore}) decreases with the platinum addition suggesting that platinum particles are probably growing inside the pores.

Table 2.1: Textural properties of the samples

	S_{BET} (m^2/g)	v_{Pore} (cm^3/g)	d_{Pore} (Å)
Al_2O_3	202	0.51	74
Puralox	165	0.40	71
CeAl HM	165	0.34	68
Pt(2%)Al_2O_3	192	0.49	70
Pt(4%)Al_2O_3	175	0.47	71
Pt(2%)/Puralox	156	0.38	66
Pt(4%)/Puralox	142	0.34	65
Pt(4%)/CeAl HM	147	0.31	69

The CeAl HM support presented similar specific surface area to that of Puralox with slight variations in pore diameter and important decrease in pore volume. The pore size distribution of the solids is shown in Fig. 3.3. By

comparison between the commercial supports, it can be observed narrower pore size distribution for the pure alumina containing solids. When Pt is deposited on alumina, no matter the content, the pore size distribution does not change, being the maximum placed at around 7.5 nm. Contrary to the alumina supported catalysts, the platinum loadings increase modifies the pore size distribution when Puralox is employed as a support. The pore size distribution becomes wider and the pore size maximum is shifted to higher pore diameter values, when platinum content changes from 2 wt.% to 4 wt.%. Even so, all the prepared solids maintain their mesoporous character.

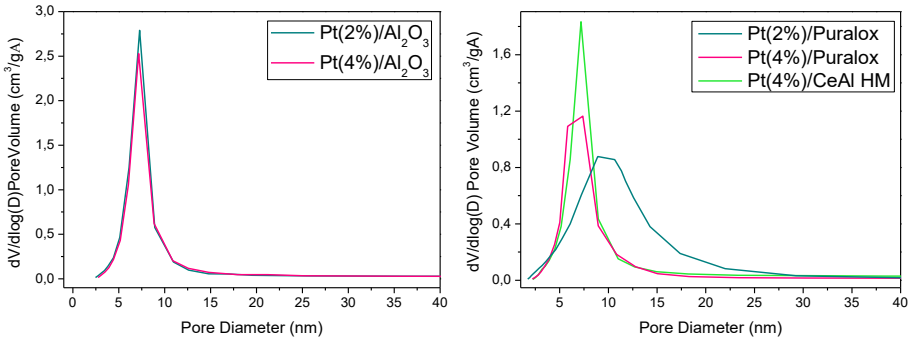

Figure 2.3: Pore size distribution of the prepared solids.

The chemical composition determined by μ-XRF is listed in Table 2.2. Although very close to the desired nominal values the chemical analysis shows some variation in the platinum contents.

All the prepared samples present chemical compositions very close to the targeted ones indicating the suitability of the synthesis method employed either for the commercial support or for the homemade one.

Table 2.2: Chemical composition of the prepared solids.

	% wt. Al_2O_3	% wt. CeO_2	% wt. Pt
Al_2O_3	100	-	-
Puralox	79.3	20.7	-
CeAl HM	80.1	19.9	-
Pt(2%)/Al_2O_3	98.3	-	1.7
Pt(4%)/Al_2O_3	96.5	-	3.5
Pt(2%)/Puralox	79.4	18.8	1.8
Pt(4%)/Puralox	77.5	18.1	4.4
Pt(4%)/CeAl HM	76.5	19.7	3.8

2.3.2. XRD analysis

The XRD diffraction patterns for alumina and ceria based catalysts are presented in the Figure 2.4.a and 2.4.b respectively, being the corresponding primary support also included. All the characterized solids were highly amorphous as detected from the broad signals exhibited in all the cases. The employed alumina shows the characteristic diffractions of the γ-Al_2O_3 phase (JCPDS: 00-050-0741). Regarding to the alumina supports, the platinum incorporation does not lead to any important changes in the registered diffractograms. No platinum diffractions were detected which indicates that

the platinum phase should be well dispersed with sizes lower than the detection limit of the technics, around 4 nm.

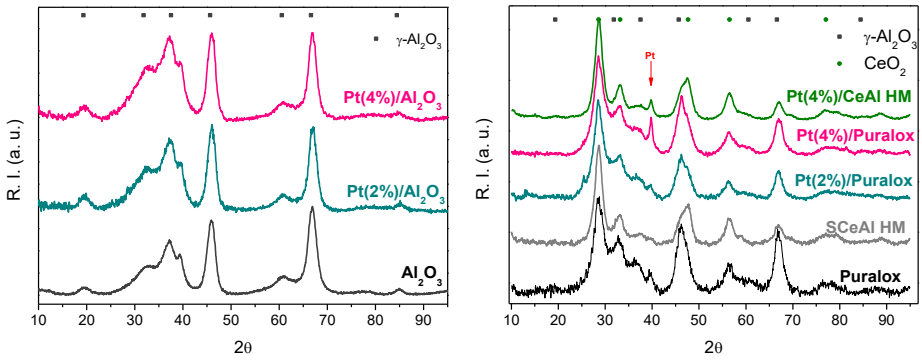

Figure 2.4: XRD diffraction patterns: a) γ-Al_2O_3 support and alumina supported platinum catalysts; b) CeO_2-Al_2O_3 supports and ceria supported platinum based catalysts

In Figure 2.4.b, it can be observed the typical diffractions corresponding to γ-Al_2O_3 (JCPDS: 00-050-0741) and CeO_2 (JCPDS: 00-004-0593). The ceria lattice parameters and crystallite size were estimated by using $a = \sqrt{h^2 + k^2 + l^2} \cdot (\frac{\lambda}{2\ sin\theta})$ and Scherrer`s equation respectively (Table 2.3). Both calculations were carried out considering the (111) ceria diffraction above 2θ = 28.5º (where no contribution of γ-Al_2O_3 phase is observed). Both supports, commercial or home-made, present a similar CeO_2 lattice parameter, typical for those kind of solids [27] and different crystallite size, being the home-made support slightly larger in size.

Table 2.3: Crystallite size for Pt and CeO_2 species. Lattice parameters for CeO_2.

	$Pt_{Crystal\ Size}$ (nm)	$CeO_{2\ Lattice\ parameter}$ (Å)	$CeO_{2\ Crystal\ Size}$ (nm)
Puralox	-	5.41	3.9
CeAl HM	-	5.41	4.7
Pt(2%)/Puralox	(not observed)	5.41	4.7
Pt(4%)/Puralox	25.6	5.39	4.4
Pt(4%)/CeAl HM	13.6	5.40	5.5

Moreover, the effect of platinum addition on the ceria phase was analyzed. When lower platinum loadings are employed, Pt(2%)/Puralox, no modifications for ceria lattice parameter are detected. On the contrary, for higher platinum contents lattice parameter diminution is observed. Regarding the ceria crystallite size, minor increment for all the systems is observed with the incorporation of platinum.

No diffraction lines corresponding to PtO_x species are observed for the lower platinum loading. However the increase of the platinum loading up to 4 wt. %, leads to signal corresponding to metallic platinum at around $2\Theta = 39.5^{o}$. This suggests: i) partial platinum reduction from Pt^{2+} to Pt^{0} happens during the calcination step and ii) at least, the presence of Pt^{0} fraction with particle size larger than 5 nm. Besides, this peak intensity appears to depend on the support, being significantly lower in the case of the CeAl HM support. The Pt particles size was estimated by Scherrer's equation and presented in Table

2.3. The Pt particle size for the Pt(4%)/CeAl HM sample is almost twice lower than that of the Pt(4%)/Puralox sample. The substantial platinum particle decrement could indicate stronger platinum support interaction able to stabilize low sized Pt particles.

2.3.3. TPR studies

The reducibility of the samples was studied by H_2-TPR experiments. H_2 consumption profiles are presented in the Figure 2.5 in which a tentative peak deconvolution was made. It should be noted that this data processing does not represent an adequate peak deconvolution process. For that, the kinetics of each process must be taken into account. Therefore, it is just a visual aid to interpret the results.

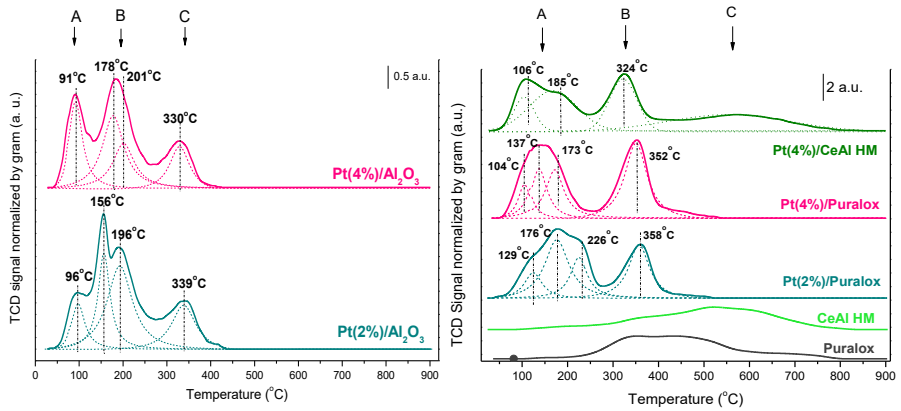

Figure 2.5: TPR profiles: a) γ-Al_2O_3 support and platinum alumina based catalysts; b) CeO_2-Al_2O_3 support and platinum ceria based catalysts

In general, the behavior of the platinum based catalysts during reductive (and/or oxidative) thermal treatment strongly depends on several parameter

such as platinum loading, metal dispersion, temperature of the treatment, synthesis method and nature of support on which the platinum is deposited

Considering that the Al_2O_3 is a non-reducible oxide, the H_2 consumption observed for the platinum/alumina samples should be solely attributed to the platinum species reduction processes (Figure 2.5.a). For both metal loadings, the platinum reduction takes place between 50 and 500ºC. The reduction profiles exhibit three H_2 consumption zones labeled A, B and C, in ascending order of temperature. In addition, the alumina based catalysts present two overlapped reduction processes in zone B.

The discussion about the reducibility of the platinum species will be developed mainly considering platinum particle sizes and noble metal support interactions being both features closely related. At this point, it should be highlighted that no platinum oxidized species are detected on XRD data. Hence, when referring to larger platinum particle sizes implies particles lower than 4 nm.

Mills et al. [28] suggested that highly dispersed Pt on Al_2O_3 rapidly oxidized to Pt^{4+} in air to form PtO_2. So, the higher H_2 uptake could reflect greater platinum oxidation degree after the calcination process where Pt^{2+} species are oxidized to form small PtO_2 particles more easily reduced than isolated Pt^{2+} species [29].

Damyanova et *al.* [30] reported for Pt/alumina catalysts that PtO_x particles were almost entirely reduced to Pt^0 at 86 ºC, although, some minor fraction can be reduced to Pt^{2+} species. In our alumina based systems, the reduction centered at 91ºC could indicate the formation and reduction of PtO_2 species. This process contribution seems to increase with Pt loading, being higher the relative H_2 consumption for the $Pt(4\%)/Al_2O_3$ sample indicating also higher PtO_x population. In addition, Fukushima et *al.* [31] proposed that the degree of oxidation of Pt species increase with the diameter of Pt crystallites. In our case, it is not unexpected that the highest platinum content leads to bigger platinum particle size. Moreover, in this zone (zone A) H_2 spillover phenomena should be also considered being commonly assumed that the first reduction step involves H_2 dissociation. This step is facilitated when two hydrogen adsorption sites are close to each other, e.g. on higher size platinum particles.

Merler et al. [32] observed two H_2 consumptions centered at around 100 ºC and 300 ºC associated to PtO_x of different particle sizes and noble metal-support interaction: stronger the interaction, higher the temperature of reduction. This zone for $Pt(2\%)/Al_2O_3$ is constituted by two different H_2 consumptions centered at 156 and 196°C. Both of them could be related to the reduction of different crystallite size PtO_x species weakly interacting with the Al_2O_3 support to Pt^0 [33–37].

Same processes are observed also for the Pt(4%)/Al_2O_3. So, increased Pt contents could lead to reduction processes shifted to higher temperatures possessing each one, different relative H_2 consumptions. No matter the content, the intermediate reduction zone appears to be composed by two kind of platinum species being lower its reduction temperature when the interaction is weaker and/or when the size is bigger. The observed changes on the relative H_2 consumptions on the intermediate reduction zone can be explained considering that higher platinum content may entail bigger platinum particles, including higher percentage of PtO_x species reduced in that zone B.

Highly dispersed PtO_x species are more difficult to reduce due to the strongest interaction with the support. Tiernan [38] described a PtO_x reduction step at *ca.* 420°C due to the strong interaction between highly dispersed PtO_x and Al_2O_3 (PtO_x-Al_2O_3) and its high capacity to stabilize the oxidized platinum particles [39–47].

The H_2-TPR profiles of the ceria based systems are presented in Figure 2.5.b. In general, cerium oxide presents two reduction processes, associated to the surface and bulk reduction process [48,49]. In our case, both ceria/alumina samples, the commercial and homemade, show one broad reduction step constituted of surface reduction process. The homemade oxide presents higher temperature of reduction. No bulk reduction process is observed for any support indicating either that the whole ceria is behaving as surface ceria or

that the bulk reduction process overlaps with the surface one. However, the possibility that the bulk ceria is no reduced even at 900 ºC cannot be totally discarded. The platinum addition to those supports strongly enhances the reducibility, mainly by shifting the H_2 take up towards lower temperatures. Platinum/Puralox based samples present two reduction zones. The reduction step situated at lower temperature (A) is composed by few contributions - reduction of PtO_x species weakly interacting with the support, spillover effects and support reduction processes. The second reduction zone (B) is associated with PtO_x-CeO_2 interface reduction, lower the Pt particle size higher the noble metal-support interactions and higher the temperature of reduction.

The main difference regarding the reducibility among the commercial and the homemade support remains on the third reduction step only observed for the Pt/homemade sample. While A and B zones should comprise similar reduction processes as described for Puralox based catalysts, the new C zone appear to be mainly due to pure support reduction process.

It is also possible to calculate and compare the reducibility percentage (RP) within the samples series by using the Equation 2.1.

$$RP = \frac{E_{HC}}{T_{HC}} \times 100 \qquad \textit{Equation 2.1}$$

The PR relates the experimentally measured H_2 consumption (E_{HC}) to the total theoretical H_2 consumption (T_{HC}). The T_{HC} will depend on the oxidation state considered for the reducible species. So, Ce^{4+} species were assumed as the initial oxidation state for ceria ones. As it will be shown on Chapter 6, Pt species in ceria presence were identified mainly as Pt^{2+}. However, a possible oxidation reaction from Pt^{2+} to Pt^{4+} species during the calcination step cannot be definitely excluded in the case of the alumina supported catalysts. Hence, the reduction reactions considered for each oxide are:

$$2\,CeO_2 + H_2 \rightarrow Ce_2O_3 + H_2O \qquad \textit{Equation 2. 2}$$

$$PtO + H_2 \rightarrow Pt + H_2O \qquad \textit{Equation 2. 3}$$

$$PtO_2 + 2H_2 \rightarrow Pt + 2H_2O \qquad \textit{Equation 2. 4}$$

The calculated RPs of the samples are presented in Table 2.3 and the relative H_2 consumption in the differently defined reduction zones in Figure 2.6. Except the alumina based catalysts when Pt^{4+} species are considered, all the samples present reducibility percentages close to 100%. Since metallic platinum species were detected for the calcined samples, those higher RP values mean H_2 overconsumption which could be assigned to hydrogenation reactions of carbon deposits around Pt particles as well as organic rests from the synthesis method. Moreover, the detected H_2 overconsumptions should be also related to spillover effects that happen on Pt particles and lead to a reversible dynamic surface equilibrium through which the H_2 molecules are

continuously dissociated and reassociated [50]. Then, the H dissociated species can be diffused to the support resulting on a favored support reduction [51] and/or on H species incorporation to the in the case of ceria based supports [52].

Table 2.3: Reducibility percentages (RP) of the prepared samples.

	Pt(2%)/ Al_2O_3	Pt(4%)/ Al_2O_3	Puralox	Pt(2%)/ Puralox	Pt(4%)/ Puralox	CeAl HM	Pt(4%)/ CeAl HM
RP (%)	90 (192)	95 (196)	78	90	95	76	91

In parenthesis, the RP calculated just for alumina based catalysts assuming Pt^{4+} species.

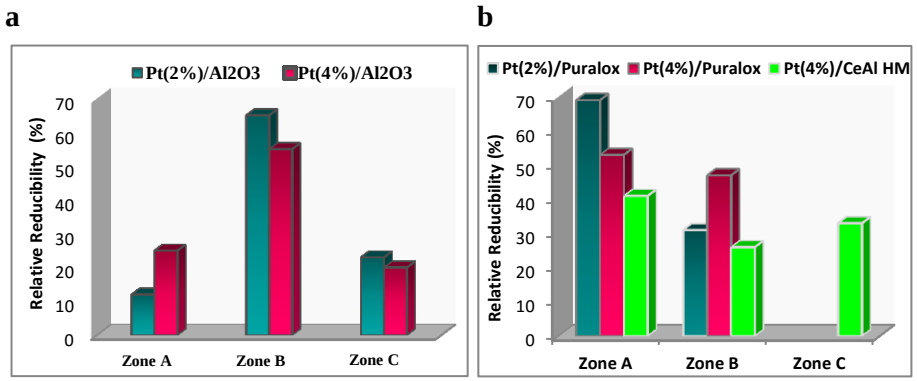

Figure. 2.6. Relative RP of each H_2 consumption zones as a function of the employed support: a) alumina support; b) ceria supports.

For the alumina based catalysts, a variation on the relative H_2 uptake for the first reduction step (zone A) is observed as a function of the noble metal

content: higher the platinum content, higher the H_2 consumption. This could be tentatively related to higher PtO_x particles, more easily reducibly because of the lower metal-support interaction. Hence, higher platinum loading results in higher oxidized platinum fraction, formed during the calcination. The Pt loading increase does not affect significantly the other zones of reduction (zone B and C).

For the platinum/ceria based catalysts, the relative H_2 consumption distribution within the zones changes the tendency. High relative H_2 consumption in the low temperature zone (A) is observed for the Pt(2%)/Puralox sample, suggesting the presence of higher size Pt particles for this sample. On the other side, the higher relative H_2 consumption in zone B for Pt(4%)/Puralox sample indicates lower Pt size, contrary to the expected for the increased Pt content.

2. 4. Catalytic activity

The WGS activity of the samples is shown in Figure 2.7. All platinum catalysts reach the equilibrium CO conversion. The temperatures at which the catalysts achieve the equilibrium conversion strongly depend on the support. For example, $Pt(2\%)/Al_2O_3$ sample reach the equilibrium conversion at around 310 ^{o}C while Pt(2%)/Puralox does it at 230 ºC. The catalytic results clearly evidence the importance of the support nature for this reaction. The ceria based catalysts show an important enhancement of the catalytic activity

in respect to alumina supported samples. The boosted catalytic performance could be related to the Ce^{3+}/Ce^{4+} redox couple presence and its fast interconversion and imperative participation in the WGS reaction.

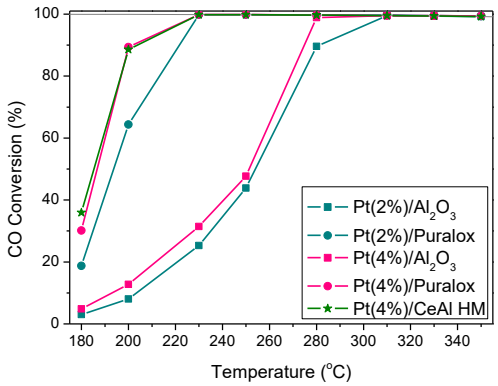

Figure 2.7. WGS activity of the analyzed catalysts in model conditions (4.5%CO + 30%H_2 + N_2 balanced) at GHSV=4000h^{-1}.

Regarding the platinum content, the increment of the metal concentration leads to CO conversion improvement. However in the selected reaction conditions, the Pt 2wt. % sample does not result in very different CO conversion, suggesting sufficient active sites concentration number.

No significant improvement in CO conversion terms are detected among the Pt(4%)/Puralox and Pt(4%)/CeAl HM samples being slightly better the later, showing that the support preparation method does not influence a lot the catalyst performance. In turn, if those catalysts are compared in mol CO converted·g_{Pt}^{-1}·s^{-1} at 180 ºC (where the equilibrium conversion is not reached), the Pt(4%)/CeAl HM activity is superior to that of Pt(4%)/Puralox,

$3.22 \cdot 10^{-5}$ *vs.* $2.32 \cdot 10^{-5}$ respectively. In addition, the commercial support could be hardly modified in order to improve its performances in respect to the homemade one, being therefore the latter undoubtedly the catalyst support chosen for the further modifications in the next chapter.

3.5. Partial conclusions

The influence of the support nature and platinum loading were studied for platinum based catalysts. Commercially available γ-alumina and ceria-alumina supports (Sasol) were compared to homemade ceria-alumina. Two different Pt loadings (2 and 4wt. %) were considered.

The samples were characterized by some techniques, such as μXRF, BET surface area measurements, XRD analysis and reduction properties under H_2 stream and the differences between the samples discussed. The most important conclusion could be resumed as follows:

The obtained catalyst composition is very close to the targeted one.

All the samples are mesoporous solids with similar BET surface area, slightly decreasing with the platinum deposition attributed to the platinum particles deposition inside the pores.

Regarding the reducibility studies, all the commercially supported catalysts are completely reduced at 400 ºC, contrary to the homemade support based sample which present still support fraction at this temperature. Within the

sample series the relative H_2 consumptions changes between the reduction zones indicate Pt particle size variation and modification of the noble metal-support interaction.

The catalytic results highlight the importance of suitable support choice for the WGS reaction. The ceria containing solids are better catalsts than the alumina based one.

The Pt(4%)/CeAl HM was the best catalyst in this study highly active and viable for easily support modifications. This sample is further chosen for posterior support modification studies in the next chapter.

References

[1] P. Davidson, J. Process Control 5 (1995) 191.

[2] D. Trimm, A. Stanislaus, Applield Catal. 21 (1986) 215.

[3] I.H. Son, A.M. Lane, Catal. Letters 76 (2001) 151.

[4] Z. Zhao, M.M. Yung, U.S. Ozkan, Catal. Commun. 9 (2008) 1465.

[5] S.J. Tauster, S.C. Fung, R.T. Baker, J. A. Horsley, Science 211 (1981) 1121.

[6] M. Trueba, S.P. Trasatti, Eur. J. Inorg. Chem. (2005) 3393.

[7] X. Krokidis, P. Raybaud, A.E. Gobichon, B. Rebours, P. Euzen, H. Toulhoat, J. Phys. Chem. B 105 (2001) 5121.

[8] P. Panagiotopoulou, J. Papavasiliou, G. Avgouropoulos, T. Ioannides, D.I. Kondarides, Chem. Eng. J. 134 (2007) 16.

[9] D. Pierre, W. Deng, M. Flytzani-Stephanopoulos, Top. Catal. 46 (2007) 363.

[10] S. Ryberg, Characterization of Pt / CeO 2 Catalysts Thermal Ageing Studies of High Surface Area Support and Evaluation of Chemisorption Based Disperson Measurements, (2010).

[11] A. Trovarelli, Catal. Rev. 38 (2006) 439.

[12] T.X.T. Sayle, S.C. Parker, C.R.A. Catlow, Surf. Sci. 316 (1994) 329.

[13] P.J. Gellings, H.J.M. Bouwmeester, Catal. Today 12 (1992) 1.

[14] P. Gellings, Catal. Today 58 (2000) 1.

[15] M. Gonzalez Castaño, T.R. Reina, S. Ivanova, M. A. Centeno, J. A. Odriozola, J. Catal. 314 (2014) 1.

[16] D. Çakír, O. Gülseren, J. Phys. Chem. C 116 (2012) 5735.

[17] T.X.T. Sayle, S.C. Parker, C.R.A. Catlow, J. Phys. Chem. 98 (1994) 13625.

[18] J.L. Ma, F. Ye, D.R. Ou, L.L. Li, T. Mori, J. Phys. Chem. C 116 (2012) 25777.

[19] C. Zhang, A. Michaelides, D. A. King, S.J. Jenkins, J. Phys. Chem. C 113 (2009) 6411.

[20] A. Sepúlveda-Escribano, F. Coloma, F. Rodríguez-Reinoso, J. Catal. 178 (1998) 649.

[21] C. Hardacre, R.M. Ormerod, R.M. Lambert, J. Phys. Chem. 98 (1994) 10901.

[22] D. Andreeva, I. Ivanov, L. Ilieva, M. V. Abrashev, Appl. Catal. A Gen. 302 (2006) 127.

[23] G. Germani, P. Alphonse, M. Courty, Y. Schuurman, C. Mirodatos, Catal. Today 110 (2005) 114.

[24] T.R. Reina, W. Xu, S. Ivanova, M.A. Centeno, J. Hanson, J.A. Rodriguez, J.A. Odriozola, Catal. Today 205 (2013) 41.

[25] M.A. Centeno, C. Portales, I. Carrizosa, J.A. Odriozola, Catal. Letters 102 (2005) 289.

[26] G. Leofanti, M. Padovan, G. Tozzola, B. Venturelli, Catal. Today 41 (1998) 207.

[27] O.H. Laguna, M. A. Centeno, G. Arzamendi, L.M. Gandía, F. Romero-Sarria, J. A. Odriozola, Catal. Today 157 (2010) 155.

[28] G.A. Mill, S. Weller, E.B. Cornelius, Actes Du Zieme Congr. Intern. Catal. 2 (1962).

[29] C.P. Hwang, C.T. Yeh, J. Mol. Catal. A Chem. 112 (1996) 295.

[30] S. Damyanova, J.M.C. Bueno, Appl. Catal. A Gen. 253 (2003) 135.

[31] T. Fukushima, J.R. Katzer, D.E. Sayer, J.Cook, 7th Intern. Congr. On Catal. Tokyo (1980).

[32] E. Merlen, P. Beccat, J.C. Bertolini, P. Delich, 188 (1996) 178.

[33] M. El Doukkali, A. Iriondo, P.L. Arias, J. Requies, I. Gandarías, L. Jalowiecki-Duhamel, F. Dumeignil, Appl. Catal. B Environ. 125 (2012) 516.

[34] A. Iriondo, J.F. Cambra, V.L. Barrio, M.B. Guemez, P.L. Arias, M.C. Sanchez-Sanchez, R.M. Navarro, J.L.G. Fierro, Appl. Catal. B Environ. 106 (2011) 83.

[35] V. A. Mazzieri, J.M. Grau, J.C. Yori, C.R. Vera, C.L. Pieck, Appl. Catal. A Gen. 354 (2009) 161.

[36] P. Ciambelli, V. Palma, A. Ruggiero, Applied Catal. B Environ. 96 (2010) 18.

[37] M. El Doukkali, A. Iriondo, J.F. Cambra, L. Jalowiecki-duhamel, A.S. Mamede, F. Dumeignil, P.L. Arias, Journal Mol. Catal. A, Chem. 368-369 (2013) 125.

[38] M.J. Tiernan, O.E. Finlayson, Appl. Catal. B Environ. 19 (1998) 23.

[39] H.C. Yao, M. Sieg, J. Plummer H.K., J. Catal. 59 (1979) 365.

[40] G. Lietz, H. Lieske, H. Spindler, W. Hanke, J. Völter J.Catal. 81 (1983) 17.

[41] S.H. Park, M.S. Tzou, W.M.H. Sachtler App. Catalysis 24 (1986) 85.

[42] J.Z. Shyu, K. Otto, J. Catal. 115 (1989) 16.

[43] K. Shyu, J Z, Otto, Appl. Surf. Sci. 32 (1988) 246.

[44] N.W. Hurst, S.J. Gentry, B.D. Mcnicol, Catal. Letters 24 (1982) 233.

[45] C. H.C. Yao, H.S. Gandhi, M. Shelef, B. Imelik, P. Naccache, G. Coudurier, H. Praliaud, P. Meriaudeau, P. Gallezot, G.A. Martin, J.C. Vedrine, Stud. Surf. Sci. Catal. 11 (1982) 159.

[46] H.C. Yao, M. Sieg, H.K. Plummer Jr. J. Catal. 59 (1979) 365.

[47] A. P. Ferreira, J.C.S. Araújo, J.W.C. Liberatoria, S. Damyanova, D. Zanchetc, F.B. Noronha, J.M.C. Bueno, Stud. Surf. Sci. Catal. 167 (2007) 433.

[48] W.Y. Hernández, O.H. Laguna, M. A. Centeno, J. A. Odriozola, J. Solid State Chem. 184 (2011) 3014.

[49] T.R. Reina, E. Papadopoulou, S. Palma, S. Ivanova, M. A. Centeno, T. Ioannides, J. A. Odriozola, Appl. Catal. B Environ. 150-151 (2014) 554.

[50] W.C. Conner, J.L. Falconer, Chem. Rev. 95 (1995) 759.

[51] G. Jacobs, U.M. Graham, E. Chenu, P.M. Patterson, A. Dozier, B.H. Davis, J. Catal. 229 (2005) 499.

[52] A. Badri, C. Binet, J. Lavalley, 92 (1996) 4669.

Chapter 3

Electronic and structural promoters of $Pt(4\%)/CeO_2/Al_2O_3$ catalyst

Summary

An electronic and structural promotion of the $Pt/CeO_2/Al_2O_3$ catalytic system was pretended and achieved by the addition of two different ceria promoters, Zr and Fe. Zr appears to be very efficient structural promoter resulting in lower platinum particle size and stronger Pt-CO interactions meanwhile Fe improves the electronic properties of the system reflecting oxygen vacancies concentration and the band gap energy alterations. The combination of both doping agents maintains the beneficial effects provided by both separately but also manifest a synergistic effect reflected on significant changes on the band gap energies, chemisorptive properties as well as catalyst's behavior regarding deactivation phenomena.

3.1. Introduction

Along the previous Chapter, the beneficial effect provided by the ceria addition to the platinum catalysts was clearly established. The enhanced activity of the ceria supported NM catalysts is frequently attributed to the ceria ability to undergo fast storage/release oxygen cycles via reversible Ce^{4+} to Ce^{3+} species conversions [1,2]. These redox cycles imply oxygen vacancies (O_v) formation mechanism which normally correlates to an enhanced catalytic activity [3,4].

As shown in the Figure 3.1, no matter the mechanism through which the reaction happens the role of the oxygen vacancies is markedly important. Simplified, the redox mechanism consists of two consecutive steps where i) the CO is oxidized to CO_2 resulting on Ce^{3+}- O_v couples on the support and ii) the water molecules are dissociated on the O_v entailing the reoxidation of Ce^{3+} to Ce^{+4} species.

On the other hand, the associative mechanism proposes the reaction of activated CO species with the OH groups already created on the support, through water dissociation process, leading to intermediates carbonaceous species which subsequently decomposes to CO_2 and H_2. The created oxygen vacancies are then replenished by the water and the cycle repeats. Therefore, an oxygen vacancy increment on the surface should lead to enhanced catalytic performances.

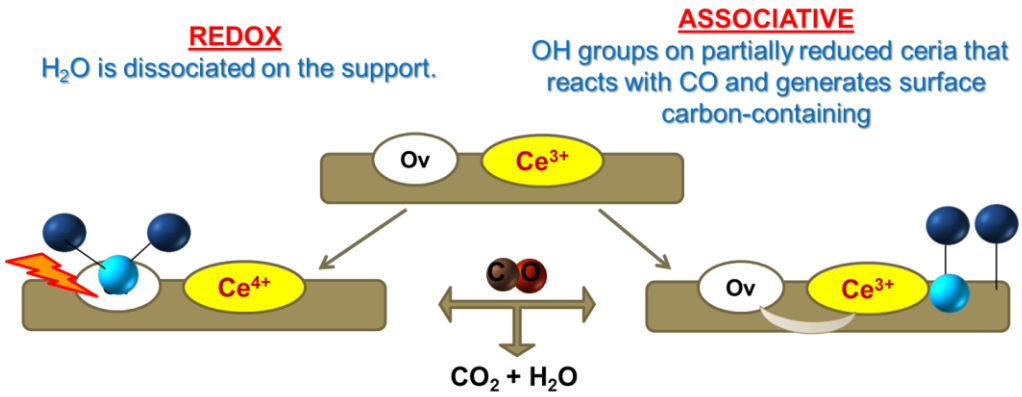

Figure 3.1. Possible role of ceria vacancies on WGS reaction depending on the reaction mechanism reaction

In the case of CeO_2, it has been widely demonstrated that the concentration of oxygen vacancies can be enhanced by the modification of its structure through doping with different cations such as Zr [5–9], Fe [10–13], Eu [12] and Zn [14,15] among others. Several studies published the use of Zr as doping agent on the basis of its good thermal stability, ability to decrease the ceria sintering [16,17] or interesting acid-base and redox properties [18]. A significant improvement of the catalytic behavior in the presence of Zr, in comparison with Pt/ CeO_2 samples, was reported [19,20]. On the contrary when Fe is used as dopant, either decrease [21], increase [22] or even no effect [23] were reported for the WGS reaction.

Although the both dopants could be successfully used for promoting the CeO_2 properties, its properties largely depend on the preparation method, the nature of the present phases and their relative content [6,24,25]. Actually, the

influence of these features may explain the diversity of conclusions published in several works regarding the Ce doped systems.

In this context, a careful design of Pt-mixed oxides catalyst is needed for apprehension the role of the dopants in the WGS reaction. For this reason, in the present chapter, a platinum based catalyst series was prepared employing as support ceria zirconia mixed oxide with increased Zr amounts. These catalysts were characterized and tested in WGS conditions.

With the optimal Ce/Zr relation established, the sample was employed as a starting point for the second part of the chapter. New Zr and Fe doped system were prepared in order to promote the Pt/CeO_2 activity. Both doping agent are used separately or in a mixed manner in order to study their synergism in ceria promotion but always maintaining the Ce/doping metal proportion. In addition, for all the samples prepared in this thesis, the ceria quantity was optimized by dispersing it on Al_2O_3 matrix with the aim to diminish the ceria waste and to increase its surface to volume ratio.

3.2. Experimental

- *Catalyst synthesis*

Six different supports were synthesized, CeO_2/Al_2O_3, $Ce_{0.9}Zr_{0.1}O_2/Al_2O_3$, $Ce_{0.75}Zr_{0.25}O_2/Al_2O_3$ $Ce_{0.5}Zr_{0.5}O_2/Al_2O_3$, $Ce_{0.9}Fe_{0.1}O_2/Al_2O_3$ and $Ce_{0.9}Zr_{0.05}Fe_{0.05}O_2/Al_2O_3$. The precursor quantities were calculated to obtain cerium oxide or cerium/promoter mixed oxide loading of 20 wt.% over

alumina in the final material. Nominally, the desired cerium - doping agent proportions were calculated in molar ratio. The supports preparation was carried out by wetness impregnation on a high surface ɣ-Al_2O_3 powder (Sasol). The metal oxide precursors were $Ce(NO_3)_3 \cdot 6H_2O$, $Fe(NO_3)_3 \cdot 9H_2O$ and $ZrO(NO_3)_2 \cdot xH_2O$ (Aldrich). After drying, the solids were calcined at 450°C for 4h with a 10ºC/min heating rate. In the adopted nomenclature, the oxygen and the subscripts were omitted. The supports CeO_2/Al_2O_3, $Ce_{0.9}Zr_{0.1}O_2/Al_2O_3$, $Ce_{0.75}Zr_{0.25}O_2/Al_2O_3$, $Ce_{0.5}Zr_{0.5}O_2/Al_2O_3$, $Ce_{0.9}Fe_{0.1}O_2/Al_2O_3$ and $Ce_{0.9}Zr_{0.05}Fe_{0.05}O_2/Al_2O_3$ are then labeled CeAl, $Ce_{0.9}$ZrAl, $Ce_{0.75}$ZrAl, $Ce_{0.5}$ZrAl, $Ce_{0.9}$FeAl and $Ce_{0.9}$ZrFeAl, respectively.

The nominal platinum content was fixed to 4 wt. %. The platinum deposition was carried out by wetness impregnation using as a precursor tetrammonium nitrate platinate (Johnson-Matthey) slightly modified by 1M acetic acid in a 1:1.1 ratio. The solids were dried and, then, calcined at 350 ºC for 8h at 5 ºC/min. The resulting samples were named Pt/CeAl, Pt/$Ce_{0.9}$ZrAl, Pt/$Ce_{0.75}$ZrAl, Pt/$Ce_{0.5}$ZrAl, Pt/$Ce_{0.9}$FeAl, and Pt/ $Ce_{0.9}$ZrAl.

3.3. Support optimization for Pt based $Ce_xZr_{1-x}O_2/Al_2O_3$

3.3.1. Physicochemical characterization results

3.3.1.1. Textural properties and chemical composition of the prepared solids

The textural properties of the prepared solids are presented on the Table 3.1. It can be observed that the ceria incorporation to alumina leads to lower specific surface areas, average pore volume and diameter. Regarding the zirconia doped samples, higher zirconia contents result in increase of the specific surface areas and pore volumes values.

On the other hand, as a general trend, the platinum incorporation to the supports leads to surface area diminutions and increase of the pore volume except for the Pt/CeAl catalyst which exhibits an important decrement of its pore volume in comparison to its parent support.

Table 3.1. Textural properties and chemical composition of the prepared solids

	S_{BET} (m^2 /g)	V_{pore} (cm^3 /g)	Al_2O_3 (*wt.* %)	CeO_2 (*wt.* %)	ZrO_2 (*wt.* %)	Pt (*wt.* %)
Al_2O_3	202	0.51	100	---	---	---
CeAl	186	0.41	74.3	24.7	---	---
$Ce_{0.9}$ZrAl	160	0.36	80.1	17.7	2.2	---
$Ce_{0.75}$ZrAl	167	0.38	80.0	18.0	2.0	---
$Ce_{0.5}$ZrAl	173	0.39	80.8	16.7	2.5	---
Pt/CeAl	147	0.31	72.0	24.2	---	3.8
Pt/$Ce_{0.9}$ZrAl	150	0.36	74.7	18.8	1.6	4.9
Pt/$Ce_{0.75}$ZrAl	156	0.38	75.9	17.4	2.0	4.7
Pt/$Ce_{0.5}$ZrAl	166	0.38	76.7	16.2	2.4	4.7

Regarding the chemical compositions, the supports and their corresponding catalysts present chemical compositions closer to the desired ones. Nevertheless, all the catalysts showed slightly higher platinum contents in

respect to the nominal loadings value (4 wt.%) suggesting some support dissolution during the preparation process.

3.3.1.2. XRD analysis of the prepared solids

The XRD patterns of the prepared solids are presented in the Figure 3.2.a. The characteristic γ-Al_2O_3 (JCPDS# 00-050-0741) and CeO_2 (JCPDS# 00-004-0593) diffractions are present in all prepared solids. Moreover, zirconia typical diffractions were not observed.

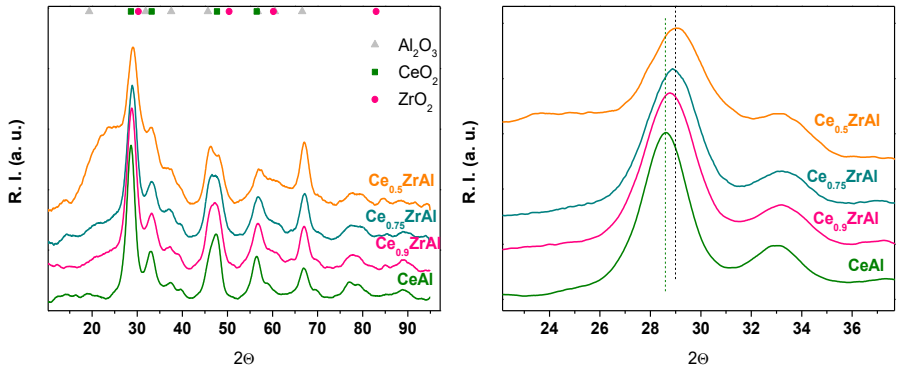

Figure 3.2. XRD of the synthesized supports a) 10-95 2θrange; b) Main diffraction of ceria lattice (111)

In Figure 3.2.b, the main ceria diffraction (111) is amplified. As it can be observed, the increased zirconia loadings lead to pronounced shift of this diffraction towards higher 2θ in comparison to the bare CeAl support. The observed shifts can be explained with an substitutional solid solution formation. Indeed, ceria lattice contraction should occur when a replacement of ceria cations by lower ionic radii zirconia cations takes place (0.97 Å and

0.84 Å for Ce^{4+} and Zr^{4+} respectively) reflecting on a diffraction lines shift to higher 2θ values.

Hence, the CeO_2 lattice parameters could be estimated using the main (111) CeO_2 diffraction and the eq. $d_{hkl} = \frac{a}{\sqrt{(h^2+k^2+l^2)}}$. In the Figure 3.3, the obtained lattice parameters are represented as a function of the Ce/Zr ratio. While the characteristic ceria lattice parameter was obtained for the unmodified support (5.395 Å), the zirconia containing samples show a lattice diminution indicating the formation of ceria-zirconia solid solution for all tested Ce/Zr molar ratios.

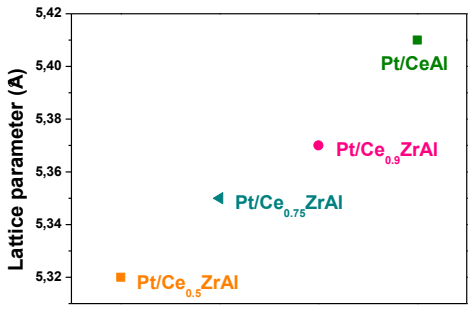

Figure 3.3. Ceria lattice parameter obtained for the prepared Zr containing supports

The effect on the ceria crystallite size induced by the zirconia addition is also determined by using the Scherrer's equation. The observed increment of the mixed oxide crystallite size (40 Å) in comparison to the undoped CeAl support (36 Å) indicates that the obtained distortions are not sufficiently important to hinder the crystallite growth and results in higher ceria crystals,

no matter the used zirconia amount. Besides, the higher particle size could be also related to a higher Ce^{3+} population possessing higher ionic radii in comparison to Ce^{4+} (Ce^{4+} = 0,97 and Ce^{3+} = 1,14). Similar particle size effect were published by Duarte et al [19], for ceria zirconia mixed oxides.

The XRD patterns of the prepared catalysts were also analyzed and the results are shown in the Figure 3.4. The main platinum diffraction line can be discerned in Pt/CeAl and Pt/$Ce_{0.5}$ZrAl catalysts with some significant differences, depending on support compositions.

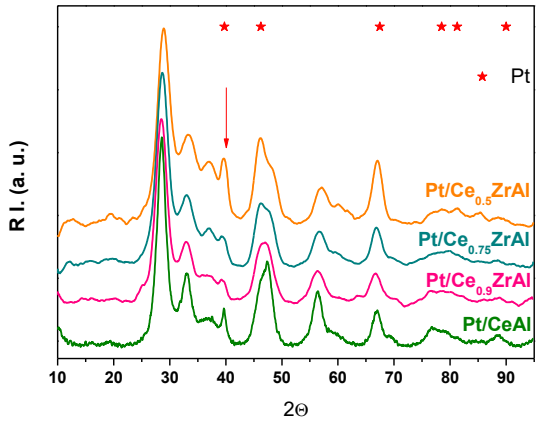

Figure 3.4. XRD patterns for the prepared catalysts

The Pt/$Ce_{0.5}$ZrAl and Pt/CeAl samples clearly exhibit metallic platinum (111) diffraction. On the other hand, the platinum catalysts supported on intermediate Ce/Zr ratios, such as Pt/$Ce_{0.9}$ZrAl and Pt/$Ce_{0.75}$ZrAl, do not shown any Pt diffraction which can be attributed either to the masking effect of the employed alumina matrix or to a lower crystallite size. Clear dependence of the support composition on the Pt particle size can be

perceived. It looks like the intermediate Ce/Zr ratios stabilized lower platinum sizes whereas the total absence or an excess of Zr provokes platinum agglomeration.

3.3.1.3. TPR characterization

The reducibility of the samples was analyzed by H_2-TPR studies (Figure 3.5). The supports, presented in dotted lines, show a broad reduction zone around 500 ºC commonly ascribed to surface Ce^{4+} to Ce^{3+} species reduction [26,27].

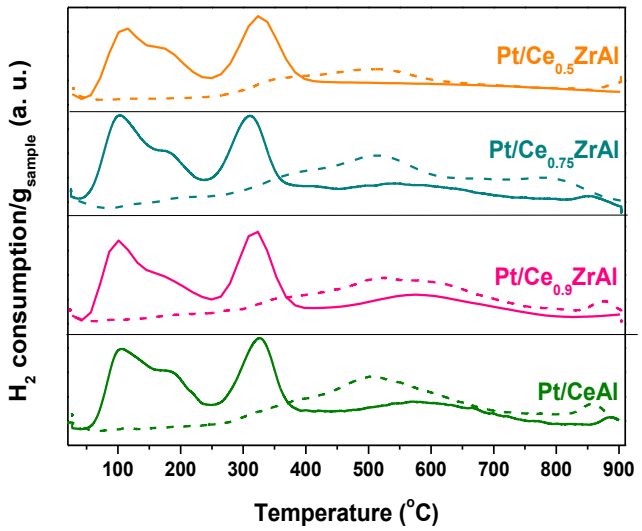

Figure 3.5. H_2-TPR of the prepared supports and catalysts

For the platinum catalysts (solid lines), the observed reduction profiles are composed by three reduction zones for which several observations could be made. First of all, the H_2 consumed in the two lower temperature zones cannot be attributed only to platinum species reduction; the hydrogen consumption is

superior to that necessary for Pt species reduction only. The platinum presence should promote the ceria reduction and a shift of its reduction to lower temperatures is expected. This effect is related in the literature to the spillover effects in which the platinum metal is involved [19,28]; i.e. platinum dissociates H_2 molecules either to be reduced itself or to diffuse the dissociated hydrogen species to the ceria support thus favoring its reducibility. Concerning platinum species, its reduction at lower temperature is usually related to weaker platinum-support interaction [29,30] and/or to higher platinum particle size [31]. Therefore, the different platinum particle size is also intuited for these solids (Fig. 3.5). The higher temperature reduction zone present for all solids is related to the reduction processes of the ceria species only; bulk Ce^{4+} to Ce^{3+} reduction.

3.3.2. Catalytic behavior

The catalytic screening of the prepared catalysts was performed under WGS model mixture conditions (Figure 3.6.a). The catalysts present similar catalytic activity reaching all of them the equilibrium conversion at 230 ºC. Only minor differences can be discerned at temperature below equilibrium and the following trend is observed (T=200 ºC)

$$Pt/Ce_{0.9}ZrAl > Pt/Ce_{0.75}ZrAl > Pt/Ce_{0.5}ZrAl \approx Pt/CeAl.$$

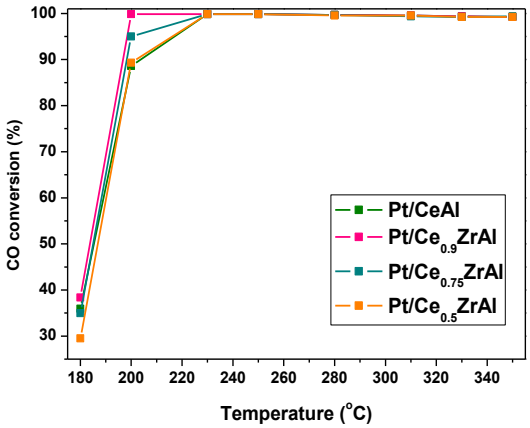

Figure 3.6: Catalytic activity of the prepared catalysts

Although no significant differences on the catalytic behavior were observed, the Ce/Zr ratio of 9 presents slightly improved activity in the studied conditions. In addition, this sample shows also higher capacity to stabilize lower platinum particle sizes (Figure 3.4). Optimal beneficial effect for 10 at.% of doping metal have been also reported in the literature. This effect was assigned to optimal oxygen vacancies concentration, leading to sites responsible for metal stabilization and dispersion [12,32,33]. Although the minor differences on the catalytic performance could be tentatively attributed to the difference in the sample's platinum particle size, for the WGS model conditions this effect could be rather obviated as the number of Pt active sites exceeds the needed for these conditions.

Thus, along the following section, the Ce to dopant molar ratio of 9 is selected as the optimal beneficial ratio and will be maintained with the introduction of Fe either as a second doping metal or as the unique ceria promoter. The role

and provided promotion by both metals and the possible synergic effect from the metals combination will be studied.

3.4. Structural and electronic effect of Zr and/or Fe addition over Pt-ceria catalysts

3.4.1. Physicochemical characterization of the prepared solids

3.4.1.1. Textural properties and chemical composition

The textural properties of the supports (Table 3.2), as expected are dominated by the presence of γ-Al_2O_3 (202 m^2/g; pore volume 0.49 cm^3/g; pore size 74 Å). The addition of CeO_2 with or without doping metals decreases the specific surface area, being this decrease more pronounced for the iron containing samples (Table 3.2).

Table 3.2. Textural properties of the prepared supports and catalysts

	S_{BET} (m^2/g)	V_{pore} (cm^3/g)	D_{pore} (Å)
CeAl	165	0.34	68
$Ce_{0.9}$ZrAl	160	0.36	71
$Ce_{0.9}$FeAl	151	0.32	66
$Ce_{0.9}$ZrFeAl	156	0.32	66
Pt/CeAl	147	0.31	69
Pt/ $Ce_{0.9}$ZrAl	150	0.36	72
Pt/ $Ce_{0.9}$FeAl	147	0.32	67
Pt/ $Ce_{0.9}$ZrFeAl	153	0.32	67

Although, the changes do not seem very significant for V_{Pore} and D_{Pore}, opposite tendencies are observed. While the zirconia addition increases the V_{Pore} and D_{Pore}, the Fe decreases them. When both doping agents are present, the surface area of the sample results in an intermediate value between the monometallic substitutions. The V_{Pore} and D_{Pore} show the same values as for the Fe-doped sample. The Zr-doped sample presents very similar textural properties to the parent CeO_2/Al_2O_3 support, which could indicate higher similarities of the samples on molecular level, i.e. solid solution formation. The decrease of the S_{BET} and D_{Pore} for the Fe-doped sample, however, suggests the deposition of a second phase but do not exclude the solid solution formation.

The chemical composition of the studied systems is presented in Table 3.3.

Table 3.3. Chemical composition of the synthetized solids

	Al_2O_3 (wt.%)	**CeO_2 (wt.%)**	**ZrO_2 (wt.%)**	**Fe_2O_3 (wt.%)**	**Pt (wt.%)**
CeAl	75.3	24.7	---	---	---
$Ce_{0.9}$ZrAl	80.1	17.7	2.2	---	---
$Ce_{0.9}$FeAl	81.4	17.4	---	1.2	---
$Ce_{0.9}$ZrFeAl	81.0	18.0	0.6	0.4	---
Pt/CeAl	72.0	24.2	---	---	3.8
Pt/ $Ce_{0.9}$ZrAl	74.7	18.8	1.6	---	4.9
Pt/ $Ce_{0.9}$FeAl	78.3	15.9	---	1.1	4.7
Pt/ $Ce_{0.9}$ZrFeAl	78.8	16.5	0.5	0.4	3.8

Although a slight enrichment in Zr observed for the CeZr sample, probably due to the cerium content loss during the preparation; the obtained compositions are very close to the nominal values.

3.4.1.2. XRD results

The XRD patterns of the employed supports are presented in Figure 3.7.a where Al_2O_3 is also included for clarity. All the supports show the characteristic diffractions of the cubic CeO_2 fluorite structure (JCPDS# 00-004-0593) and γ- Al_2O_3 phase (JCPDS# 00-050-0741).

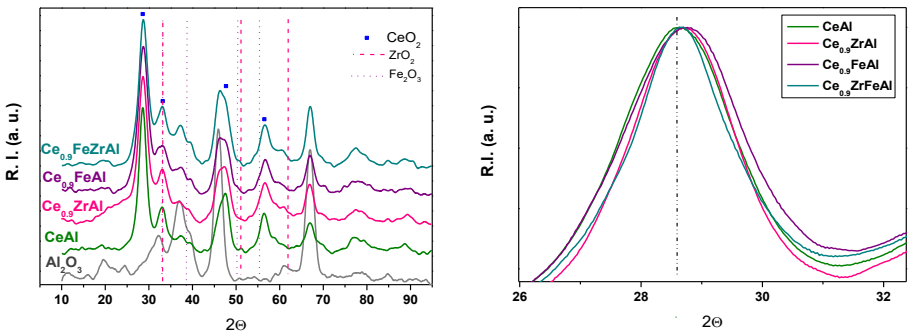

Figure 3.7. a) XRD of the prepared supports; b) (111) ceria diffraction line

Neither Fe_2O_3 nor ZrO_2 XRD signals are detected probably due to the small amount of doping agents or to the inclusion of these cations in the ceria lattice forming solid solution. Iron or zirconium doped cerium solid solutions systems are widely described, especially in this range of concentration [11,13,34]. In fact, the diffractions of the doped-ceria supports shift towards higher angles, as illustrated in Figure 3.7.b. The calculated parameters are

presented in the Table 3.4, being the lattice parameter similar for all doped systems and inferior to that of the parent CeAl.

This behavior is caused by the substitution of Ce^{4+} with Fe^{3+} or Zr^{4+} ions. Taking into account, the ionic radii (0.97Å, 0.64Å and 0.84Å for Ce^{4+}, Fe^{3+} and Zr^{4+} respectively) a higher contraction of the ceria lattice is expected when iron is used as doping agent. However, the same lattice contraction is observed for all doped samples no matter the doping metal. This fact could indicate a partial segregation of the iron oxide species forming interstitial solid solution, as reported by Reina et al. [14,24]. Although the segregated Fe oxide is not detected by XRD because of its low concentration, its presence cannot be discarded.

Table 3.4. For supports, ceria lattice parameters and crystallite size.

	CeO_2 Crystal Domain (Å)	**CeO_2 Lat. parameter (Å)**
CeAl	36	5.41
$Ce_{0.9}$ZrAl	40	5.39
$Ce_{0.9}$FeAl	35	5.39
$Ce_{0.9}$ZrFeAl	41	5.39

The crystallite size was also calculated by using Scherrer equation (Table 3.4). A slight increase of the ceria particle size is observed when Zr is used as dopant and, on the contrary, the Fe addition does not provoke variations on the particle size. When both doping agents are present, the observed particle size is similar to that of the Zr-doped system.

The XRD patterns for the calcined platinum containing samples are shown in the Figure 3.8.a. For all Pt doped samples, narrowing in the main cerium oxide diffraction (111) was detected being associated to ceria particle size increment during the platinum addition. This increase might be the consequence of a partial re-dissolution of the support during the platinum deposition, resulting in reorganization of the latter with higher particle size or to the sintering during the second calcination process after Pt deposition.

In the case of $Pt/Ce_{0.9}FeAl$, an additional ceria lattice contraction from 5.39 to 5.38 Å was detected during the second calcination, which could indicate that some of the interstitial Ce-Fe solid solution converts into substitutional one.

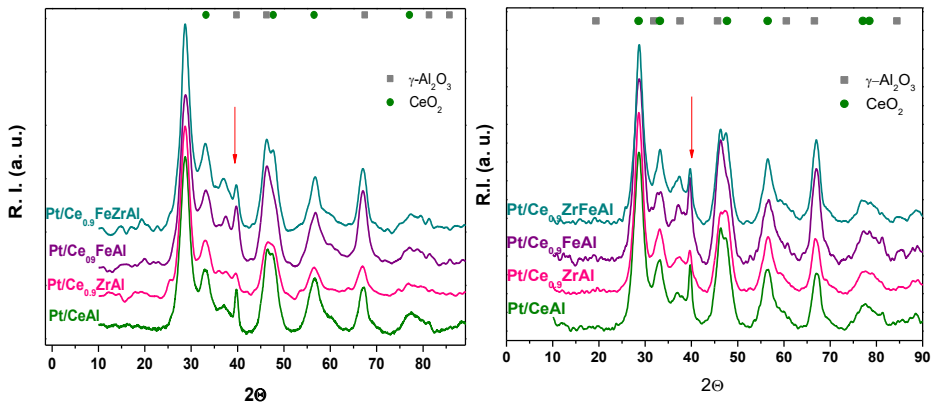

Figure 3.8. XRD of the prepared catalysts a) calcined; b) reduced at 350ºC

The XRD diffractions of the reduced catalysts, in the conditions of pretreatment prior the catalytic test, are presented in Figure 3.8.b. The main Pt^0 diffraction (111) is detected at $2\theta=39.7^o$ for all the catalysts. Some important differences can be observed depending on the support. Minor Pt

particles size is observed for the Pt/$Ce_{0.9}$ZrAl sample suggesting a strong metal support interaction able to stabilize the Pt particles upon reduction. The platinum particle size calculated from XRD for all the samples is shown in Table 3.5. It should be mentioned however that at 39.7º some alumina diffractions are also present, which implies that the Pt particle size estimations is only approximated.

Table 3.5: Ceria crystal domain and lattice parameters for the fresh catalysts and platinum crystal domain estimated for the reduced catalysts

	CeO_2 Crystal Domain (Å)	**CeO_2 Lat. parameter (Å)**	**Pt Crystal Domain (nm)**
Pt/CeAl	36	5.395	21.1
Pt/$Ce_{0.9}$ZrAl	43	5.385	7.7
Pt/$Ce_{0.9}$FeAl	38	5.379	11.7
Pt/ $Ce_{0.9}$ZrFeAl	45	5.381	10.8

All the doped systems present lower platinum sizes, in comparison with the unpromoted sample. Both dopants provoked significant decrement on the resulting Pt size, being Pt/$Ce_{0.9}$ZrAl the sample with the lowest crystalline domain.

3.4.1.3. CO chemisorption and HR-TEM microscopy.

The metal dispersion was determined by CO chemisorption at liquid N_2 temperature in order to avoid the ceria contribution through CO oxidation. The metal dispersion as the number of surface exposed Pt atoms was

calculated from the total amount of adsorbed CO. More precisely, it was assumed that each surface platinum atom only chemisorbs one CO molecule and that the particles are cubic with one non-exposed face (Shape Factor = 5).

From the metal dispersion, the average metallic sizes were estimated by Spinadel and Boudart method being the details of the used model reported elsewhere [28]. Both, dispersion results and estimated platinum particle size are shown in Table 3.6. The calculated particle size values are significantly lower than those obtained from XRD.

Table 3.6. Estimated Pt dispersion and particle size from CO chemisorption.

	Dispersion (%)	**Pt calculated size (nm)**
Pt/CeAl	59	2.7
Pt/$Ce_{0.9}$ZrAl	56	2.7
Pt/ $Ce_{0.9}$FeAl	58	2.7
Pt/ $Ce_{0.9}$ZrFeAl	53	2.7

Considering that great difference, the HR-TEM was employed in order to determine the real platinum particle size. In Fig. 3.9 are shown the HADAF images obtained for the reduced Pt/CeAl and Pt/$Ce_{0.9}$ZrFeAl catalysts. A very homogeneous Pt particle size distribution was observed with an average size estimated at 1 ± 0.2 nm.

The Pt size distribution appears to be even lower than the size calculated from the CO chemisorption experiments and much inferior to the crystallite size

estimated by the XRD's Scherrer equation. Although not observed in HR-TEM, the existence of some agglomerates should not be excluded, as the Pt (111) diffraction was detected or higher Pt sizes were calculated by the chemisorption study.

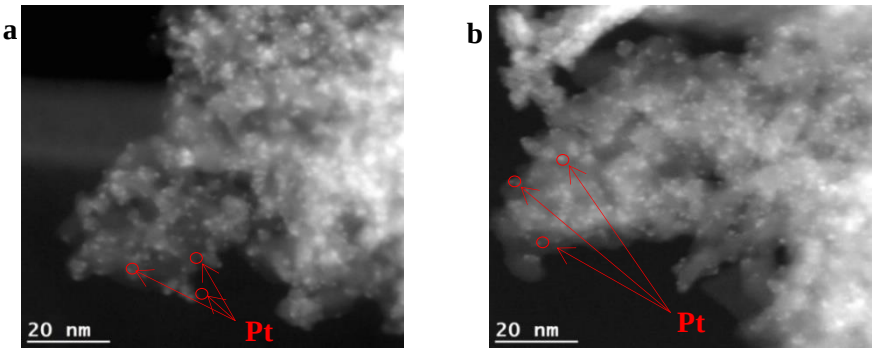

Figure 3.9. HR-TEM microphotographs of reduced samples: a) Pt/CeAl; b) Pt/CeZrFe

Therefore, all the catalyst should present two different platinum species: a minor fraction constituted by platinum agglomerates and a major one composed by highly dispersed platinum species. Within the series the doping agent introduction leads to lower fraction of agglomerated Pt, as confirmed by XRD. On the other hand no matter the agglomerates formation the results obtained from HR-TEM and CO chemisorption indicates that the obtained Pt size is similar for all the samples. From this moment one the Pt dispersion on these samples will be considered always the same.

3.4.1.4. Raman and UV-Vis characterization

An approach to the electronic properties of the studied materials is obtained by DR UV-Vis spectroscopy. The DR UV-Vis spectra of the synthesized supports are shown in the Fig. 3.10.a.

All the supports present a broad band, centered at *ca*. 280 nm, associated to $O_{2p} \rightarrow Ce_{4f}$ charge transfer transition characteristic for CeO_2 [35]. The iron addition leads to the widening of this band, which is commonly attributed to the contribution of the iron oxide absorption features at around 530 nm [3]. In the case of $Ce_{0.9}$ZrFeAl system, a substantial widening in the absorption band is observed.

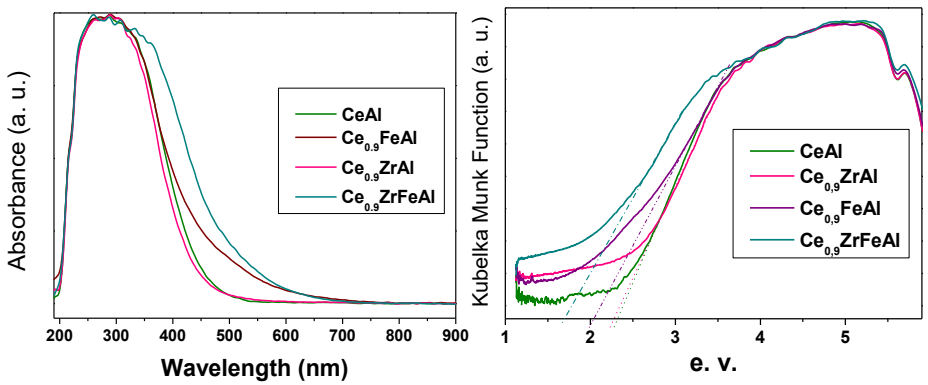

Figure 3.10. a) UV-Vis spectra of the prepared supports; b) represented in Kubelka-Munk mode

The indirect band gap energies of prepared supports estimated by extrapolating to zero the energy dependence of the $[F(R)h\nu]^{1/2}$ are presented in Table 3.7. The corresponding band gap energies are not calculated for the catalysts because of the addition of the platinum plasmon band [36]. The latter

appears at around 500-600 nm, as a consequence of a collective oscillation of the conduction electrons stimulated by the incident light and does not permit the accurate calculation of the band gaps [37].

The CeAl sample presents indirect band gap energy of 2.36 eV, in good agreement with the literature [34]. The measured band gap for our ceria sample is smaller than that found for ceria monocrystal (6 eV.) and could be associated to higher Ce^{3+} to Ce^{4+} species ratio indicating partially reduced ceria on the surface [34,38].

Table 3.7. Band gap energies calculated for the synthetized supports

	BG (eV)
CeAl	2.36
$Ce_{0.9}$ZrAl	2.33
$Ce_{0.9}$FeAl	2.01
$Ce_{0.9}$ZrFeAl	1.65

The addition of doping metal lowers the CeAl band gap energies. The zirconium promoted sample presents a minor band gap energy decrease, in comparison to the iron promoted one. In the case of $Ce_{0.9}$ZrFeAl, a significant decrease in the indirect band gap energies values is observed (1.65 eV).

Several factors, as particle sizes and/or introductions of electronic levels between the valence and the conduction bands, could involve changes in the electronic properties and, hence, in the band gap energies [39,40]. Raman

spectroscopy was also used for electronic properties investigation. The Raman spectra of the studied supports are shown in the Figure 3.11.

As it can be observed, CeAl system shows a wide band at 458 cm^{-1} which is assigned to F_{2g} Raman-active mode of the CeO_2 fluorite structure due to the symmetric oxygen breathing vibration around Ce^{4+}. It should be mentioned that no bands attributed to segregated iron species were discerned indicating that the segregation although not excluded, should not be so important. Additionally, in the Figure 3.11.b, a small band at around 600 cm^{-1} ascribed to the presence of oxygen vacancies (O_v) is perceived [12,13,41]. It has been established in the literature that the Ov/F_{2g} bands area ratio is a correct way to evaluate the surface oxygen vacancies concentration [13].

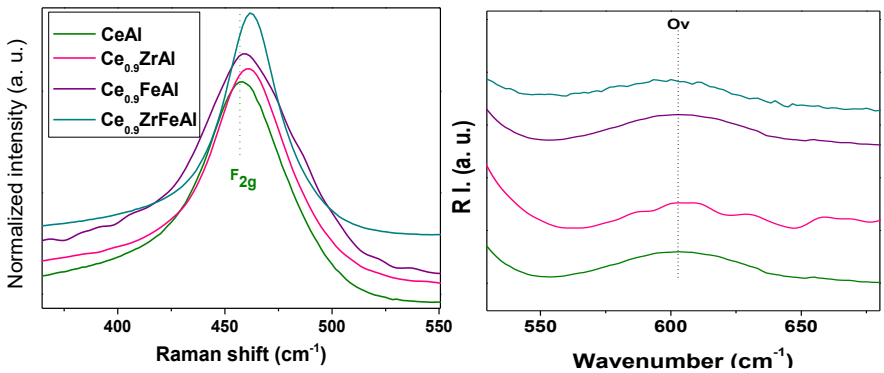

Figure 3.11. Raman spectra obtained for the synthesized supports: a) F_{2g} b) O_v Raman band

In order to elucidate the variations of the electronic properties in the doped ceria based systems, the most important parameters calculated from Raman study are listed in Table 3.8.

In comparison with the unpromoted system, the $Ce_{0.9}ZrAl$ sample shows an UV-Vis red shift of the CeO_2 absorption edge and a weak band gap energy decrease. These variations could be associated with the higher particle size and/or with a higher concentration of defects population on the surface. As for the Raman spectra, a blue shifted and narrowed F_{2g} band is observed. Both associated with an increment of the particle size, being in concordance with the XRD and UV-Vis results. A slight increment in the Ov/F_{2g} ratio is also detected, indicating that the Ce^{3+}/Ce^{4+} ratio increases in agreement with the band gap reduction observed by the UV-Vis spectroscopy.

Table 3.8. Raman position, width and F_{2g}/Ov ratio estimated for the supports

	Raman Shift (cm^{-1})	**Width (cm^{-1})**	**O_v/F_{2g}**
CeAl	458	46	0.034
$Ce_{0.9}ZrAl$	462	40	0.036
$Ce_{0.9}FeAl$	460	53	0.065
$Ce_{0.9}ZrFeAl$	462	32	0.056

On the other hand, the iron doped $Ce_{0.9}FeAl$ system exhibits widening of its ceria's UV-Vis absorption band associated to red shift. It is also observed an important band gap energy decrease. Considering the particle size decrease, a shift to lower wavenumbers for the F_{2g} band is expected. However, the F_{2g}

absorption is shifted in the opposite direction, which might be assigned to the significant increment of the ceria defects population. From the Raman spectra, the observed red shift and widening of the F_{2g} band, is not consistent with the particle size diminution. However, the ratio Ov/F_{2g} enhances indicating, in agreement with the band gap energy calculated by UV-Vis spectroscopy, an increase of the oxygen vacancies population.

Therefore, it should be underlined the different changes resulting when ceria is doped either by zirconium or by iron. The observed changes in the UV-Vis and Raman features for $Ce_{0.9}ZrAl$ sample could be associated mainly to structural modifications, meanwhile for the $Ce_{0.9}FeAl$ system the spectroscopic variations may be correlated mainly to electronic properties modification.

When both promoters, Zr and Fe, are present, an intermediate Ov/F_{2g} ratio is observed being closer to that of the iron sample. On the other hand, the band gap energy suffers a significant decrease, accentuated by the larger crystalline domain, which in turn seems to be important when Zr is present. A strong synergistic effect is apparently achieved with both metals incorporated to the ceria lattice, demonstrated by the important band gap decrease, superior to the same provided by both metals separately.

3.4.1.5. Oxygen Storage Capacity (OSC) and Oxygen Storage Complete Capacity (OSCC)

The redox properties of the supports were also analyzed by measuring the sample's Oxygen Storage Capacity (OSC) and the Oxygen Storage Capacity Complete (OSCC) which provides information above the most reactive and available oxygen species and the maximum reducibility degree of the samples achieved under exposure to CO. The OSCC provides information above the total oxygen species available on the sample and it is estimated from the CO_2 amounts formed during ten consecutive CO pulses. Meanwhile, the OSC arrange for the most accessible species being calculated from the average of the CO_2 species formed when the sample are exposed to consecutive CO – O_2 pulse sequences. The OSCC and OSC measurements expressed in μmol CO_2 formed are presented on the Figure 3.12.

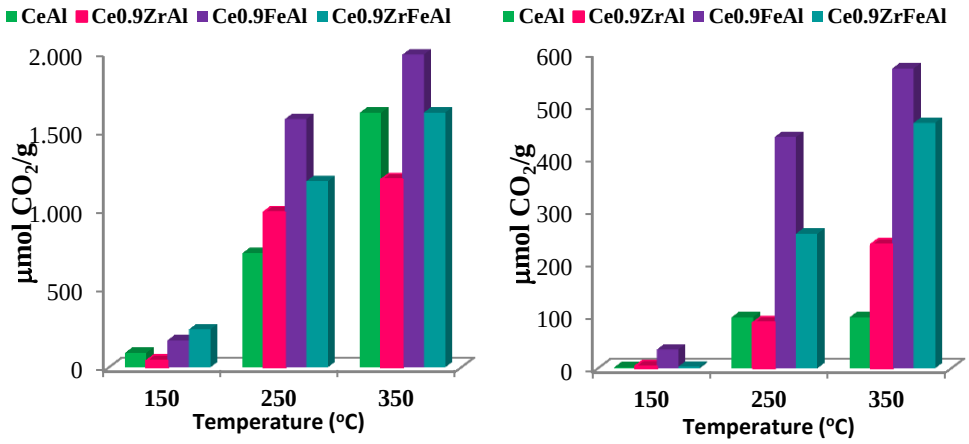

Figure 3.13. H_2-TPR profiles of the supports (dot lines) compared with their respective catalysts (solid lines)

As a general trend, the CO_2 amount released from the supports increases with the temperature for both tests. The OSCC increases for all samples as a function of the temperature, indicating the easiness of reduction in this temperature range. The only exception is $Ce_{0.9}ZrAl$ sample which shows a decrease of its reduction ability at 350 ºC in comparison to 250 ºC. The highest reducibility in terms of CO_2 total formation was achieved for the samples containing Fe as doping metal which could be due also to the participation of that metal to the total reducibility meanwhile the $Ce_{0.9}ZrFeAl$ exhibits intermediates values.

Regarding the immediate oxygen storage capacity, OSC, the iron presence leads to a significant promotion of the fast interchange oxygen species being, for all the tested temperatures, always superior to the zirconia doped sample.

When both promoters are present an intermediate exchange capacity is reached. The beneficial effect provided by zirconia, when compared to CeAl, is only clearly observed at 350 ºC but was achieved at lower temperatures.

From the OSC measurements, the number of layers involved on the oxygen exchange could be theoretically estimated. The number of layers (NL) was calculated by the equation:

$$NL = \frac{OSC_{Experimental}}{OSC_{Theoretical}} \qquad \textit{Equation 4.1}$$

The $OSC_{Theoretical}$ accounts for the total reducible oxygen of the surface and could be calculated with the equation:

$$OSC_{Theoretical}\left(\frac{\mu mol\ CO_2}{g}\right) = N_O S_{BET} \frac{1}{N_A}\frac{1}{a^2}10^6 \qquad \textit{Equation 4.2}$$

Where N_O is the number of oxygen atoms that participate in the process, S_{BET} is the specific surface of the sample N_A is the Avogadro's number and a is the ceria lattice parameter in m. The calculations of the $OSC_{Theoretical}$ were proposed by Duprez et al. [42]. More precisely, it was considered that: i) only oxygen atoms bonded to ceria participate in the oxygen storage processes; ii) homogeneous surface and iii) only one of the O atoms is evolved in the process ($2\ CeO_2 \rightarrow\ Ce_2O_3 + O$). The resulted NL calculations are presented on Table 3.9.

Table 3.9. Number of oxygen layers as a function of temperature

	NL (150ºC)	NL (250ºC)	NL (350ºC)
CeAl	0.09	5.32	5.29
$Ce_{0.9}$ZrAl	0.24	5.47	14.79
$Ce_{0.9}$FeAl	2.59	31.82	41.25
$Ce_{0.9}$ZrFeAl	1.78	16.64	30.36

It is worth to clarify that NL ≤ 1 means that only oxygen from the surface is playing on the reduction process while, NL > 1 indicates the participation of oxygen from the bulk. Accordingly, all the samples use the surface and bulk oxygen at higher temperatures and only the iron containing samples are able to use the bulk fraction at 150 ºC. All the supports, exhibit increased oxygen mobility capacities with the rise of the temperature. However, no significant changes are obtained between 250 ºC and 350ºC for the Pt/CeAl sample.

Concerning to the doping agent influence, the iron incorporation leads to significantly improved OSC values. The $Ce_{0.9}ZrFeAl$ presents intermediate values in respect to the monodoped samples.

3.4.1.6. H_2-TPR

The samples reducibility when exposes to H_2 streams is also analyzed. The H_2-TPR profiles of the supports compared with their corresponding catalysts are shown in Figure 3.13. Usually two reduction steps associated with ceria's surface and bulk reduction are reported in the literature [43,44]. However for our CeAl support, wide one-step H_2 consumption is observed with no reduction occurring at higher temperatures indicating that probably the whole cerium oxide is behaving as surface ceria with no presence of bulk fraction.

Regarding the shape of the profiles, when zirconia is added no significant modifications are observed. However, the iron doped sample exhibits some differences in the profiles. These differences are expected on the basis that the mixed oxides normally show complex profiles in which multiple reduction process occurs simultaneously. Some of these variations could be related with the reduction profile of the bare Fe_2O_3 [45], which would imply the presence of partially segregated iron oxide. The shape of the $Ce_{0.9}ZrFeAl$ profile is more similar to that of $Ce_{0.9}FeAl$ than to the $Ce_{0.9}ZrAl$ one, and hence, the reducibility of the $Ce_{0.9}ZrFeAl$ is mainly ruled by the iron presence.

No matter the doping metal, a shift to lower temperatures of the ceria reduction process is observed, being for $Ce_{0.9}FeAl$ and $Ce_{0.9}ZrFeAl$ supports

more significant. These shifts reveal an improvement on the reducibility, probably due to synergic effect obtained through the solid solution formation, in particular, when iron is present.

The H_2-TPR of the platinum based catalysts is shown in the Fig. 3.13. All platinum based catalysts exhibit three clearly differentiated reduction zones. Various factors have to be taken into consideration when comparing the relative contribution of the reduction processes; the particle size of all reducible species and their interaction within the sample.

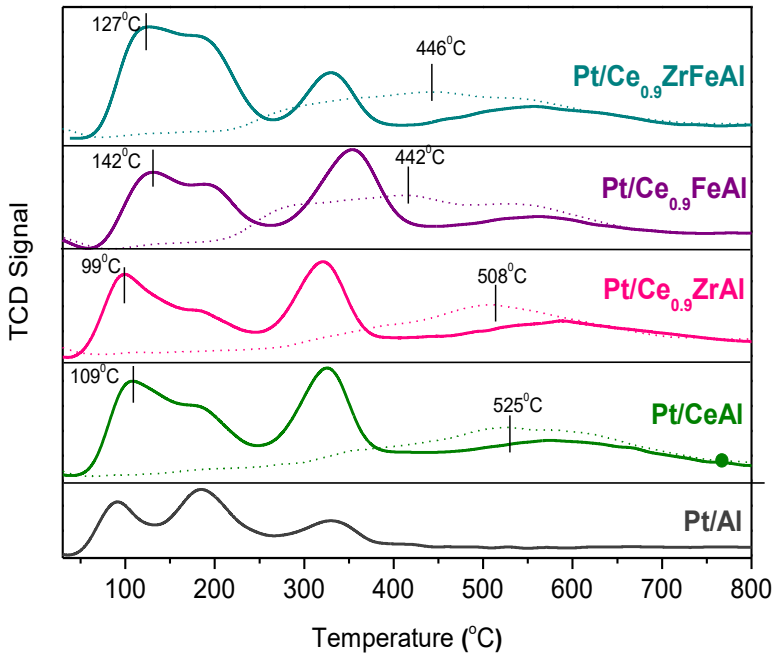

Figure 3.13. H_2-TPR profiles of the supports (dot lines) compared with their respective catalysts (solid lines)

The first H_2 consumption zone takes place up to 250°C, the second in the 250-425°C range and the third above 425ºC. The first zone is attributed to the

reduction of weakly interacting PtO_x species. It could be explained considering that the first reduction step is H_2 dissociation. The H_2 dissociation is easier when two H adsorption sites are adjacent; a case more probable on higher Pt particle sizes [30,46,47]. So, the higher the particle size, the lower the temperature of reduction. Nevertheless, the absence of XRD diffraction for PtO_x indicates that the highest particle size should be typically lower than 5 nm, which is in concordance with HR-TEM results.

The second reduction zone could be associated to highly dispersed PtO_x species strongly interacting with the support and to partial support reduction. In general, the temperature of reduction depends on particle size and the NM-support interaction [31]. Strong NM-support interaction increases the reduction temperatures, because of the NM-support synergism.

The third zone could be only associated to the support reduction, which occurs at temperatures superiors to the final WGS temperature (350 ºC), indicating that the support will not be completely reduced during the WGS reaction [48,49].

The reducibility percentages (RP) calculated considering Pt^{2+}, Fe^{3+} and Ce^{4+} species are presented on the Table 3.10. None of the support, achieves RP of 100% probably related with the bulk ceria fraction not reduced during the TPR experiments.

On the other hand, the platinum incorporation leads to superior RP values for all the samples. Actually, the platinum samples exhibit RPs higher than 100%

being the H_2 overconsumption especially noticeable for Pt/$Ce_{0.9}$ZrFeAl sample. Indeed, the platinum metallic diffraction clearly detected for Pt/CeAl and Pt/$Ce_{0.9}$FeAl and then, RPs above 100% also will indicate H_2 overconsumptions. These overconsumptions could be explained by hydrogen species incorporation into the ceria matrix forming H_yCeO_{2-x} bronze like species [27,50]. Fiero et al. [51] published similar results and concluded that an important amount of H_2 was incorporated in bronze like species into the ceria lattice by heating under H_2 at 300 ºC.

Table 3.10. Reducibility percentages (RP) obtained for supports and catalysts

	RP (%)		RP (%)
CeAl	76	**Pt/CeAl**	91
$Ce_{0.9}$ZrAl	86	**Pt/ $Ce_{0.9}$ZrAl**	105
$Ce_{0.9}$FeAl	71	**Pt/ $Ce_{0.9}$FeAl**	100
$Ce_{0.9}$ZrFeAl	79	**Pt/ $Ce_{0.9}$ZrFeAl**	118

The relative H_2 consumption for all the three zones is estimated and presented on the Figure 3.14. The first, second and third zone corresponds to the temperature ranges between 25-250 ºC, 250-425 ºC and 425-900 ºC, respectively. Comparing the three relative H_2 consumption processes for each system, an improvement of the redox behavior is detected for the Pt/$Ce_{0.9}$ZrFeAl system. For this system, the area of the first H_2 consumption step is qualitatively higher than the second one, contrary to all the other Pt based catalysts. This improvement appears to be the consequence of several

factors induced from both promoters. The zirconia lowers the temperature of reduction and the iron enhances the reducibility, by making easier H_2 dissociations and diffusions. As a result the relative reduction degree in the lower temperature zone is enhanced and an excellent redox behavior for this sample is achieved.

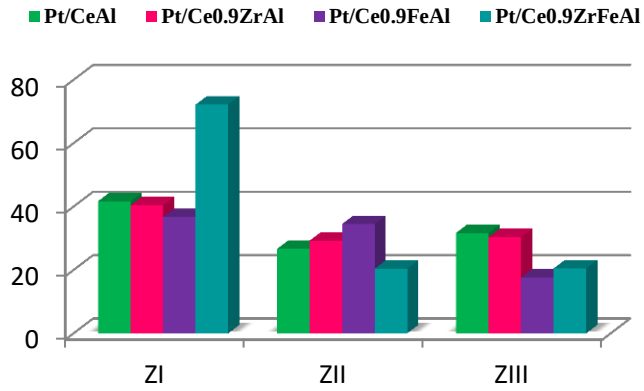

Figure 3.14. Relatives H_2 consumptions as a function of the temperature

Considering that all the catalysts are activated in H_2 at 350 ºC during 2h prior the catalytic tests, the reduction processes observed in ZI and ZII should be performed.

From the TPR data, the ceria reduction degree presented for the catalysts after the activation step can be also estimated. For that different assumptions are made i) all the platinum species are reduced along the ZI and ZII processes; ii) ceria reduction happens along the three reduction zones iii) the third and highest temperature reduction zone is uniquely due to ceria support. The reduction degree (Ce^{4+}/Ce^{3+}) estimations obtained are presented in Table 3.11.

Table 3.11. % Reducibility degree of supports exhibited for the catalysts after the H_2 pretreatment performed on the catalytic test

Pt/CeAl	Pt/ $Ce_{0.9}$ZrAl	Pt/ $Ce_{0.9}$FeAl	Pt/ $Ce_{0.9}$ZrFeAl
48.6	56.1	76.0	73.6

As it can be observed, the ceria lattice modification, no matter the doping metal, leads to significant differences in the redox behavior of the samples. Meanwhile the zirconia addition leads to slightly increased Ce^{3+}/Ce^{4+} ratio in comparison to the unpromoted sample, the Fe containing samples exhibits much higher reduction capacities. The iron presence induces similar reduction degree no matter the presence or not of a second metal.

At this point, the modifications performed by each doping agents can be appreciated. The redox behavior is prominently enhanced through the iron incorporation to the ceria lattice while, the most remarkable effect of zirconia is attributed to the stronger noble metal support interaction achieved and confirmed by the Pt size reduction.

3.4.1.7. Temperature Programmed Desorption (TPD) experiments

TPD characterization techniques can be used as a simple tool to obtain more detailed information about the gas-solid interactions during the WGS reaction. Indeed, in heterogeneous catalysts the reactive species should arrive to the catalytic surfaces, should adsorb, reacts and leave the surface liberating the active sites. Thus, knowledge about interactions of H_2, CO and CO_2 species

with the surface should provide useful understanding and correlation to the catalyst' reactivity.

The TPD experiments were carefully designed in order to obtain clean and similar catalytic surfaces before any gas adsorption or reaction. On first place the catalysts are preheated in inert gas (Ar) then reduced under H_2 and finally, the surface species generated by the reduction were removed by secondary heating in inert atmosphere. The adsorption desorption experiment includes the absorption of the reactive species till surface saturation, removal of the weakly physisorbed species under inert flow and then desorption as a function of the temperature.

The H_2-TPD profiles, presented on the Figure 3.15, were obtained after H_2 adsorption at room temperature. All the catalysts exhibited two similar and well discerned desorption zones with the increasing of the temperature. The low temperature H_2 desorption for all the samples suggests physically adsorbed H_2 on the catalysts surface meanwhile the majority of H_2 desorbed at higher temperature proposes strong chemisorption [52].

Moreover, the higher temperature desorption zone appears to be composed by multiple desorption processes accounting for different states of the adsorbed species on the surface. Although, the evolved desorption processes cannot be properly separated, several desorption processes could be appreciated especially for the Pt/CeAl and Pt/$Ce_{0.9}$FeAl samples. The observed wide

desorption process also indicates a strong dependence of the chemisorption properties on the surface coverage degree.

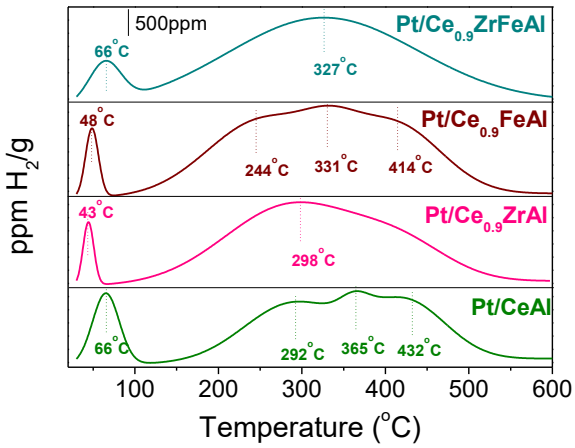

Figure 3.15. H_2-TPD profiles of the catalysts after H_2 adsorption at 25 ºC

Normally, H_2 species desorbed at temperatures around 115 ºC, are ascribed to chemisorbed hydrogen on dispersed platinum particles [53]. The H_2 desorption initiates at lower temperatures for Zr or Fe doped samples compared to the unpromoted sample, indicating that the presence of any of both metals can modify the platinum adsorption properties, either by modifying Pt particle size or by affecting its electronic properties. In fact, the $Pt/Ce_{0.9}ZrFeAl$ sample exhibits the above mentioned desorption immediately after evacuating the physisorbed H_2 being the later process even overlapped. That easiness of H species desorption, probably via reverse spillover process, suggests a substantial increment of the H species transfer ability, in good agreement with the high H_2 consumption observed at lower temperatures during the TPR test for this sample.

On the other hand, the introduction of both metals into the ceria lattice may increase the electron density on the surface. Considering the electron donor character of the H_2 species, the Pt-H_2 bond strength should decrease and thus, the chemisorbed H_2 species should be more easily removed from the surface.

The evolved H_2 species at higher temperatures, around 285 ºC, were related in the literature to hydrogen species adsorbed at the perimeter sites located at the metal support interface [53]. Any temperature shift of these desorption accounts for stronger electronic interactions between those sites and H_2.

The higher temperature desorption should be also related to reverse spillover of the H_2 species from the support to the platinum [52]. Multiple processes can be observed in the 250-350 ºC temperature range, usually assigned either to desorption of strongly chemisorbed spillover hydrogen or to that of adsorbed hydrogen in the subsurface layers.

The H_2-TPD profiles when H_2 is absorbed at 300 ºC are presented on the Figure 3.16. It should be underlined the difference in the desorbed H_2 amounts which is a function of the adsorption conditions. The hydrogen amount desorbed after H_2 adsorption at 300 ºC, is noticeably higher in respect to that observed at 25 ºC. This is in good agreement with Menon and Froment [54] work where the effect of the H_2 treatment temperature on the platinum samples adsorption was studied. They reported that higher the treatment temperature higher the spillover capacity of the samples, suggesting different interactions at every H_2 chemisorption temperatures.

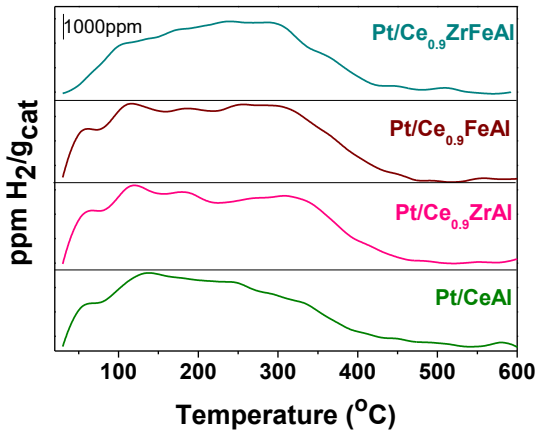

Figure 3.16. H_2-TPD profiles of the catalysts after H_2 absorption at 300ºC

Regarding the shape of the H_2-TPD profiles, the main difference relays on the H_2 desorbed at around 100 ºC. This desorption process is present when the H_2 chemisorption is carried out at 300 ºC, but absent at room temperature adsorption. This absence at low temperature could be attributed to the dissociative H_2 chemisorption through which the hydrogen species will be consumed and spillover to the support. Meanwhile, when H_2 is adsorbed at high temperature, the spillover processes should be already performed and chemisorbed hydrogen species readily desorbed. Therefore, the higher H_2 amounts at 300ºC could be attributed to reverse spillover effects during the whole desorption process.

The observed H_2-TPD results could be also correlated to the bronze like species formation. The presence of stabilized hydrogen species, as bronze like entities, must affect the adsorption and therefore the catalytic properties of the

samples [51]. The significantly higher H_2 amounts desorbed after adsorption at 300 ºC suggests that the incorporation of hydrogen species into the support is favored by the temperature and that those hydrogen species are later desorbed via reverse spillover through the platinum metal as H_2 molecules.

The CO/catalyst interactions are also analyzed by CO-TPD experiments. In this case during the desorption process the CO_2, H_2 and CO profiles are evaluated and presented in the Figure 3.17. The m/z=28 signal, is attributed only to the CO species and the relative contribution arising from the CO_2 species is properly subtracted.

For all the catalysts, two CO desorption zones (signal m/z=28) can be separated as a function of temperature: one below 250 ºC and another above that temperature. On first place a difference in the relative desorbed CO amounts is detected, being the Pt/$Ce_{0.9}$ZrAl and Pt/$Ce_{0.9}$FeAl the samples with the highest desorbed quantities. For similar systems, comparable profiles has been described in the literature [20,55,56]. For example, Du et al. [20] report weakly interacting CO species desorbing at temperatures below 100 ºC and hardly interacting ones evolving at around 320 ºC. The CO species desorbed between 170-260 ºC are generally ascribed to moderately adsorbed CO molecules, and can be discerned for all the catalysts, except for the Pt/$Ce_{0.9}$ZrFeAl system.

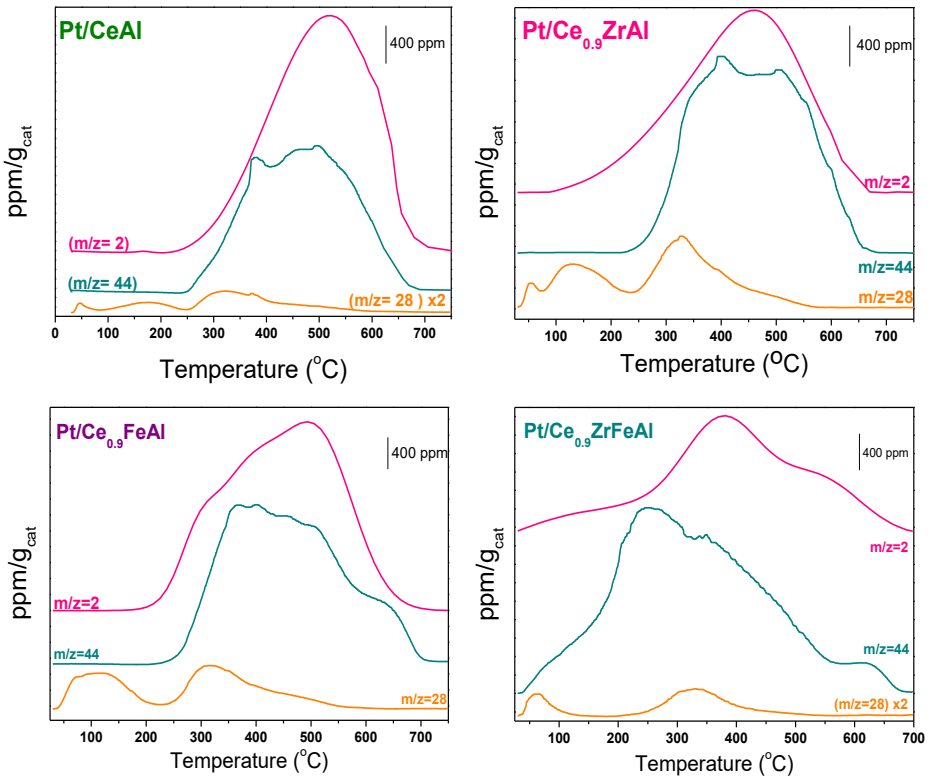

Figure 3.17. CO-TPD obtained for a) Pt/CeAl; b) Pt/Ce$_{0.9}$ZrAl; c) Pt/Ce$_{0.9}$FeAl and d) Pt/Ce$_{0.9}$ZrFeAl

Moreover, the CO_2 and H_2 desorption processes present complex profiles for all the samples. Pt/CeAl, Pt/Ce$_{0.9}$ZrAl and Pt/Ce$_{0.9}$FeAl samples show comparable CO_2 profiles comprising a wide desorption process which starts at 300 ºC and continuous till the final temperature. Simultaneously, H_2 species are evolved in the same temperature range. Normally, simultaneous CO_2 and H_2 desorption processes are related to bicarbonate decomposition processes. Considering that the surface was pre-cleaned before and after the reduction treatment, the catalytic surface should be clean of H_2 species. The observed

bicarbonates species are then only formed through the reaction of the adsorbed CO with the OH species on the catalyst surface.

Furthermore, all the samples exhibit CO species desorption at similar temperatures with maximum edge placed above 330 ºC, also related to H_2 species evolved in this temperature range, especially evident for the Pt/CeAl, Pt/$Ce_{0.9}$ZrAl and Pt/$Ce_{0.9}$FeAl sample. Simultaneous CO and H_2 desorptions are generally ascribed to hydrogen-carbonaceous species decomposition, most probably carboxyl or formate species.

The sample Pt/$Ce_{0.9}$ZrFeAl shows clear difference in its CO-TPD profile pointing to significant changes on its adsorption properties. The CO_2 and H_2 species desorb along the whole temperature range with their respective desorption edges centered at around 240 ºC and 370 ºC. It appears that the presence of both doping agents on the ceria lattice strongly modifies solid's chemisorption properties. Mullins et *al*. [55] reported that at temperatures below 127 ºC the CO_2 species released after CO adsorption, could be attributed to the reaction between adsorbed CO and lattice oxygen species on Pt metallic sites.

The presence of both doping agents could provoke an enhanced electronic density on the catalyst surface which could favor the CO adsorption and oxidation with subsequent formation of carbonaceous species. The easier CO-surface reaction could also be associated to the lower desorption temperature observed for CO_2 and H_2.

On the other hand, the increased electronic density on the catalyst surface should also favor the surface species mobility (H, OH or O species) through the high oxygen vacancies concentration. For the platinum ceria samples, it was described that the oxygen vacancies concentration is higher in the metallic platinum particles surroundings, decorating them. So, the mobility of the OH and/or O species through electronic delocalization within the electronic vacancies should increase leading to a chemical environment continuously altered around the oxygen vacancies.

Considering the carbonaceous species that could remain on the catalysts surface after CO-TPD experiments, a TPO was carried out. For this experiment (Figure 3.18), it was assumed that all the carbonaceous species will be oxidized in oxygen presence to CO_2.

Very different CO_2 profiles are observed for all the catalysts. The Pt/CeAl and Pt/$Ce_{0.9}$ZrAl systems exhibited two different desorption processes. For both, the lower temperature desorption was significantly less important than that at higher temperature. In addition, the CO_2 desorption process begins at lower temperatures compared to those for Fe-containing samples.

In fact, Pt/$Ce_{0.9}$FeAl and Pt/$Ce_{0.9}$ZrFeAl samples show one CO_2 zone centered at 369 ºC and 259 ºC respectively. It should be noted that the CO_2 profile intensity for the Pt/CeAl sample was reduced by half in order to be comparable to the others results. Therefore, the introduction of the doping agents lead to decrease of the overall CO_2 amounts in respect to the

unpromoted sample, confirming the statement that the oxygen vacancies creation results in more labile carbonaceous species on the catalyst surface, species more readily desorbed in TPD conditions.

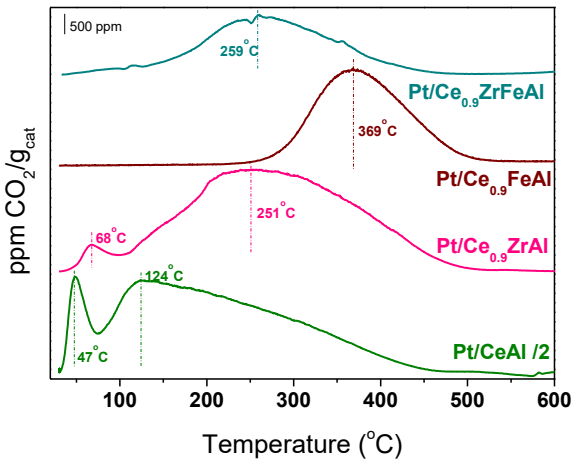

Figure 3.18. CO_2 profiles obtained during the TPO experiment, after CO-TPD

Similarly, Goguet et *al*. [57] reported DRIFT studies of the adsorbed species after CO adsorption. They observed, that the species associated to the deactivation are generally formates and carbonates, and that they are not affected by the exposure time and desorbed at low temperature (room temperature to 250 ºC) in the presence of oxygen. At room temperature, the oxidation products proceeds from adsorbed carbonyl species and at higher temperature, in the 260-290 ºC range, CO_2 species originates from the oxidation of carbon deposits. It was also reported that the carbon deposits quantity varies with CO exposure time, indicating a continuous accumulation of oxidizable carbon.

The carbon depositions on noble metal of the X group are well known as cause of deactivation. The formation of carbon deposits in the presence of CO could be ascribed to the Boudouard's reaction ($2\,CO \rightarrow C + CO_2$). Some works relates the carbon deposit formation to the platinum species and to the oxygen vacancies (Ce^{3+} population) [58,59]. Holmgren et al. [56,60] reported that the CO disproportionation occurs on oxygen vacancies, but important carbon deposits were set up when ceria catalysts are promoted with platinum. Then, although the CO dissociation happens on the support surface, carbon species can migrate from the support to metallic platinum constructing carbon rings around the Pt particles.

Our TPO results show a decrease of the carbonaceous and carbon deposits with the addition of doping agents. Moreover, the carbonaceous species appearing under 250 ºC are not observed for the iron promoted samples. The iron presence appears to enhance the decomposition rate of those species, thus lowering the rate of catalyst's deactivation. On the other hand, the $Pt/Ce_{0.9}FeAl$ shows increased carbon deposits stability, confirmed by the highest temperature of oxidation observed in its TPO profile.

For the bi-doped sample, the beneficial effect provided by the iron presence, regarding the easier decomposition of intermediate species, is maintained. Additionally, the $Pt/Ce_{0.9}ZrFeAl$ shifts the desorption edge to lower temperatures in respect to the $Pt/Ce_{0.9}FeAl$. It appears that the carbon deposits stability is ruled out by the zirconia presence, higher the Zr concentration

lower the temperature of oxidation. Furthermore, the bi-doped sample apparently forms lower amounts of carbon depositions. A combination of beneficial effects on the deactivation degree of both doping metals is achieved for this sample.

The quantification of the desorbed species is performed with the following assumptions: i) the CO_2 desorbed in CO-TPD is mainly formed by the reaction of CO with an oxygen atom ($CO + [O]_s \rightarrow CO_2$) from the support lattice; ii) CO_2 species can be also formed by reacting the OH species ($CO + [OH]_s \rightarrow {}^1/_2\, H_2 + CO_2$) also provided by the supports and iii) CO could react through Boudouard's reaction ($2CO \rightarrow C + CO_2$) or desorb without reaction during the CO-TPD experiments. From all stated above, the CO species reacting with the OH species could be calculated from the H_2 amount. Besides, from the difference between the total CO_2 and the CO_2 derived from the OH species, the CO reacting through the O species of the support can be calculated.

On the other hand, the CO_2 species desorbed during the TPO post CO-TPD should proceed from: i) intermediate species not desorbed along CO-TPD experiments or ii) carbon deposits produced through the Boudouard's reaction. No matter the origin of the CO_2 species in the TPO experiments, it can be assumed that those CO_2 species are responsible for the deactivation processes on the catalyst surface. In the Table 3.12, it is presented the relative proportion of all those processes.

Table 3.12. Relative proportion of products after TPD-TPO

	% CO_{OH}	% $CO_{[o]sup}$	% CO_{total}	% CO_{deact}
Pt/CeAl	17.31	45.08	62.39	37.61
Pt/$Ce_{0.9}$ZrAl	18.45	53.36	71.81	28.18
Pt/$Ce_{0.9}$FeAl	26.56	55.10	81.66	18.34
Pt/$Ce_{0.9}$ZrFeAl	25.00	57.00	82.00	18.00

Apparently, all the doping agents promote the CO to CO_2 oxidation in comparison to the unpromoted sample. The promotion origin depends on the doping metal, as for example, the iron presence boosts the CO reactivity via OH. In the same time, an enhance of the O species mobility occurs (reaction through support`s O species) no matter the doping agent, which is in a good agreement with the OSCC and OSC measurements for those samples.

Also, important improvements concerning the deactivation species formation are achieved when both doping metals are added to the ceria matrix. While zirconia addition helps the rapid evacuation of the species susceptible to deactivate the catalysts from the surface, the iron incorporation significantly diminish their concentration. And when both are combined, the stability of the deactivation species decreases considerably, being apparently ruled by the zirconia presence.

As a final TPD experiment WGS mixture containing CO and H_2O in 1:1 volumetric ratio was passed through the samples at room temperature. After

the adsorptions and once the signal stabilized the temperature was increased up to 600 ºC and the results resumed in Figure 3.19.

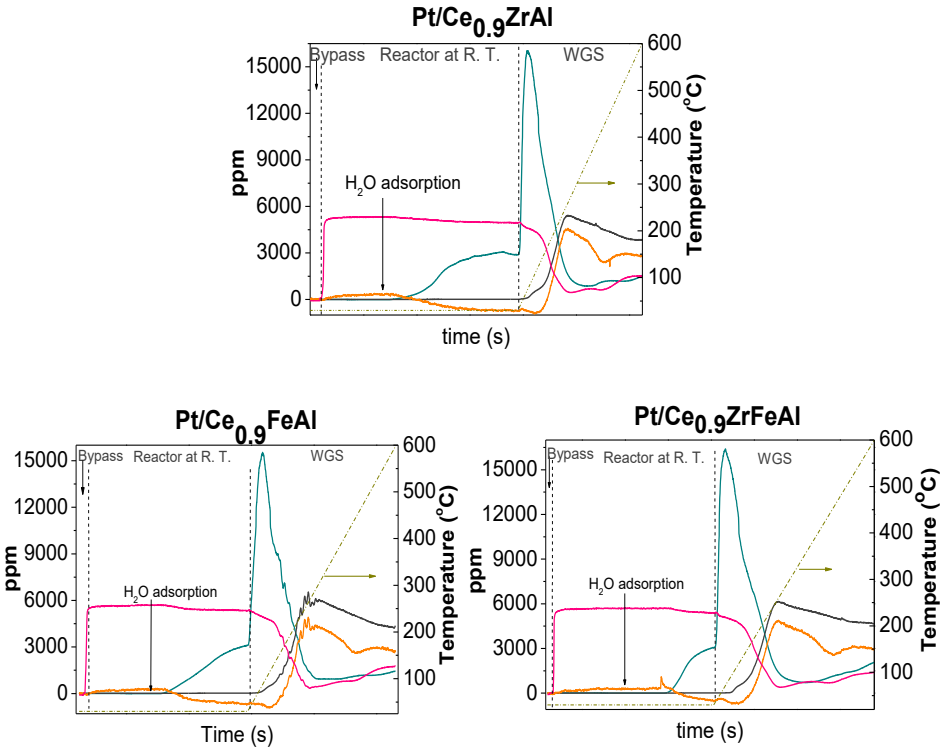

Figure 3.19. CO and H_2O adsorption at R. T, followed by WGS reaction

During the adsorption step at room temperature, H_2 formation is observed in absence of water signal suggesting that those H_2 species should proceed from the re-oxidation processes performed within the oxygen vacancies proceeding through water dissociation. Once the surface saturated, the water signal starts to appear meanwhile CO and H_2 signals decreased without formation of CO_2. The reaching of surface reduction-oxidation equilibrium could be imagined.

With the start of the heating ramp, prominent water signal is observed accounting for the physically absorbed water on the surface. However, a second contribution also arises. At around 150 ºC the WGS reaction products CO_2 and H_2 start to appear. At the same time, the CO signal decays accompanied with a change in the slope of water desorption. Thus, the important changes of the water signal are due not only to physisorbed water but also to water consumptions via WSG reaction.

At higher temperatures, a change in the behavior tendency of the H_2O and CO species occurs. The water signal intensity increases, which could indicate WGS reaction limitation at higher temperatures. Actually, the H_2 and CO_2 signals exhibit a parallel diminution when the temperature is increased indicating the reverse WGS reaction. Besides, the H_2 signal shows a diminution at around 450 ºC for all the samples which could be attributed to the support reduction in H_2 presence as observed by the TPR experiments.

Within the series of samples besides, the water desorption behavior change, some other differences could be also detailed in Figure 3.20. Although the water desorption process appears to be the main contribution on the water signal at lower temperature, some water species reacts with CO via WGS reaction. The maximum of activity is placed at around 350 ºC, temperature at which the water concentration reaches its minimum. Above this temperature the water concentration steadily increases following the WGS CO conversion equilibrium limitation with the temperature.

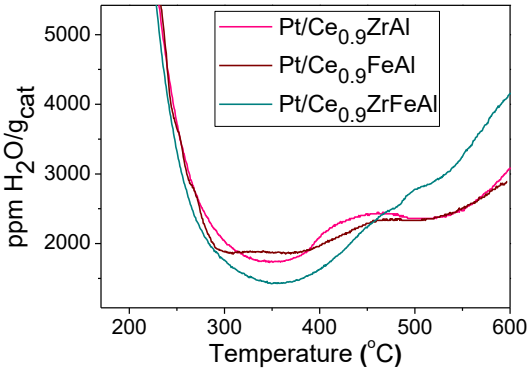

Figure 3.20. Water desorption profile under WGS conditions in the 180-600 °C temperature range

The $Pt/Ce_{0.9}ZrFeAl$ sample exhibits the lowest water concentration between 300 ºC and 450 ºC which could be related to a possible higher activity in comparison to the other samples. Moreover, the water signal observed after the optimal WGS temperature range present different profiles. Apparently, the most active sample desorbs higher amounts of water with the increase of temperature.

Considering the WGS equilibrium, higher partial pressure of water on the catalyst surface should lead to higher CO conversion. Thus, the better catalytic performance achieved for this sample could be associated to its apparently enhanced capacity to maintain more absorbed water on the surface. The water dissociation, the limiting step of the WGS reaction, should be easier when the adsorbed water concentration is maintained high, a case suggested for the $Pt/Ce_{0.9}ZrFeAl$ sample.

3.4.1.8. CO adsorption and CO-TPD followed by FTIR spectroscopy

The adsorption of CO over a catalyst's surface is often followed by IR spectroscopy which constitutes a very powerful tool for supported transition and noble metals characterization. In the case of Pt, CO adsorption leads to IR spectra mainly composed by two ν(CO) adsorption regions: 2090-2000 cm^{-1} and 1860-1780 cm^{-1} characteristic respectively, to a linear CO adsorption on a single Pt atoms and to a a bridged CO adsorption on two Pt atoms.

The chemical interaction CO-Pt was established by Blyholder [61,62] and it is considered that the bond proceeds through the 5σ bonding and $2\pi^*$ antibonding orbitals of CO and Pt interaction. The 5σ–Pt interaction is electron donating towards Pt and strengths the Pt-C bond. The antibonding $2\pi^*$-Pt interaction corresponds to an electron transfers from Pt to the antibonding CO orbital, decreasing the C-O bond strength through increasing of the electron density on the $2\pi^*$ orbital. Thus, higher the back donation from Pt to CO $2\pi^*$, lower the ν(CO) vibration. The ν(CO) band position depend on several factors such as: the number of Pt bonded to the CO molecules, the coordination of the Pt atoms in which the CO is adsorbed, the oxidation state of Pt, the CO coverage and the presence of electron donating or accepting centers in contact with the Pt particles.

The combination of CO used as probe molecule, and IR spectroscopy are widely used to characterize the metal oxides such as cerium simple or mixed oxides [63,64]. Indeed, many studies have been carried out addressing the CO

ceria interaction and the Pt promotor effect. Contrasting to the assignments of Pt-CO interaction, the interactions are less clear for the ceria surfaces. For example, on highly ordered CeO_2 (111) surfaces only weakly adsorbed CO was found suggesting some oxygen vacancies role on the CO-ceria interactions [65,66]. Similar conclusions on the importance of the oxygen defects were reported by Berner and Schierbaum [66]. They found that the CO adsorption was not possible on stoichiometric CeO_2 supported on Pt(111) but, on a partially reduced ceria surfaces where several interactions were registered.

Even though for Pt/ceria samples strong metal support interaction (SMSI) is commonly accepted there is not a scientific agreement concerning the molecular mechanism. The explanations are normally related to Pt decoration by a reduced ceria and/or to purely electronic effect arising from an intimate Pt ceria surface contact.

O adsorptions till saturation followed by FTIR techniques are performed. For that, the samples were pretreated in H_2 atmosphere at 350 ºC then, degassed at 500 ºC in secondary vacuum in order to clean the surface before the adsorption and then the CO was adsorbed in portions till saturation. The CO adsorption spectra are presented in the Figure 3.21 for all the samples.

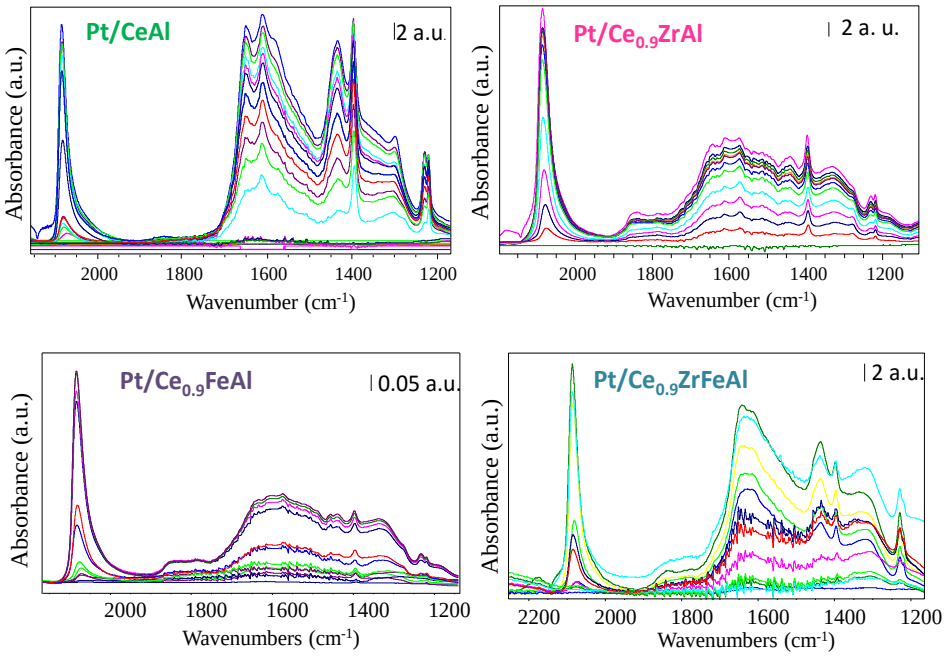

Figure 3.21. Spectra obtained during the CO adsorption on the catalysts

In all the samples, the CO adsorption leads to increased intensities of the Pt-CO bands at 2100 cm^{-1} indicating that all the platinum species were successfully reduced to Pt^0 during the H_2 pretreatment. Furthermore, several other species are observed in the 1800-1100 cm^{-1} region and in the hydroxyl region (3500-3200 cm^{-1}). It should be noted that the bands in the former region, ascribed to carbonaceous species, increased more rapidly than the Pt-CO stretching band saturation. The bands placed at 1650, 1611, 1434, 1397, 1229 and 1219 cm^{-1} could be ascribed to different kinds of hydrogen-carbonates, being also discerned its corresponding υ(OH) stretching vibrations

at 3617 cm^{-1} [63,67,68]. In addition the bands situated at 1630 and 1550 cm^{-1} are attributed to carbonates species. The CO adsorption yields to bands at 1840 and 1790 cm^{-1} for all the catalysts, being their intensity significantly lower for the Pt/CeAl sample. The band placed at 1840 cm^{-1} is usually related to bridged carbonyls [69] but could also be attributed to bridged carbonates [2].

On the other hand the 1790 cm^{-1} band, could be related to tilt CO adsorbed on very dispersed Pt complexes [70]. Yee et al. [52] related those CO species to altered support properties and indicated that the ceria cations present in the supports influence the adsorption state of CO by enhancing the backbonding through the metal.

Moreover, the main Pt-CO band exhibits significant changes on its position as a function of the introduced CO amount. As shown on the Figure 3.22.a, the adsorption of 1.4 μmol of CO within the series of samples leads to different relative intensities and provokes a shift of the band position to higher wavenumbers as a function of the CO coverage.

The coverage effect can be explained considering both, the static or chemical and the dynamic effect. The chemical effect considers the platinum species as electron reservoir. Thus, an increment of the adsorbed CO molecules should result in decrease of the back-donation which involves decrease of the Pt-CO strength appearing at higher ν(CO). The dynamic approach accounts for the coupling effect between the CO molecule dipoles which results in a shift to a

higher wavenumbers. Once the surface saturated all the samples present the same ν(CO) maximum at 2086 cm^{-1} (Figure 3.22.b) which indicates that the platinum particles distribution is for all the catalysts.

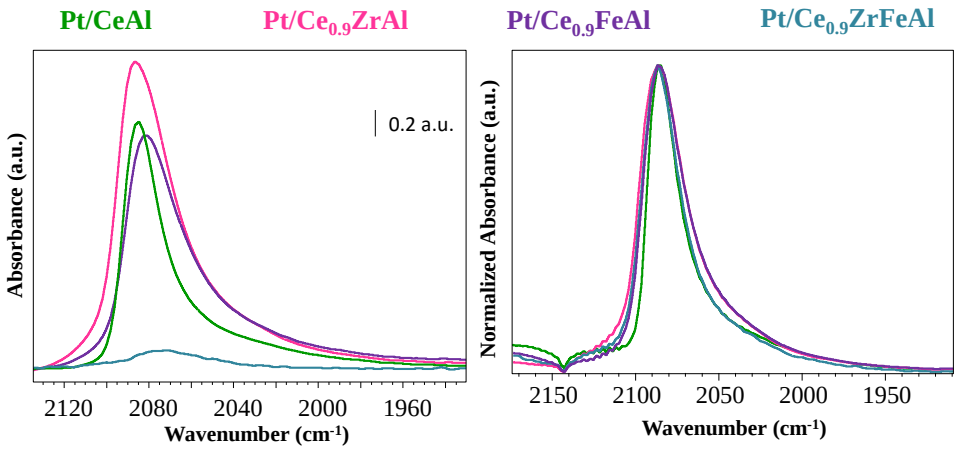

Figure 3.22. Pt-CO stretching at: a) 1.4 μmol CO and b) saturation

The TPO experiment pointed out the formation of carbon deposits on the catalytic surfaces during the CO adsorption via Boudouard`s reaction. Although the C deposits could not be observed by IR directly an account for them could be intuited through the alteration of the CO adsorption capacity for the equally dispersed samples, i.e. samples with the same Pt particles size. If the Boudouard's reaction occurs only on the Pt particles an indirect indication of the C formation could be obtained by the estimation of the CO adsorption capacity, in a way that higher the C deposit lower the surface of the site for the CO adsorption and thus lower the CO quantity for monolayer

formation. Figure 3.23, shows the integrated Pt-CO stretching band area normalized by the Pt content as a function of the introduced CO. All the samples exhibit two different trends being the intersection between them commonly related to the monolayer formation.

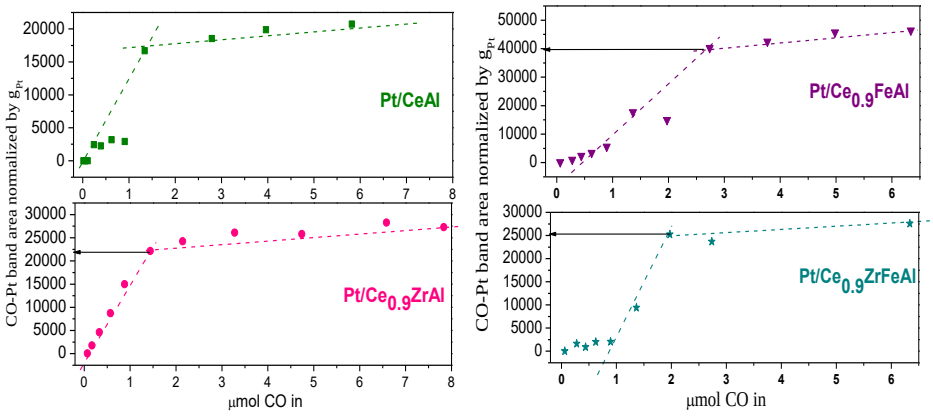

Figure 3.23. Pt-CO band area normalized by the Pt content vs. µmol CO introduced

From this point, it is possible to establish a relationship between the monolayer area and the Pt particles available for the adsorption of CO molecules. The following order of monolayer formation is observed:

$$Pt/CeAl < PtCe_{0.9}ZrAl < PtCe_{0.9}ZrFeAl \leq PtCe_{0.9}FeAl$$

This trend shows on first place that the introduction of any doping agents leads to improvement of the sample`s resistance to carbon deposits formation, being the iron containing solids and $Pt/Ce_{0.9}FeAl$ in particular especially resistant. The results obtained for the $Pt/Ce_{0.9}ZrFeAl$ sample are rather unexpected regarding the lowest CO_2 amounts desorbed during the TPO

experiment. However, it should be kept in mind that the susceptible to deactivate species observed in the TPO experiments could include not only carbon deposits but also other carbonaceous species. Therefore, the $Pt/Ce_{0.9}ZrFeAl$ appears to be resistant not only regarding only the C formation but also to carbonaceous species deposition resulting from the synergism between both dopants presence, with Fe responsible for the C deposits decrease and Zr to the other carbonaceous species lability.

Further considerations regarding the easiness of desorption processes could be extracted from the IR experiments. In the Figure 3.24, the spectra obtained after normalization by the sample amount at approximately 1.4 μmol CO introduction are present. Although, all the samples show the characteristic bands of carbonaceous species (1800-1100 cm^{-1} region) before Pt-CO band saturation, significant differences are found in the relative intensity of each region. Normally, it is accepted that CO is absorbed and activated on Pt particles. Once activated, the CO can directly reacts to an adjacent O which initially should desorb as $CO_{2(g)}$. However, it is also plausible that those already oxidized CO_2 species re-adsorb on the support forming carbonates or hydrogen-carbonates. In this way the activated CO species could be transferred to the support where carbonaceous species are formed. Hence, the differences found in the relative intensity may be correlated to the catalysts capacity to activate CO molecules and to transfer those already activated species on the support. Within the studied samples the $Pt/Ce_{0.9}ZrFeAl$ shows a significantly enhanced capacity to transfer CO species to the support

confirmed by the lowest intensity of the Pt-CO band (at 2086 cm^{-1}) and compared to the carbon containing species placed in the 1800-1180 cm^{-1} region.

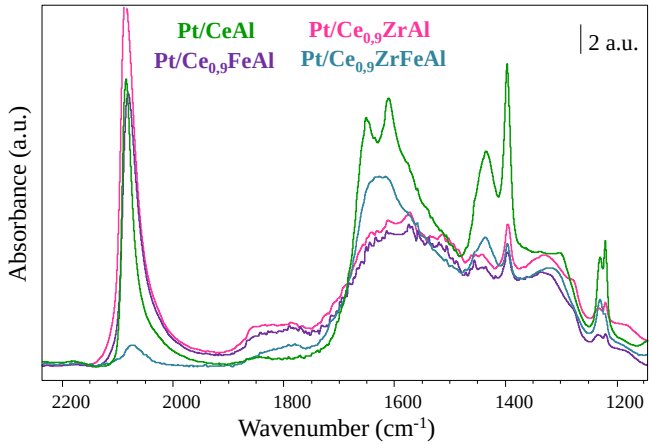

Figure 3.24. CO adsorption at 1.4 μmol CO coverage

After the surface saturation, the corresponding CO–TPD experiments were also performed following the sequence: saturation, second vacuum, 50 ºC, 100 ºC and 150 ºC. The CO-TPD obtained for all the catalysts are presented on Figure 3.25 and shows important differences on the desorption behavior of the formed species.

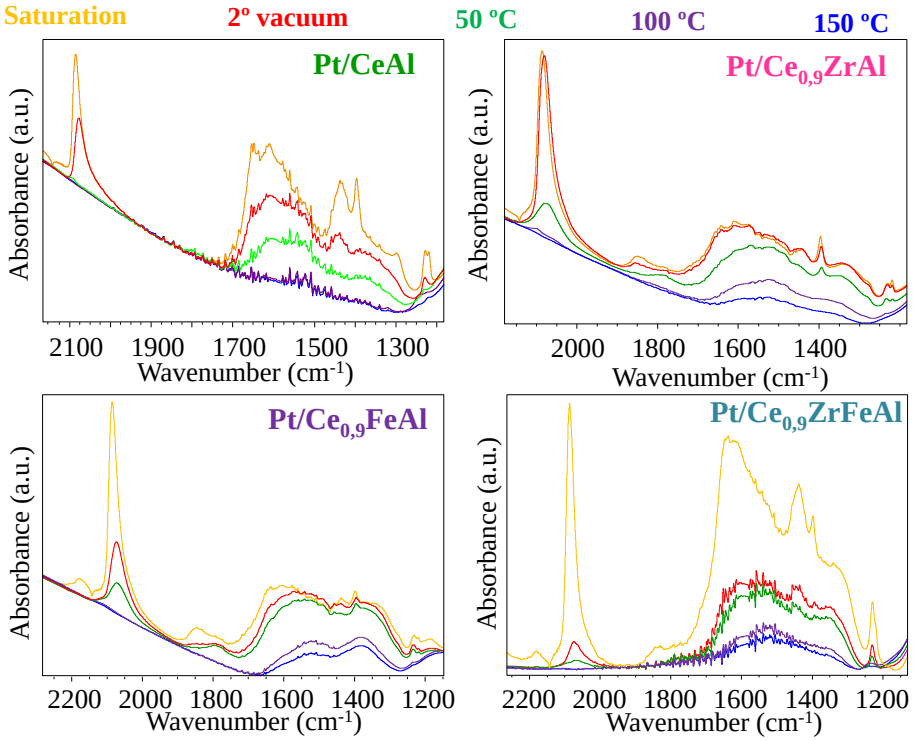

Figure 3.25. Spectra recorded, after saturation, and during the CO – TPD

The spectra obtained for the samples submitted to secondary vacuum and normalized by the sample amount are also presented in Figure 3.26.a and 3.26.b, respectively. When the secondary vacuum is applied, the Pt/CeAl sample diminishes all surface adsorbed species, on both Pt and support. Oppositely, the Pt/$Ce_{0.9}$ZrAl sample does not show any significant change indicating stronger interaction of the adsorbed CO species. It is likely, that the Pt electron density alteration is responsible for stronger CO interaction with this sample. Moreover, if the support is considered as an electron reservoir the

electron density there should be quite important and could explain the lowest degree of desorption of species such as CO_2 and H_2 because of their donor character.

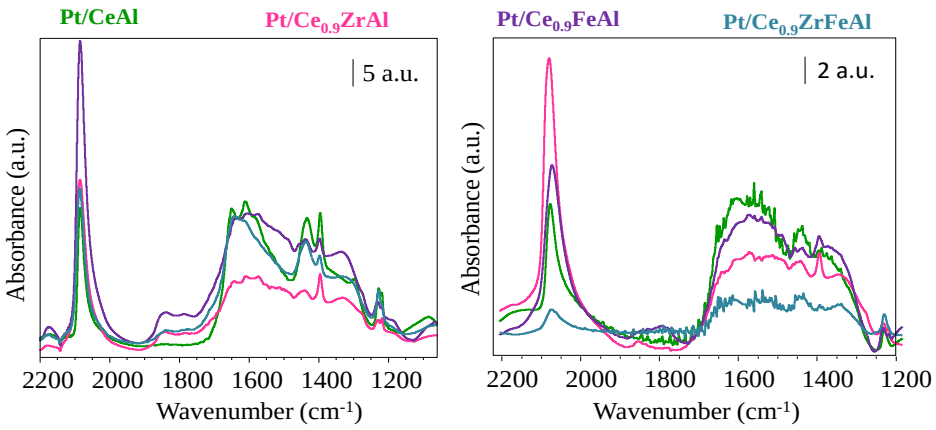

Figure 3.26. Comparison of the spectra at: a) saturation; b) after exposure to 2º vacuum

By its part, the $Pt/Ce_{0.9}FeAl$ sample shows a pronounced desorption for Pt-CO species meanwhile minor alteration of the support species implying that the system is not able to provide enough electron density neither to Pt particles nor to the species adsorbed on the support. Related to the lowest degree of carbon deposition on this sample one could suppose that any possible deactivation of this sample could arise from less labile carbonaceous species at the temperature of WGS reaction.

In agreement to the CO-TPD results, the Pt/$Ce_{0.9}$ZrFeAl sample easily desorbs all the surface species. This implies that the Pt/$Ce_{0.9}$ZrFeAl is the system that is able to provide higher electronic densities to support species thus promoting their desorption. And in summary this sample exhibits higher capacities to activate CO molecules, to transfer them to the support and to desorb them.

3.4.2. Catalytic behavior

The catalytic activity of the studied samples is evaluated in the WGS reaction. In the Figure 3.27.a, the performance of the catalysts in model mixture (4.5% CO + 30% H_2O + N_2 as balance) is presented. No important changes can be observed for this gas composition and conditions, reaching the equilibrium conversion at 230 ^oC. The differences between the samples appear only at lower temperatures. While both iron containing samples are more active at T=180 ^oC, the zirconia doped sample arrives first to the equilibrium conversions at T=200 ^oC.

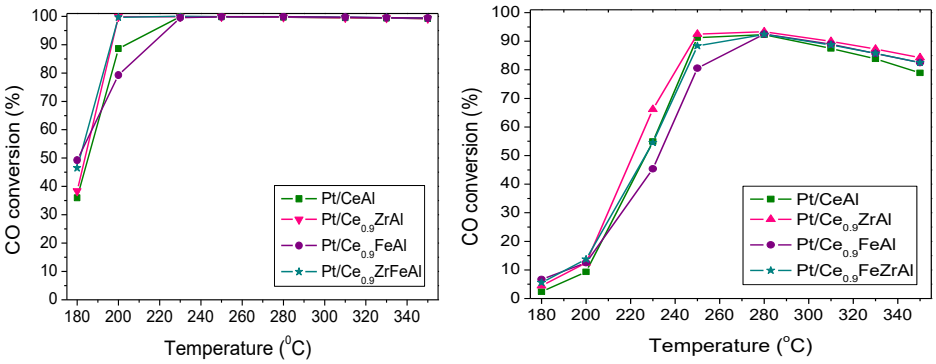

Figure 3.27. % CO conversions obtained for the catalytst in a) model conditions; b) "real" conditions

The catalysts are also tested in "real" conditions (Figure 3.27.b). Compared to the model mixture, all the samples reach the equilibrium conversions at higher temperatures. Considering that this reaction is an equilibrium reaction, this shift is expected due the presence of the H_2 and CO_2 in the feed stream in agreement with the Le Châtelier principle. On the other hand as for the model conditions no significant improve of the catalytic behavior is observed.

However, as the efficiency of the process depends on the space velocity per unit of catalyst, the effect of the GHSV on the catalytic activity under "real" conditions is also studied at T = 280 ºC. In the Figure 3.28.a, the catalytic performance in CO conversion terms is shown. Opposite results are obtained depending on the GHSV: meanwhile the Pt/$Ce_{0.9}$ZrFeAl exhibits greater CO conversion at lower space velocities, the Pt/$Ce_{0.9}$ZrAl sample takes advantage at the higher ones. The higher activity of the Pt/$Ce_{0.9}$ZrAl sample at higher spaces velocities suggests the conclusion that the platinum loading could rule the catalytic performances at higher space velocities becoming the support modifications secondary features.

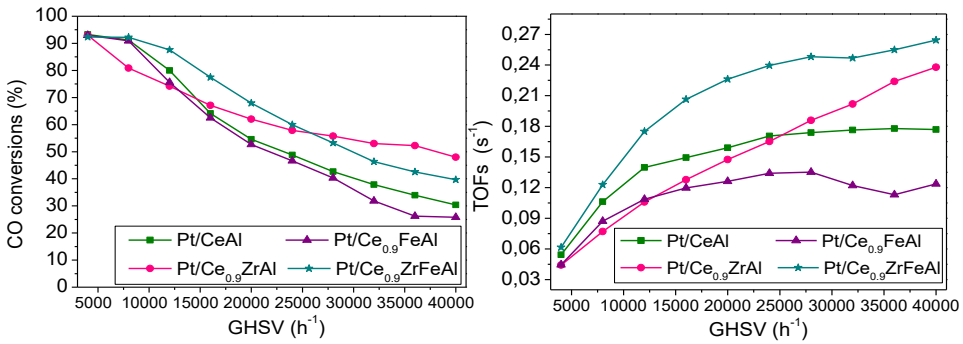

Figure 3.28. GSHV effect on the obtained catalysts: a) % CO conversions; b) TOFs

In order to elucidate the support effect, the catalytic activity was normalized by the mole of exposed platinum atoms by using the dispersion values obtained in CO chemisorption measurements. The turnover frequencies (TOF, s^{-1}) are estimated for different GHSV and presented in Figure 3.28.b. The $Pt/Ce_{0.9}ZrFeAl$ sample appears now as the most active along all the tested GHSV range.

However with the purpose to ensure the beneficial effect provided by the support and to discard the platinum content role, 2 wt.% of Pt was deposited on the same supports. For all the catalysts similar platinum contents were achieved. The catalytic behavior of the samples tested in real conditions at 280ºC and as a function of the GHSV is presented in Figure 3.29.

Now the tendency in CO conversion terms confirms the beneficial effect of the support on the catalytic activity. However, when comparing the 2 wt.% series with the 4wt.% one similar conversions are observed suggesting that at the higher Pt loading and lower space velocity, the Pt atoms are not entirely involved in the reaction.

Thus in agreement to all the characterization results the sample presenting lower cerium oxide particle size, the highest reducibility, the lowest BG energy and relatively high F_{2g}/Ov ratio, pointing to the most important electronic and structural promotion is the most active sample. In addition lower degree of deactivation is expected for this sample on the basis of the TPD and the IR studies.

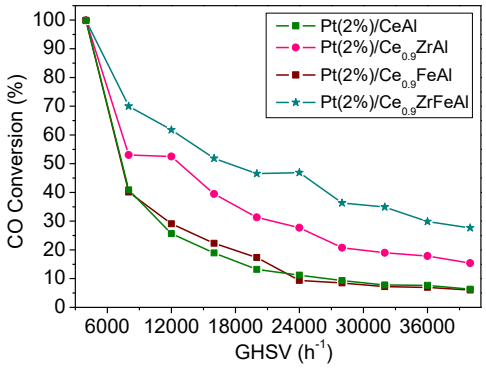

Figure 3.29. GSHV effect on the 2 wt. % Pt catalysts in % CO conversions terms

3.5. Partial conclusions

Catalytic screening of a series of different ratio Ce/Zr based supports was successfully achieved. Within the series no matter the doping metal proportion the solid solution formation was detected. Although minor, the differences obtained in the catalytic performance of the samples allowed the choice of an optimal Ce/Zr molar ratio of 9. The improvement on the catalytic behavior on this catalyst was associated to the absence of platinum metallic diffraction which implies higher platinum dispersions and, as an outcome, higher catalytic activity.

From that point the Ce/doping metal ratio was maintained and the zirconia and iron were incorporated as doping metals separately or in combined manner. For these samples and concerning the structural changes, the zirconium presence provokes larger ceria particle sizes meanwhile the iron causes the opposite effect.

Concerning to the Pt metal, all the samples are constituted by two types of Pt particles: one fraction highly dispersed and the other one agglomerates being the later detected on the XRD patterns (Figure 3.8). However, the HR-TEM and the CO chemisorption results suggest that the agglomerated fraction was significantly minor than the dispersed ones, above 1 nm. In good agreement to the XRD results, all the doped samples showed, on the CO-TPD/FTIR experiments, features related to highly active Pt species, strongly interacting with the support.

The iron as promoter leads to especially enhanced OSC capacities, higher band gap contraction and higher oxygen vacancies population. Its promotion could be then mainly related to electronic and redox features also in concordance with the results observed by Raman spectroscopy.

On the other hand, the zirconia promotion should be principally related to the Pt metal and it provokes the most important diminution of the size of the Pt agglomerates accounting for a strong metal support interaction confirmed also by the FTIR experiments.

The combination of both Fe and Zr results in finely balanced structurally and electronically promoted system. The Pt/$Ce_{0.9}$ZrFeAl sample shows beneficial promotions from both doping agents resulting in lower Pt sizes and the enhanced redox properties provided by Zr and Fe, respectively. Besides, the prominent band gap diminution detected from UV-Vis characterization suggesting also an important synergic effect achieved in the case of the

$Pt/Ce_{0.9}ZrFeAl$ sample. Taking into account the greater H_2 consumption at lower temperatures and the significant H_2 overconsumption showed by this sample during the TPR experiment, a superior mobility of the oxygen species was found (OH and O species). However, the oxygen vacancies population and the oxygen mobility ability for the $Pt/Ce_{0.9}FeAl$ sample were superior to that observed for the $Pt/Ce_{0.9}ZrFeAl$ ones.

In addition a superior mobility of the H species was also found, resulting from a reverse spillover processes confirmed by the lower temperatures of H_2 species desorption on the $Pt/Ce_{0.9}ZrFeAl$ sample during the H_2-TPD experiment (Figure 3.15). Similar conclusions can be extracted from the FTIR experiments where the $Pt/Ce_{0.9}ZrFeAl$ sample exhibited higher capacities to activate and to transfer the CO species (Figure 3.22). In addition, the fact that the $Pt/Ce_{0.9}ZrFeAl$ sample shows higher water absorption capacity at higher temperatures should be also considered (Figure 3.20), and related to the improved H/OH species transfer.

The introduction of doping agents modifies the stability of the carbonaceous species formed on the support (Figure 3.18). Furthermore, different features were obtained for the $Pt/Ce_{0.9}FeAl$ and $Pt/Ce_{0.9}ZrAl$ catalysts. While the former strongly decreases the desorbed amounts, the later leads to easier oxidations reactions at lower temperatures. Again, $Pt/Ce_{0.9}ZrFeAl$ combined both beneficial effects of the doping metals, exhibiting the lowest amount of desorbed CO_2, issued from the carbonaceous species at similar temperatures

observed for the $Pt/Ce_{0.9}ZrAl$. In good concordance, with the FTIR results where desorption occurs at secondary vacuum (Figure 3.26.b).

Therefore, the combination of Zr and Fe on the $Pt/Ce_{0.9}ZrFeAl$ provides enough electron density to the Pt to activate the CO molecules but also a sufficient electron mobility to transfer the activated species to the support and finally, to desorb CO_2 and H_2. In fact, the enhanced catalytic performance of the $Pt/Ce_{0.9}ZrFeAl$ appears to be a conjunction of strong interaction and lower Pt particle size provided by Zr and to the prominent improvement of the redox properties offered by Fe. It should be also highlighted the strong diminution on the band gap and the easier H transferences found for this sample, which clearly indicates the achieved synergism by the combination of the promoters. As a consequence, the combination of both promoters allows not just better catalytic activity but also higher resistance towards deactivation effects.

References

[1] T.R. Reina, S. Ivanova, V. Idakiev, J.J. Delgado, I. Ivanov, T. Tabakova, M.A. Centeno, J.A. Odriozola, Catal. Sci. Technol. 3 (2013) 779.

[2] A. Holmgren, B. Andersson, D. Duprez, Appl. Catal. B Environ. 22 (1999) 215.

[3] M.A. Centeno, M. Paulis, M. Montes, J.A. Odriozola, Appl. Catal. A Gen. 234 (2002) 65.

[4] A. Trovarelli, Catal. Rev. 38 (2006) 439.

[5] A. Martinez-Arias, J.M. Coronado, R. Cataluna, J.C. Conesa, J. Soria, J. Phys. Chem. B 102 (1998) 4357.

[6] S. Damyanova, B. Pawelec, K. Arishtirova, M.V.M. Huerta, J.L.G. Fierro, Appl. Catal. A Gen. 337 (2008) 86.

[7] M. Ozawa, H. Yuzuriha, M. Haneda, Catal. Commun. 30 (2013) 32.

[8] J. Li, J. Chen, W. Song, J. Liu, W. Shen, Appl. Catal. A Gen. 334 (2008) 321.

[9] Y.T. Kim, S.J. You, E.D. Park, Int. J. Hydrogen Energy 37 (2012) 1465.

[10] F.J. Pérez-Alonso, M. Lopez Granados, M. Ojeda, P. Terreros, S. Rojas, T. Herranz, J.L.G. Fierro, Chem. Mater. 17 (2005) 2329.

[11] T.R. Reina, W. Xu, S. Ivanova, M.Á. Centeno, J. Hanson, J.A. Rodriguez, J.A. Odriozola, Catal. Today 205 (2013) 41.

[12] W.Y. Hernández, O.H. Laguna, M.A. Centeno, J.A. Odriozola, J. Solid State Chem. 184 (2011) 3014.

[13] O.H. Laguna, F. Romero Sarria, M.A. Centeno, J.A. Odriozola, J. Catal. 276 (2010) 360.

[14] T.R. Reina, S. Ivanova, J.J. Delgado, I. Ivanov, V. Idakiev, T. Tabakova, M.A. Centeno, J.A. Odriozola, ChemCatChem 6 (2014) 1401.

[15] J.A. Rodriguez, P. Liu, J. Hrbek, J. Evans, M. Pérez, Angew. Chemie - Int. Ed. 46 (2007) 1329.

[16] J.C. Duchet, M.J. Tilliette, D. Cornet, Catal. Today 10 (1991) 507.

[17] S. Damyanova, B. Pawelec, K. Arishtirova, M.V.M. Huerta, J.L.G. Fierro, Appl. Catal. B Environ. 89 (2009) 149.

[18] S. Ricote, G. Jacobs, M. Milling, Y. Ji, P.M. Patterson, B.H. Davis, Appl. Catal. A Gen. 303 (2006) 35.

[19] A.M. Duarte de Farias, D. Nguyen-Thanh, M.A. Fraga, Appl. Catal. B Environ. 93 (2010) 250.

[20] H. Liang, H. Yuan, F. Wei, X. Zhang, Y. Liu, J. Rare Earths 29 (2011) 753.

[21] T. Dhannia, S. Jayalekshmi, M.C. Santhosh Kumar, T. Prasada Rao, A. Chandra Bose, J. Phys. Chem. Solids 71 (2010) 1020.

[22] P.C.A. Brito, D.A.A. Santos, J.G.S. Duque, M.A. Macêdo, Phys. B Condens. Matter 405 (2010) 1821.

[23] L. Yue, X.M. Zhang, J. Alloys Compd. 475 (2009) 702.

[24] O.H. Laguna, M.A. Centeno, M. Boutonnet, J.A. Odriozola, Appl. Catal. B Environ. 106 (2011) 621.

[25] T.R. Reina, E. Papadopoulou, S. Palma, S. Ivanova, M.A. Centeno, T. Ioannides, J.A. Odriozola, Appl. Catal. B Environ. 150-151 (2014)

554.

[26] G. Jacobs, U.M. Graham, E. Chenu, P.M. Patterson, A. Dozier, B.H. Davis, J. Catal. 229 (2005) 499.

[27] D. Andreeva, I. Ivanov, L. Ilieva, M. V. Abrashev, Appl. Catal. A Gen. 302 (2006) 127.

[28] M. Fadoni, L. Lucarelli, Stud. Surf. Sci. Catal. 120 (1999) 177.

[29] J.Z. Shyu, K. Otto, J. Catal. 115 (1989) 16.

[30] S. Damyanova, J.M.C. Bueno, Appl. Catal. A Gen. 253 (2003) 135.

[31] M.J. Tiernan, O.E. Finlayson, Appl. Catal. B Environ. 19 (1998) 23.

[32] O.H. Laguna, M.A. Centeno, G. Arzamendi, L.M. Gandía, F. Romero-Sarria, J.A. Odriozola, Catal. Today 157 (2010) 155.

[33] H. Bao, X. Chen, J. Fang, Z. Jiang, W. Huang, Catal. Letters 125 (2008) 160.

[34] M. Gonzalez Castaño, T.R. Reina, S. Ivanova, M.A. Centeno, J.A. Odriozola, J. Catal. 314 (2014) 1.

[35] B.M. Reddy, P. Bharali, P. Saikia, S.-E. Park, M.W.E. Van Den Berg, M. Muhler, W. Grunert, J. Phys. Chem. C 112 (2008) 11729.

[36] I. Zorić, M. Zäch, B. Kasemo, C. Langhammer, ACS Nano 5 (2011) 2535.

[37] C.W.M. Castleton, J. Kullgren, K. Hermansson, J. Chem. Phys. 127 (2007) 1.

[38] V. Petrovsky, B.P. Gorman, H.U. Anderson, T. Petrovsky, J. Appl. Phys. 90 (2001) 2517.

[39] N. Acerbi, S. Golunski, S.C. Tsang, H. Daly, C. Hardacre, R. Smith, P. Collier, J. Phys. Chem. C 116 (2012) 13569.

[40] P. Patsalas, S. Logothetidis, L. Sygellou, S. Kennou, Phys. Rev. B 68 (2003) 1.

[41] J. Spanier, R. Robinson, F. Zhang, S.-W. Chan, I. Herman, Phys. Rev. B 64 (2001) 1.

[42] Y. Madier, C. Descorme, A.M. Le Govic, D. Duprez, J. Phys. Chem. B 103 (1999) 10999.

[43] G. Balducci, P. Fornasiero, R. Di Monte, J. Kaspar, S. Meriani, M. Graziani, Catal. Letters 33 (1995) 193.

[44] H. Vidal, J. Kašpar, M. Pijolat, G. Colon, S. Bernal, A. Cordón, V. Perrichon, F. Fally, Appl. Catal. B Environ. 30 (2001) 75.

[45] P. Arnoldy, A. Moulijn, O.J. Wimmers, J. Phys. Chem 90 (1986) 1331.

[46] K. Shyu, J Z, Otto, Appl. Surf. Sci. 32 (1988) 246.

[47] W.C. Conner, J.L. Falconer, Chem. Rev. 95 (1995) 759.

[48] S. Damyanova, C.A. Perez, M. Schmal, J.M.C. Bueno, Appl. Catal. A Gen. 234 (2002) 271.

[49] T. Yamaguchi, J. Catal. 67 (1981) 324.

[50] C.B.L. I, V. Cedex, A. Badri, J. Lamotte, E. Catherine, J.C. Lavalley, J. El Fallah, L. Hilaire, F. Normand, B. Pascal, S. Cedex, E. Quemere, G.N. Sauvion, 87 (1991) 1601.

[51] J.L.G. Fierro, J. Soria, J. Sanz, J.M. Rojo, J. Solid State Chem. 66

(1987) 154.

[52] A. Yee, S.J. Morrison, H. Idriss, 295 (1999) 279.

[53] P. Panagiotopoulou, D.I. Kondarides, J. Catal. 260 (2008) 141.

[54] P.G. Menon, G.F. Froment, J. Catal. 59 (1979) 138.

[55] D.R. Mullins, K.Z. Zhang, Surf. Sci. 513 (2002) 163.

[56] A. Holmgren, B. Andersson, J. Catal. 25 (1998) 14.

[57] A. Goguet, F. Meunier, J.P. Breen, R. Burch, M.I. Petch, A. Faur Ghenciu, J. Catal. 226 (2004) 382.

[58] E. Rogemond, R. Frety, V. Perrichon, M. Primet, S. Salasc, M. Chevrier, C. Gauthier, F. Mathis, J. Catal. 169 (1997) 120.

[59] G. Pitchon, V. Zins, J. F., Hilaire, L., Maire, 59 (1996) 203.

[60] C. Li, Y. Sakata, T. Arai, K. Domen, K. Maruya, T. Onishi, J. Chem. Soc. Faraday Trans. 1 85 (1989) 929.

[61] G. Blyholder, J. Phys. Chem. 79 (1975) 756.

[62] G. Blyholder, J. Phys. Chem. A 68 (1964) 2772.

[63] C. Binet, M. Daturi, J.-C. Lavalley, Catal. Today 50 (1999) 207.

[64] V. Sánchez Escribano, E. Fernández López, M. Panizza, C. Resini, J.M. Gallardo Amores, G. Busca, Solid State Sci. 5 (2003) 1369.

[65] D. Mullins, J. Catal. 188 (1999) 340.

[66] U. Berner, K. Schierbaum, G. Jones, P. Wincott, S. Haq, G. Thornton,

Surf. Sci. 467 (2000) 201.

[67] C.M. Kalamaras, S. Americanou, A.M. Efstathiou, J. Catal. 279 (2011) 287.

[68] G. Jacobs, P.M. Patterson, U.M. Graham, D.E. Sparks, B.H. Davis, Appl. Catal. A Gen. 269 (2004) 63.

[69] P. Bazin, O. Saur, J.C. Lavalley, M. Daturi, G. Blanchard, Phys. Chem. Chem. Phys. 7 (2005) 187.

[70] P. Panagiotopoulou, J. Papavasiliou, G. Avgouropoulos, T. Ioannides, D.I. Kondarides, Chem. Eng. J. 134 (2007) 16.

Chapter 4

Structuring Pt(2%)/CeO_2/Al_2O_3 WGS catalyst: introduction of a buffer layer

Summary

This chapter is devoted to the development of a structured catalytic system for the WGS reaction. A new concept is introduced, the presence of pre-catalytic layer formed by a WGS-inert oxide, which may be the catalyst support, aiming to increase the number of participating sites in the water dissociation step . Its performance appears to strongly depend on the stream composition showing a strong beneficial effect in highly reducing atmospheres. This concept provides an interesting approach solution for a structured catalyst development as a function of the reaction variables.

4.1. Introduction

Besides a proper chemical catalyst design, structuring processes should be also considered as a necessary approach to achieve WGS units able to operate in actual industrial applications. As stablished on the previous chapter, the WGS is characterized by the high contact times needed to achieve high CO conversions being also moderately exothermic. This fact implies high reactor volume making difficult its implementation in actual on-board H_2 production and application processes [1].

In this line, longitudinal parallel channels monoliths or micromonoliths are an interesting solution by itself but also may provide clues on the behavior of microreactors [2–4]. For example, Fu et al. [5] studied WGS catalysts structured on metallic monoliths claiming that monolith-based designs provide the necessary mechanical strength allowing a better platinum use and, hence, to lower reactor volumes. Indeed, it has been reported than micromonolithic reactors can diminish the WGS reactor units one or two times [6]. Farrauto *et al.* [7,8] also reported promising results regarding activity and stability for Pt based catalysts through combining metallic micromonolithic devices and well catalytic designs.

Therefore, these structures are a valuable alternative to packed fixed bed reactors (PBR) allowing higher space velocities. The process intensification is normally related to the higher surface to volume ratio provided by micromonoliths resulting in volume reduction that allows higher efficiencies.

The micromonolith structures may be ceramic or metallic. The metallic ones present high thermal conductivities and lower heat capacities as well as superior thermal and mechanical shock resistances [9,10].

Particularly, the improved mass and heat transferences allowed on structured catalysts are of mandatory importance on the WGS reaction [11,12]. Indeed, considering that the WGS is exothermic and thermodynamic limited, an optimal temperature control, as that provided by metallic micromonoliths, becomes a very interesting feature which should enhance the catalytic performance and avoid or minimize the hot spot formation.

The heterogeneous catalytic process involves a series of mass transport phenomena that may be significantly important since their nature implies two separates phases. Thus, the chemical transformation relies on a number of physical transport processes, which might introduce additional dependency on the operating variables. The reaction between a porous catalyst and the gas reactants involves several steps:

I. Diffusion of the reactants through the boundary layer: external or interphase diffusion.
II. Diffusion of the reactant through the porous interior of the catalyst to the point at which the reaction occurs: internal, pore and intraparticle diffusion.
III. Adsorption on the active site, reaction and desorption from the active site.

IV. Diffusion of the products through the porous to the external surface: internal, pore or intraparticle diffusion.

V. Diffusion of the products through the external boundary layer into the bulk fluid: external or interphase diffusion.

Together to all these macroscopic transport phenomena surface diffusion, a microscopic process, underwent by the reactants to get closer enough to react together must be considered.

Besides, most chemical reactions involve heat effects. Thus, in addition to the interphase and pore diffusion, pore and interphase heat transfers can happen. The net kinetics of the overall reaction (effective kinetic or macrokinetic) can differs from the chemical transformation one (intrinsic kinetic or microkinetic). Therefore, heat and mass transports are parameters that influence significantly the WGS catalyst's performance.

The intrinsic chemical rate, as well as the diffusion rates, increases with temperature according to the Arrhenius law. However, the rate increment associated to interparticle and intraparticle diffusion processes is proportionally lower. The overall kinetic rate observed for a given process can be chemically, pore or interphase limited, depending on temperature. Thus, at lower temperatures the chemical reaction is slow and it becomes the rate limiting. Opposite situations could be reached at higher temperatures where the diffusional processes can become slower and thus rate limiting.

These effects must be considered in practical situations; otherwise, wrong predictions with respect to the catalytic behaviors may result. Considering that those processes are controlled by the layer thickness, the use of micromonolithic structures should improve the diffusional processes and allow a better control of the reaction through an appropriate catalytic layer thickness providing a better temperature control hindering the hot spot formation [13,14]. Therefore, the layer thickness should be well-controlled in order to maintain the enhancement of the transport phenomena provided by the micromonoliths.

On the other hand, a second approach was considered along this chapter considering several mechanisms proposed in literature for WGS reaction (carboxyl, carboxyl hydroxyl, redox, dual hydroxyl, one step carboxyl formation). Thus, whatever the mechanism through which the WGS reaction occurs, several authors propose the water activation as rate limiting on the WGS. Indeed, the water dissociation as rate limiting step has been proposed in literature for different noble metals as Co, Cu, Ni, Ag, Rh, Ir, Au and Pt [15–18]. More precisely, Phatak et al. [19] proposed the hydroxyl dissociation as limiting step for Pt and other noble metals by comparison of the binding energies of noble metals to the binding energies of H_2O, OH and H species. In accordance, the superior WGS rate exhibited by Pt metal was also related directly to the slightly lower water dissociation barrier.

Actually, the water activation step is commonly associated to the support oxygen vacancies becoming then, a key chemical site for the WGS reaction [20]. Therefore, oxygen vacancies play an important role concerning water molecules dissociation that will occur on the support [11,21]. That is why supports having redox properties, as ceria, are preferred and found to be very helpful [22].

In this study different amounts of Pt(2%)/CeAl catalyst were washcoated on micromonoliths. The catalyst layer deposition was carefully controlled for obtaining a series of catalytic wall reactors (CWR) having different catalyst thicknesses. Besides this, a series of CWRs constituted by two different layers were prepared: i) a first layer based on CeO_2-Al_2O_3, named *buffer* layer and ii) a Pt(2%)/CeO_2-Al_2O_3 layer, the catalyst layer, supported over the buffer one. For such system, equal amounts were deposited for each catalytic layer supported. This procedure was chosen on the basis of the concept that increasing the concentration of cerium oxide in the system should increase the number of oxygen vacancies and therefore the number of water activation sites. The idea was to introduce a second active sublayer able of increasing the water dissociation capacity and buffer the amount of water dissociated species in the WGS reaction. If this hypothesis is correct, the incorporation of the buffer layer should increase the catalytic performance.

4.2. Experimental

- *Preparation of the metallic monolithic substrates*: The micromolithic structures were manufactured by rolling up, around a spindle, a flat and a corrugated foil constituted by ferritic stainless steel (Fecralloy). The micromonolithic adopt cylindrical structure of 3 cm height and 1.6 cm in diameter resulting in geometric surface area of 540 cm^2 and cell density of 2067 cpsi. Prior the catalyst deposition the micromonoliths were thermally treated at 900 ^{0}C during 22h in order to grow an α-Al_2O_3 surface layer improving the subsequent catalyst adhesion [23–25].

Figure 4.1. Ferritic stainless steel micromonolithic structure

- *Catalyst and buffer synthesis:* A commercial CeO_2/Al_2O_3 (Puralox, Sasol) in 20wt.%CeO_2/80 wt.% Al_2O_3 proportion was used as catalyst support and buffer. The platinum was deposited by wet impregnation using tetrammoniun nitrate platinate (Johnson-Matthey) as precursor. The nominal composition of the catalyst was Pt(2wt.%)/CeO_2/Al_2O_3. Then the catalyst was calcined at 350^{o}C-8h-5^{o}C/min. For the sake of briefness, the support and the catalyst, CeO_2/Al_2O_3 and Pt(2%)/CeO_2/Al_2O_3 are labelled CeAl and Pt/CeAl.

- *Preparation of the micromonolithic catalysts:* The deposition process was carried out using the washcoating method. Firstly, the catalyst suspension is prepared and the bare micromonolith immersed into the suspension during a minute. After structure extraction at constant speed the excess suspension is blown in order to avoid the channel obstruction. After, the micromonolith is dried at 120^{o}C and weighted to register the amount of deposited catalyst. The same process is repeated as many times as required to achieve the desired amount of deposited catalyst. Finally, the monoliths are calcined at the same temperature that the initial solids but using a heating ramp of 2^{o}C/min in order to avoid loss of catalysts caused by monolith peeling provoked by the different expansion coefficients of the substrate and the coated layer.

Regarding the catalyst suspension, the most appropriate composition after following a previously reported optimization procedure [4] appears to be 1.96 wt.% of polyvinylalcohol (PVA) solution (1.5 wt.% PVA in water), 17.65 wt.% of Al_2O_3 colloidal suspension (Nyacol, 20 wt.% in water), 18.14 wt.% of catalyst and 62.25 wt.% of water. The solids were grinded and sieved to achieve particle sizes around 10 μm. In this suspension composition the rheological properties were controlled by the additives. While the colloidal alumina was added to obtain more stable suspension the PVA was added, as tensioactive agent, in order to help the suspension to rise up within the monolith channels [13,23]. The prepared suspension allows the deposition of around 80 mg at each coating step. Once the catalyst is deposited, the

suspensions were dried and calcined in the same conditions than their respective monoliths. Two different suspensions prepared for the buffer and the catalyst layer resulted in two suspensions called S-Pt/CeAl and S-CeAl prepared from Pt/CeAl and CeAl respectively.

Three different monoliths were prepared by this method, these monoliths were nominally loaded with 0.3, 0.6 and 1 g of the Pt/CeAl catalyst. These micromonoliths are named M0.3, M0.6 and M1, respectively.

The effect of the buffer layer was studied over micromonoliths containing 0.3 g of the Pt/CeAl catalyst deposited on a 0,3g of the CeAl buffer layer. The structured catalyst composed by the two differentiated layers was named M0.3-B0.3. The actual amounts deposited on the catalysts for each structured systems are presented in Table 4.1.

Table 4.1. Nominal and real catalyst and buffer amounts achieved on the structured catalysts

System	Nominal amounts (g)	Deposited amounts (g)
M0.3	0.3	0.3
M0.6	0.6	0.6
M1	1	0.8
M0.3-B0.3	0.3 (0.3)	0.4 (0.4)

**In parenthesis, the amounts of buffer layer*

4.3. Physicochemical characterization results

4.3.1. Textural properties and chemical composition of the prepared solids

The chemical composition of the synthesized samples is shown in Table 4.2. The obtained platinum content achieved was very close to the targeted one (2%). The addition of colloidal alumina in the slurry formulation accounts for the differences in the alumina content of the slurry and the prepared powders.

Table 4.2. Chemical composition of the prepared solids

	Al_2O_3 (wt.%)	CeO_2 (wt.%)	Pt (wt.%)
Pt/CeAl	77.6	20.2	2.2
CeAl	79.0	21.0	-
S-Pt/CeAl	80.7	17.3	2.0
S-CeAl	82.8	17.2	-

The textural properties of the prepared catalysts and devices are shown in table 4.3. The calcined suspensions exhibit higher surface areas and smaller pore diameter (d_{pore}) values than their parent powders, which also relates to the amount of colloidal alumina. As a general trend, an increase in the number of supported layers onto monoliths results in an increase of the specific surface area and pore volume (V_{pore}) meanwhile the obtained d_{pore} values are lower.

Table 4.3. Textural properties of the prepared solids and monoliths

	S_{BET} (m^2/g)	V_{pore} (cm^3/g)	D_{pore}(Å)
CeAl	146	0.38	73.2
Pt/CeAl	142	0.30	70.9
S-CeAl	187	0.37	62.6
S-Pt/CeAl	156	0.34	65.3
M0.3	152	0.34	70.7
M0.6	183	0.36	63.4
M1	190	0.32	62.9
M0.3-B0.3	143	0.32	70.7

The micromonolith containing two different buffer/catalyst layers shows relatively lower surface areas, in comparison to the bare M03, M06 and M1 microstructures, being slightly minor to that expected if the textural properties of S-CeAl and S-Pt/CeAl are considered. Despite the commented changes, all the prepared systems present similar textural properties being dominated by the support (Puralox - S_{BET}=202 m^2/g) and by the colloidal alumina within the suspensions.

4.3.2. XRD of the prepared solids

From the XRD diffraction analysis two main phases could be detected, the cubic CeO_2 fluorite and the γ-Al_2O_3 one for all the samples (Figure 4.2.).

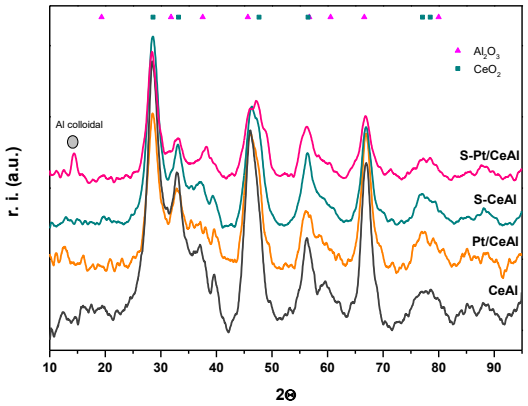

Figure 4.2. XRD obtained for the prepared powder catalysts

It is worth to mention that no important changes occur during the washcoating process being the suspension very similar to the initial solid. No platinum diffraction can be discerned, probably due to the low platinum content and/or to platinum particles sizes, lower than the detection limit (< 4 nm).

In the case of the S-Pt/CeAl, a diffraction attributed to the boehmite phase, γ-AlO(OH) (JCPDS 21-1307) originated from the colloidal alumina is detected. For the S-CeAl suspension, these diffractions are not detected which could be attributed to the higher calcination temperature employed for this sample leading to γ-Al_2O_3 phase.

4.3.3. SEM and adherence test

The homogeneity of the deposition process for all the micromonolithic structures was studied by SEM. For example, the microphotographs obtained for M1 sample are shown in Figure 3. It can be observed a well-dispersed

homogenous catalyst layer (Fig. 3a). The EDX analysis (Fig. 3b), from left to right, shows firstly a region rich on Fe and Cr corresponding to the stainless steel substrate followed by a zone composed by alumina grown during the oxidizing pretreatment and then, the catalyst layer composed mainly by aluminum, oxygen and cerium. No Pt was detected due to the low amount of the later in comparison to the other elements.

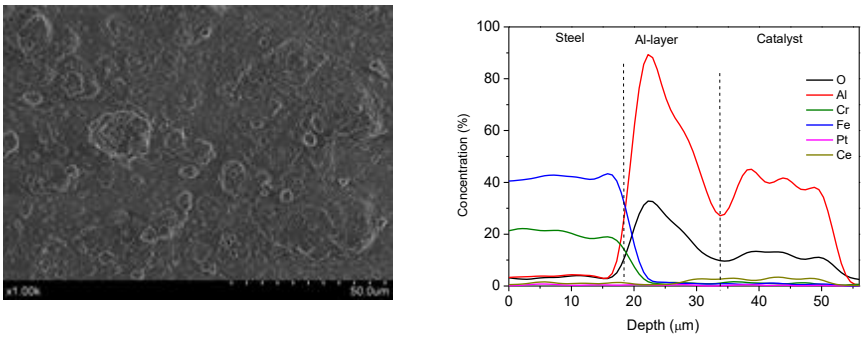

Figure 4.3. SEM microscopy: a) front microphotograph; b) maping elemental analysis

The adherence test results in 97% of catalyst weight deposited after drying on the metallic substrate indicating that the powders were well fixed on the metallic substrates.

Besides, the layer thickness was also estimated for all the structured catalysts, Table 4.4. For that purpose, the actual amounts of deposited catalysts on the monoliths and the chemical compositions, as well as the pore volumes of the calcined slurries were considered. An estimate of the layer thickness for the

M0.3 monolith is performed. First, the amounts of each specie present on the monolith, as well as their densities, were used to obtain the volume of those species assuming they are non-porous solids.

Table 4.4. For the M0.3, the relative amounts contained and volumes

	Weight (g)	**ρ (kg/m^3)**	**Volume (cm^3)**
Al_2O_3	0.274	4000	$6.862 \cdot 10^{-2}$
CeO_2	$5.872 \cdot 10^{-2}$	7650	$7.676 \cdot 10^{-3}$
Pt	$6.777 \cdot 10^{-3}$	21090	$3.213 \cdot 10^{-4}$

* Density values taken from web of elements.

The total volume occupied by these solids (V_S) are calculated by adding the respective volumes, this results in $7.662 \cdot 10^{-2}$ cm^3. Then, the porous volume (V_P) of the suspension was also calculated and added to the solids volume, $V_T = V_S + V_P$. The V_P was obtained from the textural properties results, V_P = gram deposited on M0.3 x pore volume. Hence:

$$Vp = 0.34g \text{ x } 0.34 \text{ cm}^3/g = 0.1156 \text{ cm}^3.$$

Therefore, the total volume of the solid should be:

$$V_T = V_S + V_P = 7.662 \cdot 10^{-2} \text{ cm}^3 + 0.1156 \text{ cm}^3 = 0{,}1922 \text{ cm}^3.$$

The layer thickness will depend on the surface area of the monolith (540 cm^2). The layer thickness (LT) estimate this way, will be:

$$LT = \frac{V_T}{Monolith\ area} = 0.000355\ cm = 3.5\ \mu m$$

Thus, the same approach was followed for the layer thickness estimates of all prepared solids. The obtained layer thicknesses for the structured systems are presented in Table 4.5.

Table 4.5. Layer thickness (LT) and particle sizes estimated for the prepared solids

	M0.3	**M0.6**	**M1**	**M0.3-B0.3**
LT (μm)	3.5	6.6	8.7	8.6
r (μm)	10.5	19.8	26.1	25,8

For the sake of comparison with packed bed reactors, the layer thickness is transformed in the equivalent radius of spherical particles. The calculated equivalent particle sizes for these catalytic layer thicknesses are presented in Table 4.5.

4.4. Catalytic behavior

The catalytic behavior of the powder samples was firstly tested in order to determine if during the slurry preparation changes were induced in the catalyst. The catalytic results are shown in Figure 4.4.

Regarding the powders, the catalytic activity of the Pt/CeAl hardly changes on preparing the suspension in agreement with the XRD results. The minor differences observed could be attributed to the decrement of the platinum concentration.

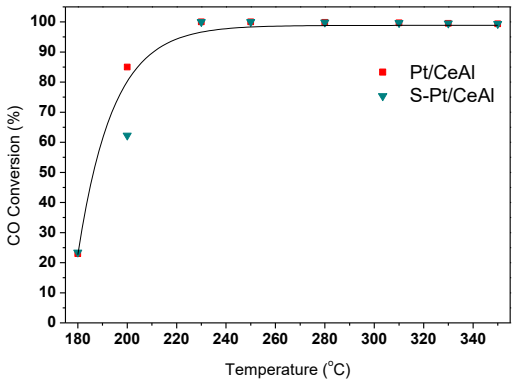

Figure 4.4. Catalytic activity in model conditions of the obtained powder samples. GHSV=4000 h^{-1} and 6 $L \cdot h^{-1} \cdot g^{-1}$

As expected, structuring the catalyst results in higher efficiencies on the WGS reaction (Figure 4.5). In this figure the catalytic activity of the M0.3 monolith and 0.3 g of the Pt/CeAl slurry are compared. The so call model mixture was used for the catalytic test run at 80 L/g·h. Both, enhanced mass and heat transport may account for the observed increment in catalytic performances. This result is in agreement to Fu et al. [5] data that observe better catalytic activities for lower Pt loadings on structuring the WGS catalysts.

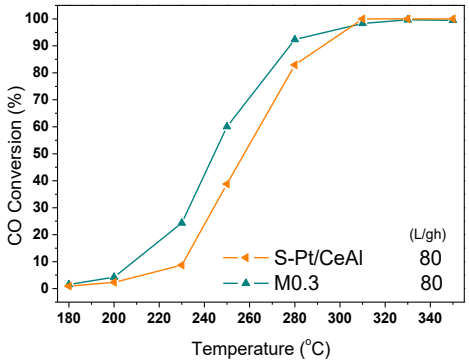

Figure 4.5-. Catalytic activity in model conditions of the obtained powder samples.

The effect of catalyst loading (catalytic layer thickness) was also studied in order to determine if the increased catalyst amount result in higher catalytic activities or, on the contrary, mass and heat transfer capacities hinder the effect provide by the higher number of active sites.

Although the mass and heat transferences should be minimized employing metallic micromonolithic devices, an effectiveness factor for CO (η) was calculated for the M0.3, M0.6 and M1 monoliths. The effectiveness factor provides information on the influence of mass transfer on the effective reaction rate. For that evaluation, the methodology proposed by Weisz and Hicks allows estimating an efficiency factor from observable features [26] but accounting certain assumptions as, for example, the interparticle mass transferences were assumed as insignificant. Moreover, the effectiveness factor was just estimated for CO but no for the others reaction components.

The difficulty to estimate an efficiency factor for example for water, relays on the absence of a kinetic equation described for this specie.

From that assumption, the effectiveness factor calculation requires three parameters denoted as: ϕ, γ and β which are respectively defined by:

$$\varphi = \frac{dN}{dt} \cdot \frac{1}{C_0} \cdot \frac{r^2}{D} \qquad \textit{(Equation 4.1)}$$

$$\gamma = \frac{E_a}{RT} \qquad \textit{(Equation 4.2)}$$

$$\beta = \frac{C_0 HD}{FT} \qquad \textit{(Equation 4.3)}$$

Where:

- $\frac{dN}{dt}$: is the reaction rate
- $\frac{1}{C_0}$ is the partial pressure of the CO at the equilibrium
- r: is the particle radii obtained from the layer thickness and assuming equivalent spherical particles
- D: is the effective diffusivity which account for the molecular and knudsen diffusion (taken from ref. [27])
- E_a: is the activation energy
- R: is the ideal gas constant (8.314 J/Kmol)
- T: is the temperature (K)
- H: is the WGS enthalpy

- F: is the thermal conductivity (intermediate value for alumina solids taken from ref. [26])

Thus, the estimate of the efficiency factor requires a kinetic equation. Considering that the own kinetic law was not developed being this the most convenient, the literature data above WGS kinetic studies was used. Actually, the WGS kinetic has been widely reported in literature for several systems [12,28,29]. Among them, Mirodatos *et al.* [30] reported a kinetic study properly obtained for a very similar system based also in $Pt/CeO_2/Al_2O_3$. The kinetic equation stated on this study is presented on Eq. 4.4. Where, the K_{eq} (Equation 4.5) employed was also stablished in another publication by Germani *et al.* [30]

$$-r_{CO} = (1 \cdot 10^8) \times \left(e^{-\frac{86000}{RT}}\right) \times CO^{0.13} \times H_2O^{0.49} \times H_2^{-0.45} \times CO_2^{-0.12} \times \left(1 - \frac{H_2 \times CO_2}{K_{eq} \times CO \times H_2O}\right) \quad \textit{(Euation 4.4)}$$

$$K_{eq} = e^{\left(\frac{4577,8}{T} - 4,33\right)} \quad \textit{(Equation 4.5)}$$

Therefore, for the effectiveness factor (η), assuming the latter kinetic study, can be estimated. Table 4.6 shows the values obtained for the rate and ϕ, γ and β parameters for each system at T=180 ºC. Similar ϕ values were exhibited by all the systems for the temperatures tested.

Table 4.6. Rate, ϕ γ and β parameters estimated for M0.3, M0.6 and M1 for T=180 ºC

	$\frac{dN}{dt}$	ϕ	γ	β
M0.3	5.09E-01	8.35E-07 ≈ 0	22.83	-0.01
M0.6	4.15E-01	6.77E-07 ≈ 0	22.83	-0.01
M1	3.23E-01	5.20E-07 ≈ 0	22.83	-0.01

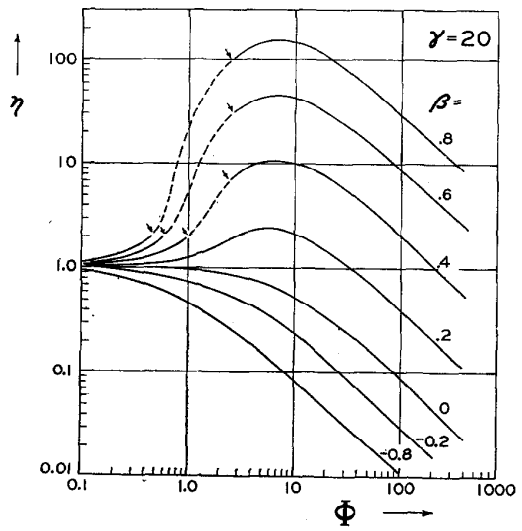

Figure 4.6. Adapted from [26]**, functional dependence of utilization factors of observable quantities**

So, the efficiency factor can be estimated interpolating the ϕ, γ and β factors employing the Figure 4.6 reported by Weisz and Hicks [26]. No matter the β values, the lower ϕ values obtained for all the systems and temperatures, lead

to efficiency factors above 1 indicating the absence of diffusional intraparticle control.

Therefore, it can be stated that the catalytic activity results were not strongly influenced by diffusional processes related to CO species, this allowing superior catalytic performances on increasing the amount of catalyst deposited on the micromonolithic structures at least for the thicknesses tested in this study. The benefits provided by the process intensification is nor limited by the catalytic layer thickness in the studied ranges in good agreement to previous literature reported. For example, Laguna et al. [14] recently demonstrated, for layer thickness around 10 μm, that no significant diffusional limitations were controlling the catalytic performances. Meanwhile Potemkin et al. [31] stablished a superior layer thickness limit, above 20 μm, for which the diffusional processes were not rate controlling. Also in concordance, Farrauto et al. [32] claimed that WGS structured catalysts are usually not pore diffusion limited.

From the previous results, the effect of buffer presence should be also properly evaluated implying that behavior differences can be mainly related to chemical features.

The absence of pore diffusion limitations were checked by running the reaction at on the different monoliths at several contact times and WSHV. Figure 4.7 presents examples of these experiments showing the conversion of

CO in the so-called model conditions as a function of temperature for the three monoliths tested at two different GHSV.

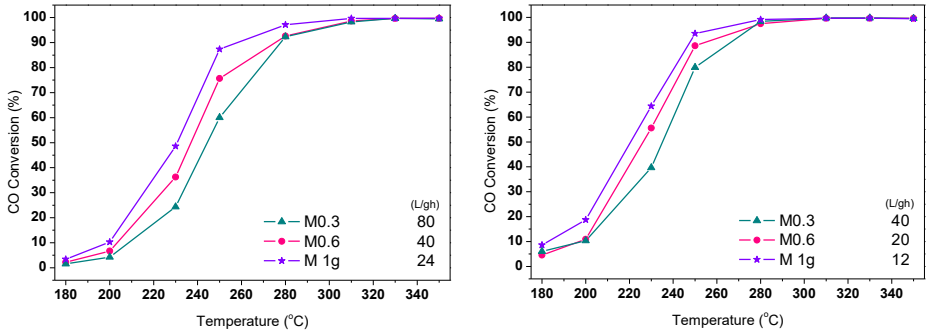

Figure 4.7. Catalytic activity in model conditions of the monoliths tested at a) 4000 h^{-1} and b) 2000 h^{-1}

Experimental limitations related to the operating range of the MFCs prevent the comparison of the three monoliths at the same WHSV. Therefore, the M0.3 and M0.6 monoliths were tested at 40 L/g·h and the M0.6 and M1 ones at *ca.* 20 L/g·h. Figure 4.8 presents the catalytic activity of these monoliths. It is clear from the figure that increasing the amount of catalyst the catalytic activity proportionally increases while keeping constant the WHSV. Therefore, as it should be expected from the calculations of the effectiveness factor, pore diffusion limitations can be excluded in the studied monoliths.

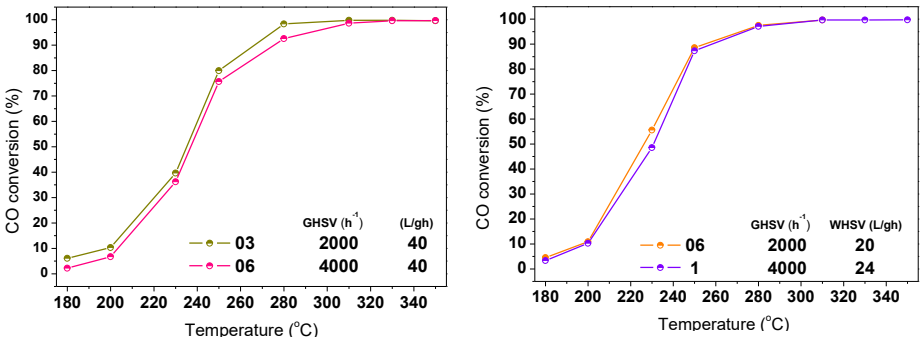

Figure 4.8. Catalytic activity in model conditions of monoliths. Effect of the catalyst loading

The addition of a buffer layer behind the catalytic layer on the studied monoliths should not affect the mass transport properties since de thickness of the catalytic layer remains constant. However, heat transport properties may be affected since the ceramic layer thickness is increased by the thickness of this buffer layer. These monoliths have been tested in model conditions at both 2000 h^{-1} and 4000 h^{-1}. Figure 4.9 presents the CO conversion as a function of temperature; it is clear that the buffer layer hardly influences the catalytic activity.

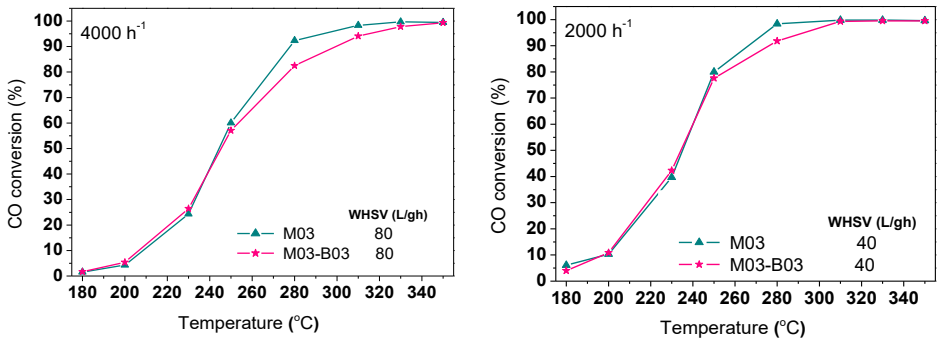

Figure 4.9. Effect of the buffer layer on the catalytic activity in model conditions of monoliths. a) 4000 h^{-1}; b) 2000 h^{-1}

Testing the catalyst in the so-called real conditions, a reactive flow with a feed composition typical of the outlet of an autothermal reformer, after steam addition for favoring the WGS (50% H_2, 7% CO, 9% CO_2, 30% H_2O, balance N_2), the CO equilibrium conversion decreases and shift to higher temperatures, figure 4.10. In this figure the CO conversion is compared to that obtained by Germani et al. [30] for a two platelet microreactor coated with 1.4%Pt/CeO_2/Al_2O_3 catalyst operated at ~73 $L \cdot g^{-1} \cdot h^{-1}$ and a reactive flow with a similar composition to that used in the present work (32.2% H_2, 9.6% CO, 8.4% CO_2, 23% H_2O, balance Ar). Despite the differences in Pt loading, WSHV and reactive flow composition the catalytic activity in both the monolith and the microreactor device is similar. Therefore, it can be assumed that the same rate law may fit our experimental results but just considering the different platinum loading and dispersion for the pre-exponential value of the

Arrhenius expression presented on Equation 4.4.

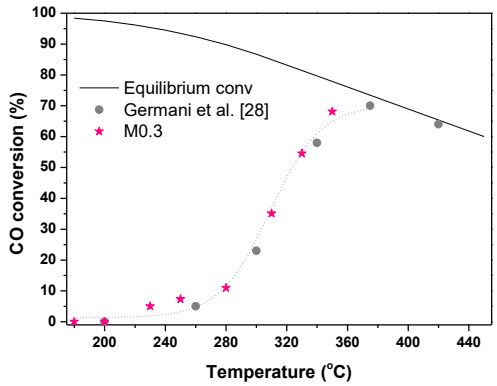

Figure 4.10. Comparison of the M0.3 monolith operated at 80 $L \cdot g^{-1} \cdot h^{-1}$ under a reactive flow of 50% H_2, 7% CO, 9% CO_2, 30% H_2O, balance N_2 and data from Germani et al. [28] for a two platelet microreactor operated at 73 $L \cdot g^{-1} \cdot h^{-1}$ under a reactive flow of 32.2% H_2, 9,6% CO, 8.4% CO_2, 23% H_2O, balance Ar

However, the presence of the buffer layer clearly affects the catalytic activity if the monoliths are tested in a reactive flow with a feed composition typical of the outlet of an autothermal reformer, after steam addition, figure 4.11 and table 4.7, roughly duplicating the turnover frequency at 260ºC. This enhancement of the catalytic activity must be due to the presence of the buffer layer since the catalyst $Pt/CeO_2/Al_2O_3$ has not changed. Moreover, the presence of the buffer layer does not affect the activity of the $Pt/CeO_2/Al_2O_3$ catalyst in the so-called model conditions. The difference must be ascribed to a modification of the CeO_2/Al_2O_3 buffer layer in the presence of the outlet reformer surrogate. Figure 4.9 shows the comparison of the observed and calculated reaction rates for the monoliths assuming the rate law proposed by Germani et al. [28]. There is an excellent agreement between the observed and

calculated reaction rates for the M0.3 monolith with all data fitting a straight line with a slope of 1.01±0.05. However, when testing the monoliths that contain the buffer layer the slope of the straight line is much higher (1.42±0.08) accounting for the observed increase in the catalytic activity (figure 4.11.b).

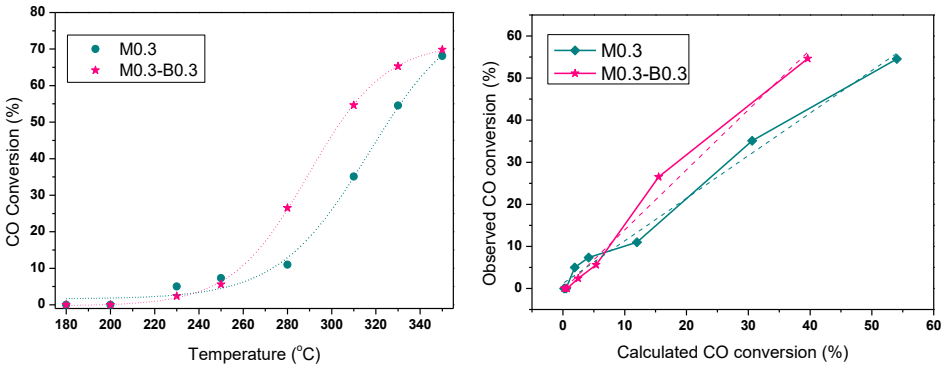

Figure 4.11. a) Effect of the buffer layer on the catalytic activity of the M0.3 monolith operated at 80 $L \cdot g^{-1} \cdot h^{-1}$ under a reactive flow of 50% H_2, 7% CO, 9% CO_2, 30% H_2O, balance N_2; b) Comparison of the observed and calculated CO conversions assuming the rate law proposed by Germani et al. [30]. **The monoliths are operated at 80 $L \cdot g^{-1} \cdot h^{-1}$ under a reactive flow of 50% H_2, 7% CO, 9% CO_2, 30% H_2O, balance N_2.**

Table 4.7. Summary of the key parameters of the monolithic catalysts. The catalytic test was carried out at 80 $L \cdot g^{-1} \cdot h^{-1}$ under a reactive flow of 50% H_2, 7% CO, 9% CO_2, 30% H_2O, balance N_2. Literature data are also included for comparison

Monolith	T (ºC)	Rate ($mmol_{CO} \cdot s^{-1} \cdot g_{Pt}^{-1}$)	Rate ($mmol_{CO} \cdot s^{-1} \cdot kg_{cat}^{-1}$)	Ref
M0.3	260	0.19	3.86	This work
M0.3-B0.3	260	0.28	5.60	This work
P2C1[a]	260	---	19.72	Adapted from [28]

The presence of the buffer layer does not affect the catalyst nature and therefore, the intrinsic activity should not be affected by its presence; hence the Arrhenius plot parameters must remain unchanged, as they must present the same CO adsorption enthalpy and coverage.

Table 4.8 presents a summary of reported reaction orders for Pt/Al_2O_3 and Pt/CeO_2 catalysts. The main differences in reaction order are obtained when carbon dioxide and hydrogen are not included in the calculation of the rate law [33,34]. In general, on including the effect of CO_2 and H_2 on the WGS reaction rate the apparent reaction orders and activation energy values are quite close despite the differences in the support nature, Pt loading and feed stream composition. The major difference between all of these studies occurs for the apparent reaction order for water that varies in the range 0.44-1.10. Obviously these differences must be associate to the presence of Re and/or the different nature of the support.

The apparent reaction order for carbon oxides species is close to zero for all catalysts referenced as stated by Farrauto et al. [34]. The weak interaction of CO_2 with the Pt surface is responsible for the negative order close to zero reaction order. The decrease in the binding strength of CO adsorbed on Pt as the coverage increase [35–38] may account for the observed variation in the reaction order for CO, varying in the range [-0.05, +0.14] (Table 4.8), together with the negative order for H_2. As far the CO surface coverage increases, its binding energy to the Pt surface decreases and hence the H_2

inhibition of the WGS activity is enhanced [39]. Phatak et al. suggest that the negative and close to -0.5 apparent reaction order for H_2 implies that after CO attains its saturation coverage, atomic hydrogen will be the dominant surface species on the remaining Pt sites [34]. The increase in the surface coverage of atomic hydrogen results in fewer sites available for water activation of the Pt surface, which results in the inhibition of the WGS reaction. In their explanation for the different rate laws observed they argued that the calculated range of apparent activation orders for water should account for different reaction mechanisms as a function of the support.

Table 4.8. Summary of reported reaction orders for Pt/Al_2O_3 and Pt/CeO_2 catalysts

Catalyst	T (K)	Reaction order				$E^{\#}$ (kJ·mol^{-1})	Feed stream	Ref
		CO	H_2O	H_2	CO_2			
Pt/Al_2O_3	543	-0.21	0.75			84	24%CO 31%H_2O	[33]
1% Pt/Al_2O_3	558	0.06	1.00	-0.44	-0.10	68	7% CO 22% H_2O 8.5% CO_2 37% H_2	[34]
	588	0.10	1.10	-0.44	-0.07	84		
1.66% Pt/Al_2O_3	558	0.11	0.82	-0.49	-0.06	81		
	573	0.10	0.77	-0.46	-0.08	81		
1% Pt/CeO_2	473	-0.03	0.44	-0.38	-0.09	75		
Pt/CeO_2	573	0	1			47	2.6%CO 2.0%H_2O	[40]
2%$Pt/Ce_{0.5}Zr_{0.5}O_2$	513-573	0.07	0.67	-0.57	-0.16	73	1.5-4.0%CO 31-44%H_2O 7-22%CO_{2c} 39-63%H_2	[41]
2%$Pt_{0.66}Re_{0.33}$/ $Ce_{0.5}Zr_{0.5}O_2$	513-573	-0.05	0.85	-0.32	-0.05	73		
1.7% $Pt/CeO_2/Al_2O_3$	533	0.13	0.49	-0.45	-0.12	86	7% CO 30% H_2O 9% CO_2 50% H_2	[30]
1% Pt/CeO_2	473	-0.03	0.44	-0.48	-0.09	77	7% CO 22% H_2O 8.5% CO_2 37%H_2	[36]
	573	0.14	0.66	-0.54	-0.08	93		

The data presented on this work do not support the assumption of Phatak et al.

[34] on different reaction mechanisms as a function of the support. In these figures the catalyst is always the same a 1.99% $Pt/CeO_2/Al_2O_3$ catalysts but placed or not on top of a CeO_2/Al_2O_3 buffer layer. On submitting the catalyst to the so-called model mixture the presence of the buffer layer does not alter the catalytic activity and the reaction rate can be simulated using the rate law described in Equation 4.6. However, in the presence of the surrogate feed stream the buffer layer alters the performances of the catalysts being now more active. The experimental data can now be fitted by a rate law similar to the previous one but increasing the reaction order for water:

$$-r_{CO} = (1.6 \cdot 10^8) \times \left(e^{-\frac{86000}{RT}}\right) \times CO^{0.13} \times H_2O^{0.70} \times H_2^{-0.45} \times CO_2^{-0.12} \times \left(1 - \frac{H_2 \times CO_2}{K_{eq} \times CO \times H_2O}\right) \quad \textit{(Equation 4.6)}$$

The increase in the apparent reaction order of water should account for an increase on the availability of water at the metal/support interface.

In a very recent paper Clay et al. [42] model the intrinsic WGS kinetics over Pt by DFT and compare their results with experimental ones. These authors utilize four pathways for modeling the microkinetics of the WGS reaction: the carboxyl, the carboxyl-hydroxyl, the redox and the dual hydroxyl paths, figure 4.12. The best fitting model is the one considering the carboxyl intermediate pathway and water dissociation the rate limiting step.

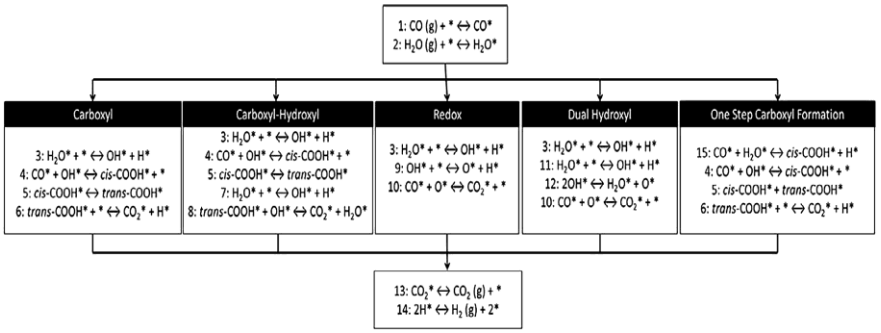

Figure 4.12. Commonly proposed WGS pathways. (*) represents a surface site. Adapted from reference [42]

According to this model, they claim changes on the rate limiting step depending on the CO coverage, in such a way that, at higher CO partial pressures, the rate limiting step shift from water activation to carboxyl formation. These shifts on the rate limiting steps account for the dependency of the reaction orders depending on the reaction conditions, which will determine the surface coverage as a function on the surface partial pressures. Consequently, increased H_2 surface presence should results in a water splitting inhibition leading to hinders CO_2 formation via CO + OH reaction. However, these authors conclude that their *"kinetic models satisfactorily recover the experimentally observed ordering of relative rates but fail to recover kinetic parameters observed on γ-Al_2O_3-supported materials, the least active of commonly studied supports. Even on these materials, the support itself likely has a role in the WGS mechanism"*.

Olimpiou et al. use SSITKA methodology for investigating the "H-path", the reaction pathway of the WGS reaction that results in the formation of H_2 from H_2O [43]. These authors estimate the coverage of H-containing species for γ-Al_2O_3-supported Pt and Rh and states that this coverage is well above that can be assumed for the metal particles. Therefore, most of the concentration of these species is present on the surface of γ-alumina. Labile hydroxyl groups and H species coming from water dissociated are the species postulated by these authors. However, just a small fraction of these species under WGS reaction conditions are energetically able to surface diffuse towards the metal particle for producing H_2 gas [44,45]. Moreover, it has been demonstrated that all these H-containing species cannot be at the periphery of the supported metal particles [43].

DFT studies on model Pt/CeO_2(111) points that adsorption of molecular water on stoichiometric ceria terraces is favored over dissociatively adsorbed water by 0.2 eV. However, on partially reduced CeO_2(111) surfaces water dissociated takes place readily [46]. More recently Anarifard et al. performed a DFT study of the microkinetic model for the WGS reaction on Pt/CeO_2 catalysts [47]. On the ceria surface H_2O dissociates at the oxygen vacancies transferring the H atom to neighboring oxygen surface atoms and only when complete surface coverage is attained water dissociation occurs at the metal-support interface. Their results suggest the importance of the metal-support interface sites. The role of the oxygen vacancies has also been associated to

the higher capacity of the support to stabilize the fragments originated in the water dissociation process [47].

A significant enhancement of the water splitting process on partially reduced ceria has been already reported [29,48–51]. As postulated by Anarifard et al.[47] coadsorption effects of CO and H_2O are important in the WGS reaction by lowering the adsorption energy of CO molecules and facilitating the carboxyl dissociation step. This may explain the observed enhancement of the WGS activity for Pt/ceria based catalysts [22,47].

The CeO_2/Al_2O_3 buffer layer provides an increased number of sites for the adsorption of water molecules. If an out-gas reformate feed stream is submitted to the WGS catalysts the high partial pressure of H_2 will results in the formation of partially reduced ceria surfaces favoring then water dissociation and stabilization on the support and the buffer layer [44–47,52]. Moreover, the increased number of oxygen vacancies leads to an increase in the electronic densities of the metal particles [53–57]. The higher electron density of the metal particles also hinder the H_2 absorption due to its donor character allows a decrease on the surface coverage of hydrogen atoms and hence, an increased number of surface sites available for CO adsorption while simultaneously reducing the binding energy of CO on platinum. Similar conclusions were established by Farrauto et al. [37] indicating that increased electron densities on platinum active sites leads to higher selectivities on PrOx reaction by decreasing the H_2-metal interaction strength. However, this effect

is independent on the presence of the buffer layer and, therefore, cannot explain by itself the enhanced activity due to the presence of this layer.

Assuming that the rate-limiting step is the transfer of hydroxyl groups to the metal-support interface and that surface diffusion rates are much higher than the reaction rates and increased number of surface sites able of dissociating water molecules should provide and increased number of hydroxyl species at the metal particle periphery increasing the WGS reaction rate. The surface diffusion follows Fick's laws and therefore diffusion rate increase as the temperature increase.

In the Figure 4.13, it is presented the catalytic behavior of M0.3 and M0.3-B0.3 when the partial pressures of the reactives and products are varied on the feed stream. The achieved higher OH concentrations on the support and at the periphery of the metal active sites may be also apparently responsible for the trends exhibited depending on the CO_2 partial pressure when the buffer layer is incorporated to the system (Figure 4.13.d). So, CO_2 species may be adsorbed on the support. Considering the OH partial pressure should be higher, the reaction between CO_2 and OH species will be also favored producing H-containing carbonaceous species favoring their desorption process from the surface because of their low thermal stability [58].

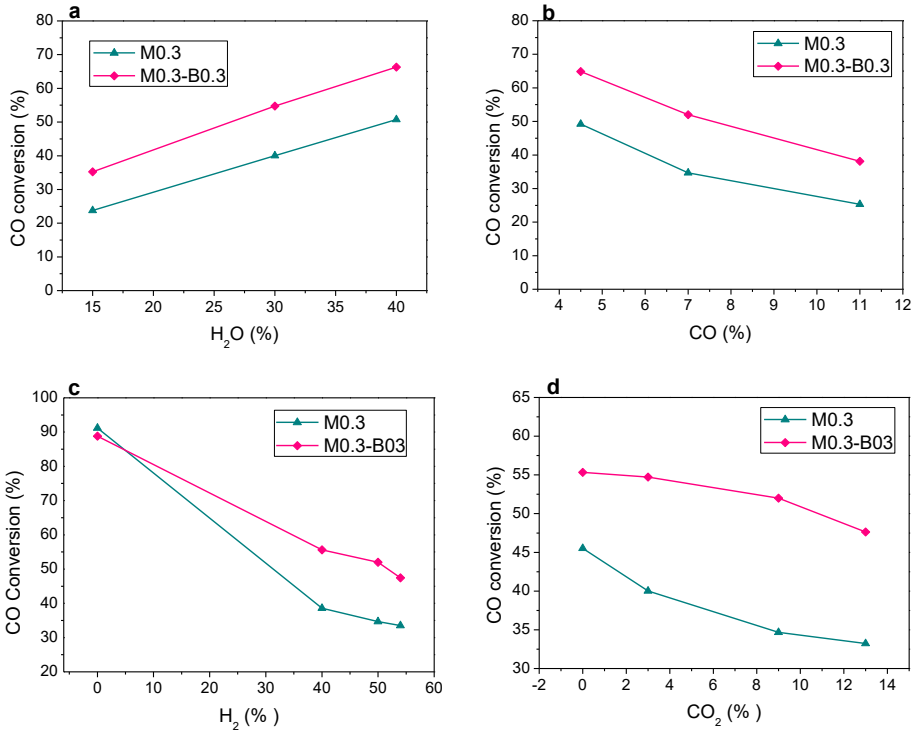

Figure 4.13. Relation between the catalytic activity and the feed stream composition at GHSV= 4000h-1; and T=310 ºC: a) H_2O; b) CO; c) H_2 and d) CO_2

Besides this, an interesting feature was observed by Ruettinger et al. [59] where noticed that, after aging a Pt ceria based catalysts, two differentiated colors were observed being darkness the top one and lighter the bottom one. This suggests that deactivation effects depend on the catalytic layer thickness. In turn, considering the platinum absence at the buffer layer, the intermediate carbonaceous species formed on the top layers (the ones containing the catalysts) should be lower on the buffer layer maintaining an elevated concentration of hydroxyl groups able to diffuse to the metal-support interface

keeping the WGS reaction rate constant despite the formation of such carbonaceous species on the catalyst top layers.

Going back to the initial idea, it is evident that the hypothesis of a buffer layer for increasing the number of adsorbed water molecules that may be activated enhancing the WGS reaction rate is fulfilled. By increasing the concentration of cerium oxide on introducing a buffer layer and consequently increasing the number of oxygen vacancies under reductive atmospheres, the catalytic performance of the $Pt/CeO_2/Al_2O_3$ catalyst are enhanced. However, the balance between the reductive and oxidative properties of the reformer out-gas feed stream controls this enhancement. If the oxidative character of the feed stream overrides the reductive one (model mixture as the limiting case) water molecules may oxidize the buffer layer hindering its beneficial behavior, but if the reductive character overcomes the oxidative one the buffer layer acts as a reservoir of hydroxyl groups that surface diffuses to the metal active centers at rates higher that the reaction ones.

4.5. Partial conclusions

A series of structured catalyst were developed and tested in the WGS reaction. The micromonolithic structures present stable and homogeneous washcoated layers, no matter its composition, e.g. catalyst only or buffer/catalyst. Moreover, no significant catalyst changes were performed during the washcoating process considering the similar catalytic behaviors showed by Pt/CeAl and S-Pt/CeAl.

The comparison between powder and structured catalysts demonstrates the positive effect provided by micromonolithic structures when equal catalyst amounts and conditions were employed. Those positive features offered by the micromonolithic structures leaded to more efficient catalytic behavior probably because of the improve heat and mass transferences which allow a greater platinum use.

The incorporation of buffer layer leads to different behavior as a function of the test conditions. In "model" mixture the best performance is obtained without buffer incorporated to the monolith. On the contrary, the buffer layer leads to an enhancement on the catalytic activity in the "real" conditions. From the feed stream variations experiments, higher catalytic efficiency was observed for the bilayer micromonoliths in the presence of H_2 and CO_2.

The main contribution of the buffer layer is associated to its capacity for dissociating water under reductive atmospheres. The higher number of oxygen vacancies allows surface diffusion to the metal-support interface increasing the WGS reaction rate.

A second positive effect was achieved through increasing the OH population with respect to deactivation by CO_2 species. This beneficial effect should be related to the easiness of the OH + CO_2 reaction due to the increased hydroxyl coverage. These H-containing carbonaceous species formed on the surface may show lower decomposition temperatures therefore increasing the catalyst stability.

The beneficial effects of the buffer layer are closely related to the presence of an extra number of cerium oxide defects and their associated electronic properties, which results in changes on the catalytic coverages. These changes in coverage could, indeed, increase the positive reaction order generally identified for H_2O species making that the resulted water partial pressures higher on the catalytic active sites.

In conclusion, a structured catalytic system able to increase the activity in H_2-rich feed streams was achieved. Although further studies are required, the bilayered micromonolithic catalysts, as novel approach, become an interesting catalytic strategy on the real WGS process intensification.

References

[1] H. Liang, H. Yuan, F. Wei, X. Zhang, Y. Liu, J. Rare Earths 29 (2011) 753.

[2] D.H. Prasad, J. Lee, H. Lee, B. Kim, J. Park, 10 (2009) 748.

[3] J.V. G. Lietz, H. Lieske, H. Spindler, W. Hanke, 81 (1983) 17.

[4] S. Ivanova, O.H. Laguna, M.Á. Centeno, A. Eleta, M. Montes, J.A. Odriozola, Renew. Hydrog. Technol. (2013) 225.

[5] Q. Fu, H. Saltsburg, M. Flytzani-Stephanopoulos, Science 301 (2003) 935.

[6] a. Y. Tonkovich, J.L. Zilka, M.J. LaMont, Y. Wang, R.S. Wegeng, Chem. Eng. Sci. 54 (1999) 2947.

[7] R.J. Farrauto, Y. Liu, W. Ruettinger, O. Ilinich, L. Shore, T. Giroux, Catal. Rev. 49 (2007) 141.

[8] W. Ruettinger, X. Liu, X. Xu, R.J. Farrauto, Top. Catal. 51 (2008) 60.

[9] A. Cybulski, J. a Moulijn, Cell 49 (1994) 19.

[10] E. Tronconi, G. Groppi, Chem. Eng. Sci. 55 (2000) 6021.

[11] C. Ratnasamy, J.P. Wagner, Catal. Rev. 51 (2009) 325.

[12] a. S. Quiney, G. Germani, Y. Schuurman, J. Power Sources 160 (2006) 1163.

[13] L.M. Martínez Tejada, M.I. Domínguez, O. Sanz, M.A. Centeno, J.A. Odriozola, Gold Bull. 46 (2013) 221.

[14] O.H. Laguna, M. González Castaño, M.A. Centeno, J.A. Odriozola, Chem. Eng. J. 275 (2015) 45.

[15] A. a. Gokhale, J. a. Dumesic, M. Mavrikakis, J. Am. Chem. Soc. 130 (2008) 1402.

[16] R.J. Madon, D. Braden, S. Kandoi, P. Nagel, M. Mavrikakis, J. a. Dumesic, J. Catal. 281 (2011) 1.

[17] C.H. Lin, C.L. Chen, J.H. Wang, J. Phys. Chem. C 115 (2011) 18582.

[18] S.-C. Huang, C.-H. Lin, J.-H. Wang, J. Phys. Chem. C 114 (2010) 9826.

[19] A. Phatak, W. Delgass, J. Phys. Chem. C 113 (2009) 7269.

[20] X. Wang, R.J. Gorte, J.P. Wagner, J. Catal. 212 (2002) 225.

[21] J.A. Rodriguez, S. Ma, P. Liu, J. Hrbek, J. Evans, M. Pérez, Science 318 (2007) 1757.

[22] M. Gonzalez Castaño, T.R. Reina, S. Ivanova, M.A. Centeno, J.A. Odriozola, J. Catal. 314 (2014) 1.

[23] O. Sanz, L.M. Martínez T, F.J. Echave, M.I. Domínguez, M.A. Centeno, J.A. Odriozola, M. Montes, Chem. Eng. J. 151 (2009) 324.

[24] J. Stringer, Mater. Sci. Eng. A 120-121 (1989) 129.

[25] V.G. Milt, S. Ivanova, O. Sanz, M.I. Domínguez, A. Corrales, J.A. Odriozola, M.A. Centeno, Appl. Surf. Sci. 270 (2013) 169.

[26] P.B. Weisz, J.S. Hicks, (1961).

[27] N. Dupont, G. Germani, A.C. van Veen, Y. Schuurman, G. Schäfer, C. Mirodatos, Int. J. Hydrogen Energy 32 (2007) 1443.

[28] C.M. Kalamaras, K.C. Petallidou, A.M. Efstathiou, Appl. Catal. B Environ. 136-137 (2013) 225.

[29] G. Jacobs, P.M. Patterson, U.M. Graham, D.E. Sparks, B.H. Davis, Appl. Catal. A Gen. 269 (2004) 63.

[30] G. Germani, P. Alphonse, M. Courty, Y. Schuurman, C. Mirodatos, Catal. Today 110 (2005) 114.

[31] D.I. Potemkin, P.V. Snytnikov, V.D. Belyaev, V. a. Sobyanin, Chem. Eng. J. 176-177 (2011) 165.

[32] R.J. Farrauto, Y. Liu, W. Ruettinger, O. Ilinich, L. Shore, T. Giroux, Catal. Rev. 49 (2007) 141.

[33] D.C. Grenoble, M.M. Estadt, D.F. Ollis, J. Catal. 67 (1981) 90.

[34] A.A. Phatak, N. Koryabkina, S. Rai, J.L. Ratts, W. Ruettinger, R.J. Farrauto, G.E. Blau, W.N. Delgass, F.H. Ribeiro, Catal. Today 123 (2007) 224.

[35] X. Zheng, J. Mantzaras, R. Bombach, Combust. Flame 161 (2014) 332.

[36] S. Aranifard, S.C. Ammal, A. Heyden, J. Phys. Chem. C 116 (2012) 9029.

[37] X. Liu, O. Korotkikh, R. Farrauto, Appl. Catal. A Gen. 226 (2002) 293.

[38] L. Grabow, Y. Xu, M. Mavrikakis, Phys. Chem. Chem. Phys. 8 (2006) 3369.

[39] P. Thormählen, M. Skoglundh, E. Fridell, B. Andersson, J. Catal. 188 (1999) 300.

[40] T. Bunluesin, R.J. Gorte, G.W. Graham, Appl. Catal. B Environ. 15 (1998) 107.

[41] R. Radhakrishnan, R.R. Willigan, Z. Dardas, T.H. Vanderspurt, Appl. Catal. B Environ. 66 (2006) 23.

[42] J.P. Clay, J.P. Greeley, F.H. Ribeiro, W.N. Delgass, W.F. Schneider, J. Catal. 320 (2014) 106.

[43] G.G. Olympiou, C.M. Kalamaras, C.D. Zeinalipour-Yazdi, A.M. Efstathiou, Catal. Today 127 (2007) 304.

[44] D. Martin, D. Duprez, J. Phys. Chem. B 112 (2006) 4428.

[45] D. Duprez, Catal. Today 112 (2006) 17.

[46] Y. Lykhach, V. Johánek, H. a. Aleksandrov, S.M. Kozlov, M. Happel, T. Skála, P. St. Petkov, N. Tsud, G.N. Vayssilov, K.C. Prince, K.M. Neyman, V. Matolín, J. Libuda, J. Phys. Chem. C 116 (2012) 12103.

[47] S. Aranifard, S.C. Ammal, A. Heyden, J. Phys. Chem. C 118 (2014) 6314.

[48] G. Jacobs, U.M. Graham, E. Chenu, P.M. Patterson, A. Dozier, B.H. Davis, J. Catal. 229 (2005) 499.

[49] T.R. Reina, W. Xu, S. Ivanova, M.Á. Centeno, J. Hanson, J.A. Rodriguez, J.A. Odriozola, Catal. Today 205 (2013) 41.

[50] A. Trovarelli, Catal. Rev. 38 (2006) 439.

[51] J. a Rodriguez, J.C. Hanson, D. Stacchiola, S.D. Senanayake, Phys. Chem. Chem. Phys. 15 (2013) 12004.

[52] G. Jacobs, P.M. Patterson, L. Williams, E. Chenu, D. Sparks, G. Thomas, B.H. Davis, Appl. Catal. A Gen. 262 (2004) 177.

[53] S.M. Opalka, T.H. Vanderspurt, R. Radhakrishnan, Y. She, R.R. Willigan, J. Phys. Condens. Matter 20 (2008) 064237.

[54] F.W. Poulsen, M. Glerup, P. Holtappels, Solid State Ionics 135 (2000) 595.

[55] C.T. Campbell, C.H.F. Peden, Science 309 (2005) 713.

[56] M. Gonzalez Castaño, T.R. Reina, S. Ivanova, M.A. Centeno, J.A. Odriozola, J. Catal. 314 (2014) 1.

[57] Z. V. Popović, Z.D. Dohčević-Mitrović, N. Paunović, M. Radović, Phys. Rev. B - Condens. Matter Mater. Phys. 85 (2012) 1.

[58] M.M. Schubert, A. Venugopal, M.J. Kahlich, V. Plzak, R.J. Behm, J. Catal. 222 (2004) 32.

[59] W. Ruettinger, X. Liu, R.J. Farrauto, Appl. Catal. B Environ. 65 (2006) 135.

Chapter 5

Structured WGS catalysts: Influence of the buffer nature on the water activation step

Summary

Structured systems containing two different layers were prepared being the buffer layer placed under the catalyst one. The nature, i.e. the chemical composition of this buffer layer was varied, whereas the catalyst layer, platinum/ceria, was maintained constant. The buffer layer nature influenced the WGS activity by acting on the water activation step. Depending on the composition, enhanced water dissociation capacities were found and judged responsible for the improved WGS activity, especially at high water partial pressures. Several evidences about the participation of the oxygen vacancies, as key sites, for water dissociations process and the buffer's capacity to keep absorbed water on the surface were established.

5.1. Introduction

Considering the improved WGS performance, achieved in H_2-rich CO-containing streams, in the presence of ceria based buffer layer, this Chapter tries to enlighten the layer's role in the WGS reaction and to provide a way to further improve those layers. The observed differences on the catalytic behaviors explained in the previous chapter were tentatively related to the favored water activation step and the participation of the ceria related materials in it.

In general, the boosted catalytic activity for ceria based systems is normally related with the Ce^{3+}/Ce^{4+} redox par behavior [1–3]. The change of the oxidation state within the par entails oxygen exchange with the media and oxygen vacancies formation [4–6], being the latter defects which received the greatest attention in relation to the water activation step [7–10]. It was demonstrated that doping the cerium oxide with an ad-metal to form solid solution, results in oxygen vacancies concentration increase [11–14].

In addition, the approach presented in the previous chapter, shows to the benefit of using metallic micromonoliths [15–18]. This system takes the advantage of being easily modified and controlled by the addition of buffer and/or catalytic layer of different composition.

Our working hypothesis was made assuming that the buffer layer introduced prior the platinum catalyst layer, should be able to absorb water, activate and

release the activated species when needed. Therefore, the buffer layer should keep activated water always available for the WGS reaction. This layer should act like a "sponge" by storing water and then, making easier its activation. In order to elucidate the effect of the buffer layer, its nature was varied and three different compositions were tested: a) γ-Al_2O_3 layer, because of its compatibility with the surface of the oxidized ferritic monoliths and the catalyst, and more importantly assuming that this layer will not play any chemical role in the reaction. It is well known, that alumina is considered as inactive support for the WGS reaction [4]. However, this layer must be added in order to maintain in all tested monoliths the same total layer thickness; b) CeO_2/Al_2O_3, a layer for which improvement of the catalytic activity due to the CeO_2 presence and ability to activate water is expected. It should be noted that in the conditions of the reaction the CeO_2 layer might be partially reduced and the presence of some oxygen vacancies, able to activate water, could be expected; c) $Ce_{0.9}Eu_{0.1}O_2/Al_2O_3$, a layer chosen mainly for the expected increase of the oxygen vacancies concentration due to solid solution formation [12,19]. In addition, Eu was also selected because of its null intrinsic activity in the WGS reaction. If our hypothesis is correct and assuming that all the sample show he similar textural properties of the introduced layers the WGS activity sequence should correlate with the buffer ability to activate water, CeEu > CeAl > Al.

The influence of the contact surface was also evaluated. So, in the second part of this study the contact surface between buffer and catalyst was increased by using the mixed layer approach. The same layer thickness was kept in the preparation, but a physical mixture of $Ce_{0.9}Eu_{0.1}O_2/Al_2O_3$ and the $Pt(2\%)/CeO_2/Al_2O3$ catalyst was used for the monolith deposition.

Thus, the main aim of this chapter is to demonstrate the direct relationship between the oxygen vacancies concentration and the water activation step correlating it with the catalytic activity. The role of the layer should be discerned regarding to its "sponge" capacity and/or to its water activation ability. Two different approaches were considered i) layer by layer deposition, with the buffer layer prior the catalytic one and ii) mixed layer deposition, in order to increase the contact between the buffer and the catalyst.

5.2. Experimental

5.2.1. Synthesis of the buffer solids and catalyst. Physical mixture preparation.

The same catalyst, used in the previous chapter, was maintained, Pt(2 wt.%)/Puralox, labelled as Pt/CeAl.

High specific surface area γ-Al_2O_3 was employed as alumina based buffer layer, labeled from this moment on Al. Contrary to the platinum catalyst, for

which a commercial support was employed, the ceria containing buffer systems were homemade prepared by using $Ce(NO_3)_3 \cdot 6H_2O$ (Aldrich) as cerium oxide precursor. 20 wt.% of CeO_2 was supported on γ-Al_2O_3 (Sasol) by wetness impregnation. Once the ethanol solution employed to dissolve ceria precursor removed by rotary evaporation, the solid was dried and calcined at 450 ºC during 4h with 10ºC/min heating ramp. This solid was labeled CeAl.

Regarding the europium doped ceria based solid, 20 wt.% of mixed oxide was deposited on the same γ-Al_2O_3 (Sasol) using $Eu(NO_3)_3 \cdot 5H_2O$ (Aldrich) as europium precursor. The nominal Ce/Eu molar proportion was 0.9/0.1. In a similar manner both precursors were dissolved in ethanol and impregnated on alumina matrix. The ethanolic solution was then removed and the solid was treated during 30 min in 10 M NH_3 solution with the purpose of fully convert the nitrates to hydroxides. Finally, the solid was filtered, washed, dried and calcined using the above detailed procedure. This sample was denominated CeEuAl.

On the other hand, the physical mixtures were prepared from equivalent powder amounts of Pt/CeAl catalyst and CeAl or CeEuAl solids, respectively. Considering that Pt/CeAl catalyst is the constant element of the mixture, the samples were labeled PMix_CeAl and PMix_CeEuAl attending to the changing phase.

5.2.2. Washcoating process

The metallic micromonolithic manufacture and treatment was explained in details in Section 4.2.

For the successive layers systems, four different slurries based on Al, CeAl, CeEuAl and Pt/CeAl were prepared. Two different layers were deposited being the first one based on Al_2O_3, CeAl or CeEuAl respectively and the second, the external one, based on Pt/CeAl for all the systems (Figure 5.1.A). For each layer, it was deposited 0.3 g of solid being the total amount 0.6 g of solid (buffer + catalyst). Moreover, structured catalysts containing just the buffer layer were prepared in order to evaluate its intrinsic activity in WGS reaction.

Structured catalyst using PMix_CeEuAl was also prepared. The micromonolith was composed only by one layer of 0.6 g of sample (Figure 5.1.D).

For clarity, the structured systems prepared along this chapter are schematically summarized on Figure 5.1. It can be observed that between the bi-layered systems (buffer + catalyst), the only change is the chemical composition of the buffer layer meanwhile the amounts of both buffer and external catalyst´s layer is maintained constant (Figure 5.1: A, B and C). For the system constituted by one single layer (Figure 5.1 D), assuming perfect

physical mixture, the amount of CeEuAl and Pt/CeAl should be the same than on the bi-layered structured catalysts presented in Figure 5.1.C.

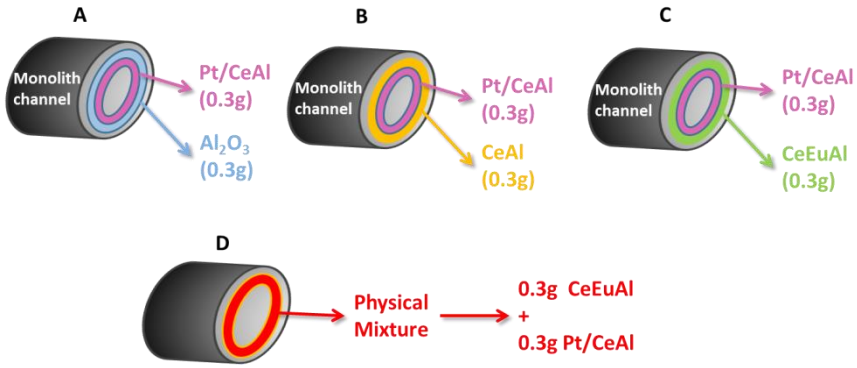

Figure 5.1. Scheme of the prepared structured catalysts.

The solid deposition on the micromonolith surface was made by washcoating. Slurry with properly adjusted rheological properties was prepared for each employed sample. The prepared suspensions were composed by approximately: 18.14 wt.% of solid, 1.96 wt.% of PVA (1.5% wt. polyvinylalcohol in water), 17.65 wt.% of colloidal Al_2O_3 suspension (Nyacol, 20 wt.% in water) and 62.25 wt.% of water. The PVA, as a surfactant, was added to facilitate the suspension capillary impregnation within the channels. The colloidal alumina (Nyacol) was used to obtain well dispersed stable colloidal solid particles solution [20,21]. Prior to the slurries preparation, the solids were milled and sieved in order to obtain adequate

particle sizes allowing stable suspensions. For each suspension, the grinder procedures and the obtained particle sizes are presented on Table 5.1.

Table 5. 1. Milling procedure, achieved particle sizes and Z point of the prepared solids

	Al	CeAl	CeEuAl	Pt/CeAl	PMix_CeEuAl
Procedure	1h at 400rpm	1h at 400rpm + 40 min at 500rpm	1h at 500rpm	40 min at 500rpm	80 min at 500rpm
Part. size (μm)	11.7	4.8	6.4	8.7	16.3
Z point	7	7.2	9.5	6.7	4.5

The pH of the slurries should be also controlled and properly modified, if necessary, in order to avoid pH closer to the solid's isoelectrical point, in which the particles attract each other and agglomerate. As a consequence, the slurries stability is altered in general negatively. The isoelectrical points of the prepared solids are presented on Table 5.1. In the moment of each slurry preparation, the pH of the suspension was finely (drop by drop under agitation) adjusted to pH values inferior to the isoelectric points by employing concentrated nitric acid. The latter is used in order to leave the suspension concentrations practically unchanged.

The buffer and catalyst layers were deposited consecutively on the micromonolith surface. Once the suspensions deposited, the structured catalysts were dried and calcined with the same procedure (temperature, time

and heating rate) employed for their respective solids. The rest of the slurries were dried and calcined till powder and used for comparison with the parent powder samples, to determine the possible changes which could happen during the washcoating procedure. The nomenclature of the parent solids was maintained but a prefix "S_" was added to the name indicating that the sample corresponds to the slurry used for its deposition. For example, the slurry prepared from the CeAl solid is labeled S_CeAl.

For the bi-layered micromonoliths, the used nomenclature consists of adding "M_" prefix followed by the sample name corresponding to the buffer layer (M_CeAl corresponds to micromonolith containing two layers, CeAl buffer and Pt(2%)/Puralox catalyst). Meanwhile, for the micromonolith prepared with buffer layer only, to the above described nomenclature the prefix was changed to "M_j" prefix where "j" accounts for just. For example, both micromonolithic systems prepared from CeAl will be named M_CeAl and M_jCeAl and correspond to the bi-layered monolith and to the buffer only monolith, respectively. The slurry amounts deposited on each layer are listed in Table 5.2, being indicated in parenthesis, the amount corresponding to the catalyst. The layer quantity was estimated assuming that water and PVA are completely removed during the calcination, but the alumina phases originated from colloidal alumina (Nyacol) are still present and provoked an diminishing of the active component layer amount.

Table 5.2. Suspension quantities deposited for the buffer and catalyst layers. In parenthesis, the corresponding parent solid amounts

	Buffer layer (g)	Catalyst Layer (g)
Mj_Al	0.33 (0.27)	---
Mj_CeAl	0.34 (0.28)	---
Mj_CeEuAl	0.32 (0.27)	---
M_Al	0.34 (0.29)	0.31 (0.26)
M_CeAl	0.38 (0.32)	0.31 (0.26)
M_CeEuAl	0.32 (0.27)	0.31 (0.26)
M_Pmix_CeEuAl	0.65 (0.54)	

5.3. Physicochemical characterization

5.3.1.Textural properties and chemical composition of the prepared solids

The textural properties of the buffer solids, catalyst and the respective suspensions are shown in Table 5.3. All the prepared solids are mesoporous with specific surface area dominated by the presence of alumina. Among the initial buffer solids, the pure alumina presents the highest specific surface area which diminishes in the same extent with the addition of CeO_2 or Ce-Eu mixed oxide.

The suspensions show higher specific surface areas than the parent powders. Lower pore diameter and slight increase of the pore volume for the suspensions are also observed, caused by the presence of colloidal alumina. Therefore, the textural properties of the suspensions are modified by the presence of the colloidal alumina (Nyacol). The catalyst Pt/CeAl follows the same trend as the buffers.

Table 5.3. Textural properties of the prepared powders, suspensions and structured catalysts

	Area (m^2/g)	V_{pore} (cm^3/g)	D_{pore} (Å)
Al	169	0.38	74
S_ Al	178	0.37	64
CeAl	133	0.28	74
S_CeAl	166	0.32	64
CeEuAl	132	0.29	69
S_CeEuAl	187	0.36	63
Pt/CeAl	142	0.30	70
S_ Pt/CeAl	156	0.34	65
PMix_CeAl	182	0.36	66
PMix_CeEuAl	181	0,33	67
S_PMix_CeEuAl	187	0.39	70

The catalyst textural properties are also studied in the micromonolithic devices and presented in Table 5.4. The structured catalysts exhibited similar textural properties to that shown by the suspensions. From the amount of the deposited solid, its chemical composition and textural properties, the layer thickness of all the solids can be estimated using the respective densities. The obtained calculations are presented in Table 5.4. The layer thickness exhibited by the Mj_ and M_ systems is around 4 and 7 μm respectively being allowed therefore, to perform a proper comparison.

Table 5. 4: Textural properties of the prepared structured samples

	Area (m^2/g)	V_{pore} (cm^3/g)	D_{pore} (Å)	Thickness (μm)
Mj_Al	189	0.41	69	4.2
Mj_ CeAl	159	0.33	68	3.7
Mj_CeEuAl	174	0.37	72	3.6
M_Al	220	0.40	71	7.2
M_ CeAl	167	0.37	71	6.8
M_CeEuAl	157	0.34	72	6.7
M_PMix_CeEuAl	178	0.37	70	7.2

The chemical composition of the catalyst, buffers and their respective suspensions are presented in Table 5.5. All the buffer systems present compositions close to the desired loading, only minimal loss of CeO_2 component is detected. The calculated Ce/Eu molar ratio is 8 instead of 9 in the originally designed solid. The catalyst Pt/CeAl also presents similar compositions to the desired one. Moreover, the observed changes on the suspensions chemical compositions should be attributed to the alumina added during the slurry preparation; in fact, the incorporation of the colloidal alumina (Nyacol) increases the alumina content and hence, automatically decreases the ceria, europia and platinum loadings. On the other hand, the obtained chemical compositions for the slurries are in very good agreement

with the theoretical compositions calculated considering the amounts employed during the suspension synthesis.

Table 5. 5. Chemical composition of the prepared powders in wt.%

	Al_2O_3 (wt.%)	CeO_2 (wt.%)	Eu_2O_3 (wt.%)	Pt (wt.%)
Al	100	---	---	---
S_ Al	100	---	---	---
CeAl				
S_CeAl	82.1	17.9	---	---
CeEuAl				
S_CeEuAl	82.2	15.7	2.1	---
Pt/CeAl	75.6	21.8	---	2.6
S_ Pt/CeAl	80.7	17.3	---	2.0
PMix_CeAl	78.8	20.1	0.0	1.1
PMix_CeEuAl	78.8	20.1	0.0	1.1
S_PMix_CeEuAl	78.9	18.8	1.1	1.2

5.3.2. XRD analysis

The XRD patterns of the powder samples are shown in Figure 5.2. The Al, CeAl, CeEuAl and Pt/CeAl patterns present diffraction lines of the fluorite structure of CeO_2 (JCPDS# 00-004-0593) and γ-Al_2O_3 (JCDPS# 00-048-0267). In the case of CeEuAl, no diffraction lines due to pure europium oxide are detected. Moreover, slight shift on the CeO_2 diffractions were observed

with respect to those of CeAl. From the position of the main CeO_2 (111) diffraction the calculation of the lattice parameters was performed for both ceria containing buffers, showing an increase of the value from CeEuAl to CeAl (5.40Å *vs.* 5.39Å) accounting for the CeO_2-Eu_2O_3 solid solution formation and partial substitution of Ce^{4+} by Eu^{3+} ions accompanied by the formation of oxygen vacancies [22,23]. This substitution should increase the lattice parameter because of higher ionic radii presented by Eu^{3+} in respect to the Ce^{4+}.

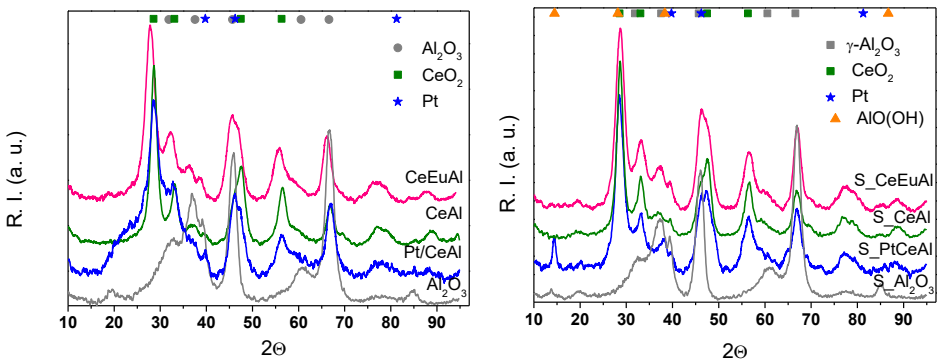

Figure 5.2. XRD of the prepared solids: a) Al_2O_3, CeAl, CeEuAl and Pt/CeAl; b) S_Al_2O_3, S_CeAl, S_CeEuAl and S_Pt/CeAl

In addition, smaller CeO_2 crystal size for the Eu-promoted system was estimated from Scherrer`s equation 38 *vs.* 55 nm for CeAl. This fact could be attributed to the lattice distortion, produced by the europium insertion, after which the crystal growth is restricted, resulting in smaller crystal domains. On the other hand, no Pt reflections are observed for the Pt/CeAl sample

suggesting high dispersion of the noble metal, with crystalline domains under the detection limit of the technique (5nm). XRD results of the suspensions are shown in Figure 5.2.b.

As for the suspensions, no important differences are detected with respect to the XRD of the parent solids, indicating that no structural changes occur during the suspension preparation. However, the Al_2O_3 phase added to the suspension (Nyacol) can be distinguished, being the additional difractions commonly attributed to the boehmite phase (JCDPS# 00-21-1307).

5.3.3. Adherence test and SEM

Within the micromonoliths series, the catalyst adherence was excellent remaining around 94-97% of catalyst layer left after the adherence test. The obtained results account for the suitability of the washcoating method for catalyst deposition when properly carried out. SEM micrographs show in all cases, the presence of well dispersed homogeneous catalytic layer onto metallic substrates. As an example, Figure 5.3 the SEM micrographs obtained for M_CeAl are shown, including the cross section micrograph (Figure 5.3.b). From bottom to top (left to right in the image), three layers can be distinguished: i) the metallic substrate characterized by Fe-Cr presence; ii) an alumina layer constituted by the alumina produced during the thermal pretreatment of the monolith´s steel the colloidal Al_2O_3 added during to the slurry preparation and the alumina component coming from the buffer itself and iii) the external surface layer rich in CeO_2.

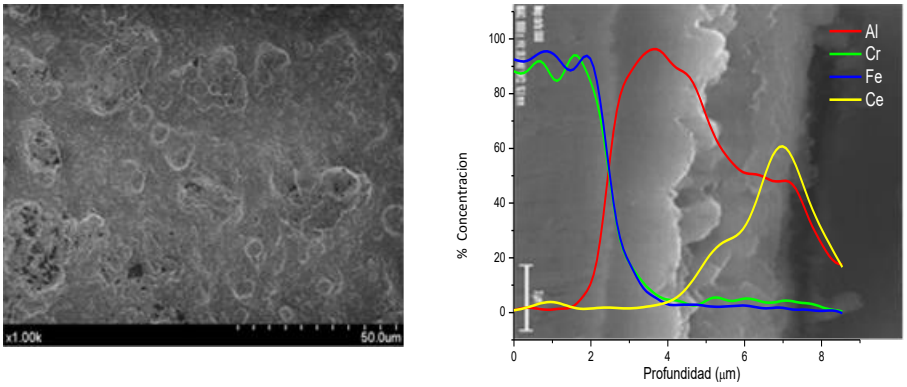

Figure 5.3. SEM microphotographs a) front surface image; b) cross section image overlapped with line analysis

5.3.4. IR spectroscopy and H_2O-TPD

Infrared-spectroscopy was carried out in order to better understand the role of the buffers in the water activation step and to correlate the catalytic results to the buffer's nature. In general, the introduction of certain water quantities to the system could lead either to water adsorption and/or to water dissociation. The presence of dissociated water should involve an increment of the hydroxyl bands intensity. The Figure 5.4 presents the hydroxyl band intensities evolution exhibited by the Al, CeAl and CeEuAl solids during the water introduction steps. The spectra of Al sample (Figure 5.4.a), present hydroxyl species adsorbed on alumina surface with their corresponding bands placed at 3785, 3733, 3693, 3585 and 3521 cm^{-1}. The bands at around 3785, 3733, 3693 cm^{-1} frequency values (υOH) could be attributed to OH groups bound to tetrahedrally monocoordinated or bicoordinated Al^{3+}, according to Knözinger et al. [24–26]. The bands positioned at 3585 and 3521 cm^{-1} are

typical for an H-bonded to OH's species [24] and corresponds to nondissociated molecular water. It can be observed, that the successive water adsorptions leads to diminution of the hydroxyl band situated at 3733 cm^{-1} and to an increase of the bands placed at 3585 and 3521 cm^{-1}. Both changes could be explained by the presence of molecular water absorbed on the sample. The strength of the O-H bond becomes weaker because of the OH – H_2O dipole formation and interaction, being this in agreement with the increase observed for the 3585 and 3521 cm^{-1} bands.

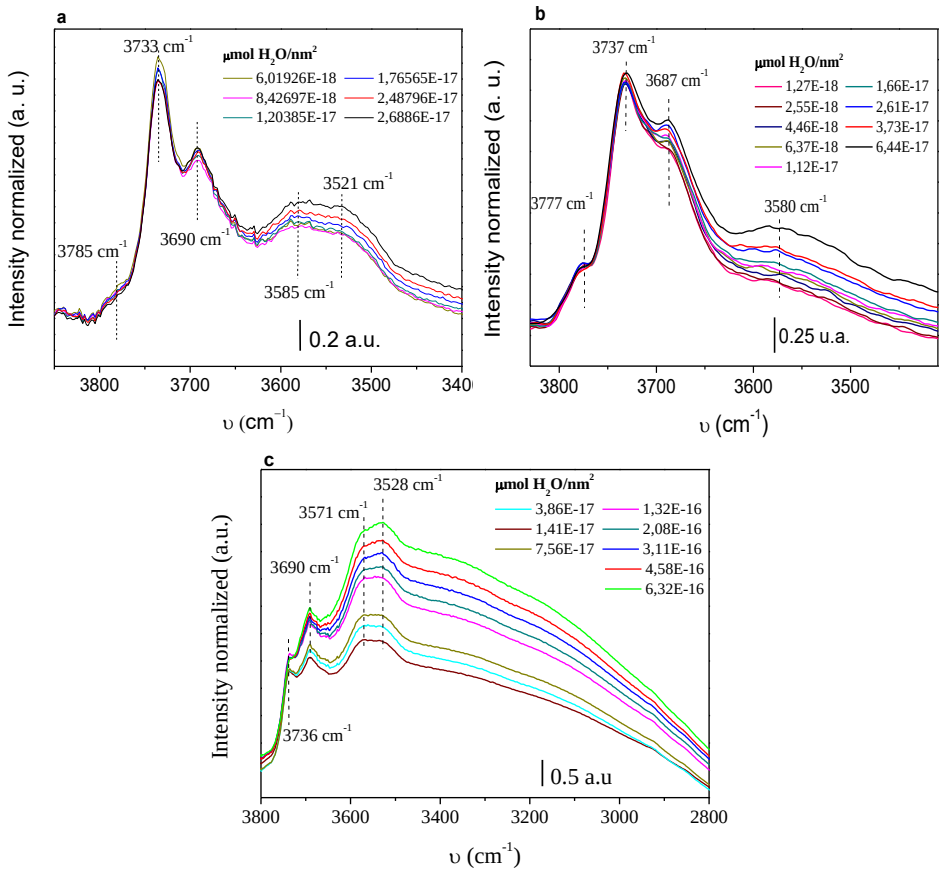

Figure 5.4. FTIR spectra obtained during the water absorption for: a) Al; b) CeAl; c) CeEuAl

Taking into account the high alumina content present in CeAl sample, the obtained spectra (Figure 5.4.b) during the water experiment are quite similar to that obtained for Al sample. In the spectra, bands placed at 3777, 3737, 3687 and 3580 cm^{-1} are observed. For comparison the Al sample exhibited a band placed at 3785 cm^{-1}, whereas for the CeAl this band is shifted to 3777 cm^{-1} approx., probably related to different chemical environment provoked by the cerium oxide presence. Moreover, the band placed at 3733 cm^{-1} also shift slightly which could be due to the low intensity band reported for cerium oxide at 3710 cm^{-1} attributed to OH(I) species [27]. Similar effects could lead to different positions respect to the Al bands accounting mainly for the ceria presence and interactions with water; for example, the bands situated at 3686 and 3580 cm^{-1} should be related to isolated hydroxyl groups (3684 cm^{-1}) and to H-bonded species (3583 cm^{-1}) reported for cerium oxide [24,28].

In the Figure 5.4.b, it can be discerned the increment of the both bands intensity. The CeAl sample, exhibit higher proportional intensity increase of the band placed at 3585 cm^{-1} suggesting higher water absorption capacity in respect to the Al sample. It should be noted that if the introduced water only leads to molecularly absorbed water species, a decrease of the hydroxyl bands intensity should occur. On the contrary, the hydroxyl bands do not change, nor by position or intensity, implying certain capacity to dissociate water acquired with ceria addition.

The spectra recorded during the water absorption for the CeEuAl sample are shown in Figure 5.4.c. The sample presents bands situated at 3736, 3690, 3571 and 3528 cm^{-1}, respectively. The additional shift of the band position could be again tentatively correlated with different chemical environment achieved with the europium incorporation to the cerium oxide lattice. No bands of europium oxide – H_2O interaction are detected. The sample CeEuAl seems to be able to absorb higher amounts of water, suggested by the relatively higher band intensity at 3571 and 3528 cm^{-1} shown by this sample in respect to the other solids. The wide band in the 3490 to 2800 cm^{-1} range could be directly linked to higher absorbed water quantities. The hydroxyl bands positioned at 3736 and 3690 cm^{-1} also increase their intensities with the introduction of water. Hence, this sample appears to be able to absorb higher amounts of water on its surface and also more pronounced water dissociative capacity is observed especially when higher partial water pressures are used. Actually, the water dissociation and oxygen vacancies concentration could be directly related: higher the oxygen vacancies concentration, higher the water splitting capacity [9,29].

In order to properly compare the three samples, the spectra obtained when equal amount of water are introduced ($3 \cdot 10^{-18}$ $\mu mol/nm^2$) are presented on the Figure 5.5. Regarding the 2240 – 1320 cm^{-1} region, a wide band around 1600 cm^{-1} can be discerned and attributed to absorbed molecular water. This band is probably constituted by several contributions due to different chemical

environments in which the water species are absorbed. In agreement to the previously discussed, the water was not just dissociated but also molecularly retained on the samples and the following sequence of absorbed quantity could be established: CeEuAl > CeAl > Al.

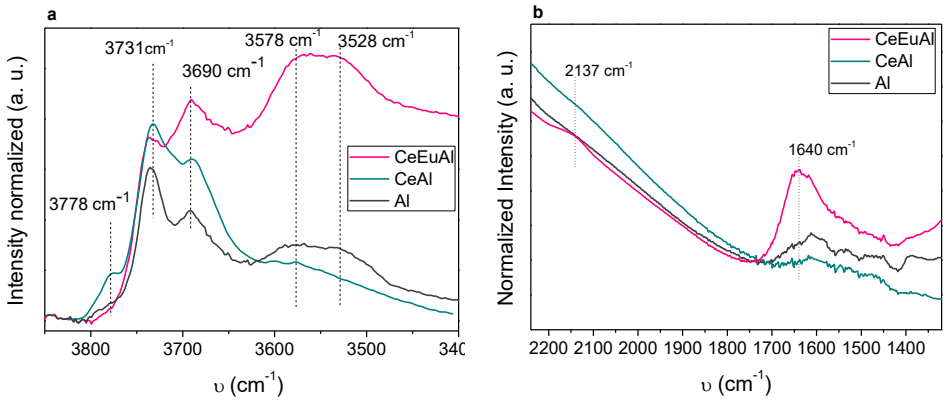

Figure 5.5. FT-IR spectra obtained when $3 \cdot 10^{-18}$ µmol/nm^2 water were absorbed for Al, CeAl and CeEuAl: a) 3900 – 3400 cm^{-1}; b) 2250 – 1320 cm^{-1}

After water saturation, the samples were degassed first by applying different pressures (ϕ_1, ϕ_2) and, then by heating at T = 50, 100, 150 y 200 °C. For the 2240 – 1320 cm^{-1} region, the spectra evolution obtained during the water absorption and desorption for CeAl and CeEuAl are shown in the Fig. 5.6.

Higher amount of water molecules appears to be absorbed in the case of Eu-doped system. Moreover, contrary to the CeAl sample, the CeEuAl maintains an appreciable amount of absorbed water at 200°C during the desorption process. Therefore, the europium insertion to the ceria lattice allows not only

increased number of oxygen vacancies as sites for water dissociation but also keep it more tightly absorbed.

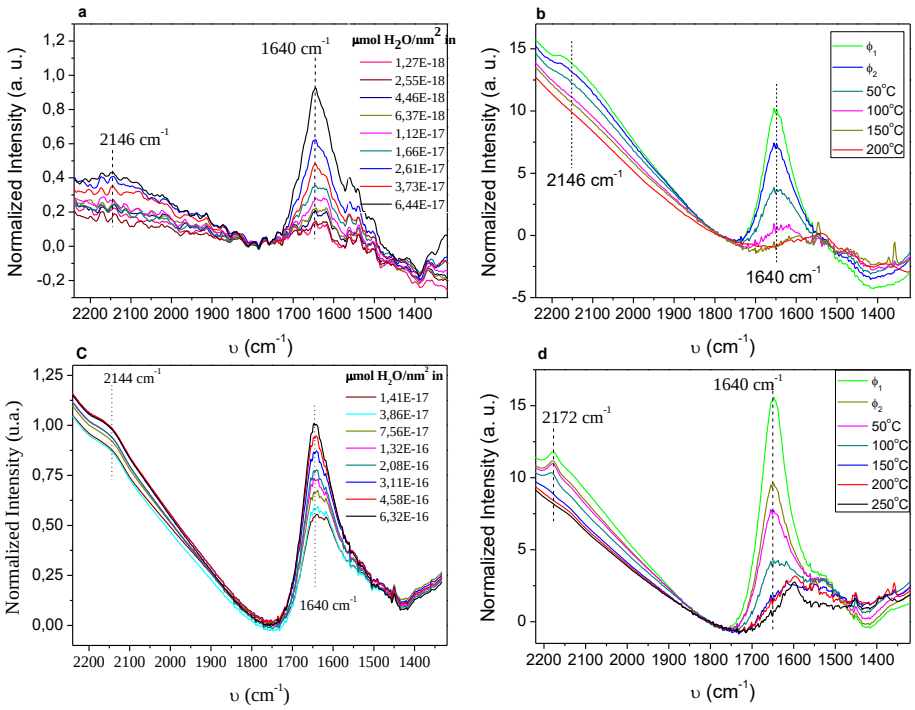

Figure 5.6. FT-IR spectra recorded for the 2240 1320 cm^{-1} region during: a) water absorption on CeAl; b) water desorption on CeAl; c) water absorption on CeEuAl and d) water desorption on CeEuAl

The desorption process also showed differences concerning the CeEuAl sample capacity to maintain on the surface molecular water species. In Figure 5.7, the CeAl and CeEuAl spectra are compared when heated to 200ºC during the desorption process. The Al sample do not present any important modifications along the water absorption process and, therefore, the desorption was not performed. In the Figure 5.7.a, the higher intensity of the

broad band placed in the 3500 to 2800 cm^{-1} range indicates higher quantity of absorbed molecular water. This increase in intensity was also accompanied by the increase in the 1600 cm^{-1} band intensity, specific for the presence of molecular water. The amount of molecular water retained even at 200 ºC was significantly higher for CeEuAl than the one kept by the CeAl sample.

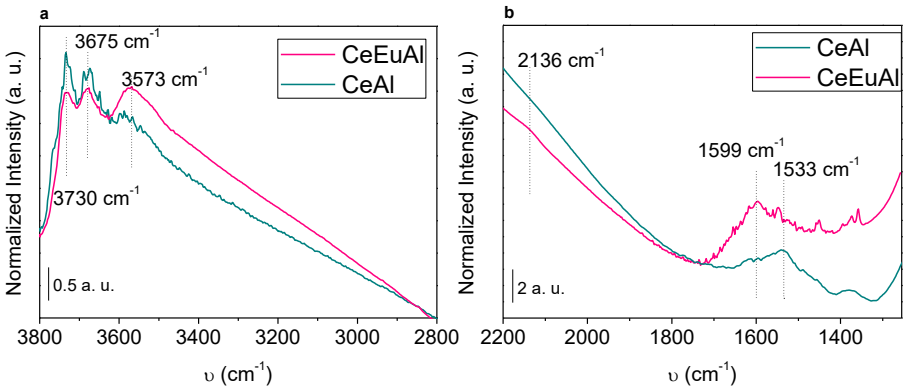

Figure 5.7. FT-IR spectra obtained at T=200 ºC during the water desorption experiment for CeAl and CeEuAl samples: a) 3900 – 3400 cm^{-1}; b) 2250 – 1320 cm^{-1} range

In order to confirm these observations, H_2O-TPD experiments were carried out over S_Al, S_CeAl and S_CeEuAl powder samples. Small quantities of water (500 μL) were injected on the sample using N_2 as carrier at 120 ºC. Once the water signal (m/z) = 18 stabilized after the pulse experiments the sample was heated at 5 ºC/min up to 600 ºC the necessary time to desorb all water species.

In the Figure 5.8, the m/z=18 profile normalized by the surface area of each sample during the H_2O-TPD is presented. Considering the comparable H_2O amounts introduced for all the samples, the similar surface areas presented for all the samples and the equivalent heating rate employed, the influence of the water surface coverage on the resulted TPD can be neglected. Thus, especially for the lower temperature range, the observed changes should account for the different adsorptions performed by water molecules as a function of the support nature.

Similar profiles are observed for all samples with two main desorption zones: 120-350 ºC and 350-600 ºC. The desorption processes observed at the lower temperature zone should be ascribed to water adsorption on ceria surfaces meanwhile the highest temperature desorption zone can be tentatively attributed to processes related to the alumina [30]. The obtained profiles are quite similar to that reported by Thinon et al. [31] when performed similar H_2O-TPD experiences. Besides, the TPD spectra were simulated employing the kinetic law proposed by Germani et al. [32] achieving very good fits to the experimental law. In this study, they reports two main desorption processes placed respectively at 120 ºC and 260 ºC which were respectively attributed to molecular and dissociative desorption processes. Moreover, in good agreement the obtained spectra, they also argue that the second broad peak could be also modulated by molecularly adsorbed water that presents strong lateral interaction through H bonding.

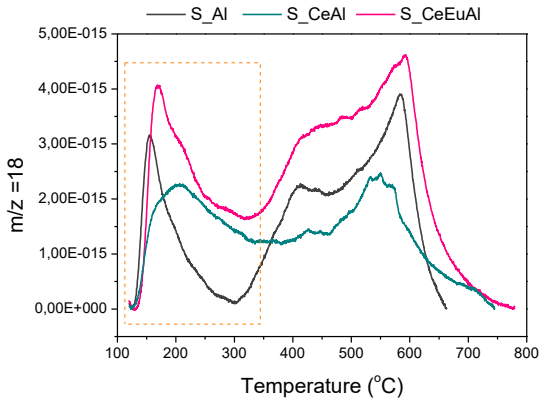

Figure 5.8. FT-IR spectra obtained during the water absorption experiment for Al, CeAl and CeEuAl: a) 3900 – 3400 cm^{-1}; b) 2250 – 1320 cm^{-1}

Graphically, it can be discerned that S_Al based sample loose water earlier than both ceria based ones. Actually, the ceria samples exhibit important amounts of water desorbed at above 260 ºC implying that the ceria presence leads to superior capacities to absorb molecular and/or dissociated water species. The highest water signal exhibited by the S_CeEuAl samples should implies a superior capacity for keeping water species adsorbed at those temperatures which in turn, is in good agreement to the results obtained by FT-IR spectroscopy.

Peden et al. [33] studied the water interactions to oxidized and reduced ceria surfaces by H_2O-TPD performed under UHV claiming that water molecules were not adsorbed on reduced $CeO_2(111)$ crystallites but rather on Ce^{3+} sites of non-(111) systems. Considering the incremented number of oxygen vacancies existent on the S_CeEuAl sample in comparsion to the S_CeAl, the superior capacities to dissociates and retain adsorbed water species should be

directly related to the electronic effect induced by that superior oxygen defect on the ceria lattice.

5.4. Catalytic activity results

The buffer samples, both in powder or in micromonolithic devices, do not show any catalytic activity in the WGS reaction. Only the systems containing platinum catalyst are active. In the Figure 5.9.a, the catalytic activity of the powder platinum based solids is presented. Both samples exhibit very similar performances indicating, in agreement with characterization results, that no important changes during the washcoating process are produced.

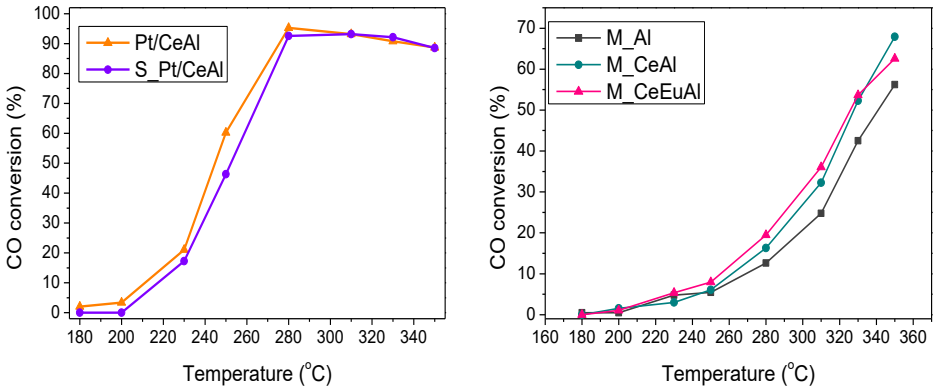

Figure 5.8. Catalytic activity using a feed stream composed by 7% CO + 9% CO_2 + 50% H_2 + 30% H_2O (N_2 balanced) in CO conversion terms: a) Pt/CeAl and S_Pt/CeAl powder catalysts; b) structured M_Al, M_CeAl and M_CeEuAl

In term of CO conversion, the micromonolithic devices (M_Al, M_CeAl and M_CeEuAl) are less active than the Pt/CeAl powder and its suspension, Figure 5.9.b. The lower catalytic activity observed for the structured catalysts

can be easily explained considering that the quantity of the powder catalyst used in the catalytic test was 3 times the one deposited on the micromonolith device. In addition, as the GHSV was maintained constant, different flows are imposed because of the different catalytic volumes (1.5 and 6 cm^3), which varies the contact time, one of the most important parameters in the WGS reaction.

The comparison between micromonoliths and powder homologues do not takes into account the change of those parameters and could result erroneous. That is why the evaluation of the catalytic performance will be made from now on only within the same group of catalysts, powders or micromonoliths. The powder catalytic conditions were chosen in order to make them comparable to the rest of powder catalytic test carried out along the Thesis. On the other hand, the structured catalyst amount were chosen in order to obtain the proper catalyst layer thickness stablished on the previous chapter. So, the micromonoliths are compared, the worst catalytic activity is shown by M_Al meanwhile M_CeAl and M_CeEuAl perform similarly being the latter slightly better in terms of CO conversion.

In order to determine the contribution of the buffer layer in regards to the employed feed stream and buffer compositions, the relative concentration of each component introduced on the reaction was analyzed. The composition of the feed is varied in order to determine the effect of the feed on the buffer and on the WSG activity. In order to broaden the composition variation range but

also by keeping the conditions similar to all previous experiments, the CO_2 concentration was decreased from 9% to 3%. The resulted basic composition was then 7% CO + 3% CO_2 + 50% H_2 + 30% H_2O within which only one component is varied in each experiment. The observed changes in the catalytic behaviors are presented on the Figure 5.10 corresponding to % CO, % CO_2 % H_2 and % H_2O variations, respectively. Considering that the WGS reaction is an equilibrium reaction, the incorporation of products should lead to lowering of the CO conversions.

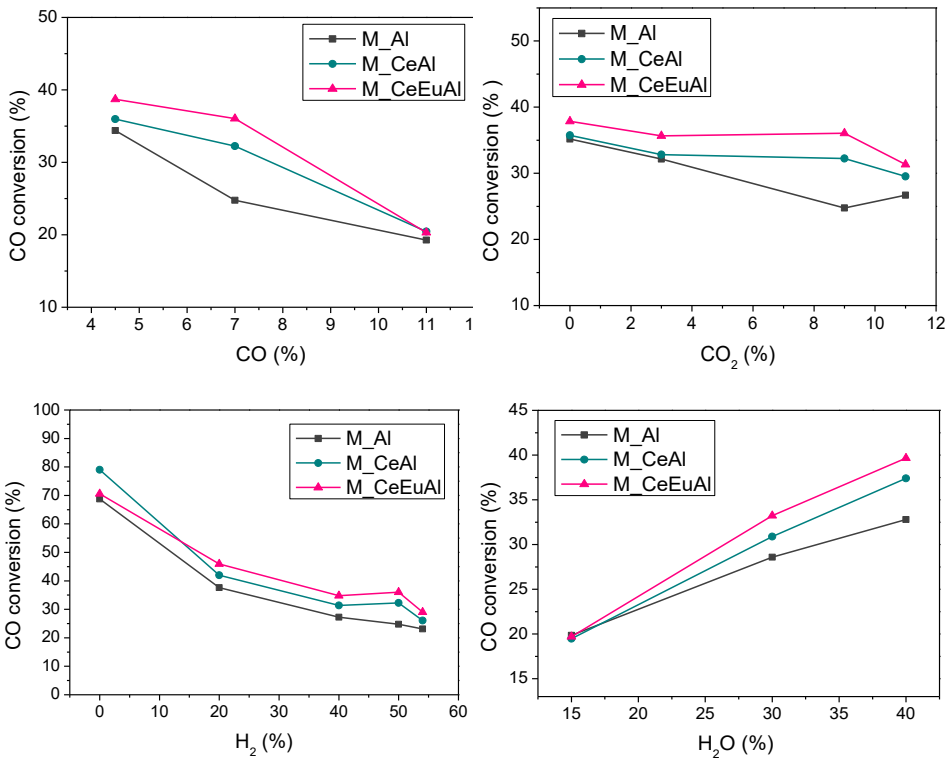

Figure 5.10. Effect obtained on the catalytic activity of M_Al, M_CeAl and M_CeEuAl catalysts when: a) % CO; b) % CO_2; c) % H_2 and d) % H_2O are varied on the feed stream.

No important changes with CO_2 addition were observed especially for ceria containing buffers. On the contrary, notorious H_2 effect was observed, a rapid decrease of the CO conversion was detected with the addition of hydrogen. This fact could be essentially attributed to the higher number of CO molecules that have to be converted by the same number of platinum sites. For those three stream components, the changes provoked by the concentration variations remain within the same magnitude and no marked difference between the samples is observed.

The increase of the H_2O concentration (Figure 5.9.d), however, involves significant changes on the catalytic activity. At low water concentrations, all the micromonoliths present the same conversion values. By increasing the water quantity in the stream, the activity for all the micromonoliths increases. Taking into account the WGS equilibrium, an enhancement of the catalytic activity with the water partial pressure is expected. Our catalytic activity shows that this improvement in activity depends on the buffer`s composition following the sequence: M_CeEuAl > M_CeAl > M_Al. According to the initial hypothesis, this could be related to the water activation capacity modulated by the buffers composition. Therefore, the sequence of activity correlates with the increasing concentration of oxygen vacancies which favors and makes easier the water activation.

Till now, an enhancement of the catalytic activity was achieved by the two layers approach, being this improvement attributed to the higher number of

oxygen vacancies created by doping ceria by europia and resulting in greater capacity to activate H_2O. However, the contact between the two layers could be improved by their physical mixing and therefore superior catalytic performances might be expected. The catalytic activity of powder PMix_CeAl and PMix_CeEuAl was tested and obtained results are presented in the Figure 5.11.a. The influence of the water partial pressures was also studied at 250 ºC for both physical mixtures (Figure 5.11.b).

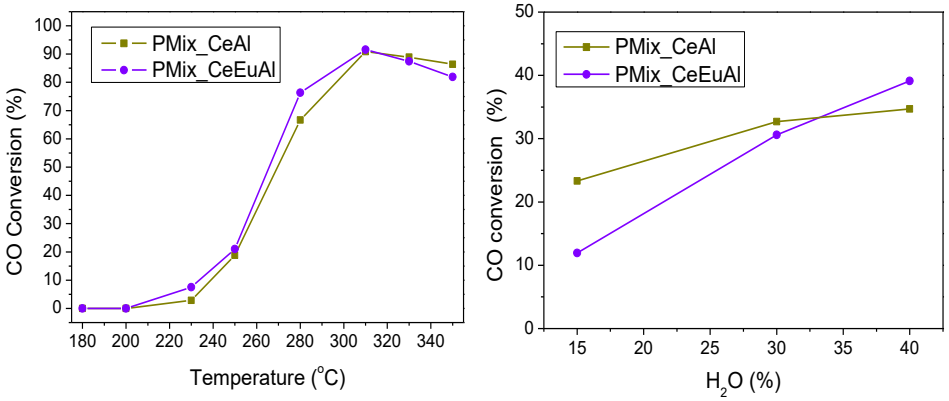

Figure 5.11. Catalytic test for PMix_CeAl and PMix_CeEuAl: a) Feed composition: 7% CO + 9% CO_2 + 30% H_2O + 50% H_2; b) water partial pressure influence at T=250 ºC feed composition 7%CO + 3%CO_2 + 50%H_2

Although no significant improvements were obtained for PMix_CeEuAl in respect to PMix_CeAl in CO conversion terms, the water partial pressure variations lead to interesting changes. Indeed, higher water concentrations enhance the catalytic behavior of both samples, especially at the highest water partial pressure for the PMix_CeEuAl sample. The observed improvement could be probably due to the greater water dissociation capacity achieved by

the increased oxygen vacancies number reached by europium introduction, but also by the intimate contact obtained when mixed.

Structured catalyst using the PMix_CeEuAl was also prepared, for which only one layer containing 0.6 g of catalyst was deposited, M_PMix_CeEuAl. The catalytic activity of the monolith is shown in Figure 5.12 compared to the other catalysts. The results show that the catalytic behavior for M_PMix_CeEuAl does not obey our expectations. Although the improvement of the contact buffer-catalyst is present lower catalytic activity was observed, a possible burial of the Pt active sites might be responsible for the lower catalytic performance.

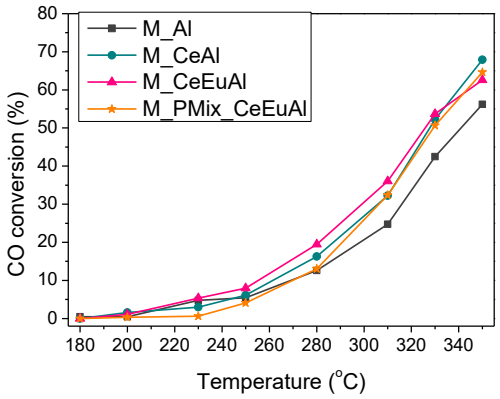

Figure 5.12. Catalytic test for M_Al, M_CeAl, M_CeEuAl and M_PMix_CeEuAl, feed 7%CO + 9%CO_2 + 30%H_2O + 50%H_2

The effect of the water partial pressures is presented in the Figure 5.13.a. The M_PMix_CeEuAl sample shows superior catalytic activity in these conditions

in comparison to the other structured samples. The increasing of the water partial pressure induces greater effect in respect to the bi-layer monoliths, especially at the highest water concentration. This result is in concordance with the initial hypothesis. Improved buffer/catalyst contact seems to provide shorter distances that water activated species have to travel to arrive to the noble metal interface and to complete the reaction.

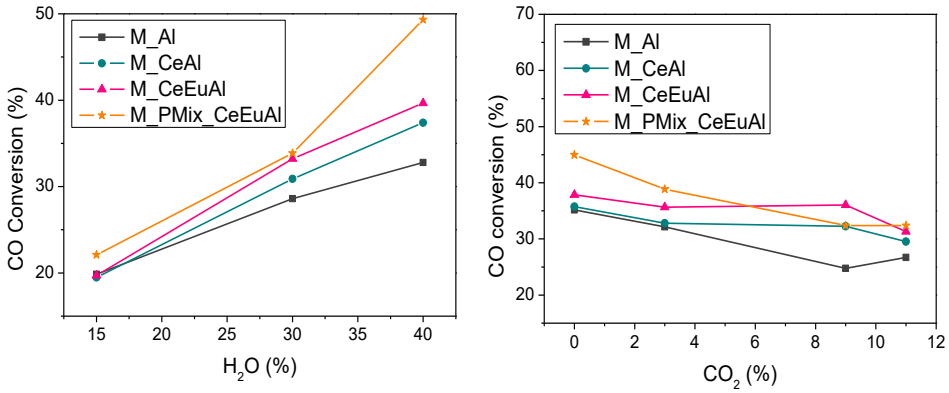

Figure 5.13. Catalytic performance for M_Al, M_CeAl, M_CeEuAl and M_PMix_CeEuAl when a) % H_2O and b) % CO_2 are varied

Considering that the only difference between the water test and the light off is the % CO_2 introduced, the CO_2 effect was also analyzed (Figure 5.13.b). In this experience, it can be observed that the CO_2 presence affects in a greater extent the catalytic performances of M_PMix_CeEuAl, in comparison to the bi-layered structured catalysts. For similar ceria based catalysts, the deactivation by carbonaceous species strongly linked to Ce^{3+} sites has been well established in literature [45]. An interesting fact was noticed by

Ruettinger et al. [34] observing two differentiated colors were observed being darkness the top one and lighter the bottom one, after aging a Pt ceria based catalysts. This implies that the bilayered approach increases the catalytic resistances hindering the blocking of the catalytic sites present on the buffer layer. Therefore, the decrement of the M_PMix_CeEuAl activity could be correlated with the amount of poisoned Ce^{3+} on the surface of this monolith.

This feature also explains that a superior CO_2 concentration on the feed stream leads to catalytic decrease in minor extent for the buffer containing structured catalysts in comparison to the bare systems. It could be suggested then that in bi-layered systems the catalyst layer could act not only like a catalyst layer but also like a CO_2 hindering system. Therefore, the bi-layered structured systems are interesting catalysts, maintaining the noble metal based catalysts on the surface, in close contact with the feed stream, and at the same time partially avoiding the deactivation effects on the buffer layer allowing that the water activation step continue in the CO_2 free oxygen vacancies.

5.5. Partial conclusions

The benefits of the use of micromonolithic devices have been confirmed by testing known platinum ceria based catalyst. The buffer layer incorporation leads to significant improvement of the catalytic activity of the micromonolithc systems. This catalytic activity was modulated by the layer composition or more precisely by the increase of the number of oxygen vacancies. A direct correlation between the water activation capacity and the

oxygen vacancies concentration was demonstrated emphasizing the importance of the water activation step in the WGSR.

In good agreement with the catalytic results, FT-IR analysis showed different capacities to absorb and dissociate water depending on the buffer composition. This statement was confirmed by some H_2O-TPD pulses experiments.

This water activation was even more enhanced when the buffer-catalyst contact was increased probably by increasing the easiness of transport of the activated water to the active noble metal surface.

The buffer layer incorporation also provides an interesting approach against the important deactivation processes commonly reported for ceria based catalysts when carbonaceous species block the support active sites hindering the water dissociation step.

References

[1] A. Holmgren, B. Andersson, D. Duprez, Appl. Catal. B Environ. 22 (1999) 215.

[2] G. Kim, Ind. Eng. Chem. Prod. Res. Dev. 21 (1982) 267.

[3] A. Trovarelli, Catal. Rev. 38 (2006) 439.

[4] M. Gonzalez Castaño, T.R. Reina, S. Ivanova, M.A. Centeno, J.A. Odriozola, J. Catal. 314 (2014) 1.

[5] T.X.T. Sayle, S.C. Parker, C.R.A. Catlow, Surf. Sci. 316 (1994) 329.

[6] C.T. Campbell, C.H.F. Peden, Science 309 (2005) 713.

[7] A.Y. Stakheev, Y. Zhang, A. V. Ivanov, G.N. Baeva, D.E. Ramaker, D.C. Koningsberger, J. Phys. Chem. C 111 (2007) 3938.

[8] C.W.M. Castleton, J. Kullgren, K. Hermansson, J. Chem. Phys. 127 (2007) 1.

[9] F. Esch, S. Fabris, L. Zhou, T. Montini, C. Africh, P. Fornasiero, G. Comelli, R. Rosei, Science 309 (2005) 752.

[10] C. Zhang, A. Michaelides, D.A. King, S.J. Jenkins, J. Chem. Phys. 129 (2008) 1.

[11] L. Yue, X.M. Zhang, J. Alloys Compd. 475 (2009) 702.

[12] W.Y. Hernández, O.H. Laguna, M.A. Centeno, J.A. Odriozola, J. Solid State Chem. 184 (2011) 3014.

[13] O.H. Laguna, M.A. Centeno, M. Boutonnet, J.A. Odriozola, Appl. Catal. B Environ. 106 (2011) 621.

[14] H. Liang, H. Yuan, F. Wei, X. Zhang, Y. Liu, J. Rare Earths 29

(2011) 753.

[15] R.J. Farrauto, Y. Liu, W. Ruettinger, O. Ilinich, L. Shore, T. Giroux, Catal. Rev. 49 (2007) 141.

[16] P. Avila, M. Montes, E.E. Miró, Chem. Eng. J. 109 (2005) 11.

[17] E. Tronconi, G. Groppi, Chem. Eng. Sci. 55 (2000) 6021.

[18] C. Ratnasamy, J.P. Wagner, Catal. Rev. 51 (2009) 325.

[19] W.Y. Hernández, M.A. Centeno, F. Romero-sarria, J.A. Odriozola, J. Phys. Chem. C 113 (2009) 5629.

[20] O. Sanz, L.M. Martínez T, F.J. Echave, M.I. Domínguez, M.A. Centeno, J.A. Odriozola, M. Montes, Chem. Eng. J. 151 (2009) 324.

[21] L.M. Martínez Tejada, M.I. Domínguez, O. Sanz, M.A. Centeno, J.A. Odriozola, Gold Bull. 46 (2013) 221.

[22] T.R. Reina, W. Xu, S. Ivanova, M.Á. Centeno, J. Hanson, J.A. Rodriguez, J.A. Odriozola, Catal. Today 205 (2013) 41.

[23] O.H. Laguna, F. Romero Sarria, M.A. Centeno, J.A. Odriozola, J. Catal. 276 (2010) 360.

[24] M.I. Zaki, M.A. Hasan, F.A. Al-Sagheer, L. Pasupulety, Colloids Surfaces A Physicochem. Eng. Asp. 190 (2001) 261.

[25] A. Davydov, Molecular Spectroscopy of Oxide Catalyst, 2003.

[26] P. Nortier, P. Fourre, A.B. Mohammed, J.C. Lavalley, Appl. Catal. 61 (1990) 141.

[27] C. Binet, M. Daturi, J.-C. Lavalley, Catal. Today 50 (1999) 207.

[28] C. Li, Y. Sakata, T. Arai, K. Domen, K. Maruya, T. Onishi, J. Chem.

Soc. Faraday Trans. 1 85 (1989) 1451.

[29] M. Gonzalez Castaño, T.R. Reina, S. Ivanova, M.A. Centeno, J.A. Odriozola, J. Catal. 314 (2014) 1.

[30] J.H. Kwak, R.J. Chimentao, C.H.F. Peden, J. Phys. Chem. C 111 (2007) 2661.

[31] O. Thinon, K. Rachedi, F. Diehl, P. Avenier, Y. Schuurman, Top. Catal. 52 (2009) 1940.

[32] G. Germani, P. Alphonse, M. Courty, Y. Schuurman, C. Mirodatos, Catal. Today 110 (2005) 114.

[33] M.A. Henderson, C.L. Perkins, M.H. Engelhard, S. Thevuthasan, C.H.F. Peden, Surf. Sci. 526 (2003) 1.

[34] W. Ruettinger, X. Liu, R.J. Farrauto, Appl. Catal. B Environ. 65 (2006) 135.

Chapter 6

Understanding the NM role in WGS reaction: Pt vs. Au

Summary

This chapter, divided in three parts, compares the behavior of gold and platinum catalysts in the WGS reaction. The study of the physicochemical properties of supported gold and platinum catalysts on different supports is analyzed in the first part. The correlation of the catalyst UV-Vis features with the WGS activity is specially emphasized. Higher catalytic activities are obtained when the energy levels of the supported noble metal stands closer in energy to the O (2p) levels of ceria, e.g., when the easiness of the electron transfer between oxygen atoms of ceria and the noble metal is higher. The findings in this part reveal some fundamental aspects regarding the correlation of catalyst's electronic properties with its catalytic activity in the WGS reaction. In the second part, structured Pt and Au catalysts are compared. The O_2-assisted WGS reaction was also studied as a possibility to increase the structured catalysts performances. In the last part, *operando* XANES-EXAFS studies were analyzed for both noble metals and the differences observed in the metal dynamics, catalyst structure and oxidation states under WGS reaction conditions discussed.

6.1. Introduction

Although the development of Pt based WGS catalysts is the main focus along this thesis, other noble metals systems are reported as promising candidates for the WGS reaction. Unambiguously, gold gained much attention particularly since Haruta [1] and Huchings [2] separately reported high catalytic activities for small and well dispersed gold nanoparticles in different processes. Andreev's group in the late 1990s presented the very first report on gold based catalysts for WGS reaction employing α-Fe_2O_3 as support [3]. The important activity described for this catalyst, in the low temperature range, where iron oxide is hardly active, was ascribed to specific gold-support interaction in the active sites. Similarly to the platinum based catalysts, several oxides can be found in the literature as supports of the gold catalysts, being the ceria judged as the most appropriate support [4–12]. Similar results were reported by Luengnaruemitchai et *al.* [13] confirming that the catalytic activity strongly depends on the nature of the noble metal and support, with ceria being a better choice for the WGS reaction than iron oxide.

Concerning the nature of the noble metal importance, contrasting results can be found in the literature for Au and Pt. Flytziani-Stephanopoulous [14] found gold based catalyst much active than the platinum based ones, while the platinum based systems in the work of Tibilleti at al. [15] and Luengnaruemitchai et *al.* [13] were two times more active than their gold homologues. In contrast, Jacobs and co-workers [16] claimed that the activity

of the latter is about 20 times higher than that of the Pt catalysts, but ascribed that fact of the non-adequate pre-activation of the Pt sites.

Burch [17] summarizes the advantages and drawbacks of gold catalysts in comparison to their platinum analogs for the WGS reaction. Both noble metals are not pyrophoric, an essential advantage to be employed in practical applications. Gold catalysts can offer some advantages in the low temperature range (180-250 ºC) where the platinum catalysts are insufficiently active. Though, at higher temperatures the reported inherent activity of the gold catalysts is lower than that of properly activated platinum catalysts [18]. Other benefit exhibited by gold is the fact that those samples do not needs pre-treatment while platinum does require a proper pre-reduction. At this point, the capacity exhibited only by platinum (not for gold) to activate water molecules should be highlighted and considered especially when this process is often ascribed as the slowest step of the WGS reaction [18,19].

Furthermore, the debate is not limited only to the intrinsic activity of each metal but also is extended to the active species responsible for the catalysts activity. Once more, there is no consensus and opposite outcomes are reported in the literature. In fact, the active species evolved in the reaction are closely related with the metal particles size and degree of noble metal/support interaction being both features extremely dependent on the catalysts synthesis. For example, for gold based catalysts Flytzani-Stephanopoulos *et al.* [14] claimed that cationic species are the responsible for the high performance of

the gold based catalysts. On the contrary, Rodriguez et al. [20] concluded from XANES and XPS spectroscopies results, the absence of cationic gold in the WGS reaction. Similar controversies on the nature of the oxidation state of active platinum species are reported being both, Pt-O_x or Pt^0 species, reported as active phase [21–23].

Despite of the vast number of published works, platinum and gold ceria based catalysts are still enthusiastically studied and their potential for the WGS reaction keeps appealing the attention of many researchers. In general the diversity of the results concerning these metals is due to the strong influence of several features, such as the choice of precursors, synthesis method, calcination and the activation procedures, noble metal content and operational conditions in which the catalysts are tested [22]. Thereby, notwithstanding the extended number of studies published for gold and platinum WGS catalysts, the scientific community still does not agree on the most suitable noble metal for the processes. A proper comparison between both metals is hardly available especially regarding the use of structured catalysts.

This scarceness is, in fact, even more noticeable considering that the structured catalysts are the logical step for future catalyst implementation on real and portable systems. Farrauto's group provided an intense research concerning the use of structured platinum based catalysts for WGS reaction. The prepared monolithic devices achieve high CO conversions and remain stables during start up and shut-down cycles [18,24–26]. Fiorot et al. [27]

prepared Pt/CeO_2 and Au/CeO_2 monolithic catalysts and compare them with commercial $Cu/Zn/Al_2O_3$. While the commercial catalyst was the most active in the low temperature range, the Pt containing system exhibited comparable activity in the 300-350 ºC one. In all those studies the use of structured catalysts is reported as beneficial for mobile application, however, they are dealing with ceramic monolithic devices. The use of their metallic homologues is not available to our knowledge.

The present chapter is divided in 3 principal parts to shed light on platinum and gold WGS catalysts through their comparison. Along the first part the catalysts were prepared, characterized and tested in the WGS reaction. In the second part, selected catalysts are structured on metallic micromonolithic devices, and examined in classical WGS and in O_2-assisted WGS reaction and finally, a XANES-EXAFS study was carried out, offering results concerning the noble metals dynamics during the WGS reaction. To simplify the measurements and in order to diminish the complexity of the systems, by keeping a similar catalyst nature, gold and platinum catalysts supported on undoped ceria-alumina are chosen for this study.

6.2. Part I: Au and Pt powder catalysts over different supports for WGS reaction

6.2.1. Catalysts preparation

The same synthesis procedure was followed for the supports and the platinum catalysts as described in chapter 2, employing the same precursors and

calcination programs. For CeO_2/Al_2O_3 and $Ce_{0.8}Fe_{0.2}O_2/Al_2O_3$ supports, 20 wt.% of pure ceria or iron doped ceria was supported over high surface γ-Al_2O_3. Regarding the ceria iron mixed oxide, the Ce/Fe molar ratio was 0.8/0.2. The gold was deposited by direct anionic exchange method, assisted by NH_3 using $HAuCl_4$ (Alfa Aesar) as gold precursor [28]. The catalyst was calcined at 350ºC during 4h and 10ºC/min as heating ramp. For both noble metals, the total noble metal (NM) loading was set to 2 wt.%.

The nomenclature chosen for the γ-Al_2O_3, CeO_2/Al_2O_3 and $Ce_{0.8}Fe_{0.2}O_2/Al_2O_3$ supports was Al_2O_3, CeAl and CeFeAl respectively where the oxygen and subscripts were omitted. This terminology was extended to the platinum and gold based catalysts being labeled, for example, when supported over the CeFeAl support, Pt/CeFeAl and Au/CeFeAl respectively.

6.2.2. Physicochemical characterization

6.2.2.1. Chemical composition and textural properties

The chemical composition of the prepared supports is summarized on the Table 6.1. All the systems show close compositions to the targeted ones. Even so, when pure alumina is used as a support, lower noble metal contents are observed pointing out to weaker noble metal support interactions.

Table 6.1. Chemical composition of the prepared materials

Sample	Al_2O_3 (wt.%)	CeO_2 (wt.%)	Fe_2O_3 (wt.%)	Au (wt.%)	Pt (wt.%)
Al_2O_3	100.0	-	-	-	-
CeAl	85.3	14.7	-	-	-
CeFeAl	82.3	15.6	2.1	-	-
Pt/Al	98.4	-	-	-	1.6
Au/Al	98.8	1.2	-	-	-
Pt/CeAl	83.4	14.4	-	-	2.2
Au/CeAl	83.5	14.8	-	1.7	-
Pt/CeFeAl	84.3	12.3	1.3	-	2.1
Au/CeFeAl	81.2	14.9	1.7	2.2	-

Although the ceria introduction leads to improved noble metal support contact, the gold contents are lower than those presented by platinum based catalysts.

The gold deposition, as pointed by Moreau and Bond [29], is strongly influenced by several parameters such as temperature, the supports specific surface area and the pH of the media. Thus, the decrement in the Au loading is probably caused by the basic media employed in the synthesis. In fact, the basic pH imposed during its synthesis is above the isoelectrical point of the ceria support (≈ 7.2) leading to modifications on the ceria surface charges and becoming increasingly more negative. This results in an electrostatic repulsion of gold-containing anions limiting their deposition.

The textural properties of the synthesized materials are presented on Table 6.2. All the samples are mesoporous solids being the textural properties evidently controlled by the γ-Al_2O_3 used as dispersant matrix. The ceria

addition to the γ-Al_2O_3 leads to a diminution on the surface area, pore volume and diameter values. This tendency is more accentuated when iron is incorporated to the supports. Concerning to the noble metal additions, the gold entails an increment of the surface area and pore volume. This effect has been previously explicated by Somorjai et al. [30] claiming that the inclusion of gold nanoparticles in the pore structure would lead to a pore widening and therefore to an increase in the specific surface area. On the contrary, the opposite effect is observed for the platinum-based catalyst pointing to some blocking of the pores by the presence of platinum species.

Table 6.2. Textural properties of the prepared materials

Sample	S_{BET} (m^2/g)	V_{Pore} (cm^3/g)	D_{part} (Å)
Al_2O_3	202	0.49	74
CeAl	186	0.42	69
CeFeAl	175	0.39	68
Pt/Al	192	0.49	70
Au/Al	219	0.56	75
Pt/CeAl	156	0.38	76
Au/CeAl	197	0.45	69
Pt/CeFeAl	170	0.39	69
Au/CeFeAl	184	0.42	69

6.2.2.2. XRD analysis

In the Figure 6.1 are shown the XRD patterns of the employed supports. All the supports present the characteristic diffraction lines of the cubic CeO_2

fluorite structure (JCPDS#00-004-0593) and the γ-Al_2O_3 phase (JCDPS# 00-048-0267). Nevertheless, no diffraction peaks of iron phases are detected either for the small amount of the doping agent or for the possible inclusion of these cations in the ceria lattice resulting in a solid solution formation. Actually, the ceria diffraction peaks of the CeFeAl sample appear shifted toward higher 2θ angles, suggesting the formation of CeO_2–FeO_x solid solution.

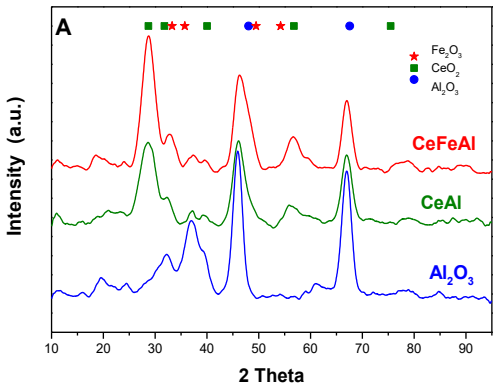

Figure 6.1. XRD diffraction patterns of the prepared supports

In order to confirm the suggested solid solution formation, the lattice parameters of the ceria containing systems were estimated using the main (1 1 1) CeO_2 diffraction line (where no contribution of the γ-alumina phase is observed), the Bragg's equation and the expression that relates the lattice parameter of the fluorite structure with the *d* spacing for cubic structure:

$$a = \frac{\lambda \sqrt{k^2 + h^2 + l^2}}{2dsin\theta}$$

The estimated parameter for the CeAl support was 5.407 Å, being this very close to that reported for bare ceria [31]. Ceria lattice contraction was detected for the CeFeAl support with calculated *a* parameter of 5.395Å. The formation of substitutional Ce–Fe solid solution must result in a lattice contraction for ceria since Fe^{3+} (0.64 Å ionic radius) ions are smaller than the substituting Ce^{4+} (0.97 Å ionic radius) ions. As previously reported for ceria iron mixed oxides [31,32], the formed solid solution can be either substitutional or interstitial, depending on the ceria:iron ratio. Although the solid solution formation is clearly demonstrated, partial segregation of iron species cannot be totally discarded [33] since the small amount of iron limits its detection by XRD.

As a secondary effect of the addition of Fe to the CeO_2 lattice, an increase in the CeO_2 particle size was observed. The ceria crystallite sizes for the CeAl and CeFeAl were estimated by using Scherrer equation as, 21 Å and 37 Å respectively. Therefore, the iron incorporation doubles the ceria crystal size. The XRD diffraction patterns of Au and Pt catalysts are presented in Figure 6.2.a and 6.2.b respectively.

Neither gold nor platinum crystalline phases were observed indicating that both are undetectable by XRD, implying good dispersion and an average crystallite size below 5 nm. Moreover, the lattice parameter of ceria remains unaltered upon the incorporation of the NMs, which indicates that the metallic species are dispersed on the multicomponent support.

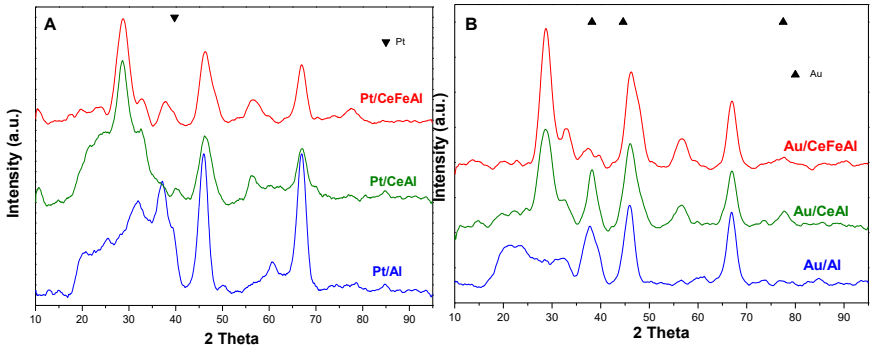

Figure 6.2. XRD diffraction patterns obtained for: a) Pt catalysts; b) Au catalysts

6.2.2.3. UV-Vis and Raman spectroscopies

In order to analyze the electronic properties of the prepared samples, UV-Vis spectroscopy was employed. All the supports presented a broad band, centered at *ca*. 280 nm, associated with CeO_2 and assigned to a charge transfer $O_{2p} \rightarrow Ce_{4f}$ transition. In the case of the CeFeAl support, the absorption bands are wider than those of the CeAl one. This phenomenon is probably due to the contribution of iron oxide absorption features at about 530 nm associated to the d-d transition band of α-Fe_2O_3 [34].

The direct and indirect band gaps of the prepared supports were estimated and the results are listed in the Table 6.3. The direct and indirect band gaps were calculated through extrapolating to zero the energy dependence of the $[(F(R)h\nu]^{1/2}$ and $[(F(R)h\nu]^{2}$ functions, respectively.

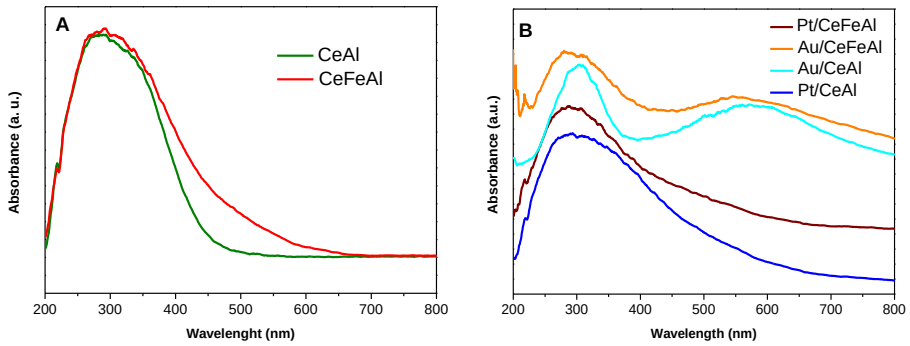

Figure 6.3. UV-Vis spectra obtained for: a) supports; b) catalysts

The CeAl support showed a direct band gap of 3.05 eV in agreement with the results obtained in previous studies for CeO_2-Al_2O_3 systems [35]. The experimental band structure of ceria is described considering the valence and conduction bands resulting from O_{2p} and Ce_{5d} states, respectively, separated *ca.* 6 eV. Between these two bands, a flat Ce_{4f} band appears. For defect-free crystals, the latter is empty and lies around *ca.* 3 eV above the valence band, but if it becomes partially occupied, the energy separation with the valence band decreases [36]. This description results in a fairly localized picture of the 4f electrons that remain on the cerium ions resulting in Ce^{3+} ions. The measured band gap for our ceria sample is smaller than that found in ceria single crystals [37] .

Table 6.3. Ceria direct and indirect band gap energies

Sample	Direct band gap (eV)	Indirect band gap (eV)
CeAl	3.05	2.80
CeFeAl	2.93	2.45
Pt/CeAl	2.94	2.12
Au/CeAl	2.97	2.90
Pt/CeFeAl	2.79	2.26
Au/CeFeAl	2.11	1.50

This red-shift band gap has been previously observed for ceria nanoparticles being dependent on the particle size [38]. The reason for this shift must be associated to the higher Ce^{3+} to Ce^{4+} ratio on decreasing the particle size [39,40].This implies that a decrease in the band gap energy should be observed when the Ce^{3+} surface population increases. This reduction is related to the concentration of the defect states associated with Ce^{3+} ions and oxygen vacancies. The presence of partially reduced ceria could indicate rearrangements of the ceria band gap structure and the degree of oxygen vacancies formation. On increasing the 4f level population, as a result of the increase in the defect concentration, a decrease in energy reducing the band gap is detected.

Regarding the CeFeAl sample, an additional ceria band gap decrease was observed, in concordance with previous results reported in literature [41,42]. However, the average crystallite size does not follow similar trends, either a decrease [11], an increase [43] or even no effect [44] in the crystallite size

has been reported on increasing the doping of ceria with iron. Therefore, the band gap modification upon doping ceria with iron cannot be associated with a size effect, but to a modification of the solid solution electronic structure.

To elucidate the primary reason for the band gap modification, further investigation by Raman spectroscopy of the CeAl and CeFeAl samples was carried out (Figure 6.4).

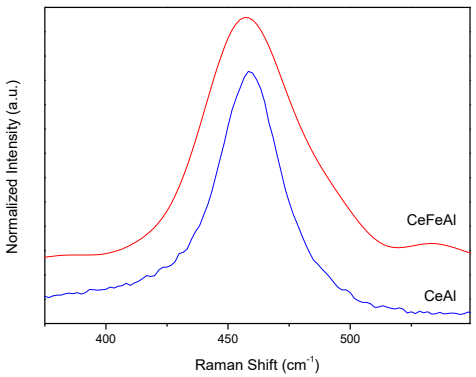

Figure 6.4. Raman spectra obtained for the synthetized supports

Pure CeO_2 exhibits a peak at 458 cm^{-1} according to its Raman active F_{2g} mode and attributed to the oxygen symmetric breathing vibration around Ce^{4+} [43–45]. The introduction of Fe^{3+} cations into the ceria lattice and the change of the crystallite size, among other factors, could generate symmetry distortions resulting generally in broadening and/or shift of the F_{2g} Raman signal [46]. Theoretically, an increase of the crystallite size should broaden and shift the band to higher wavenumbers [47] and the strong interaction between Ce and Fe should shift the same band on the opposite direction. Considering that the

particle size of the CeO_2 increases when the Fe is incorporated, as detected by XRD, a shift to higher wavenumbers is expected. However, a shift to lower wavenumbers and broadening of the F_{2g} Raman signal are observed and associated with the introduction of Fe^{3+} cations into the ceria lattice. The detected modifications in the shape of the F_{2g} signal evidence the Fe–Ce interaction in the doped systems [48] and suggest its primary role of the electronic properties modification. The distortion of the cubic lattice induced by the formation of the solid solution must be related to the changes in the population of the oxygen vacancies in the material and therefore, with the electronic properties [49].

Popovic et al. [49] report the Raman study of a set of iron-doped ceria nanocrystals, $Ce_{1-x}Fe_xO_{2-y}$ (x = 0, 0.06, and 0.12). Softening and broadening of the Raman F_{2g} mode as a function of dopant oxidation state allow the authors to propose not only the presence of highly localized *4f* electrons in Ce^{3+} ions but also electron delocalization through Ce(Fe)-O(V_O)-Ce(Fe) orbitals, in highly deficient Fe-doped solid solutions. This electron delocalization results in a split of the *4f* band inside the ceria band gap in such a way that the $4f^1$ band overlaps with the *O2p* band. This way, the $4f^0$ band is situated inside the band gap resulting in a band gap decrease with respect to the undoped ceria support. For n-type semiconductors as ceria, the band gap energy value evidences the position and the donating properties of the valence band and can be used as a measure of the basicity of the solid [35,42]. Therefore, the lower the band energy value the higher the easiness of donating electrons.

Coming back to the UV-Vis of the NM containing samples, the spectra obtained for Pt and Au ceria based catalysts are shown in Figure 6.3.B. Collective oscillation of the conduction electrons stimulated by the incident light are responsible for the broad absorption band in the 500-600 nm range (plasmon resonance absorption) observed in all the prepared gold catalysts. The size and shape of the metallic particles, as well as the dielectric properties of the support influences the intensity and position of the gold plasmon [50]. As the gold particle size is below 5 nm (as indicated by XRD) and remains approximately constant upon iron doping with ceria, the observed slight shift in the position of the plasmon maximum must be ascribed to the presence of iron. This iron presence favors the delocalization of the cerium $4f^1$ electrons through Ce(Fe)-O(V_O)-Ce(Fe) orbitals modifying the electronic density of gold as well as the dielectric properties of the iron-doped support. Besides this, both Au and Pt reduce the supports band gap, Table 3, suggesting the insertion of NM levels between the valence and conduction bands of ceria [40]. Recently, it has been proposed that oxygen vacancies in ceria may cluster [51]. The groups of exposed Ce^{3+} ions in these clusters would become a potent surface site for catalysis, as adsorbed gases or reaction intermediates could interact simultaneously with several Ce^{3+}. The interaction of these surface clusters with gold atoms results in a strengthened Au adsorption ions [52]. In this gold adsorption, the role of Ce 4f states is of paramount importance. The partially occupied *f* states of reduced cerium ions, resulting from the removal of oxide ions, act as an electron donor stabilizing the

adsorbed Au atoms. This donor-acceptor concept implies that Ce^{3+} ions are re-oxidized and gold atoms become reduced generating an ionic bonding between negatively charged gold atoms and the surrounding cerium atoms [53]. DFT studies of the Pt/CeO_2 interface showed a similar picture to that shown by gold atoms adsorbed on ceria. Platinum atoms sit on oxygen vacancies acting the partially filled *f* states of Ce^{3+} ions as donors and *5d* states of Pt as acceptor levels [54]. Our HAADF-STEM data, Figure 6.5.A, shows that gold nanoparticles sit always on iron-doped ceria nanoparticles supporting the NM-ceria interaction.

The band gap observed for the Au catalyst is lower than the one estimated for the Pt one, Table 6.3, which can be explained on the basis of the electronic structure of both catalysts. The presence of metal induced gap states (MIGS) is the result of the interaction between the NM and the iron-doped ceria surface. The ionic interaction between the negatively charged NM atoms and the surface vacancy clusters results in overlapping of Pt 5d states with the O 2p states, while Au 5d states lies in between the O 2p and Ce 4f levels. Whatever the MIGS configuration, accommodation of the extra electrons would result in the transfer of electronic density from the Ce(Fe)-O(V_O)-Ce(Fe) ensemble to the NM being the negative charge on platinum higher than the one supported by gold.

6.2.2.4. CO chemisorption and HR-TEM microscopy

In order to ascertain the platinum dispersions and determine the metal particle sizes, CO chemisorption measurements were carried out for Pt/CeFe sample. CO chemisorption experiments showed a Pt dispersion of 70% for the platinum fresh catalyst corresponding to Pt nanoparticles of 2.2 nm when assuming a cuboctahedral particle shape. The obtained platinum particles size fitted well with the crystallites size obtained by HR-TEM microscopy (Figure 6.5.B).

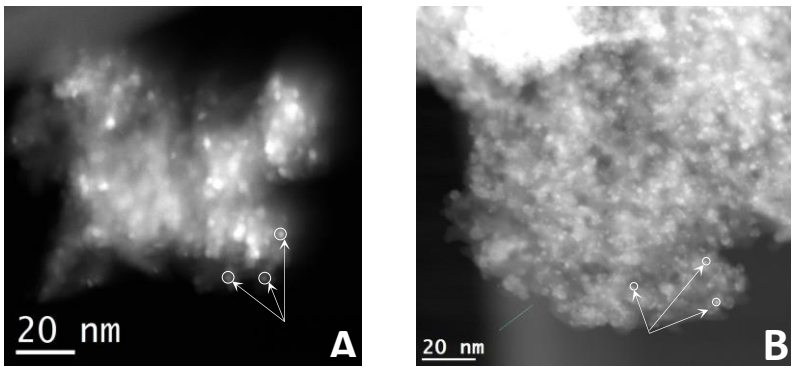

Figure 6.5. HR-TEM microphotographs obtained for a) Au/CeFeAl and b) reduced Pt/CeFeAl

For comparison the HR-TEM study of the Au/CeFeAl catalyst indicates gold particle size around 4 nm with an estimated dispersion around 37%. HAADF analysis confirmed also an intimate contact between NM and iron doped ceria support both metals are always associated with Ce and Fe on the surface.

As stated in a previous work [55], the average particle size of gold nanoparticles after WGS reaction remains constant while platinum nanoparticles sinter upon reaction resulting in dispersion of 28 % which correspond to an average particle size of 5.8 nm. Platinum sintering during the WGS reaction was also observed by Farrauto's group [56] reporting values for pre- and post- reaction particles size quite similar to those of our Pt/CeFeAl sample. Once used, the platinum catalyst stabilized its particle size and dispersion in a similar range to that of gold catalysts, and so, any effect on the differences in activity between both NM associated to particle size and/or dispersion might be discarded.

6.2.3. Catalytic activity

The catalytic tests were carried out at GHSV=4000 h^{-1} employing a catalyst bed volume of 1.5 cm^3. All the solids were pilled, milled and the $600<\phi<800$ fraction retained. Pt based catalysts were activated during 2h at 350ºC in a H_2 stream (10% vol.) while a pretreatment was not necessary for the gold based samples.

The WGS shift behavior of all platinum and gold based catalysts was evaluated and the results are presented on Figure 6.6.A. Both, gold and platinum based catalysts exhibit different conversion trends no matter the support. The NM-supported catalysts on bare Al_2O_3 show the lowest conversion for both metals confirming the strong influence of the support nature on the catalytic properties. It should be highlighted the different

catalytic performances observed for alumina based catalysts: while the Au/Al is poorly active, the Pt/Al catalyst reaches the equilibrium conversion at around 310 ºC.

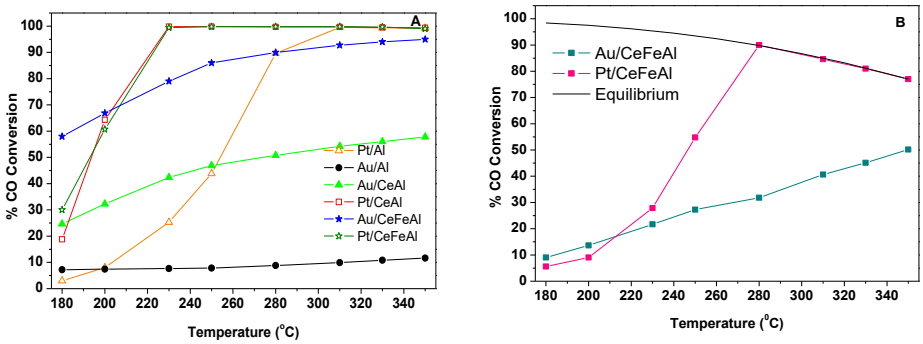

Figure 6.6. Catalytic activity obtained for the prepared catalysts a) Model Conditions and b) Real conditions

Besides this, the ceria addition to the support causes noticeable catalytic improvements for both catalysts. The same catalytic tendency as a function of the support is observed for both noble metals: CeFeAl > CeAl > Al_2O_3. Nevertheless, two temperature ranges of operation could be discerned. The gold systems are always more actives than their respective platinum homologues at lower temperatures being the latter superior at higher temperatures. By comparing the observed catalytic activities, it may be stated that the support nature has a stronger influence on the gold catalysts than on the platinum ones. In this context, it is worth to note that at low temperatures, gold catalysts are always more active than the corresponding platinum catalysts, but the reverse is true for temperatures above 200 °C.

Generally, the NM based catalysts supported on CeO_2 or ceria mixed oxides are often described in the literature as very efficient systems [17,57]. These systems show enhanced activities with respect to the bare alumina catalysts, usually attributed to fast Ce^{4+}/Ce^{3+} redox cycles that results in the promotion of the WGS reaction redox mechanism. In the regenerative redox pathway, the CO is adsorbed on the metal surface and oxidized by oxygen species proportionated by the support resulting in the CO_2 product and in an oxygen vacancy generation on the support surface. The oxygen vacancy is replenished through water dissociation with OH groups associated to oxygen vacancies.

So, the role of the noble metal should be to adsorb and activate the CO molecules and to create oxygen defects on the NM-support interface. From microkinetic studies, carboxyl intermediates have been proposed as the main intermediates through which the WGS reaction happens. This pathway implies a nucleophilic attack from OH species to the activated CO leading to carboxyl species formed on active metal surface. The carboxyl decomposition has been proposed for Au/ceria catalysts as responsible for CO_2 evolution as the simplest and most possible reaction pathway [58]. In contrast, Rodriguez et *al.* [59] proposed carbonates and bicarbonates as major reaction intermediates.

Therefore and considering that both noble metals are able to adsorb and activate the CO molecules the main dissimilarity between them may reside on water dissociation step, which cannot be performed by the gold nanoparticles

itself, an interface metal/support is required for this step. On the contraty, platinum is able to activate water species and there, the water dissociation can be carried out either on the support or on the metal. DFT calculations have found that water dissociation is highly endothermic on Au (111) and slightly endothermic on Pt (111) [60]. For that reason, the influence of the support nature in the WGS activity of gold catalysts might be far more important than for platinum based ones [46,56]. The catalytic activity observed in our alumina samples clearly sustain the commented platinum capacity to dissociate water, reaching the equilibrium conversions without the help of the support redox properties and oppositely to Au/Al sample. Nevertheless, the ceria incorporation to the platinum catalysts markedly shift to lower temperatures the achievement of equilibrium conversions implying that, an adequate support is also necessary but not obligatory for platinum samples to attain good WGS behaviors.

From the above commented WGS results tested in model mixture, only the CeFeAl supported systems were chosen to be submitted to WGS real conditions, e.g. in presence of H_2 and CO_2, being the inlet composition 50% H_2, 9% CO, 11% CO_2 and 30% H_2O (Figure 6.6.B). Both activity curves show a shift to higher temperatures with respect to those obtained under model conditions, as expected on the bases of Le Chatelier's principle. Again, a superior catalytic behavior was presented by Pt/CeFeAl respect to its gold homologue. Actually, the Pt/CeFeAl sample reaches the equilibrium

conversion at 280 ºC and the gold based system does not arrive in the whole temperature range.

The WGS behavior obtained in real conditions could be explained again considering the water activation capacity. In the case of gold catalysts where the water is only dissociated into the metal/support interface, in H_2 absence water molecules are able to reoxidize the partially reduced support thus closing the catalytic redox WGS cycle. However, it is possible that in such reductive atmosphere the water is not able to accomplish the reoxidation in an effective way resulting in decrease in the WGS activity. The unaltered catalytic activity exhibited by Pt/CeFeAl catalyst should be then associated to its water dissociation capacity and low necessity of support state to accomplish the process.

The WGS specific reaction rates (expressed in $molCO_{conv} g \cdot metal^{-1} \cdot s^{-1}$) at two different temperatures are calculated for the prepared materials in model conditions and presented in Table 6.4. As expected, the gold based catalysts present better catalytic performances when compared to the platinum samples at low temperature, revealing its superior performance in this temperature range. On the other hand, platinum catalysts take the advantage at 250 ºC. For both noble metals, the catalytic properties improvement was detected with ceria incorporation to alumina being even more pronounced with iron addition.

Table 6.4. WGS specific reaction rates ($molCO_{conv} g^{-}metal^{-1} s^{-1}$) of the prepared solids

Sample	$Rate_{180^oC}$ x 10^5	$Rate_{250^oC}$ x10^5
Pt/Al	0.61	8.95
Au/Al	2.07	2.25
Pt/CeAl	2.92	15.54
Au/CeAl	4.91	9.34
Pt/CeFeAl	4.71	15.69
Au/CeFeAl	8.94	13.26

In order to confirm the specific rate results, in the Table 6.5 the turnover frequencies (TOFs) are summarized in the same two temperatures for model and "real" WGS conditions. The platinum sintering observed from CO chemisorption measurements was also considered and for this NM, the TOFs values for fresh and post reaction catalysts are presented. As a general remark, no matter the support, the gold based catalysts behave always better at the lowest measured temperature (180ºC), and the platinum based catalysts takes the advantage at temperatures above 250ºC.

Table 6.5. Turnover frequencies (s^{-1}) of the Pt/CeFeAl and Au/CeFeAl

	TOF_{180^oC} x10^2	$TOF^*_{180^oC}$ x10^2	TOF_{250^oC} x10^2	$TOF^*_{250^oC}$ x10^2
Pt/CeFeAl	1.31(3.29)	0.49(1.14)	4.37(10.9)	4.8 (11.2)
Au/CeFeAl	5.33	1.71	7.92	5.18

**values corresponding to the realistic conditions*
() values corresponding to sintered catalysts

Confirming the specific rate trend, the TOF values for model mixture for the catalysts at 180 ºC show the superiority of gold sample. However, at 250 ºC the platinum based catalysts doubled the TOF obtained for gold system with a similar dispersion, thus converting platinum in better choice in this temperature range. When the mixture is changed to realistic the difference between the gold and platinum at low temperature significantly decrease converting the platinum catalyst in the logical choice in the whole temperature range for these conditions. The evaluated gold-based catalysts presented higher CO rates and turnover frequencies at 180ºC than some well referenced Au/CeO_2 and Au/CeO_2-MO_x systems tested in the same conditions [61,62]. Regarding the Pt samples, the specific reaction rates of our Pt based materials are superior compared to the results obtained by the group of Efstathiou using a similar WGS inlet stream [63].

Stability test in which the stream composition was varied from model to real stepwise was carried out over the Pt/CeFeAl and Au/CeFeAl samples (Figure 6.7). For both catalysts, two different temperatures were chosen in order to keep the same initials non equilibrium CO conversion with the purpose to discern the causes of catalyst's behavior changes. In the case of Au/CeFeAl catalyst, the initial temperature (280 ºC) was maintained constant during all the experiment and, in the last step the GHSV was reduced by half. For Pt/CeFeAl sample, the initial temperature of 220 ºC was kept during the experiment, excepting the last step, where the temperature was increased to 280 ºC.

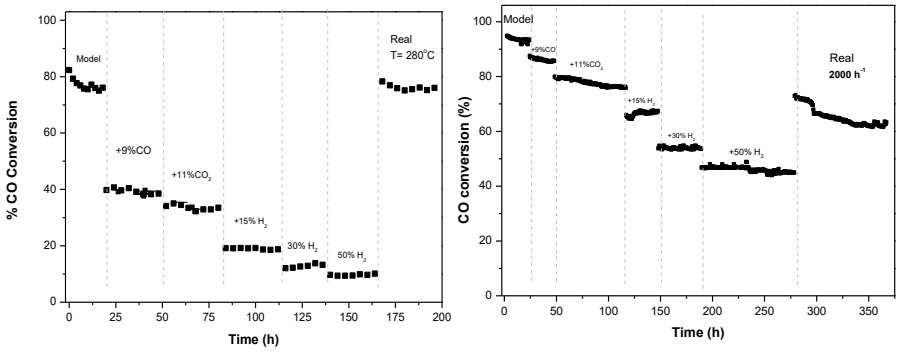

Figure 6.7. Stability test step by step from model to real at 4000h^{-1} for: a) Pt/CeFeAl and b) Adapted from Au/CeFeAl

Regarding to the catalysts stability, the Au/CeFeAl presents slight and continuous decline of the catalytic activity with time on stream being especially accentuated under complete real conditions and 2000 h^{-1}. On the other hand, the Pt/CeFeAl presents better stability in the final stage with no indications of catalyst deactivation in time on stream. Once the real mixture fed and temperature increased to 280 ºC, the catalyst exhibits CO conversion values around 80% corresponding of approximately 10% of CO conversion lost in respect to the conversion observed in the primary light off test (Figure 6.6.B).

The influence of the gas stream composition, on the other hand, provides significant dissimilarities depending on the noble metal nature. The Au/CeFeAl exhibit a progressive diminution of the catalytic activity when the feed stream is changed stepwise from model to real mixture being the

decrement more emphasized when H_2 is incorporated. The latter in concordance, with the Le Châtelier principle and with the above mentioned inability of the support to activate water molecules in H_2 presence.

Contrary to the Au based sample, its Pt homologue shows a significant decrease of the catalytic activity when the inlet CO concentration increases from 4.5 % to 9 %. This different behavior could be directly related to the different CO adsorption capacities of both metals. The CO adsorption strength can be associated to the sample's band gap model (Table 6.3). Whereas the support band gap correspond to the energy difference between the O(*2p*) and the localized Ce(*4f*) states, the catalyst band gap should account for the difference in energy between the NM 5d states and the 4f levels of cerium. The catalytic activity of the samples is a function of this band gap, in such a way that the higher the band gap the higher the activity. The higher band gaps energies exhibited by the Pt/CeFeAl vs. the Au/CeFeAl suggests that the platinum 5d states fall closer to the O(*2p*) band which implies an easier electron transfer between oxygen atoms of ceria and the NM and therefore, this excess electron density weakens the CO bond strength through back-bonding and facilitates the formation of the reaction intermediates. However, the stronger Pt-CO interaction appears to hinder excessively the CO_2 desorption processes and leads to lower catalytic activities when the CO concentration is increased.

6.2.4. Partial conclusions

Platinum and gold metals were supported on different oxide materials and the resulted catalysts characterized and tested in WGS conditions. From the characterization results, high surface areas were obtained in all the solids. Besides, the desired solid solution formation for CeFeAl was achieved and observed by XRD, UV-Vis and Raman spectroscopies.

The catalytic test reveals enhanced performances, for both noble metals, when ceria was incorporated to the support being those improvements more emphasized when iron was used as doping agent of ceria. The advantages obtained from the iron incorporation were reflected on an enhanced catalytic activity. The improvement of the catalytic behavior of the catalysts was directly related to the electronic properties modifications achieved through solid solution formation and reflected on the band gap energies changes in a way that: higher the band gap higher the activity.

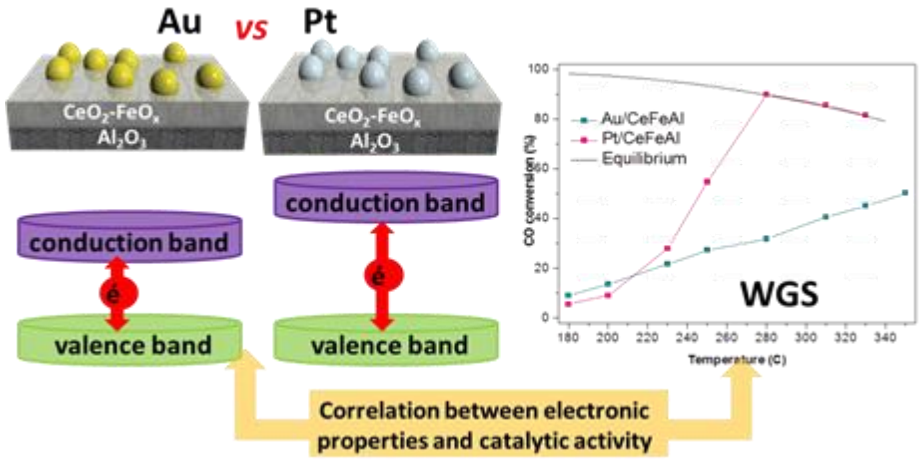

Figure 6.8. Catalytic behavior and electronic properties relationship. Adapted from [12]

No matter the stream composition, the gold based catalyst present superior activity at 180ºC, shifting its operation window to the lowest temperature range. Nevertheless, the platinum based systems are much more versatile since they are able to withstand changes in the stream composition with higher TOF than its gold homologues and attained the equilibrium conversion at temperatures close to 250ºC.

6.3. Part II: Au/CeFeAl and Pt/CeFeAl catalysts supported on metallic micromonolithic devices

Along the second part, the catalytic activity of selected Au and Pt ceria based catalysts was studied in structured systems. The deactivation effects are also

considered. Several deactivation processes were reported for ceria based catalysts, more precisely, the over-reduction of ceria and the formation of carbonaceous species blocking the catalysts' active sites are the most frequents phenomena leading to activity depletion [4,26,64–67]. Although the catalytic performance can be almost fully recovered by O_2/air treatment, such a thermal procedure is not suitable during continuous operational conditions [4,68,69]. On the other hand the addition of small quantities of oxygen within the WGS stream could be beneficial to mitigate the deactivation effects: the as called O_2-assisted WGS. This oxygen introduction should extend the catalytic life-time leading to highly active and stable WGS catalysts. In the literature, most studies related to O_2-assisted WGS concerns the bimetallic Cu-based catalysts. Some promising results were published by Kughai et *al.* [69] for bimetallic Pt-Cu/Ceria catalysts. This system remarkably enhances the H_2 yields with the addition of oxygen, due to the fast CO oxidation to CO_2 and liberation of the exposed metallic active sites, resulting in higher catalytic activity per site. The O_2-assisted WGS reaction over Au/ceria and AuCu/ceria based catalysts was also studied by Gamboa-Rosales et *al.* [68] affirming that the water dissociation is favored by the O_2 presence and highlighting the influence of the synthesis method on the gold catalysts performance. The group of Flytzani-Stephanopoulos also studied the Au and Pt powder catalysts in the O_2 assisted WGS suggesting that for both metals, the active sites were nonmetallic particles but oxidized metal species [4]. However in the scientific

literature the effect of O_2 on the WGS performance of structured catalysts, to the best of our knowledge, were not published.

Then, this study is focused on the application of platinum and gold based structured catalysts in the WGS reaction aiming to overcome the reactor volume restrictions associated to the shift process in conventional packed bed reactors and taking advantage of the excellent mass and heat transfer properties provided by the structured systems. The effect of the structuring process on the powder catalysts is also a subject of this study. Moreover, the influence of the oxygen on the catalytic performance of both systems is studied and correlation of this behavior to the metal nature, catalyst state and/or reaction conditions are proposed. For that purpose, gold and platinum were supported on iron-doped ceria mixed oxide. The obtained catalysts were standardly characterized and supported on metallic micromonolithic devices through the washcoating method. The employed slurries were dried, calcined in the same conditions as the parent catalysts and then, characterized and tested in WGS conditions in order to detect any possible modifications induced on the initial catalysts during the washcoating method.

6.3.1. Experimental

The same ceria – iron mixed oxide, $Ce_{0.8}Fe_{0.2}O_2$, was supported on γ-Al_2O_3 dispersant matrix being the nominal chemical composition and the preparation method also maintained as described in section 6.2.1. 2 wt.% of platinum and gold were deposited on this support. The Pt catalyst was prepared keeping the

same synthesis method detailed on the section 2.xx but in this case, the gold catalyst was synthetized by precipitation with K_2CO_3. Similarly, the obtained support was labeled CeFeAl and the powder catalysts Pt/CeFeAl and Au/CeFeAl, respectively.

The metallic micromonolithic devices and the slurry preparations were also prepared as explained in the Chapter 4, section 4.2. Once dried and calcined, the suspensions were called S_Pt/CeFeAl and S_Au/CeFeAl. The washcoating process was repeated till 1 g of each catalyst was deposited on the metallic substrate. The structured catalysts were labelled M_Pt/CeFeAl and M_Au/CeFeAl (where the "M" stays for micromonolith).

Concerning the catalytic tests, the same GHSV=4000 h^{-1} was kept for all performed experiments. The powder samples were tested by employing catalyst volume of 1.5 cm^3 and $600<\phi<800$ μm. The WGS tests for the structured catalysts were performed in different stream composition, e.g. model mixture, O_2-assisted model mixture, real mixture, O_2-assisted real mixture and total CO oxidation mixture (TOX) reaction. The inlet compositions used for each experiment are summarized on Table 6.6.

The platinum based catalysts were pre-activated during 2h at 350ºC in 10 vol.% H_2 meanwhile the gold catalysts were not treated prior the reaction. All the catalytic data are presented in CO conversions terms.

Table 6.6. Experimental conditions of the catalytic tests

	Model	Real	O_2-Model	O_2-Real	TOX
CO (vol%)	4.5	9	4.5	9	4.5
H_2O (vol%)	30	30	30	30	-
CO_2 (vol%)	-	6.3	-	6.3	-
H_2 (vol%)	-	50	-	50	-
N_2 (vol%)	Balance	Balance	Balance	Balance	Balance
O_2 (vol%)	-	-	-	0.7	0.7

6.3.2. Physicochemical characterization

6.3.2.1. Chemical composition and textural properties

The chemical composition of the prepared solids is summarized in Table 6.7.

All the samples presents very close composition to the targeted one.

Table 6.7. Chemical composition and textural properties of the synthetized solids.

	Al_2O_3 (wt. %)	**CeO_2 (wt. %)**	**Pt o Au (wt. %)**	**Fe_2O_3 (wt. %)**	**S_{Bet} (m^2/g)**	**V_{Pore} (cm^3/g)**
Al_2O_3	100	-	-	-	202	0.36
CeFeAl	78.9	18.9	-	2.2	172	0.38
Au/CeFeAl	77.9	17.8	2.6	1.7	182	0.40
S_Au/CeFeAl	80.2	16.2	2.3	1.3	185	0.41
Pt/CeFeAl	76.3	19.3	2.3	2.1	175	0.38
S_Pt/CeFeAl	78.1	17.7	2.2	2.0	181	0.40

The observed variations from the catalysts to slurries composition were expected because of the addition of colloidal alumina during the washcoating process, which increases the total alumina content and as a consequence decreases the contribution of the rest of the components.

Textural properties of the synthetized samples are also presented in Table 6.7. Compared to bare γ-Al_2O_3, the ceria iron mixed oxide deposition decreases the specific surface area and increases the pore volume of the samples. Pt/CeFeAl and Au/CeFeAl showed intermediate values of surface area between alumina and CeFe/Al solids. However, opposite trends are observed for pore volume being increased those of gold catalyst and decreased that of platinum. The increased values for both area and pore volume for the slurries, in comparison to their corresponding support, are directly related to the use of Nyacol colloidal alumina during the slurries preparation. Despite of the detected textural variations, in general terms the textural properties are ruled by the presence of γ-Al_2O_3. Actually, the obtained values are in a good agreement with the theoretical ones when calculated supposing a physical mixture.

6.3.2.2. XRD analysis

XRD patterns obtained for the obtained solids are presented in the Figure 6.9. All the samples show typical diffraction lines pertaining to γ-Al_2O_3 (JCDPS# 00-048-0267) and CeO_2 (JCPDS#00-004-0593) oxides. For the CeFeAl system, no diffraction peaks are detected for iron species. The absence of the

signal could be due either to the small iron amount within the sample (around 2 wt.%) or to its amorphicity. Slight shift of the main ceria diffraction line (111) to higher 2θ angles is observed. This shift probably accounts for the lattice contraction occurring when the lower ionic radii cation (Fe^{3+} species) substitutes the higher ionic radii species (Ce^{4+}). Therefore, the solid solution formation could be suggested being formed either through the replacement of some ceria cations by iron or through the interstitial iron species disposition in intimate contact with ceria within the lattice.

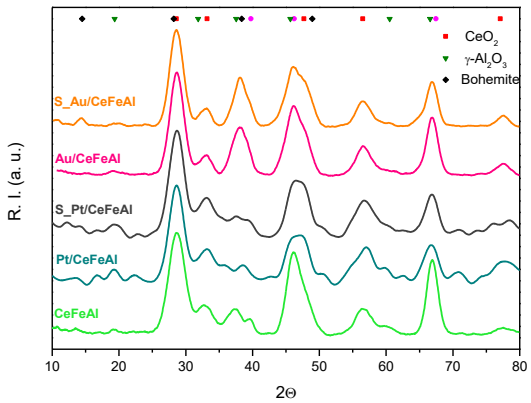

Figure 6.9. XRD diffraction patterns of the prepared solids

Although the gold species are hard to detect in the presence of γ-Al_2O_3 due to the fact that its amorphicity hinders the proper gold diffraction lines identification some changes of the relative intensities are detected. The relative increase of the alumina diffraction line at around $2\theta = 39^{o}$ suggests the presence of gold particles superior in size to the XRD detection limit. The most intense line of gold (111) should appear at $2\theta = 38^{o}$ which could provoke the observed change in relative intensity of the alumina contribution.

As for the platinum species, no typical diffraction lines are detected, neither for Pt/CeFeAl nor for S_Pt/CeFeAl.

On the other hand, the slurries exhibit very similar profiles when compared to the parent samples indicating that no important structural modifications occur on the catalysts. For both slurries, S_Pt/CeFeAl and S_Au/CeFeAl, diffraction lines pertaining to γ-Al_2O_3 (JCDPS# 01-083-2384) phase can be discerned being the latter attributed to the boehmite phase present in the colloidal alumina employed during the preparation.

The XRD obtained for both faces of the gold micromonolith are presented in Figure 6.10.

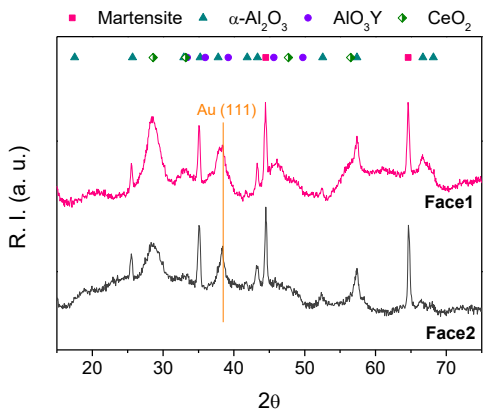

Figure 6.10. XRD diffraction obtained for the gold based micromonolith

On first place the diffraction lines pertaining to the ferritic stainless steel after the oxidative pretreatment could be detected. The γ-Al_2O_3 and CeO_2 phases can be also discerned accounting for the supported catalyst on the micromonolith. Besides, the main diffraction line characteristic of metallic

species was roughly detected indicating that gold sintering may happen during the structuring process.

6.3.2.3. SEM analysis and adherence test

Regarding all structured catalysts, the adherence test results at around 96% of catalyst weight preservation after the test. The homogeneity of the catalytic layer was confirmed by SEM imaging. A selected microphotograph of the M_Au/CeFeAl structured catalyst is shown in Figure 6.11.a in front section and on Figure 6.11.b, in a cross section imaging. The α-Al_2O_3 layer generated during the pretreatment of the bare Fecralloy monolith has a needle-like structure [70] and acts as ideal surface to anchor and disperse the catalyst.

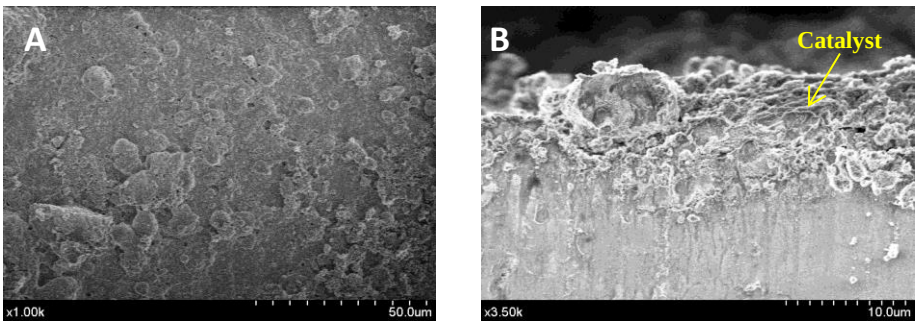

Figure 6.11: SEM microphotographs of the M_Au/CeFeAl catalyst: a) front microphotgraph; b) cross section micrograph.

As shown in the figures, the catalytic layer is perfectly settled on this oxide film with assured homogeneity by the alumina layer. The estimated theoretical layer thickness of around 8,6 μm appears to be in a good concordance with the layer thickness observed by SEM (7,5-10 μm). Assuming a perfect and homogeneous coating the theoretical layer thickness

was obtained from the estimation of the volume of the coating. For this purpose, the total area of the microchannels (60 cm^2), the mass of the coverage (1000 mg), the pores volume of the dried slurry (0.41 cm^3/g) and the apparent density of the deposited solid (5.9 g/cm^3) were considered as recently reported elsewhere [71]. From the layer thickness estimation, the average particle size could be calculated by supposing spherical particles deposited onto the micromonolithic devices using the following equation: $L = d_p/6$ where L is the layer thickness and d_p is the particle diameter [43]. In our case the particles deposited into micromonoliths, present an average particle size around 52 μm.

6.3.4. Catalytic behavior

The catalytic data obtained for Pt/CeFeAl and Au/CeFeAl catalysts in "model" mixture WGS at GHSV=4000h^{-1} are presented in Figure 6.12. Although the Au/CeFeAl reaches the equilibrium conversion at the highest temperature, the Pt/CeFeAl presents substantially better catalytic behavior reaching the equilibrium CO conversion at 230 ºC. Moreover, the different activity profiles showed by both catalysts indicate dissimilar kinetics and reaction pathways for both studied systems.

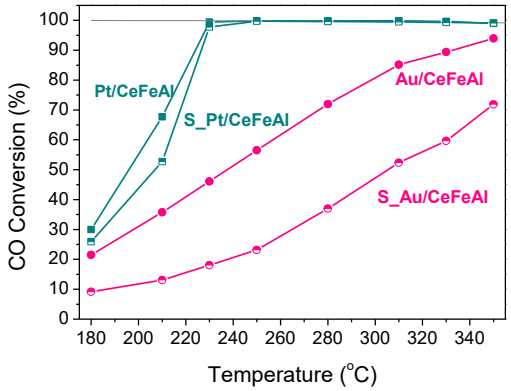

Figure 6.12. CO conversions in obtained for the prepared powder samples in model conditions

The catalytic behavior of the slurries, S_Pt/CeFeAl and S_Au/CeFeAl, was also examined in the same reaction conditions. Both showed lower catalytic performances in respect to the parent catalysts, being the observed decrease for S_Au/CeFeAl substantially more important than that presented by S_Pt/CeFeAl sample. Indeed, the platinum based micromonolith reaches the equilibrium conversions, at the same temperature - 230 ºC. The catalytic activity decrease was, in turn, expected and attributed to the NM content diminution within the slurries confirmed by μ-FRX. However, the significant catalytic lost presented for the gold slurry could be attributed on first place to the different method of preparation of the catalysts and to the increase of the gold particle size, as suggested by the XRD analysis (Figue 6.12).

The catalytic performance of the structured catalysts in model WGS reaction is summarized in Figure 6.13. When structured in micromonoliths, both noble

metals present worse catalytic activities than the corresponding slurries, being especially affected the M_Au/CeFeAl sample. The decrease of the activity observed for the structured catalysts in comparison to the fixed bed powder reaction could be related on first place to the different particle size employed in powder (600-800 μm) and in structured catalysts (52 μm) and as a consequence the different residence time of the stream during the reaction. The latter reduces the CO conversion all over the tested temperature range with 30% maximum CO conversion achieved at 350ºC. A shift to higher temperatures is also observed for the platinum structured catalyst achieving equilibrium CO conversions at higher temperatures. In this WGS conditions, the M_Pt/CeFeAl exhibits superior catalytic performances than the corresponding M_Au/CeFeAl.

The incorporation of minor O_2 amounts to the model WGS feed stream (O_2-assisted WGS reaction) provides interesting and noteworthy changes on the activity for both catalysts, Figure 6.13. Although the oxygen addition provides enhanced WGS performances for both M_Au/CeFeAl and M_Pt/CeFeAl systems, the increase of catalytic activity for gold is much higher than the one presented by platinum catalyst. Indeed, the gold micromonolith becomes markedly active in the lower temperatures range, reaching 80% CO conversion at 180 ºC *vs.* 40% for platinum based catalysts.

Given the well-known activity of gold nanoparticles for the CO oxidation, it could be argued that the observed promotional effect is a mere coupling of

WGS and CO oxidation reactions acting together to abate CO. In this context, the CO oxidation reaction was carried out for both noble metals employing the same CO/O_2 ratio used in the O_2 assisted WGS reaction. Both catalysts show the maximum possible CO conversion (above 30%) in the whole temperature range, stoichiometrically limited by the added O_2 amount (0.7%). It should be noted that the conversion obtained in CO oxidation is exactly the enhanced effect obtained for the M_Pt/CeFe when O_2 is added to the WGS feed stream at 180ºC with respect to direct WGS.

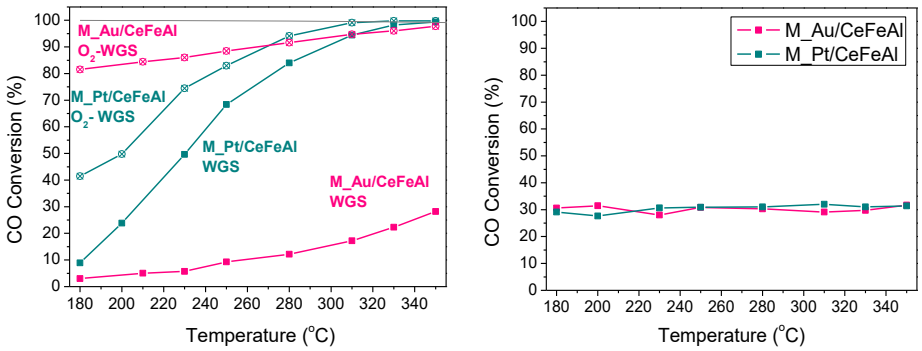

Figure 6.13. CO conversions in obtained for the micromonolithic structures in: a) model and O_2-model; b) TOX

In agreement with Duprez et *al*. [72], the observed catalytic activity improvement appears to be uniquely due to an additive effect of both, WGS and total CO oxidation reactions. Therefore, in the case of Pt the beneficial effect of oxygen is not exactly an O_2-assisted WGS but rather the result of two parallel reactions consuming CO. Moreover, a less pronounced difference

regarding the catalytic behavior of the Pt catalyst depending on the conditions was observed when the temperature increases which could be explained by the preference of the M_Pt/CeFeAl catalyst to react via WGS instead through CO oxidation route. In turn, once the CO species adsorbed on the noble metal and/or the metal/support interface quickly removed via CO oxidation, the concentration of the available active sites to WGS reaction (slower reaction) should increase. On the contrary, the noticeable catalytic enhancement observed for the gold based monolith cannot be exclusively attributed to an additive effect from CO oxidation and WGS reactions. In fact, the CO conversion obtained in the O_2-assisted WGS test exceeds by far the contribution of the direct CO oxidation (30%) in the whole temperature range. Consequently, this noticeable catalytic improvement can be clearly ascribed to an O_2-assisted WGS reaction.

The capacity exhibited by the gold based catalyst (and not for the platinum based catalysts) to be assisted by oxygen species during the WGS reaction could be partially ascribed to the redox reaction pathway described for gold ceria catalysts. Although the role of ceria support is clearly important no matter the NM (Pt or Au), it becomes absolutely necessary when gold is used as active phase due to the metal inability to dissociate water. The water dissociation is a slow step on the WGS reaction and, for gold based systems it must be carried out at the metal/support interface. The oxygen addition has been reported to favor the generation of surface OH groups leading to promoted WGS reaction [73,74].

The beneficial effect of the oxygen addition to the stream could be also related to the inhibition of the deactivation effects such as overreduction of the support and/or formation of carbonaceous species blocking catalytically active sites. Actually, it has been also reported that oxygen species facilitates the carbonaceous intermediate species decomposition avoiding the active sites blocking and pushing forward the WGS [7]. On the other hand, recent operando XAS study of an Au/CeO_2 catalyst demonstrates that the optimum Ce oxidation state to carry out the WGS is 3.3 [55]. Given that under the WGS reaction atmosphere the ceria partial reduction is likely to happen; the presence of oxygen traces could help to maintain cerium partially oxidized and close to the optimum formal valence active in WGS.

Finally, the catalytic behavior of both noble metals was tested on O_2-assisted real conditions and the results are presented on Figure 6.14.

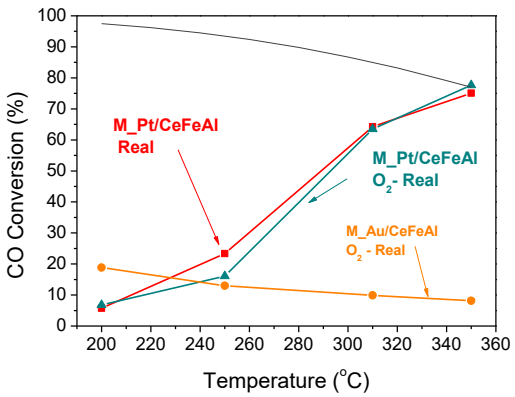

Figure 6.14. CO conversions of M_Pt/CeFe and M_Au_CeFe catalysts: a) CO conversions at GHSV = 4000h^{-1} in WGS reaction in "real" and O_2-assisted "real"

The M_Au/CeFeAl does not show any activity in the studied temperature range under real WGS mixture. The M_Pt/CeFeAl reaches the equilibrium conversions at the highest temperature. The oxygen incorporation to the real mixture does not present any advantage for the M_Pt/CeFeAl system, demonstrating the same CO conversions like in oxygen absence in the whole temperature range. It could be then suggested that the oxygen incorporation appears to affect mainly the processes occurring over the support, which is not of primordial importance when platinum is acting as active metal. Although the support capacities should be affected by the H_2 presence the water dissociation ability of platinum in this case do not seems to be altered.

On the other hand, the structured gold based catalyst presents even a negative tendency with the increase of the temperature, the CO conversions decrease with the temperature. Surprisingly, the highest catalytic conversion in real conditions presented by M_Au/CeFeAl is achieved at 180 ºC showing yields around 20%. This could be due to a favored H_2 oxidation by gold in these conditions and, as stated above, to the impossibility of ceria reoxidation in real WGS conditions and its loss of capacity for water dissociation under these conditions.

Comparing both noble metals in H_2-rich streams, no matter the type of the catalytic bed, powder fixed bed or structured micromonolithic devices, the platinum based systems present clear superiority.

6.3.5. Partial conclusions

An interesting comparison between structured gold and platinum noble metals supported on iron-doped ceria mixed oxide for WGS was carried out. The original powder catalysts were successfully deposited onto metallic micromonolithic structures achieving well fixed and homogeneous catalytic layer. Both metal based powders perform satisfactorily in the classical WGS, being Pt superior to Au in all cases. The scaling up from the powder to the structured catalysts seems to affect mainly to the gold based catalyst while the Pt monolith retains its excellent behavior, a fact not observed for the powder samples and reported here for the first time.

O_2 addition to the WGS feed stream changes the situation by boosting the WGS activity, greatly for Au and merely for Pt based monolith. Our data reveal that only the gold based monolith benefits for an actual "O_2 assisted WGS" reaction meanwhile the CO conversion increment observed for the Pt monolith results from the parallel CO oxidation reaction.

In any case, oxygen addition is a strategy to be considered to potentiate the WGS reaction over noble metals based structured catalysts especially for gold/ceria systems. Such an activity promotion together with the inherent features of the structured catalysts allowing smaller reactor volumes coverts our monoliths into an interesting alternative to be implemented in hydrogen fuel processors.

6.4. Part III: *Operando* XANES-EXAFS study of Au and Pt ceria based catalysts

Under reaction conditions, the catalysts can undergo chemical transformations that severely transform their structure with respect to the initially obtained [75]. *In situ/operando* characterizations appear as interesting techniques allowing detailed analysis of the structural, electronic and chemical properties of the catalyst under reactions and/or operation conditions. The main difference between *in-situ* and *operando* relies on the catalytic activity measurement, which is only recorded in the operando approach. So, *operando* method must involve in-situ spectroscopy measurements under true catalytic reaction conditions. For that purpose, the WGS reactor cell should be designed considering the atmospheric pressures and the temperatures in which the WGS reaction is carried out.

The main goal of the *operando* studies is to provide a complete picture of the catalytic process whereby an accurate structure-activity relationship of the substrate-catalyst species can be determined. Therefore, the purpose of operando spectroscopy is to measure the catalytic changes that happen within the reactor using time resolved and spatially resolved spectra [76]. Although time resolved spectra theoretically record the formation and disappearance of intermediate species at the active sites of the catalysts in real time, current operando instrumentation only works in second or sub-seconds scale and therefore, only relative concentrations of intermediates can be assessed.

Among the existing spectroscopic techniques, XAS (X-Ray Absorption Spectroscopy) is one of the most powerful, which provides direct information of the structural and electronic properties changes under the reaction conditions in the presence of reactants and products [77].

Concerning the WGS *in-situ/operando* studies, the lack of knowledge concerning basic questions such as nature of active species and reaction pathway hinders the proper design and optimization of the catalysts [59]. As mentioned in the General Introduction, an intense debate above the nature of the active species of metal based catalysts is still alive.

Controversial results on the oxidation state of active gold and platinum catalysts supported on ceria can be found in literature. For example, Kim et *al* [78] proposed for gold based catalysts, that the active sites associated to nanocrystalline gold domains are much more active than those associated to atomically dispersed metal. These results challenge the observations obtained by the group of Flytziani-Stephanopoulous [14,21] that associates the WGS activity with atomically dispersed cationic gold species. In this regard, Rodriguez et *al.* [20] demonstrates that the WGS activity mainly relies on the pure gold nanoparticles oxide interface. Cationic clusters were also proposed as major active species in WGS for similar gold and palladium supported on ceria.

In a similar way, the agreement on the oxidation state of the platinum species during the WGS reaction is not achieved. For low temperature WGS, Fu el al.

[14] claimed that the mechanism involves mainly cationic platinum species in the Pt-O_x-Ce sites. By XPS spectroscopy, the identified oxidation state was essentially Pt^{II} with some Pt^{IV} fraction, but not Pt^0. From *operando* studies, opposite conclusions were stablished by Xu et al. [79] affirming that at temperatures at which the catalyst exhibits maximum conversion (300ºC), most of the platinum oxide is transformed into metallic platinum.

The *operando* XAS study of the gold and platinum based catalysts were carried out in this work. Within the series of prepared catalysts in this thesis Au/CeAl(Puralox) and Pt/CeAl(Puralox) were the chosen ones for the XAS study.

6.4.1. Experimental: X-ray Absorption Spectroscopy

Time-resolved Au, Pt and Ce L3-edges were collected *in situ* during the WGS reaction. Beamlines X18B of the NSLS at Brookhaven National Laboratory (BNL), BL22-CLAESS line of the CELLS-ALBA facility and SAMBA line at SOLEIL were used for the EXAFS/XANES experiments. The spectra were taken either in the transmission-yield or fluorescence mode for platinum. The samples were mounted without diluting in capillary glass reactor. A standard mass flow controllers and gas mixer managed the gas flow. H_2O was introduced with a bubbler located at the exit of the gas mixer. The temperature of the inlet gas, controlled by heated gas pipes, determined H_2O concentration. The reaction temperature was ramped at 10 ºC/min, from RT upwards.

6.4.2. XANES results

First, the importance of the required pretreatment for the platinum based catalyst was evaluated. For that purpose, the activation conditions were reproduced being the catalyst exposed to H_2 stream and heated at 10ºC/min until 350 ºC. The evolution of the Pt-L_3 and Ce-L_3 XANES spectra with the temperature is shown in the Figure 6.15.

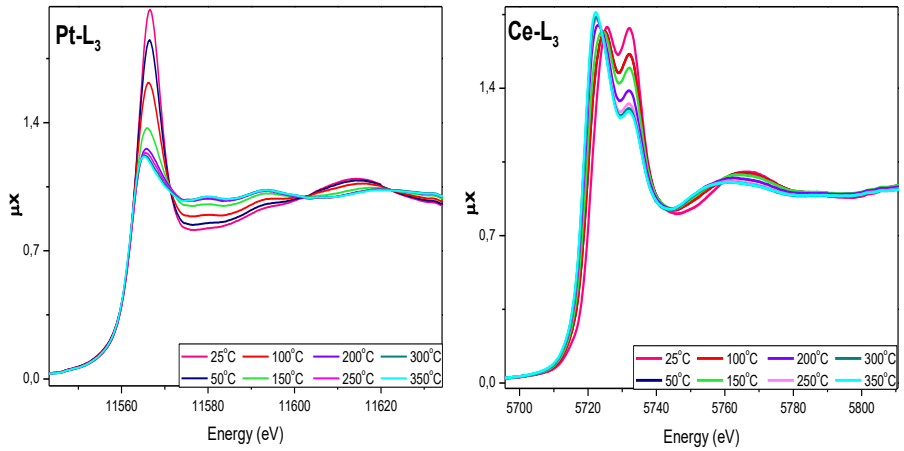

Figure 6.15. XANES spectra obtained during the H_2 preactivation treatment for: a) Pt-L_3 absorption edge; b) Ce-L_3 absorption edge

The characteristic PtO sharply rising absorption peak is observed at 11564 eV, (Figure 6.15.a), being its intensity diminished as the temperature is increased. This absorption peak, denominated the “white line”, directly accounts for the vacancies on 5d orbital when platinum species are oxidized. Higher the white line intensity, higher the platinum population in an oxidized state.

Therefore, for platinum metallic species the intensity of the absorption edge should decrease because of the complete occupation of the 5d orbitals and consequent minor probability of electron transitions. In fact, for platinum 5d orbitals nominally occupied, this transition should not be allowed because of the absence of holes. However, an s-p-d orbital hybridization allows the presence of low intensity white line in the XANES spectra for Pt bulk [80]. For the Pt/CeAl sample the Pt-L_3 XANES results show clearly an oxidized platinum population before the introduction of H_2. Moreover, the platinum species are reduced by H_2 starting from room temperatures as indicated by the decrease of the intensity of the white line. At the final temperature of the treatment, which is also the temperature of pretreatment before the WGS reaction, completely reduced platinum state is reached.

On the other hand, the modification of the Ce-L_3 XANES absorption with the temperature when exposed to H_2 rich streams is presented in the Figure 6.15.b. The XANES line shape of Ce^{3+} and Ce^{4+} are quite different [16]. At 25 ºC, Ce-L_3 XANES spectrum show two absorption peaks. The lower energy absorption peak is commonly attributed to the absorption from 2p level to the 5d with the 4f orbital remaining unoccupied, resulting in Ce $[2p^5 4f^0 5d^1]O[2p^6]$ state configuration. The second absorption characteristic of Ce^{4+} appears at higher energies and it is assigned to the transit from the oxygen valence band to the ceria 4f shell leaving a hole in the oxygen valence band, with final $Ce[2p^5 4f^1 5d^1]O[2p^5]$ state configuration.

This situation, prior the H_2 contact, significantly changes when the temperature is increased. Meanwhile, the Ce^{4+} absorption bands intensity decreases, a new peak is observed and related to the appearance of Ce^{3+} species. For the Ce^{3+} species, in which the 4f shell is partially occupied, the observed transition is associated to the absorptions from 2p to 5d, with the initial and final configuration states for the transit corresponding to $Ce[2p^6 4f^1 5d^0]O[2p^6]$ and $Ce[2p^5 4f^1 5d^1]O[2p^6]$.

The activation pretreatment normally carried out leads, for the platinum based samples, to different oxidation states on both reducible components, support and noble metal. Considering that CO is also strong reduction agent, the oxidation states evolution of the platinum catalyst when exposed to CO as a function of the temperature was analyzed. The resulted Pt-L_3 and Ce-L_3 XANES spectra are shown in the Figure 6.16.

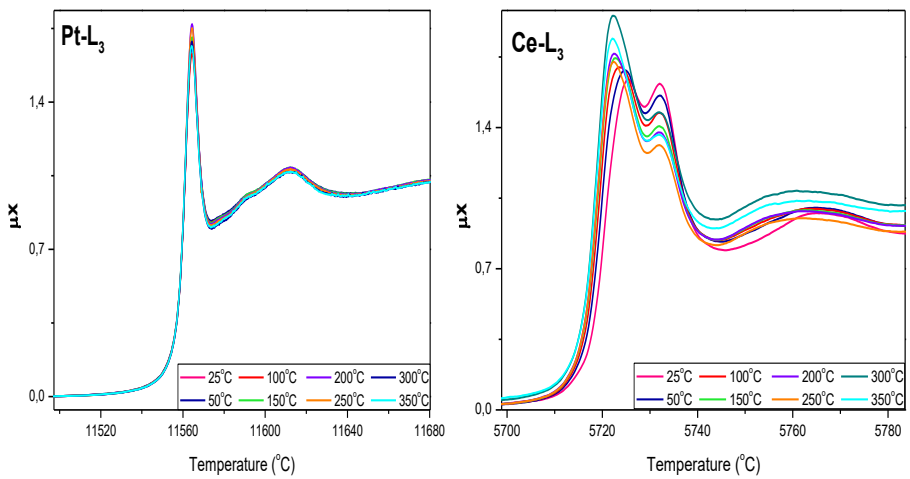

Figure 6.16. XANES spectra obtained when heated in CO atmosphere for: a) Pt-L_3 absorption edge; b) Ce-L_3 absorption edge

Different behaviors are observed for Pt and Ce when exposed to CO atmosphere. The Pt-L_3 XANES spectra do not exhibit important changes, suggesting the incapacity of Pt to be reduced by CO molecules. On the contrary, the Ce^{4+} population is strongly reduced by CO even at 50ºC. Therefore, the H_2 pretreatment is needed for platinum based catalysts when the reaction is performed in H_2 free feed stream (model mixture).

Considering that platinum and ceria absorption peaks are the fingerprints of the oxidation states of both species, their contribution could be quantitatively evaluated during the reductive experiments with the help of standard samples. This is carried out under the assumption that the oxidation states should be a linear combination between the possible oxidation states (Figure 6.17). It can be observed, that H_2 pretreatment leads to full conversion of PtO to metallic Pt, meanwhile it is almost no reduced when exposed to CO pretreatment (Pt^0/Pt^{2+} ratio around 0.2). Concerning the ceria support, both treatments lead to equal Ce^{3+}/Ce^{4+} oxidation ratio of around 0.45.

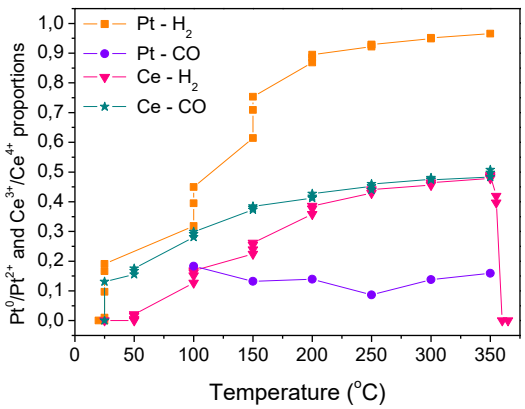

Figure 6.17. Ce^{3+}/Ce^{4+} and Pt^0/Pt^{2+} proportions calculated when exposed to CO and H_2 streams

Beside this, the WGS reaction was evaluated for noble metal ceria based catalysts using a model feed stream. The resulted Ce-L_3 and the corresponding Au-L_3 and Pt-L_3 XANES spectra for both catalysts are shown on the Figure 6.18.

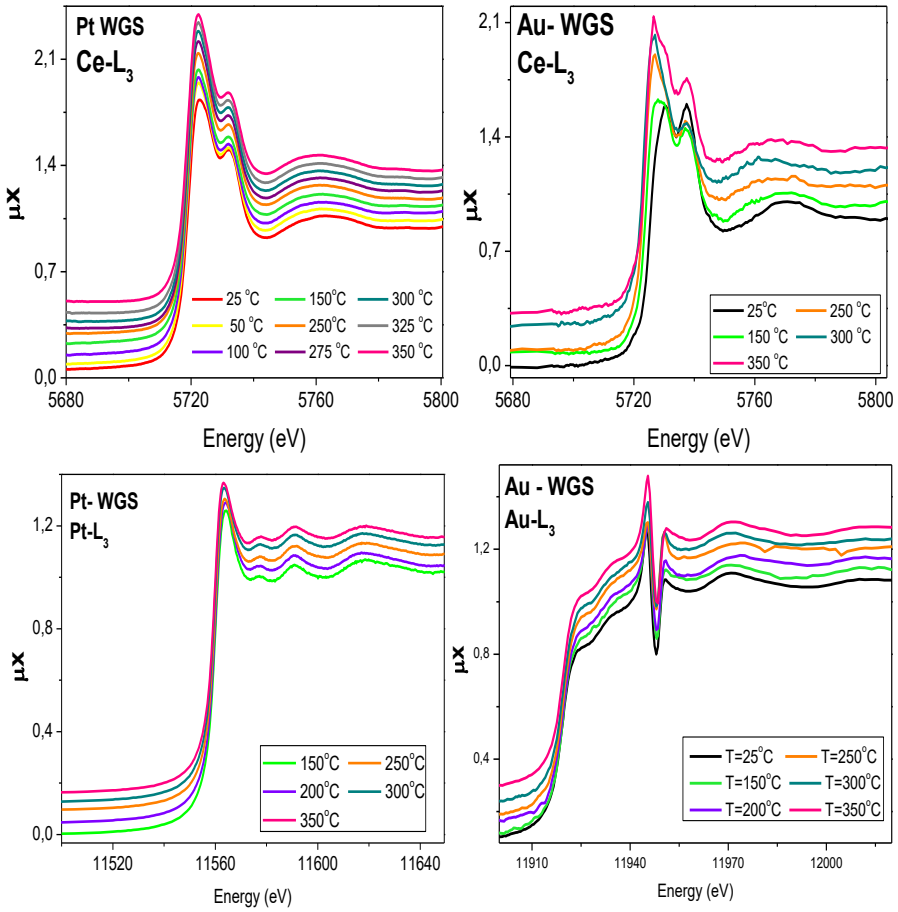

Figure 6.18. XANES spectra obtained during the WGS reaction for Pt-L_3, Au-L_3 and Ce-L_3

Regarding the gold sample, the white line arises from $2p_{3/2,1/2} \rightarrow 5d$ dipole transitions, as happens with the majority of the transition metals with a

partially occupied d-band. Similarly to platinum, metallic gold nanoparticles exhibit smaller white line with respect to that exhibited by oxidized species, allowed by the s-p-d hybridization.

In the same way, the Ce^{3+}/Ce^{4+}, Pt^{0}/Pt^{2+} and Au^{0}/Au^{+} ratios can be estimated as shown in the Figure 6.19. For Pt catalysts, the average oxidation state for cerium and platinum atoms remain almost unchanged during WGS whatever the reaction temperature. Meanwhile in the case of gold catalysts, higher oxidation states are observed for cerium at low temperatures and zero as a constant oxidation state during the WGS reaction is detected for gold. This different behavior may be understood considering that the platinum catalysts are H_2-reduced prior to the WGS and that the average oxidation states of cerium in gold catalysts follow the behavior of cerium atoms in the platinum catalysts upon reduction.

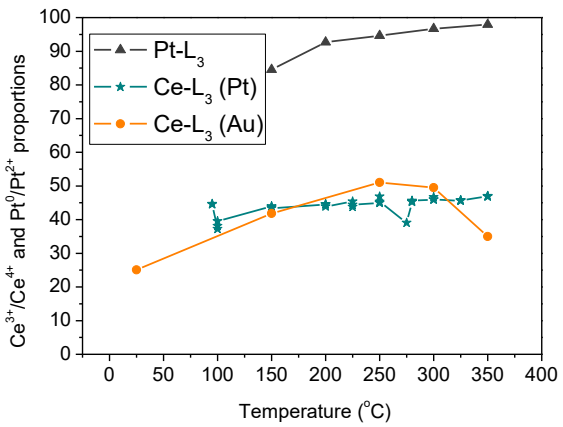

Figure 6.19. XANES spectra obtained during the WGS reaction for Pt-L_3, Au-L_3 and Pt-L_3

6.4.3. EXAFS results

The structural catalyst changes should be also considered in order to obtain a complete idea of the catalytic behaviors exhibited for both noble metals during the WGS reaction. EXAFS analysis provides useful tool to establish an accurate structure/activity correlation.

Ce-L_3 model

A complex model for Ce-L_3 EXAFS signal was made coming from a pure CeO_2 crystal, and modified in order o accommodate the features of the sample. These features are:

- Oxygen vacancies. CeO_2 looses oxygen atoms without modifying its crystal structure when partially reduced in WGS reaction, Ce^{4+} and Ce^{3+} ions coexist in the lattice.
- High surface area. The sample preparation method ensures CeO_2 nanoparticles growth on Al_2O_3 substrate, and thus a high proportion of Ce atoms remains at the surface with reduced coordination number.
- CeO_2 crystals tend to reduce their lattice parameter when the crystal size is small.
- OH and H_2O on the surface. A high amount of OH or H_2O is expected to be associated to Ce atoms on the surface.

The model is a linear combination of bulk CeO_2 and a CeO_2 average surface, with a parameter that accounts for the ratio of surface Ce atoms vs. bulk Ce atoms, and with common S_0^2 and ΔE_0

CeO_2 bulk parameters

- The first 3 coordination shells are taken (Ce-O (1/4, 1/4, 1/4), Ce-Ce (1/2, 1/2, 0), Ce-O (3/4, 1/4, 1/4), with only the single scattering paths taken into account.
- Coordination numbers are fixed values. For Ce, this is fixed to the crystalline value. In the case of both oxygen shells, the coordination numbers are reduced from the crystalline values due to the vacancies taking into account the mean Ce oxidation state calculated from the Ce^{4+}/Ce^{3+} proportion, from the XANES data.
- Coordination distances are variable, but linked to a single parameter that accounts for the variation of the lattice parameter (Δa).
- Debye-Waller factors are free for each coordination shell.

CeO_2 surface parameters

- The first 3 coordination shells are taken (Ce-O (1/4, 1/4, 1/4), Ce-Ce (1/2, 1/2, 0), Ce-O (3/4, 1/4, 1/4), with only the single scattering paths taken into account.
  - An extra shell Ce-OH is added to account for OH and H_2O presence on the surface.
- Coordination numbers are fixed to the mean of the coordination numbers for (100), (110) and (111) surfaces of crystalline CeO_2, in equal proportions, also reducing the final value of oxygen coordination numbers due to the vacancies in the same fashion as above.

  - Ce-OH coordination number is almost free (tight bond between 3 and 5)

- Coordination distances are variable, but linked to a single parameter that accounts for the variation of the lattice parameter (Δa), which is the same as the above mentioned bulk one.
  - Ce-OH coordination distance is free.
- Debye-Waller factors are the same for each coordination shell as the bulk ones.
  - Ce-OH Debye-Waller factor is free.

Therefore, the ceria model can be simplified as shown in the Figure 6.20 like a linear combination of bulk ceria and surface ceria. The main conceptual difference between them is the Ce-OH coordination shell accounted for the surface ceria species.

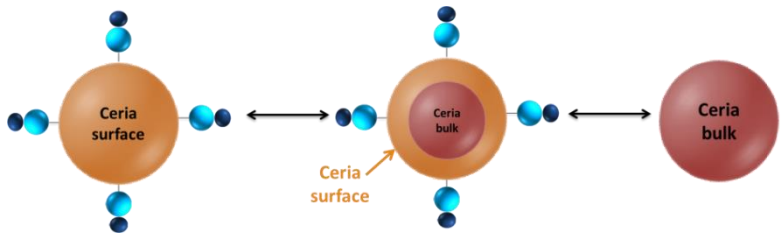

Figure 6.20. Schematized model of ceria in which the ceria surface with the hydroxyl coordination shell and ceria bulk is combined

Pt-L_3 models

The Pt model was constructed considering the XANES results where the fingerprint of the sample compared to that from metallic Pt at all temperatures

seem to be quite similar. Furthermore, the Fourier transform magnitudes of the spectra (Figure 6.24) revealed a first zone composed of what it looks like an interference from different peaks, that seem to reduce their sharpness once the temperature rises. However, as we can see in the Pt metal reference, the first Pt-Pt coordination shell gives indeed a weird arrange of peaks and shoulders by itself instead of a simple peak, so the choice of a simple Pt metal model seemed wise. The further shells are quite similar between the different spectra, so relevant changes seem to only happen at the first shell.

However, the first test fits revealed a strong reduction of the coordination numbers at all Pt coordination shells, being more severe at longer distances, ranging from 30 to 70% approximately. Even with this, the fits were not as good as required. Thus, as one would expect an intimate contact between the CeO_2 support and the Pt-metal active phase, an additional Pt-Ce shell was included in the fit, giving better results; with a resulting Ce mean coordination number around 1 or bigger. This means that the Pt atoms are most probably in very small nanoparticle form, attached firmly (maybe growing epitaxially) to the CeO_2 crystal.

There is an interesting match between the Pt-metal crystal structure and the CeO_2 (100) surface. On the (100) surface of CeO_2, the tetrahedral sites on the surface (where the O atoms would stand if we add a new layer on the surface) are disposed in a squared lattice, with a lattice parameter of 5.41/2 = 2.705 Å. On the other hand, the pure Pt metallic crystal has an fcc structure with a lattice parameter of 3.92 Å, which means a first coordination shell of 2.77 Å.

Taking into account that, in general, metallic nanoparticles tend to reduce their coordination distances as they reduce size, it seems that an epitaxial growth of small clusters of Pt on the (100) surface of the CeO_2 support might be quite likely.

In this case, the first Pt layer would have a Pt-Ce coordination number of 2. As the Ce mean coordination number calculated with the first model was around 1, we concluded that the Pt atoms will most likely grow epitaxially as bi or tri-layers on top of the (100) CeO_2 surface, following the Pt-fcc structure through the [100] direction. This is, building the squared lattice at the first layer by filling the tetrahedral holes of the CeO_2, and then filling the cubic holes in the second and third layers. For more flexibility, a parameter that accounts for the filling of the second and third layer respect to the first is introduced, thus allowing partially reconstructed layers, or even only monolayers. Besides, this parameter would take into account layers built on other CeO_2 surfaces, like (110) and (111), which would give scattering signals similar to the (100) monolayer, so the model is not as restrictive as it seems.

In order to take into account the borders of the layers due to the limited lateral size of the nanoparticles, a model of squared layers was built for simplicity. The variable taken to account for this was the total number of atoms in the nanoparticle, and then the size of each layer was calculated from the filling proportion, and supposing them squared in shape. Then, the coordination numbers are calculated for each atom, taking into account:

1. The layer at which they belong (bottom, intermediate or top)

2. Whether they are at the interior of the shell, at the border, or at the corner

This results in a complex coordination number formula for each coordination shell, which, however, only depends on 3 variables, that will finally give the mean shape and size of the nanoparticle, in the squared-trilayer model. A scheme of the model can be seen in Figure 6.21.

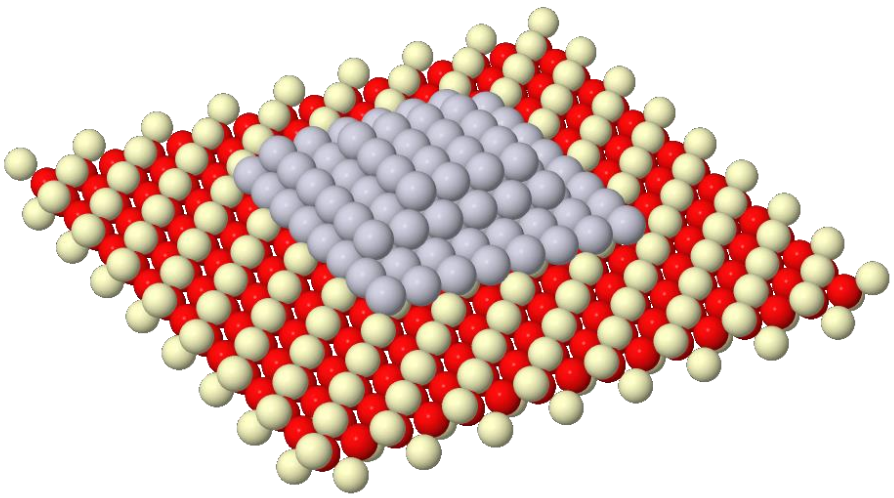

Figure 6.21. Model for the Pt-L3 EXAFS analysis. Pt atoms form epitaxial squared layers growing on top of a Ce (100) surface, with different covering proportions. The atoms color codes are: white for Ce, red for O, grey for Pt

More precisely, the model was constructed like this:

Pt bottom layer parameters:

- The first 4 Pt-Pt coordination shells were taken both the single scattering paths and the multiple-scattering paths of the 4th shell. The

Pt atoms at the intermediate and top layers (described below) were obviously taken into account.

- Coordination numbers are fixed to the ones calculated for an infinite bilayer: 8, 4, 8 and 4, respectively (crystalline 3D Pt is 12, 6, 12, 24)
- Coordination distances are variable, but linked to a single parameter that accounts for the variation of the first coordination distance, and then coherent with the structure.
- The Debye-Waller factors are independent for each shell.

- The first two Pt-Ce coordination shells were taken, only single scattering paths. These are in positions (1/2, 1/2, -1/2 - Δ*h*) and (1/2, 3/2, -1/2 - Δ*h*), being Δ*h* the increment of height of the Pt layer from the CeO_2 (100) plane, starting from the O position (see below).
  - Coordination numbers are fixed to the ones of the (100) surface: 2 and 4
  - Coordination distances depend firstly the coordination distance of the Pt-Pt lattice, and secondly, on a new parameter that accounts for the *height* of the Pt layer hovering over the CeO_2 layer. The starting positions are the O positions, thus the increment of height should be always positive, as the Pt atoms are bigger.
  - The Debye-Waller factors are independent for each shell. The multiple-scattering path has the same Debye-Waller factor as its corresponding single-scattering path.

Pt intermediate layer parameters:

At the second layer there are 2 different Pt according to their positions respect to the Ce atoms. One of them is directly on top of a Ce, and the other in the rest of the positions. Most of the parameters are the same of the bottom layer, only changing the parameters corresponding to the Pt-Ce shells.

- The first 4 Pt-Pt coordination shells were taken both the single scattering paths and the multiple-scattering paths of the 4th shell. The atoms at the first layer were obviously taken into account. Coordination numbers, distances and Debye-Waller factors are the same as the ones for the bottom layer, above described.
- For the Pt atoms on positions on top of the Ce positions (half of the top layer), the two first Pt-Ce shells were taken. The first has only a single-scattering path, while the second has single and multiple-scattering paths through some of the bottom Pt atoms.
  - Coordination numbers are fixed to the ones of the (100) surface: 1 and 4
  - Coordination distances depend on the coordination distance of the Pt-Pt lattice, and on a the *height* of the Pt layer hovering over the CeO_2 layer (see above).
  - The Debye-Waller factors are: for the first shell, the same as the first Pt-Ce of the bottom layer. This is justified as the distances are similar. The second shell, independent, but the same for the single and multiple-scattering paths.

- For the Pt atoms on rest of the positions, only the first Pt-Ce coordination shell was taken, being the second too far.
  - Coordination number is fixed to the one of the (100) surface: 4
  - Coordination distance depend on the coordination distance of the Pt-Pt lattice, and on the *height* of the Pt layer hovering over the CeO_2 layer (see above).
  - The Debye-Waller factor is the same as the second Pt-Ce shell of the bottom layer, due to the similar distance.

Pt top layer parameters:

The third layer stands too far from the Ce atoms, and thus it is modelled as a simple Pt layer, taking into account their neighbour Pt atoms in the layers below.

- The first 4 Pt-Pt coordination shells were taken both the single scattering paths and the multiple-scattering paths of the 4^{th} shell. The atoms at the layers below are taken into account. Coordination numbers, distances and Debye-Waller factors are the same as the ones for the bottom layer, above described.

Although it seems a quite sophisticated model, the number of variables is kept quite reduced due to the restrictions imposed, and the long k and R range used in the fit. There are a total of 12 variables (Number of atoms, 2 layers ratio, 2 distances, 7 Debye-Waller factors) of a possible maximum of 23 given by the Nyquist theorem, which seems quite good.

Au-L_3 model

A model similar to the ceria ones was developed for fitting the EXAFS function derived from the gold spectra. Distinction between the internal and the external part of the gold nanoparticles is imposed for the analysis as represented in Figure 6.22.

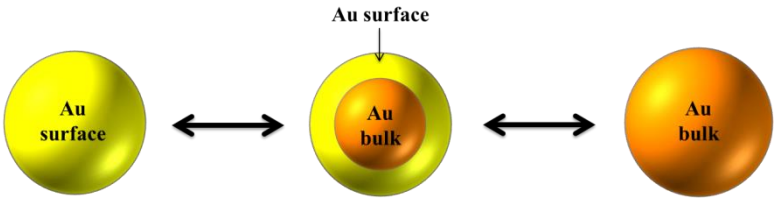

Figure 6.22. Model for the Au-L3 EXAFS analysis in which is represented, from left to right, a total gold dispersion, an intermediate situation and a agglomerated gold situation

For gold particles, the key parameter was the surface/bulk fraction which provides information about gold dispersion and dynamics during the WGS. Moreover, the intimate gold-ceria contact was also considered. So, the Au bulk was fitted using the fcc structure of metallic gold meanwhile, for the Au surface, gold atoms were placed over the oxygen atoms in the (110) plane of CeO_2.

More precisely, the model proposed for data analysis of the gold particles can be summarized:

- Au bulk: regular Au metal fcc structure including the first five coordination spheres.
  - Fixed coordination numbers

  - Variable coordination distances, linked to a single variable (lattice parameter increment)
  - Variable Debye-Waller factors, one for each coordination sphere.
- Au surface: dispersed Au atoms at the center of the 4 Oxygen atoms at the (110) surface plane of the CeO_2 considering the first two coordination shells (the first one correspond to Au-O and the second one to Au-Ce)
  - Fixed Oxygen coordination number reduced by mean number of vacancies and fixed cerium coordination number
  - Variable coordination distances
  - Variable Debye Waller factors.

The EXAFS oscillations for Ce-L_3 for both noble metals based catalysts during the WGS reaction are presented on Figure 6.23. Both samples showed two distinct peaks depending on the R value. One at low-R, which is in fact a double peak or a peak with a shoulder that will probably be the result of the interference between the Ce-O(1) shell of the bulk CeO_2 structure with the Ce-OH shell of the surface Ce, which should have different coordination distances. The second peak should be the combination of the Ce-Ce shell with the Ce-O(2) shell. The signal in between is small enough to be disregarded, and is probably due to truncated Fourier transform tails from the main peaks and to multiple-scattering signals, so it will not be fit.

The Fourier transform magnitude of the spectra (Figure 6.23.a) confirms that the ceria does not exhibit any significant change during the WGS reaction in the case of the Pt sample. So, once the sample is exposed to H_2 pretreatment, the ceria structure remains similar during all the WGS reaction. This fact is opposite to that observed for the gold based catalyst in which the ceria shows prominent changes.

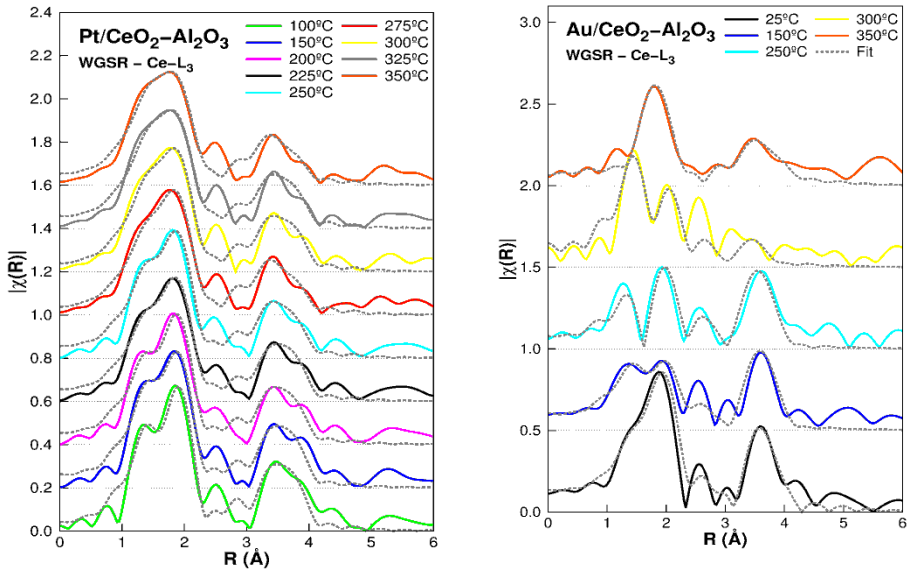

Figure 6.23. Ce-L_3 EXAFS R space spectra obtained when heated in a WGS reaction: a) Pt/CeAl; b) Au/CeAl

The characteristic PtO sharply rising absorption peak is observed at 11564 eV, (Figure 6.15.a), being its intensity diminished as the temperature is increased. This absorption peak, denominated the “white line”, directly accounts for the

vacancies on 5d orbital when platinum species are oxidized. Higher the white line intensity, higher the platinum population in an oxidized state.

The characteristic PtO sharply rising absorption peak is observed at 11564 eV, (Figure 6.15.a), being its intensity diminished as the temperature is increased. This absorption peak, denominated the "white line", directly accounts for the vacancies on 5d orbital when platinum species are oxidized. Higher the white line intensity, higher the platinum population in an oxidized state.

For both samples it was detected that the CeO_2 lattice is constrained by 0.1 Å respect to the ideal value for all the temperatures. This can be justified by the presence of oxygen vacancies which gives the lattice some space to collapse onto itself. Actually, no variation on the ceria lattice contraction was expected from Ce average oxidation state, similar at all the WGS temperatures, a result suggesting similar oxygen vacancies concentration and crystal sizes. Oppositely, in the case of the gold sample, this contraction increased from 0.05 Å at 25 ºC to 0.1 Å at higher temperatures indicating that oxygen vacancies formation happens during the reaction.

The Debye-Waller factors show an almost constant increase as the temperature rises, within the error bars in the case of the Pt sample. This seems consistent with an increase of the dynamical disorder in the lattice. Similarly to the above exposed reason for the lattice contraction, noticeable structural static disorder increase was not expected. For the gold sample, the

Debye-Waller factors seem to increase slightly with the temperature being this is consistent with an increase of dynamical disorder in the lattice.

The surface ratio was estimated for both systems being strongly correlated to the Ce-OH coordination number. This parameter shows a constant 70% at all the temperatures in the case of the Pt system Finally, it was noticed that a combined value of surface ratio around 70 % and Ce-OH coordination number around 4 seemed to reach the best fits at all the temperatures. These values are not expected to change too much, as the CeO_2 structure does not change from the initial reduction process. Thus, we maintained them as fixed values throughout all the simulations. The consistency of the rest of the free parameters proved this approach to be quite good.

In the case of the gold catalyst, the surface ratio is between 70% and 80%, without a clear trend. A combined value of surface ratio around 70%-75% and Ce-OH coordination number around 4 seemed to reach the best fits at 25 ºC, 150 ºC, and 250 ºC. The spectrum at 300 ºC abandons this trend going to a Ce-OH number of 5, and at 350 ºC this number is reduced to 1. The value of 1 for the 350 ºC spectrum might be a consequence of OH or H_2O desorption from the surface of CeO_2 at high temperatures.

Considering a 70% of surface Ce atoms and assuming a perfect cubic particle of about 6 unit cells side length, the CeO_2 crystal appears to be around 3.3 nm in side, or 5.5 nm in diagonal. Considering that this would be the ideal minimum size of the CeO_2 crystals, this value looks plausible for the current

sample. This particle size is in very good agreement to the 3.6 nm estimated for the Pt based catalyst in the XRD experiments.

A number of 4 OH or H_2O molecules associated with each surface Ce is possible from the structural point of view. We could imagine the (100) plane of CeO_2 populated with these species occupying the (1/4, 1/4), (1/4, 3/4), (3/4, 1/4), and (3/4, 3/4) positions, thus sharing 2 Ce atoms each. This is consistent with the coordination distances resulting from the fit, for the molecules in that position. In other planes, the positioning would be equivalent. The coordination distances almost do not change with the temperature, increasing slightly, which is consistent with the temperature rise, due to the increase in dynamic disorder. This coordination distances are shorter than those for isolated O, which is due to the O-H or the H-O-H polarization.

Again, a number of 5, corresponding to the spectrum at 300 ºC obtained for the gold based catalyst, seems more complicated to accommodate to the surface. This could be an error arising from the highly noisy data. On the other hand, as the coordination number is 1 at 350 ºC, it might be expected that this molecule is placed on top of the Ce atom, not being shared with other Ce atoms on the surface. This model would explain why the OH/H_2O coordination numbers shift abruptly from 4/5 to 1. The natural positions change from (1/4,1/4) places at lower temperatures, to be on top of the Ce atoms, (0,0) places, thus having only 1 OH / H_2O per Ce.

Moreover, we have not enough knowledge to state that the value of 4 OH or H_2O molecules associated with each Ce atom of the surface would be possible or convenient from the chemical or catalytic point of view. In this sense, a strong concern arises implying that the OH or H_2O species are not desorbed from the surface of the Pt catalyst even at 350 ºC. The results advise otherwise, because the need of a shorter Ce-O shell to interfere in the EXAFS signal with the Ce-O (1) from the bulk CeO_2 structure seems clear.

The behavior of the active phase is quite different for Pt and Au catalysts, Figure 6.24. The Pt fits are rather good considering the variety of features that the Fourier transform magnitudes (Figure 23.a) present in terms of peaks and shoulders. It is worth mentioning the good fit obtained at high-R. This part of the diagram carries the most information about the geometry of the system, and thus a good fit supports the model quite well. This part is also often riddled with the multiple-scattering signals, and thus difficult to model and fit. The apparent absence of these signals supports the conclusion that the Pt atoms form quite small nanoparticles.

As previously explained, coming from the original Pt trilayer, it was obtained in all the cases almost a pure bilayer, with only spurious atoms coming to the third in some cases. Furthermore, it seems that the second layer is complete and sometimes slightly bigger than the bottom one. This interesting result narrows the different models of possible shapes. It seems that the nanoparticle is building the second layer larger than the first, which would be compatible

with an incomplete cuboctahedral nanoparticle, which seems to be the preferred shape of 3D nanoparticles composed of atoms that naturally form FCC structures, as Pt does.

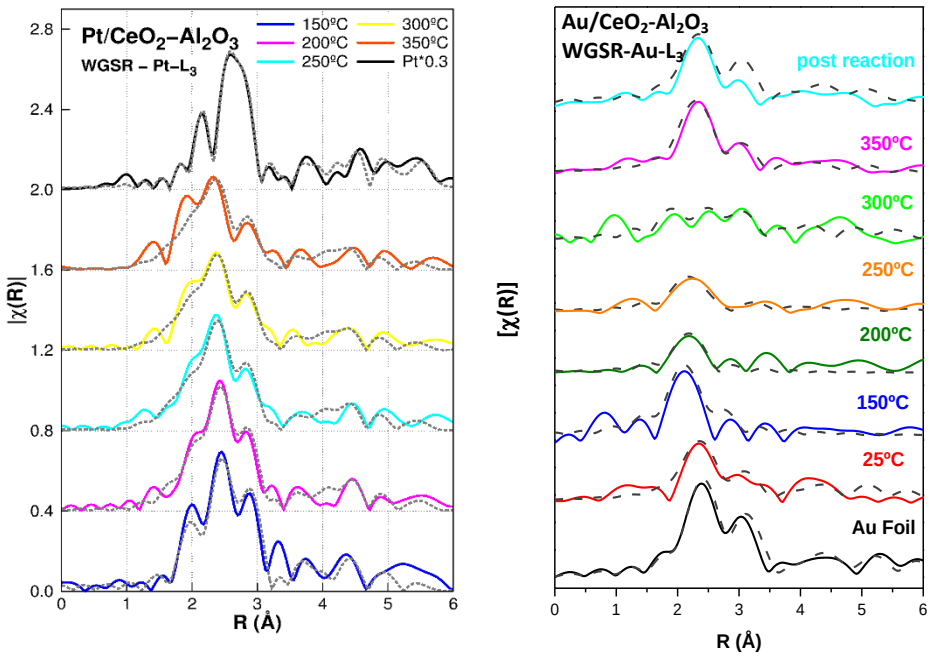

Figure 6.23. EXAFS R space spectra obtained during WGS reaction: a) Pt-L_3 for the Pt/CeAl; b) Au-L_3 for the Au/CeAl

The Pt nanoparticles shape and size does not follow a clear trend with the temperature. This may arise from the fact that the transformations are made during the previous H_2 reduction, and once the sample is in a reductive environment, it does not change significantly. Only at the lowest temperature a small difference can be found, as the intermediate layer has the same size as the bottom one, while some atoms appear at the third layer. There might be a

transformation from 3D nanoparticles to these "flat" nanoparticles at lower temperatures, but the numbers are too small to ensure this fact. The average lateral length of the nanoparticles is 1.2 nm, which is about 5-6 atoms per side, and is quite constant along the temperatures. This particle sizes is, in turn, in very good agreement to that observed for this sample already reduced by HR-TEM.

The coordination distances for Pt-Pt shells seem to follow a slight trend as the temperature rises, contracting the lattice at higher temperatures. Being a small nanoparticle, the distances are expected to be smaller than for the bulk Pt. These smaller distances at higher temperature might be related to the epitaxial growth onto a slightly smaller lattice, that has an influence as well on the distances between the Pt atoms.

The coordination distances for Pt-Ce shells experiment a transition between 150 ºC and 200 ºC. At the lowest temperature, the height from the CeO_2 surface to the Pt bottom layer is 0.23 Å above the original position at the center of the tetrahedral holes. This is expected, as the Pt atom size is larger than the O^{2-} ions. However, this height is changed to about 0.11 at 200 ºC, and then maintained around that value at higher temperatures. This abrupt step might be caused by a sudden reconstruction at the epitaxial growth process that may have some transition temperature around those values. This can be related to different bottom/intermediate layer proportions at this temperature. Moreover, it should be mentioned that between 200 ºC and 250 ºC the Pt

catalyst atains the equilibrium conversions and hence, the observed changes on the Pt-Ce shells and the increment on the catalytic performances could be related to the increment of the catalytic activity.

Once more, the Debye-Waller factors for Pt-Ce and Pt-Pt shells follow quite a regular increase as temperature rises, in accordance with the higher dynamical disorder at higher temperatures.

The EXAFS spectra of gold may be fitted just assuming Au-Au neighbors. The average coordination number of gold continuously decreases till 300ºC the number of gold atoms surrounding the Au scattered approaches zero, indicating that Au atoms redispersed and, even, stabilized probably by the ceria oxygen vacancies. However, this interaction must be considered electrostatic since no evidence of white line is observed in the Au XANES spectra.

6.4.3. Partial conclusions

The oxygen vacancies of ceria play a multirole in the reaction. On one hand, they are active sites for water splitting and, on the other hand, they act as preferential nucleation points for noble metal deposition allowing high metallic dispersion and improving the catalytic performance. The strong metal support interaction involves a charge transfer from the structural defects towards NM atoms, modulating the activity of the catalysts. In view of the later, the creation of oxygen vacancies on ceria is desirable to achieve high

catalytic performances. It is evident, from the Figure 6.6, that the support affects more importantly the Au catalysts than the Pt ones.

The average oxidation state of cerium atoms in Pt catalysts remain almost unchanged during WGS whatever the reaction temperature, while in the case of gold catalysts higher oxidation states are observed for cerium at low temperatures. This different behavior may be understood considering that the platinum catalysts are H_2-reduced prior to the WGS and that the average oxidation states of cerium in gold catalysts follow the behavior of cerium atoms in the platinum catalysts upon reduction.

For the reduced platinum catalysts the EXAFS oscillations account just for Pt-Pt interactions; the average coordination number of platinum remaining almost unaltered on increasing the reaction temperature (the Debye Waller factor may account for the lower intensities on increasing temperature). However, at low R values ~1.5 Å oscillations that decrease on increasing temperature are observed. These oscillations may be fitted to Pt-OH bonds accounting for water splitting on the metal surface even at the higher temperatures.

Besides, the Pt particles could growth epitaxially being constituted by three layers in which the Pt atoms placed at the bottom ones occupied positions which initially should be occupied by Oxygen atoms of the ceria lattice. Variations regarding the Pt-Ce coordination were also detected being related to the different relative sizes of the intermediate and the bottom Pt atoms

layer. At lower temperatures, the intermediate layer appears to be composed by fewer atoms than the bottom ones. At 200-250 ºC and coinciding to important increment on the achieved CO conversions, both layers seem to be constituted by the same Pt atoms. The later variation on the relative sizes of the layers were accompanied by Pt-Ce distances diminutions.

Concerning the gold dynamics, the proportion of Au surface atom respect to that of Au bulk increases significantly when the temperature rise up from 25 ºC to 100 ºC suggesting a complete gold redispersion. That total gold redispersion was accompanied to the increment of the Au-Ce and Au-O signals which could implies than gold atoms are located on the oxygen vacancies. The result is that metallic gold atoms may be placed at the oxygen vacancies being surrounded of oxygen atoms. Considering that the water activation steps should procced on the oxygen vacancies, gold particles at intermediate temperatures could avoid the water dissociations step.

Both platinum and gold catalysts evidence the existence of a coordination sphere at ~2 Å that corresponds to the interaction of hydroxil groups with the ceria surface. In the case of gold this adsorption starts to be evident from 150 ºC upwards and decrease again once 300 ºC is reached. On the contrary for the platinum catalyst, the ceria/OH interaction remains within the fitting in the whole temperature range, but slightly reduced at higher temperatures. This behavior is consistent with the average oxidation state of cerium estimated

from the XANES spectra indicating that water adsorption/splitting is favored over ceria oxygen vacancies.

Operando X-ray absorption data of $NM/CeO_2/Al_2O_3$ catalysts allow establishing that the activity increase observed upon supporting noble metals on ceria modified supports must be ascribed to the ability of ceria for adsorbing/splitting water molecules. This may explain why in the case of Au, which cannot dissociate water, the presence of oxygen vacancies probably at the metal/ceria interface, promotes the process to the active site and increases the reaction rate. On the other hand, platinum may activate water by itself but the required reduction pretreatment increases the number of oxygen vacancies in ceria increasing the number of water molecules at the metal nanoparticles periphery. Since the WGS reaction is controlled by water diffusion, the increase in the number of support surface sites that may hold water molecules increase the reaction rate at lower temperatures accounting for the observed increase in the catalytic activity.

References

[1] M. Haruta, Catal. Today 36 (1997) 153.

[2] M.A. Edwards, D.M. Whittle, C. Rhodes, A.M. Ward, D. Rohan, M.D. Shannon, G.J. Hutchings, C.J. Kiely, Phys. Chem. Chem. Phys. 4 (2002) 3902.

[3] D. Andreeva, V. Idakiev, T. Tabakova, A. Andreev, R. Giovanoli, Appl. Catal. A Gen. 134 (1996) 275.

[4] W. Deng, M. Flytzani-Stephanopoulos, Angew. Chemie - Int. Ed. 45 (2006) 2285.

[5] D.L. Trimm, Appl. Catal. A Gen. 296 (2005) 1.

[6] C. Zhang, A. Michaelides, D.A. King, S.J. Jenkins, J. Phys. Chem. C 113 (2009) 6411.

[7] T.R. Reina, S. Ivanova, V. Idakiev, J.J. Delgado, I. Ivanov, T. Tabakova, M.A. Centeno, J.A. Odriozola, Catal. Sci. Technol. 3 (2013) 779.

[8] K.R. Hwang, S.K. Ihm, J.S. Park, Fuel Process. Technol. 91 (2010) 729.

[9] G. Dutta, U. V. Waghmare, T. Baidya, M.S. Hegde, K.R. Priolkar, P.R. Sarode, Chem. Mater. 18 (2006) 3249.

[10] J.A. Rodriguez, P. Liu, J. Hrbek, J. Evans, M. Pérez, Angew. Chemie - Int. Ed. 46 (2007) 1329.

[11] W.Y. Hernández, M.A. Centeno, F. Romero-sarria, J.A. Odriozola, J. Phys. Chem. C 113 (2009) 5629.

[12] M. Gonzalez Castaño, T.R. Reina, S. Ivanova, M.A. Centeno, J.A. Odriozola, J. Catal. 314 (2014) 1.

[13] A. Luengnaruemitchai, S. Osuwan, E. Gulari, Catal. Commun. 4 (2003) 215.

[14] Q. Fu, H. Saltsburg, M. Flytzani-Stephanopoulos, Science 301 (2003) 935.

[15] D. Tibiletti, A. Amieiro-Fonseca, R. Burch, Y. Chen, J.M. Fisher, A. Goguet, C. Hardacre, P. Hu, D. Thompsett, J. Phys. Chem. B 109 (2005) 22553.

[16] G. Jacobs, E. Chenu, P.M. Patterson, L. Williams, D. Sparks, G. Thomas, B.H. Davis, Appl. Catal. A Gen. 258 (2004) 203.

[17] R. Burch, Phys. Chem. Chem. Phys. 8 (2006) 5483.

[18] A.A. Phatak, N. Koryabkina, S. Rai, J.L. Ratts, W. Ruettinger, R.J. Farrauto, G.E. Blau, W.N. Delgass, F.H. Ribeiro, Catal. Today 123 (2007) 224.

[19] N. Dupont, G. Germani, A.C. van Veen, Y. Schuurman, G. Schäfer, C. Mirodatos, Int. J. Hydrogen Energy 32 (2007) 1443.

[20] J.A. Rodriguez, S. Ma, P. Liu, J. Hrbek, J. Evans, M. Pérez, Science 318 (2007) 1757.

[21] M. Flytzani-Stephanopoulos, B.C. Gates, Annu. Rev. Chem. Biomol. Eng. 3 (2012) 545.

[22] P. Liu, J.A. Rodriguez, J. Chem. Phys. 126 (2007) 164705.

[23] I.D. González, R.M. Navarro, W. Wen, N. Marinkovic, J.A. Rodriguéz, F. Rosa, J.L.G. Fierro, Catal. Today 149 (2010) 372.

[24] R.J. Farrauto, Y. Liu, W. Ruettinger, O. Ilinich, L. Shore, T. Giroux, Catal. Rev. 49 (2007) 141.

[25] W. Ruettinger, O. Ilinich, R.J. Farrauto, J. Power Sources 118 (2003) 61.

[26] X. Liu, W. Ruettinger, X. Xu, R. Farrauto, Appl. Catal. B Environ. 56 (2005) 69.

[27] S. Fiorot, C. Galletti, S. Specchia, G. Saracco, V. Specchia, Int. J. Chem. React. Eng. 5 (2007).

[28] S. Ivanova, C. Petit, V. Pitchon, Appl. Catal. A Gen. 267 (2004) 191.

[29] F. Moreau, G.C. Bond, Appl. Catal. A Gen. 302 (2006) 110.

[30] Z. Kónya, V.F. Puntes, I. Kiricsi, J. Zhu, J.W. Ager, M.K. Ko, H. Frei, P. Alivisatos, G.A. Somorjai, Chem. Mater. 15 (2003) 1242.

[31] O.H. Laguna, F. Romero Sarria, M.A. Centeno, J.A. Odriozola, J. Catal. 276 (2010) 360.

[32] S. Damyanova, B. Pawelec, K. Arishtirova, M.V.M. Huerta, J.L.G. Fierro, Appl. Catal. A Gen. 337 (2008) 86.

[33] F.J. Pérez-Alonso, M. Lopez Granados, M. Ojeda, P. Terreros, S. Rojas, T. Herranz, J.L.G. Fierro, Chem. Mater. 17 (2005) 2329.

[34] A.S. Reddy, C.Y. Chen, C.C. Chen, S.H. Chien, C.J. Lin, K.H. Lin, C.L. Chen, S.C. Chang, J. Mol. Catal. A Chem. 318 (2010) 60.

[35] M.Á. Centeno, C. Portales, I. Carrizosa, J.A. Odriozola, Catal. Letters 102 (2005) 289.

[36] C.W.M. Castleton, J. Kullgren, K. Hermansson, J. Chem. Phys. 127 (2007) 1.

[37] V. Petrovsky, B.P. Gorman, H.U. Anderson, T. Petrovsky, J. Appl. Phys. 90 (2001) 2517.

[38] P. Patsalas, S. Logothetidis, L. Sygellou, S. Kennou, Phys. Rev. B 68 (2003) 1.

[39] S. Tsunekawa, T. Fukuda, A. Kasuya, Surf. Sci. 457 (2000) L437.

[40] S. Deshpande, S. Patil, S.V. Kuchibhatla, S. Seal, Appl. Phys. Lett. 87 (2005) 1.

[41] L. Wu, H. Wiesmann, A. Moodenbaugh, R. Klie, Y. Zhu, D. Welch, M. Suenaga, Phys. Rev. B 69 (2004) 1.

[42] O.H. Laguna, M.A. Centeno, M. Boutonnet, J.A. Odriozola, Appl. Catal. B Environ. 106 (2011) 621.

[43] O.H. Laguna, M.A. Centeno, G. Arzamendi, L.M. Gandía, F. Romero-Sarria, J.A. Odriozola, Catal. Today 157 (2010) 155.

[44] J. Spanier, R. Robinson, F. Zhang, S.-W. Chan, I. Herman, Phys. Rev. B 64 (2001) 1.

[45] W.Y. Hernández, O.H. Laguna, M.A. Centeno, J.A. Odriozola, J. Solid State Chem. 184 (2011) 3014.

[46] T. Tabakova, L. Ilieva, I. Ivanov, R. Zanella, J.W. Sobczak, W. Lisowski, Z. Kaszkur, D. Andreeva, Appl. Catal. B Environ. 136-137 (2013) 70.

[47] G. Graham, J. Catal. 130 (1991) 310.

[48] C.M. Kalamaras, I.D. Gonzalez, M. Navarro, L.G. Fierro, A.M. Efstathiou, J. Phys. Chem. C 115 (2011) 11595.

[49] Z. V. Popović, Z.D. Dohčević-Mitrović, N. Paunović, M. Radović, Phys. Rev. B - Condens. Matter Mater. Phys. 85 (2012) 1.

[50] M.A. Centeno, M. Paulis, M. Montes, J.A. Odriozola, Appl. Catal. A Gen. 234 (2002) 65.

[51] C.T. Campbell, C.H.F. Peden, Science 309 (2005) 713.

[52] C. Zhang, A. Michaelides, D.A. King, S.J. Jenkins, Phys. Rev. B - Condens. Matter Mater. Phys. 79 (2009) 1.

[53] C. Zhang, A. Michaelides, D.A. King, S.J. Jenkins, J. Chem. Phys.

129 (2008) 1.

[54] Z. Yang, Z. Lu, G. Luo, Phys. Rev. B - Condens. Matter Mater. Phys. 76 (2007) 1.

[55] T.R. Reina, W. Xu, S. Ivanova, M.Á. Centeno, J. Hanson, J.A. Rodriguez, J.A. Odriozola, Catal. Today 205 (2013) 41.

[56] W. Ruettinger, X. Liu, R.J. Farrauto, Appl. Catal. B Environ. 65 (2006) 135.

[57] A. Martinez-Arias, J.M. Coronado, R. Cataluna, J.C. Conesa, J. Soria, J. Phys. Chem. B 102 (1998) 4357.

[58] G. Bond, Gold Bull. 42 (2009) 337.

[59] J.A. Rodriguez, J.C. Hanson, D. Stacchiola, S.D. Senanayake, Phys. Chem. Chem. Phys. 15 (2013) 12004.

[60] A. Phatak, W. Delgass, J. Phys. Chem. C 113 (2009) 7269.

[61] Z.Y. Yuan, V. Idakiev, A. Vantomme, T. Tabakova, T.Z. Ren, B.L. Su, Catal. Today 131 (2008) 203.

[62] D. Andreeva, I. Ivanov, L. Ilieva, M. V. Abrashev, Appl. Catal. A Gen. 302 (2006) 127.

[63] K.C. Petallidou, A.M. Efstathiou, Appl. Catal. B Environ. 140-141 (2013) 333.

[64] X. Wang, R.J. Gorte, J.P. Wagner, J. Catal. 212 (2002) 225.

[65] C. Li, Y. Sakata, T. Arai, K. Domen, K. Maruya, T. Onishi, J. Chem. Soc. Faraday Trans. 1 85 (1989) 1451.

[66] J.M. Zalc, V. Sokolovskii, D.G. Löffler, J. Catal. 206 (2002) 169.

[67] A. Gayen, M. Boaro, C. De Leitenburg, J. Llorca, A. Trovarelli, J.

Catal. 270 (2010) 285.

[68] N.K. Gamboa-Rosales, J.L. Ayastuy, M.P. González-Marcos, M. a. Gutiérrez-Ortiz, Catal. Today 176 (2011) 63.

[69] J. Kugai, J.T. Miller, N. Guo, C. Song, J. Catal. 277 (2011) 46.

[70] V.G. Milt, S. Ivanova, O. Sanz, M.I. Domínguez, A. Corrales, J.A. Odriozola, M.A. Centeno, Appl. Surf. Sci. 270 (2013) 169.

[71] O.H. Laguna, M. González Castaño, M.A. Centeno, J.A. Odriozola, Chem. Eng. J. 275 (2015) 45.

[72] J. Barbier, D. Duprez, Appl. Catal. B Environ. 3 (1993) 61.

[73] T. Utaka, K. Sekizawa, K. Eguchi, Appl. Catal. A Gen. 194 (2000) 21.

[74] G.C. Chinchen, M.S. Spencer, K.C. Waugh, D.A. Whan, J. Chem. Soc. Faraday Trans. 1 83 (1987) 2193.

[75] T. Bunluesin, R.J. Gorte, G.W. Graham, Appl. Catal. B Environ. 15 (1998) 107.

[76] S.J. Tinnemans, J.G. Mesu, K. Kervinen, T. Visser, T.A. Nijhuis, A.M. Beale, D.E. Keller, A.M.J. Van Der Eerden, B.M. Weckhuysen, Catal. Today 113 (2006) 3.

[77] D.C. Koningsberger, B.L. Mojet, G.E. Van Dorssen, D.E. Ramaker, Top. Catal. 10 (2000) 143.

[78] C.H. Kim, L.T. Thompson, J. Catal. 230 (2005) 66.

[79] W. Xu, R. Si, S.D. Senanayake, J. Llorca, H. Idriss, D. Stacchiola, J.C. Hanson, J.A. Rodriguez, J. Catal. 291 (2012) 117.

[80] G. Jacobs, U.M. Graham, E. Chenu, P.M. Patterson, A. Dozier, B.H. Davis, J. Catal. 229 (2005) 499.

General conclusions

The findings presented in this Thesis represent a step forward towards the development of highly efficient catalytic systems for the WGS reaction. The boosting effect provided by cerium oxide based supports in the WGS reaction was rapidly established and the importance of the choice of a proper support for this kind of systems highlighted. Although two different approaches have been developed for the Pt catalysts, the support modifications and structured catalytic designs with buffer layers placed under the catalyst ones, the obtained catalytic outcomes always point out the key water´s role in such a way that, enhanced water dissociations and diffusions capacities, enhanced catalytic activity.

Hence, along the first approach, the idea consist in doping the ceria lattice with transition metals in order to favor the creation of oxygen vacancies considered as the main active centers able to dissociate water molecules.

The ceria properties were modulated as a function of transition metal employed, Zr or Fe. The main consequence from introducing Zr on the ceria lattice was the achievement of the strongest noble metal support interaction which entailed greater Pt stabilization against sintering and strongest Pt-CO interaction in respect to the others catalysts. In comparison to the Zr incorporation, the Fe significantly decreases the ceria band gap energies promoting the oxygen mobility of the support as perceived by the OSC measurements and the highest oxygen vacancies population. Undoubtedly,

this feature should be also related to the diminished tendency to form carbon deposits because of the highest oxidation capacities.

However, the best catalytic performance was obtained when Zr and Fe were combined as promoters into the ceria lattice provoking a synergistic effect reflected by the prominent diminution of the ceria band gap energy. Along to the intermediate OSC capacity or oxygen vacancies populations available for this sample, the most interesting feature observed were apparently related to the mobility of the H species. This enhanced H transfer was detected by the easier H_2 desorption observed during the H_2-TPD. In terms of quantification this sample also showed H_2 overconsumption, which suggests an ability to incorporate H species into the catalyst structure. This superior mobility could be also related to the higher catalyst' capacity, to develop greater amounts of H and C - containing species on the support discerned during the CO adsorption experiments. It appears that this sample, once the CO activated, is able to rapidly diffuse it to the support.

Therefore, it was not the number of oxygen defects nor stronger metal support interactions the determining feature which consents the superior catalytic performances but rather the improved capacities to diffuse the already dissociated species from water molecules, i.e. the H containing species as H and OH, through the catalytic surface.

In very good agreement, outstanding results were obtained during the second approach in which the benefits offered by the metallic micromonolithic

structures were also profited. Actually, the structuring proces should be assumed as a necessary and intermediate step for scaling up the WGS catalysts with the purpose to its real implementation on mobile applications.

For the second approach, the novelty was the incorporation of a ceria buffer layer behind the catalyst layer, in order to reach enhanced capacities to dissociate water species. The changed behaviors depending on the presence or not of the buffer layer as well as on the reaction conditions were definitively ascribed to the different capacities to activate water species. Under reductive conditions, this layer provides superior oxygen vacancies concentration and electronic densities favoring the dissociation of water molecules and the diffusion of the species resulted from the water splitting.

Similar conclusions, concerning the buffer layer's role can be claimed from the change of the buffer composition maintaining constant the catalyst layer as a function of buffer's water activation capacities. Then, the catalytic trend exhibited by the structured catalysts exactly matches the oxygen vacancies concentration and, the buffer's water splitting ability. Besides, it was detected that the oxide with superior water splitting capacity was also able to keep longer the adsorbed water molecules. This fact should imply changes on the partial pressures at the catalytic surface of the water molecules. Thus, the higher water partial pressures should lead to favored water dissociation processes and, in good concordance to the above proposed, to increment on the apparent reaction order for the water species. In conclusion, the

incorporation of a buffer layer under the catalyst one proposes an interesting approach on achieving highly efficient WGS catalysts.

Therefore, the good catalytic performances generally observed for the Pt ceria based catalysts in the WGS reaction must be associated to the water features obtained when both are combined. Indeed, the demonstrated catalytic supremacy of Pt catalysts in comparison to Au ones appear to be related, among others, to water features. The Pt is the metal able to dissociate water molecules by itself, and the incorporation of a reducible oxide (where the majority of the water molecules will be dissociated) does not tilt the balance towards the gold catalysts. The EXAFS analysis performed for both metal based catalysts showed that Pt one is able to maintain OH groups associated to partially reduced ceria even at 350 ºC meanwhile the gold based catalyst was not capable to break the ceria reduction. At the same temperatures, the gold species appear to completely redisperse occupying the oxygen vacancies thus diminishing the number of sites where water molecules could be dissociated. The ceria capacity to maintain associated OH groups explains the different optimal temperatures range for both metals in WGS reaction but especially points out the importance of the presence of OH groups associated to partially reduced ceria for achieving active WGS catalysts.

Resumen

1. Introducción

Ante el problema medioambiental derivado del continuo uso de los combustibles fósiles así como de su previsible agotamiento, se establece la necesidad de encontrar nuevas fuentes energéticas más respetuosas con el medio ambiente. Entre las posibles alternativas, el H_2 se presenta como un vector energético prometedor debido a su alta eficiencia energética, limpieza y versatilidad ante los combustibles que los alimente. El creciente interés científico ha conllevado el desarrollo de celdas de combustible capaces de convertir la energía química de la molécula de H_2 en energía eléctrica destacando las celdas de combustible tipo PEM (Polymeric Exchange Membranes) ya que han sido descritas como las más eficaces siendo capaces de trabajar a temperaturas relativamente bajas.

Sin embargo, el correcto funcionamiento de las pilas de combustible tipo PEM pasa por la casi completa eliminación del CO ya que éste se depositaría en el ánodo de las celdas PEM conllevando la desactivación de la misma. Considerando que en la mayoría de los métodos de producción de H_2, este viene acompañado de CO, surge la necesidad de desarrollar de procesos de purificación de corrientes de H_2.

La reacción de Desplazamiento del Vapor de Agua o WGS ($CO + H_2O \leftrightarrow H_2 + CO_2$) consiste en la reacción del CO con el H_2O para dar CO_2 e H_2. De esta manera, la reacción de WGS permite disminuir la concentración de CO a la par que incrementa el rendimiento total hacia H_2. Además de ser un

equilibrio moderadamente exotérmico, la reacción de WGS se caracteriza por ser cinéticamente favorecida pero termodinámicamente limitada [1]. Así, el rango óptimo de temperaturas de operación deberá permitir unas altas conversiones de CO no limitadas por el equilibrio. Además, dicha temperatura ha de favorecer la cinética de la reacción que vendrá determinada por el catalizador empleado.

Industrialmente, la reacción de WGS se lleva a cabo en dos reactores en serie denominados HTS y LTS (del inglés, High y Low Temperature Shift, respectivamente). Sin embargo, estos catalizadores presentan serias desventajas en cuanto a la implementación de la tecnología del H_2 a dispositivos móviles [2]. Por ejemplo, los catalizadores clásicos de la unidad de HTS están basados en Cr^{6+} que combinando una alta toxicidad y solubilidad en agua, resulta en un metal poco apropiado para una aplicación móvil. Por otra parte, los catalizadores basados en Cu son típicos de las unidades de LTS pero son pirofóricos en contacto con el aire lo que implicaría un cuidadoso control de tales dispositivos. Además, la sustitución de dos unidades en serie HTS y LTS por una única etapa a una temperatura intermedia, MTS (Medium Temperature Shift) se presenta como una interesante propuesta que permitiría intensificar el proceso a través de una reducción importante del volumen necesario para llevarlo a cabo.

Debido a los inconvenientes que presentan los catalizadores clásicos, nuevas formulaciones basadas en metales nobles se han desarrollado en las últimas

décadas. En este contexto, los catalizadores que usan el Pt como metal noble han sido descritos como prometedores especialmente cuando son combinados con óxidos reducibles como el CeO_2. En general, las publicaciones se focalizan en la influencia del método de síntesis, las modificaciones del soporte, la importancia de los cambios estructurales, el estado de oxidación del metal noble durante la reacción o el mecanismo de reacción a través del cual se da principalmente la reacción de WGS. Olympiou et al. [3] correlacionó la actividad de catalizadores basados en Pt, Pd y Rh soportados sobre alúmina para la reacción de WGS con la concentración de metal superficial y la fuerza de enlace del CO sobre el metal. El orden de actividad propuesto fue Pt > Rh > Pd, el cual coincide con el establecido por Grenoble et al. [4]. Sin embargo, ninguno de estos estudios consideraron la capacidad intrínseca del Pt para disociar agua [5].

El comportamiento catalítico de los catalizadores basados en Pt, y también el de otros metales nobles, experimenta notables mejoras cuando son soportados sobre óxidos reducibles [6–9]. De hecho, los óxidos reducibles no son simples expectadores en la reacción de WGS sino que juegan un importante papel [10–13]. Para catalizadores basados en Pt/Cerio, Phatak et al. [14] reportó TOFs 30 veces superiores que los obtenidos para catalizadores basados en Pt/Alúmina atribuyéndose dicha mejora al par redox Ce^{3+}/Ce^{4+}.

La fuerte interacción Pt-Cerio indicada reducibilidad del cerio superficial tras la adición del metal noble, fue reconocida como una indicación del efecto

electrónico ejercido por los sitios Pt-O_x-Ce, presumiblemente responsables de su elevada actividad catalítica. En la misma línea, Tauster et al. [15] introdujo el término SMSI (del inglés, strong metal support interaction) para describir la contribución del óxido reducible a la formación del sitio activo.

De manera general, ha sido establecido que tanto el metal como el soporte juegan un papel esencial en la reacción de WGS. Por otra parte, también es generalmente aceptado que la actividad catalítica de las partículas metálicas soportadas viene fuertemente influenciada por el tamaño de partícula, la forma de las mismas y el estado de oxidación de que presenten. El comportamiento catalítico viene además, fuertemente modulado por la naturaleza y el grado de reducción del soporte y/o de la interfaz metal-soporte.

Típicamente, las modificaciones del soporte se llevan a cabo con el objetivo de modificar sus propiedades estructurales o electrónicas de manera que se consigan mejoras en las actividades catalíticas de los catalizadores[16–20]. La sinergia entre la el óxido de cerio y el agente dopante puede con seguirse a través de la formación de solución sólida, de la interacción de óxidos segregados [21,22] o de la deposición de partículas metálicas en la superficie del cerio [23,24].

Numerosos estudios han demostrado que dopando el cerio con elementos con diferentes radios iónicos (Zr^{4+}) o estados de oxidación (Fe^{3+}) se afectan las propiedades electrónicas del cerio como la reducibilidad, la capacidad de

almacenamiento de oxígeno o la resistencia frente a fenómenos de sinterización [25,26]. La capacidad redox de las muestras determinara su actividad catalítica. De este modo, la habilidad para la formación de sitios tipo Ce^{3+}- $O_v^{\cdot}$ se ha relacionado íntimamente con la reducibilidad así como con la velocidad de oxidación de CO.

Sin embargo, el uso de catalizadores basados en metales nobles, en principio más caros que los catalizadores convencionales de las unidades de LTS normalmente basados en óxidos de metales de transición, sólo será económicamente viable si presentasen mayores resistencias frente a los fenómenos de desactivación.

Para catalizadores basados en Pt, la sinterización del metal noble ha sido descrita como una importante causa de desactivación [27–29]. Este fenómeno puede ser evitado modificando el soporte de manera que se logren interacciones más fuertes entre el metal y el soporte y, en consecuencia, mayores dispersiones de Pt [30,31].

Comparado con los catalizadores tipo Pt/Al_2O_3, la incorporación del cerio conlleva significantes mejoras catalíticas. La fuerte interacción Pt/Ceria ejemplificada por el incremento de la reducibilidad de las especies de cerio superficiales se reconoce como indicativo del efecto electrónico demostrado por sitios del tipo Pt-O_x-Ce que probablemente sean responsables de la química redox de estos sistemas [15,32].

Además de la sinterización del metal noble, existen otras causas de desactivación para los catalizadores basados en cerio como la sobrereducción del soporte que eliminaría el juego redox del par Ce^{3+}/Ce^{4+} [33]. Además, el bloqueo de los sitios activos del soporte por deposición de especies carbonáceas (tipo carbonatos, bicarbonatos, etc) o de carbón formado mediante la reacción de Boudouard suponen un serio inconveniente. La disminución de dichos efectos puede lograrse mediante el dopaje de la red del cerio consiguiendo una mayor resistencia frente a los fenómenos de desactivación y por lo tanto, una prolongación del tiempo de vida del catalizador.

Por otra parte, junto con la actividad y estabilidad catalítica de los catalizadores, existen otras dificultades intrínsecas de la reacción de WGS que deben ser tenidas en cuenta especialmente si se desean implementar la tecnología del H_2 a dispositivos portátiles. Normalmente, un requisito principal de los catalizadores de WGS para alcanzar conversiones aceptables de CO es trabajar a bajos tiempos de residencia lo cual supone un importante inconveniente ya que conlleva elevados volúmenes de reactor [34]. En comparación con las aplicaciones estáticas convencionales, una implementación tecno-económica exitosa pasa por una reducción del volumen del reactor de al menos dos órdenes de magnitud.

En este aspecto, el estructurado de los catalizadores en micromonolitos aparece como un planteamiento interesante [35,36]. Los beneficios de los

catalizadores estructurados basados en metales nobles fueron establecidos por Wagner et al. [2] donde publicaban catalizadores estructurados capaces de alcanzar conversiones de equilibrio a 20000 h^{-1}. En estas condiciones, los catalizadores convencionales de LTS basados en Cu-ZnO no lograrían conversiones de equilibrio. Además, el lecho de partículas de los catalizadores en polvo conllevaría unas enormes pérdidas de carga si trabajasen a tales velocidades espaciales.

Los micromonolitos pueden ser cerámicos o metálicos (Figura R.1). Los micromonolitos metálicos presentan sustanciales ventajas con respecto a los cerámicos como por ejemplo: una mejor distribución del flujo, una mayor velocidad de difusión de los reactivos hasta el catalizador así como mayores resistencias mecánicas. Además, los monolitos metálicos presentan mayores conductividades térmicas lo cual implica un mayor control de la temperatura de reacción ya que disipan mejor el calor producido durante la exotérmica reacción de WGS [37].

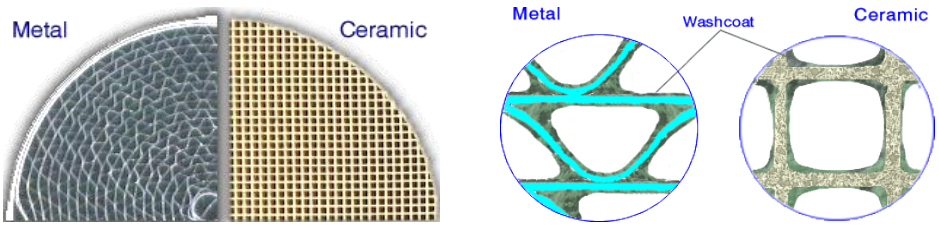

Figura R.1. Micromonolitos metálicos comparados con cerámicos

Teniendo en cuenta lo descrito, los micromonolitos metálicos son excelentes candidatos para estructurar catalizadores para la reacción de WGS debido a su elevada conductividad térmica, elevada área superficial por unidad de volumen y fácil fabricación. Normalmente, los micromonolitos metálicos se preparan co-enrollando una lámina lisa y una rizada en torno a un eje de manera que se consiguen estructuras cilíndricas compuestas por canales longitudinales perpendiculares al eje de dimensiones menores de 1 mm de diámetro.

Con respecto a los micromonolitos cerámicos, los metálicos presentan valores de cpsi superiores lo cual consiente depositar mayores cantidades de catalizador a la par que se mantienen un espesor de capa catalítica tal que conserve las capacidades de transferencias de materia y de calor proporcionadas por los micromonolitos.

Sin embargo, los micromonolitos presentan como principal desventaja la elevada dificultad del anclaje del catalizador en las paredes del monolito debido a la baja rugosidad de las mismas. Entre los sustrato metálicos posibles, los de FeCrAlloy ofrecen la posibilidad de incrementar la rugosidad de la misma mediante el crecimiento de una capa de α-Al_2O_3 de manera que se favorece una óptima deposición y anclaje del catalizador en polvo al substrato metálico [38]. Además, las aleaciones de FeCrAlloy muestran buenas estabilidades en cuanto a los fenómenos corrosivos de carburación que se pueden dar en atmósferas tan reductoras como las de la reacción de WGS.

Tras el pretratamiento inicial de las estructuras metálicas, la deposición del catalizador en las mismas se llevó a cabo empleando el método de washcoating. La óptima ejecución del método de washcoating implica un cuidadoso control de las propiedades reológicas de la suspensión o slurry [39]. Por ello, se ha de tener en cuenta la cantidad de sólido que se añade así como su diámetro partícula de manera que sea lo suficientemente pequeño como para que se mantenga en suspensión. Además, se pueden añadir aditivos como alúmina coloidal o PVA que favorezcan la estabilidad de la misma de forma que se logren capas catalíticas más homogéneas.

En este contexto, la presente tesis doctoral pretende desarrollar catalizadores basados en Pt y óxido de Ce más activos y estables. Además, se presta especial atención a los procesos de estructurado de este tipo de catalizadores sobre micromonolitos metálicos. Por último, se comparan Au y Pt ya que ambos metales nobles han sido descritos como prometedores para la reacción de WGS.

2. Síntesis y caracterización de catalizadores de Pt: screening catalítico

El objetivo del primer capítulo era seleccionar el catalizador de partida para el desarrollo de la tesis doctoral. Para ello, se depositaron dos cantidades distintas de Pt (2 y 4 p/p.%) sobre dos soportes comerciales proporcionados por Sasol: una γ-Al_2O_3 de alta superficie y un soporte CeO_2/Al_2O_3 (Puralox). Además, se preparó un soporte basado en CeO_2/Al_2O_3. Los catalizadores se

caracterizaron y se ensayaron en la reacción de WGS. Así, se intentó correlacionar la actividad catalítica de los sistemas preparados con la carga de platino y la naturaleza del soporte.

2.1. Síntesis de los materiales

El soporte CeO_2/Al_2O_3 "home-made" fue preparado por impregnación húmeda. Para ello, se partió del $Ce(NO_3)_3 \cdot 6H_2O$ como precursor del óxido de cerio; éste fue disuelto en etanol y añadido a una γ-Al_2O_3 de alta superficie. A continuación, se eliminó el exceso de disolvente en el rotavapor, se seco en estufa a 120 ºC y se calcinó durante 4h a 450 ºC con una rampa de calentamiento de 10 ºC/min. Las cantidades obtenidas fueron muy próximas a las nominales siendo éstas un 20 p/p.% de óxido de cerio sobre alúmina. Este soporte se denominó CeAl HM.

El Pt se depositó sobre los soportes por impregnación húmeda partiendo del precursor ($[Pt(NH_3)_4(NO_3)_2]$. Dicho precursor fue mezclado en proporción molar 1:1.1 con un ácido acético 1M. Tras la eliminación del exceso de disolvente en el rotavapor, los catalizadores se secaron en estufa a 120 ºC y por último, se calcinaron a 350 ºC durante 8h empleando una rampa de 5 ºC/min.

La nomenclatura empleada para los catalizadores basados en alúmina fue $Pt(2\%)/Al_2O_3$ y $Pt(4\%)/Al_2O_3$. Para los catalizadores basados en CeO_2/Al_2O_3

comercial se usó Pt(2%)/Puralox y Pt(4%)/Puralox. Por último, el catalizador basado en el soporte "home-made" se denominó Pt(4%)/CeAl HM.

2.2. Resultados y discusión

La actividad catalítica de los catalizadores cuando fueron testados en condiciones modelo o ideales, esto es 4.5 % CO y 30 % H_2O, se muestra en figura R2. A pesar de que todos los catalizadores alcanzaban las conversiones limitadas por el equilibrio, el efecto beneficioso del cerio se traducía en una disminución significativa de la temperatura a la que se alcanzaba el equilibrio. Así, todos los catalizadores que presentaban cerio en el soporte presentaban conversiones cercanas al 100 % en torno a los 230 ºC.

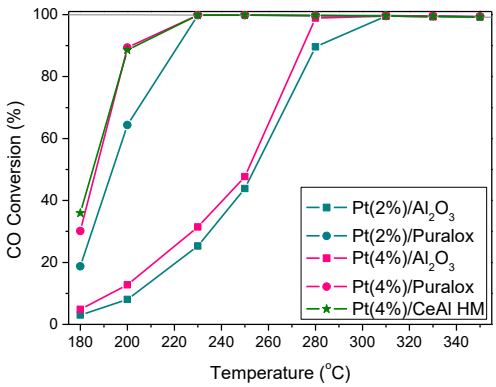

Figura R2. Actividad catalítica exhibida por los catalizadores en WGS en condiciones modelo (4.5%CO + 30%H_2O + balanceado en N_2) a GHSV=4000h^{-1}

Por otra parte, la carga de platino conllevaba mejoras sin ser demasiado significativas si tenemos en cuenta la diferencia de carga. Esto debería ser el

resultado de las suaves condiciones en las que se testaron los catalizadores indicando el que el número de Pt expuestos, incluso a bajas cargas, era suficiente para convertir el número de moléculas de CO.

Con respecto a los catalizadores Pt(4%)/Puralox and Pt(4%)/CeAl HM, no se encontraron diferencias significativas entre ellos. A pesar de todo, el soporte CeAl HM parecía mejorar el comportamiento catalítico del catalizador. De hecho, cuando los catalizadores se comparan en términos de mol CO convertidos$\cdot g_{Pt}^{-1}\cdot s^{-1}$ a 180 ºC (donde la conversión de equilibrio no se ha alcanzado todavía), el Pt(4%)/CeAl HM mostraba actividades superiores a su análogo, presentando valores de $3{,}22\cdot10^{-5}$ *vs.* $2{,}32\cdot10^{-5}$ respectivamente.

Por otra parte, la modificación del catalizador comercial con el objetivo de mejorar su comportamiento catalítico era más difícil. Por todo ello, el catalizador Pt(4%)/CeAl HM fue el seleccionado para las posteriores modificaciones que se presentan en el capítulo posterior.

3. Promotores estructurales y electrónicos en el Pt(4%)/CeO_2/Al_2O_3

En la presente parte de la tesis doctoral se sintetizaron dos series de catalizadores con objetivos diferentes. Primero, se incorporaron cantidades crecientes de Zr a la red del óxido de cerio con el objetivo de establecer el efecto del mismo en las propiedades catalíticas del catalizador así como de seleccionar la relación óptima Ce : agente dopante.

A continuación, se comparó el efecto del Zr y del Fe como promotores tanto por separado como combinados simultáneamente sobre el mismo soporte pero siempre manteniendo la proporción Ce: metal dopante.

3.1. Síntesis de los materiales

Seis soportes distintos fueron preparados: CeO_2/Al_2O_3, $Ce_{0.9}Zr_{0.1}O_2/Al_2O_3$, $Ce_{0.75}Zr_{0.25}O_2/Al_2O_3$, $Ce_{0.5}Zr_{0.5}O_2/Al_2O_3$, $Ce_{0.9}Fe_{0.1}O_2/Al_2O_3$ y $Ce_{0.9}Zr_{0.05}Fe_{0.05}O_2/Al_2O_3$. Las cantidades de precursor fueron calculadas para obtener un 20 p/p. % de óxido de cerio o óxido de cerio dopado sobre alumina. Nominalmente, la relación deseada de óxido de cerio – agente dopante fue calculada en molar. La preparación de los soportes se llevó a cabo por impregnación húmeda sobre una ɣ-Al_2O_3 de alta superficie (Sasol). Los precursores de fueron en todos los casos sus respectivos nitratos, más precisamente: $Ce(NO_3)_3{\cdot}6H_2O$, $Fe(NO_3)_3{\cdot}9H_2O$ and $ZrO(NO_3)_2{\cdot}xH_2O$ (Aldrich). Una vez secos, se calcinaron a 450 ºC durante 4 h empleando una rampa de 10 ºC/min.

En la nomenclaura usada, los oxígenos y los subíndices fueron omitidos por simplicidad. Los soportes CeO_2/Al_2O_3, $Ce_{0.9}Zr_{0.1}O_2/Al_2O_3$, $Ce_{0.75}Zr_{0.25}O_2/Al_2O_3$, $Ce_{0.5}Zr_{0.5}O_2/Al_2O_3$, $Ce_{0.9}Fe_{0.1}O_2/Al_2O_3$ y $Ce_{0.9}Zr_{0.05}Fe_{0.05}O_2/Al_2O_3$ fueron denominados respectivamente CeAl, $Ce_{0.9}$ZrAl, $Ce_{0.75}$ZrAl, $Ce_{0.5}$ZrAl, $Ce_{0.9}$FeAl and $Ce_{0.9}$ZrFeAl.

Para los catalizadores, el platino se deposite del mismo modo descrito anteriormente. La nomenclatura seleccionada para los catalizadores es análoga a los soportes pero con el prefijo Pt/ delante. Así el catalizador sintetizado a partir del CeAl, se denominó Pt/CeAl.

3.2. Resultados y discusión

La actividad catalítica de la serie de catalizadores que incorporaba cantidades crecientes de Zr como promotor se presenta en la Figura R3.a. Los catalizadores que presentaban relaciones intermedias de Ce:Zr eran los catalizadores que mejor rendimiento presentaban, destacando entre ellos el $Pt/Ce_{0.9}ZrAl$ por llegar a la conversión de equilibrio a 200 ºC. La tendencia seguida por los catalizadores a esta temperatura fue:

$$Pt/Ce_{0.9}ZrAl > Pt/Ce_{0.75}ZrAl > Pt/Ce_{0.5}ZrAl \approx Pt/CeAl.$$

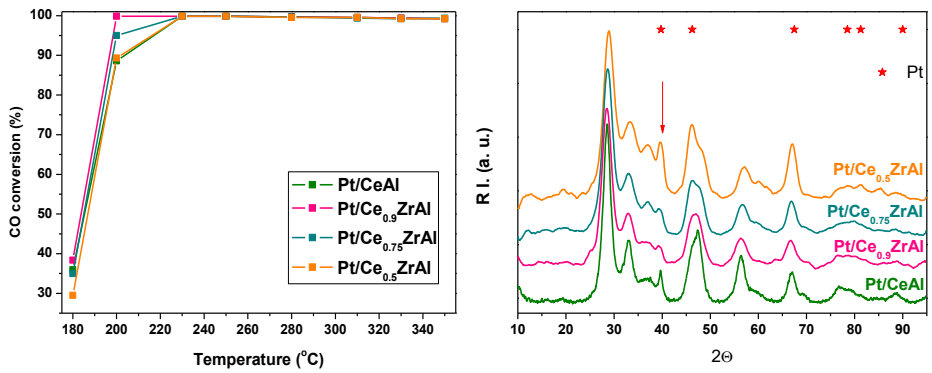

Figura R3. a) Actividad catalítica de los catalizadores en mezcla modelo a 4000 h^{-1}; b) DRX de los catalizadores

Además, las mejoras observadas en la actividad catalítica parecían ser la consecuencia del efecto estructural promovido por el Zr cuando se añadía en cantidades intermedias. Como se muestra en la figura R.3.b, la adición de Zr puede conllevar una disminución importante en la principal difracción del Pt metálico en torno a valores de $2\theta = 39^{o}$. De hecho, a estos valores de 2θ también aparecen difracciones procedentes de la γ-Al_2O_3. Por lo tanto, en el caso de Pt/$Ce_{0.9}$ZrAl y Pt/$Ce_{0.75}$ZrAl no se pueden asociar, de una forma clara, a especies de Pt metálico mientras que las muestras, Pt/$Ce_{0.5}$ZrAl y Pt/CeAl, sí que muestran una difracción afilada que parece indicar la formación de aglomerados de Pt distinguibles en DRX.

Así pues, la mejora de la actividad catalítica observada parecía estar relacionada con un efecto estructural del Zr que, en proporciones intermedias, incrementaba la dispersión de las especies de Pt lo que probablemente se debiera a una interacción más fuerte Pt-soporte.

Finalmente y en base al superior comportamiento catalítico mostrado por el catalizador Pt/$Ce_{0.9}$ZrAl, se escogió una proporción Ce : dopante de 0.9 : 0.1 y se extendió a otros agentes dopantes. De esta forma, se comparó el efecto que tenían, en ésta proporción molar, el Zr y el Fe como agentes dopantes tanto por separado como combinados. Esta nueva serie de catalizadores (Pt/$Ce_{0.9}$ZrAl, Pt/$Ce_{0.9}$FeAl y Pt/$Ce_{0.9}$ZrFeAl) se caracterizó y se ensayó en distinta condiciones para la reacción de WGS. Además, a efectos comparativos se incluyó el Pt/CeAl.

En todos los casos, las propiedades texturales parecían venir dominadas por la matriz de alúmina y las composiciones obtenidas para los catalizadores fueron bastante cercanas a las composiciones nominales.

La incorporación de los agentes dopantes a la red del cerio se detectó a partir de la disminución del parámetro de red de todos los soportes modificados con respecto al parámetro de red característico del CeO_2 obtenido para el CeAl indicando que la formación de solución sólida fue obtenida para todos los agentes dopantes.

En cuanto a las especies de Pt, de acuerdo con el HRTEM, la quimisorción de CO y la DRX, en todos los catalizadores parecían coexistir dos especies de Pt: una fracción mayoritaria constituida por partículas de Pt muy dispersas de en torno a 1 ± 0.2 nm observadas mediante HR-TEM y otra fracción, minoritaria, constituida por aglomerados de Pt detectados por DRX. Con respecto a los aglomerados de Pt, todos los agentes dopantes parecían disminuir su tamaño con respecto al Pt/CeAl siendo especialmente notable esta disminución para el catalizador $Pt/Ce_{0.9}ZrAl$ resaltando de nuevo el efecto estructural del Zr sobre las especies de Pt. A pesar de ello, de forma general, la dispersión de Pt parece ser similar en todos los casos viniendo regida por el método de síntesis de acuerdo con los resultados obtenidos por quimisorción de CO a la temperatura del N_2 líquido.

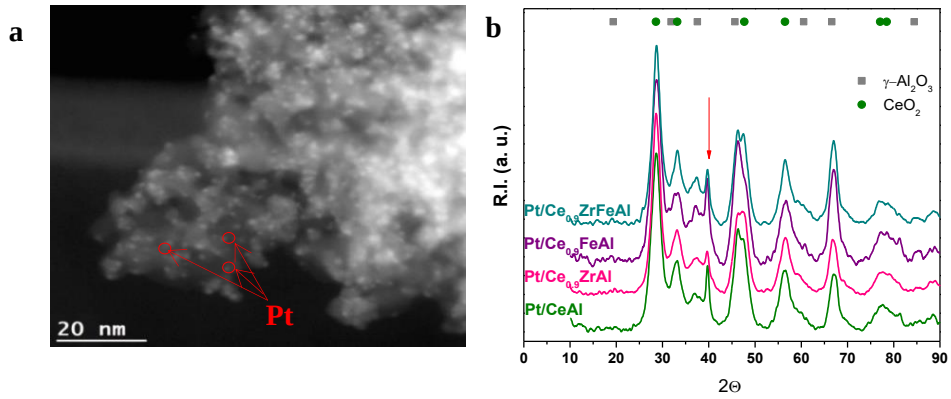

Figura R4: a) Micrografía HR-TEM del Pt/CeAl reducido; b) DRX de los catalizadores reducidos

La actividad catalítica de los catalizadores, en presencia de H_2 y CO_2, se evaluó a distintas velocidades espaciales (Figura R5). Mientras que el Fe como promotor parecía no conllevar ninguna mejora del comportamiento catalítico del sistema, el Zr sí que conseguía incrementar las conversiones de CO. Sin embargo, la combinación de ambos metales dopantes en el catalizador $Pt/Ce_{0.9}ZrFeAl$ lograba superiores rendimientos catalíticos.

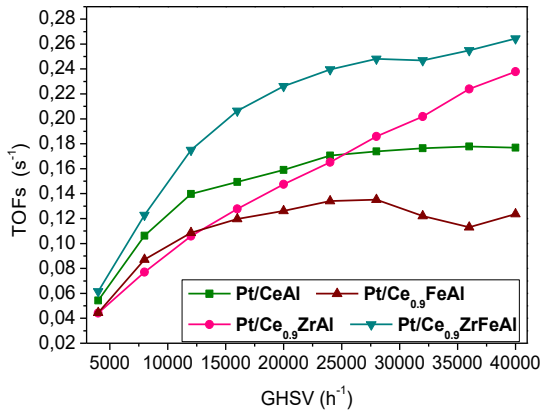

Figura R5. a) TOFs exhibidos por los catalizadores en condiciones "reales" en función de la velocidad espacial

Con el objetivo de dilucidar los cambios observados en función de la naturaleza del soporte en la actividad catalítica tanto los soportes como los catalizadores fueron examinados.

Así, las propiedades electrónicas de los soportes fueron analizadas por espectroscopía UV-VIS y Raman. En presencia de Fe, ambas técnicas indicaban modificaciones electrónicas importantes, por ejemplo, los cambios del espectro Raman exhibidos por el soporte $Ce_{0.9}FeAl$ con respecto al CeAl parecía responder a efectos electrónicos y no estructurales presentando la concentración más alta de vacantes de oxígeno en la superficie. Además, este soporte exhibía una disminución importante del valor de band gap del CeO_2 (calculado empleando la función de Kubelka-Munk) con respecto al $Ce_{0.9}ZrAl$. Sin embargo, la combinación de ambos agentes dopantes provocaba una brusca contracción del mismo indicando un efecto sinérgico (pues era superior a la suma de las disminuciones provocadas por los metales dopantes por separado) probablemente provocado por la incorporación de los niveles de ambos dopantes entre los del Ce y el O lo cual implica unas transferencias de carga especialmente facilitadas entre el cerio y el oxígeno de la red del CeO_2.

Tabla R.1. Energías de band gap y relaciónes O_v/F_{2g} calculadas para los soportes preparados

	BG (eV)	O_v/F_{2g}
CeAl	2.36	0.034
$Ce_{0.9}$ZrAl	2.33	0.036
$Ce_{0.9}$FeAl	2.01	0.065
$Ce_{0.9}$ZrFeAl	1.65	0.056

Además, las reducibilidades de los catalizadores fueron estudiadas mediante TPR-H_2. En todos los casos, se observó una reducción favorecida del soporte en presencia de Pt probablemente debida a la capacidad de spillover del Pt. Cuando se calcularon los porcentajes de reducibilidad, asumiendo que el Pt^{2+}, Ce^{4+} y Fe^{3+} se reducían respectivamente a Pt^0, Ce^{3+} y Fe^0, se obtuvieron valores en torno al 100% indicando un sobreconsumo en todos los casos si tenemos en cuenta los picos de Pt metálico observados en DRX (Figura R.6.a). Estos sobre consumos se atribuyen a la incorporación de especies de H en la red del cerio formando especies tipo bronce de la forma ref.

Con respecto a la reducibilidad, la combinación de ambos agentes dopantes conllevaba a sobreconsumos especialmente elevados tanto teniendo en cuenta el porcentaje de reducibilidad total (118 %) como la mayor reducibilidad relativa observada durante la primera zona de reducción que aparece con la subida de temperaturas.

Table R2. Reducibility percentages (RP) obtained for supports and catalysts

	RP (%)
Pt/CeAl	91
Pt/ $Ce_{0.9}$ZrAl	105
Pt/ $Ce_{0.9}$FeAl	100
Pt/ $Ce_{0.9}$ZrFeAl	118

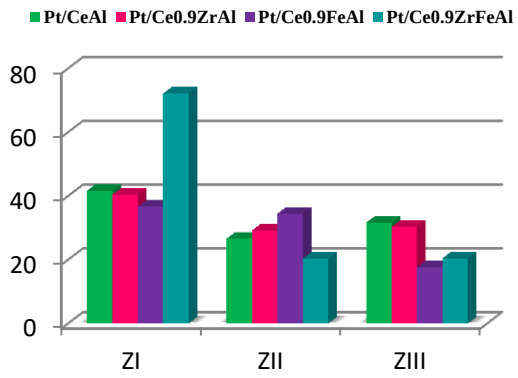

Figura R.6. a) % Reducibilidad total de los catalizadores; b) %Reducibilidad relativa

Asimismo, esta mayor facilidad para reducirse en presencia de H_2 y/o incorporar especies de H a su red, parecía ser reversible. En el TPD- H_2, el segundo y más importante proceso de desorción de H_2 se solapaba con el primero sólo en el caso del Pt/$Ce_{0.9}$ZrFeAl.

Por otra parte, se estudió por FT-IR la interacción del CO con los catalizadores de Pt. Para ello, los catalizadores se redujeron y desgasificaron previamente a la adsorción de CO. Tras las sucesivas dosis de CO, se saturaron y se desorbieron. Cuando comparamos los espectros a bajas absorciones de CO (aproximadamente, 1.4 μmol) se observó para todas las muestras el crecimiento de bandas que se pueden clasificar como: i) adsorción lineal de moléculas de CO sobre especies de Pt reducidas y ii) formación de especies carbonáceas, tipo hidrogenocarbonatos o carbonatos, en el soporte (Figura R.7) Además del desplazamiento observado en la banda de Pt-CO

debido a los diferentes cubrimientos, si comparamos el desarrollo relativo de ambas regiones (Pt-CO versus especies carbonáceas en el suporte) el catalizador Pt/$Ce_{0.9}$ZrFeAl parecía constituir una mayor cantidad de especies en el soporte con respecto a las que dejaba adsorbidas sobre el Pt. Esto podría indicar que el Pt/$Ce_{0.9}$ZrFeAl presenta una mayor tendencia a transferir las especies de CO, una vez activadas, al soporte mediante la reacción bien con especies OH o O presentes en el soporte.

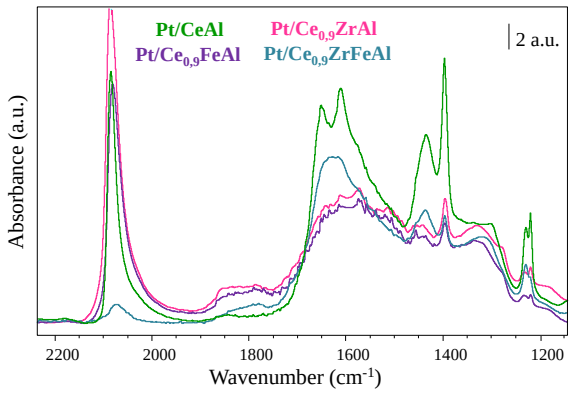

Figura R.7. Comparación de los espectros obtenidos para los catalizadores cuando se adsorben 1,4 μmol de CO

Además, en la Figura R.8 se muestra la comparación de los espectros obtenidos para la los catalizadores tras la saturación (R.8.a) y cuando son sometidos a vacío secundario (R.8.b). Como puede observarse, el Pt/$Ce_{0.9}$ZrFeAl parece tener una mayor capacidad para desorber las especies formadas en el soporte con respecto a las demás.

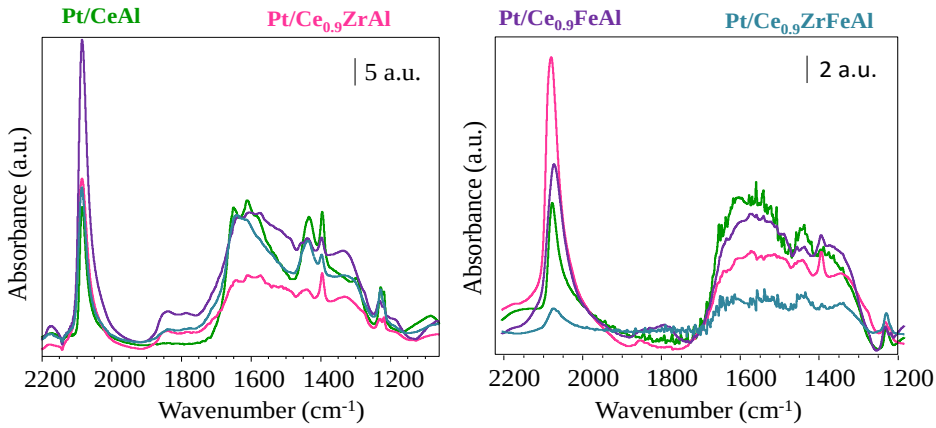

Figura R.8. Comparación de los espectros obtenidos para los catalizadores: a) Saturados; b) Vacío secundario

De acuerdo a la observada capacidad de desorción, el catalizador $Pt/Ce_{0.9}ZrFeAl$ mostró, durante un TPD-CO, desorciones de CO_2 e H_2 a más baja temperaturas que el resto de los catalizadores indicando una mayor capacidad para descomponer especies carbonáceas hacia los productos de reacción de la WGS.

De hecho, el anclaje de dichas especies en el soporte se reconoce como una causa importante de desactivación para catalizadores basados en cerio ya que bloquean los sitios activos del soporte conllevando así, a una pérdida de actividad y finalmente, a la desactivación del mismo.

Algunas consideraciones más con respecto a los fenómenos de desactivación pudieron obtenerse a partir del TPO que se llevó a cabo después del TPD-CO para todas las muestras (Figura R.9). Durante el TPO, el sistema $Pt/Ce_{0.9}ZrFeAl$ exhibió una menor cantidad de CO_2 que el resto de los

catalizadores de la serie. En este caso, el CO_2 puede proceder de la oxidación de C formado mediante la reacción de Boudouard o bien de especies como bicarbonatos o carbonatos que se forman en el soporte. Por lo tanto, el catalizador $Pt/Ce_{0.9}ZrFeAl$ presentaba una menor tendencia total al bloqueo de los sitios activos del soporte.

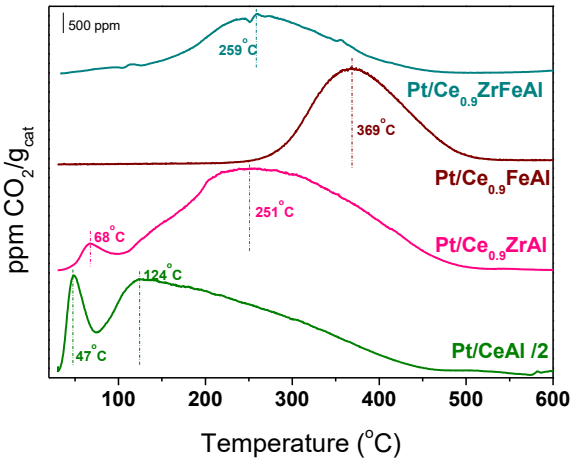

Figura R.9. Evolución de la m/z=44 exhibida por los catalizadores durante el TPO

En conclusión, la combinación de ambos promotores conseguía un catalizador más activo y con una mayor resistencia frente a dichos fenómenos de desactivación estando ambos fenómenos relacionados con la mayor movilidad de especies de H bien fueran OH o H.

4. Estructurado de catalizadores Pt(2%)/CeO_2/Al_2O_3: Introducción de una capa buffer

Este capítulo de la tesis doctoral se centra en intentar mejorar la disociación del agua ya que se considera la etapa limitante de la reacción de WGS. Además, este planteamiento se combina con el proceso de estructurado de catalizadores en micromonolitos metálicos atendiendo a los beneficios que ofrecen para reacciones lentas y exotérmicas como la WGS así como el interés que presenta como etapa intermedia ante un posible escalado.

De esta forma, se estructuraron cantidades crecientes de un catalizador basado en Pt/Cerio en una serie de micromonolitos metálicos y analizó si se conseguía mejorar la actividad catalítica mediante el estructurado así como la importancia de los fenómenos de transporte en los catalizadores estructurados. Tras esto, se comparó uno de los catalizadores estructurados constituidos por una sola capa de catalizador (Pt(2%)/CeO_2/Al_2O_3) con uno constituido por dos capas diferentes: una capa de CeO_2/Al_2O_3 depositada encima del sustrato metálico seguido de una capa de Pt(2%)/CeO_2/Al_2O_3. Los diferentes comportamientos catalíticos obtenidos en función del catalizador estructurado y las condiciones de reacción fueron estudiados.

4.1. Síntesis de los catalizadores estructurados

En primer lugar se prepararon las estructuras metálicas enrollando dos láminas de acero ferrítico, FeCrAlloy, una lisa y otra rizada en torno a un eje.

Tras esto, los micromonolitos se calcinaron durante 22 h a 900 ºC con el objetivo de generar una capa de α-Al_2O_3 que incremente la rugosidad del substrato metálico y favorezca la adhesión del catalizador.

Por su parte, como catalizador se usó Pt(2 p/p.%)/CeO_2/Al_2O_3. Tanto para el soporte del catalizador como el buffer, se empleó un CeO_2/Al_2O_3 comercial (Puralox) que contenía un 20 p/p.% de CeO_2. El Pt se depositó por impregnación húmeda siguiendo el procedimiento descrito anteriormente. La nomenclatura empleada para el catalizador y el buffer fue Pt/CeAl y CeAl.

Los polvos, catalizador y buffer, se impregnaron en los micromonolitos metálicos mediante el método de washcoating. Las suspensión estaban compuestas por 1.96 p/p.% de una solución de PVA (1.5 p/p.% PVA en agua), 17.65 p/p.% de Al_2O_3 coloidal (Nyacol, 20 p/p.% en agua), 18.14 p/p.% de catalizador y 62.25 wt.% de agua. Los sólidos añadidos a la suspensión fueron previamente molidos de manera que presentasen tamaños de en torno a 10 μm. Las propiedades reologicas fueron modificadas añadiendo aditivos, PVA y alúmina coloidal, para conseguir unas deposiciones más homogéneas y suspensiones más estables ya que estos actúan como "binders" y surfactantes.

Una vez depositados, los monolitos fueron calcinados en las mismas condiciones que sus polvos iniciales (350 ºC – 8h en el caso del Pt/CeAl y 450 ºC – 4h en el caso del bufer CeAl) pero empleando una rampa de calentamiento de 2 ºC/min de manera que se evitase el resquebrajamiento de

la capa de catalizador debido a los diferentes coeficientes de expansión que presentan estos frente al substrato metálico. Las suspensiones fueron secadas y calcinadas en las mismas condiciones. Tras esto, las suspensiones del catalizador Pt/CeAl y el buffer CeAl se denominaron S_Pt/CeAl y S_CeAl, respectivamente.

Por una parte, se sintetizaron 3 micromonolitos en los que se depositaron 0.3, 0.6 y 1g de catalizador. La nomenclatura usada para estos monolitos fue M0.3, M0.6 y M1, respectivamente. Por otra, se sintetizó otro catalizador estructurado que contenía una capa de 0.3g de buffer CeAl seguida de una capa que contenía 0.3 g de catalizador Pt/CeAl. A este micromonolito se le denominó M0.3-B0.3.

4.2. Resultados y discusión

En primer lugar y con el objetivo de determinar si se producen cambios importantes durante el método de washcoating, se testaron los catalizadores Pt/CeAl y S_Pt/CeAl en model mixture y a GHSV = 4000 h^{-1} (Figura R.10.a). De acuerdo con los resultados obtenidos en DRX, ambos sistemas presentaban actividades catalíticas similares indicando la ausencia de cambios importantes durante la preparación de la suspensión. Las mínimas diferencias podrían ser atribuidas a la menor carga de Pt presente en la suspensión debido a la adición de alúmina coloidal durante la síntesis de la misma.

Por otra parte, en la Figura R.10.b se analiza el efecto del estructurado a través de la comparación de la actividad catalítica que presenta el catalizador inicial, en polvo, y la que exhibe una vez estructurado. La diferencia de actividad catalítica entre las Figuras R.10.a y R.10.b se debe atribuir a las distintas relaciones flujo/carga de catalizador empleadas en las mismas siendo 6 L/gh y 80 L/gh, respectivamente.

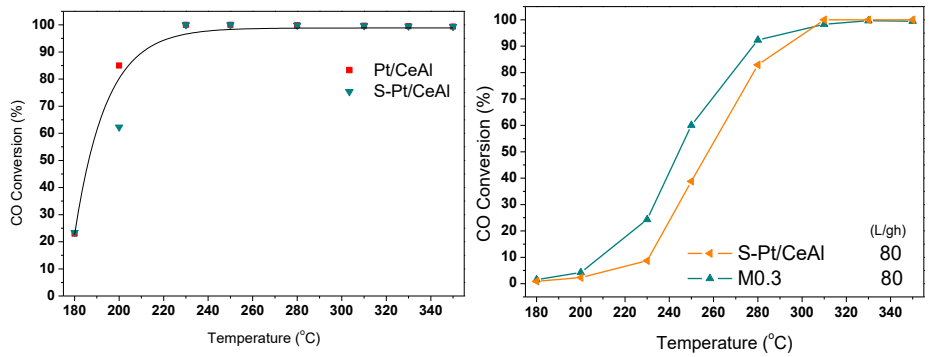

Figura R.10. Comparación de las actividades catalíticas en condiciones modelo exhibida por a) Pt/CeAl y S_Pt/CeAl a 6L/gh; b) S-Pt/CeAl y M0.3 a 80L/gh

Tal y como se esperaba, el empleo de micromonolitos metálicos conlleva mejores comportamientos catalíticos probablemente debidos a las mejores transferencias de masa y calor proporcionadas por los micromonolitos metálicos. Dicho resultado concuerda con los datos presentados por Fu et al. en [40] donde alcanzaban mejores resultados para catalizadores de Pt a través de procesos de estructurado.

Por otra parte, se calcularon los factores de eficiencia (η) para el CO para M0.3, M0.6 y M1. Esto se llevó a cabo empleando el modelo propuesto por Weisz and Hicks [41] que permite estimarlos a partir de variables observables resultando, para todos los casos, en factores de eficiencia para el CO $\eta = 1$.

Esto concuerda bastante bien con los resultados que se presentan en la Figura R.11.a y R.11.b donde la actividad catalítica de los sistemas estructurados depende de la relación L/gh a la que se ensayan. Así, para un mismo flujo, mayores cantidades de catalizador conllevan mayores conversiones mientras que distintas cantidades de catalizador, ensayadas con relaciones L/gh equivalentes, presentan las mismas conversiones.

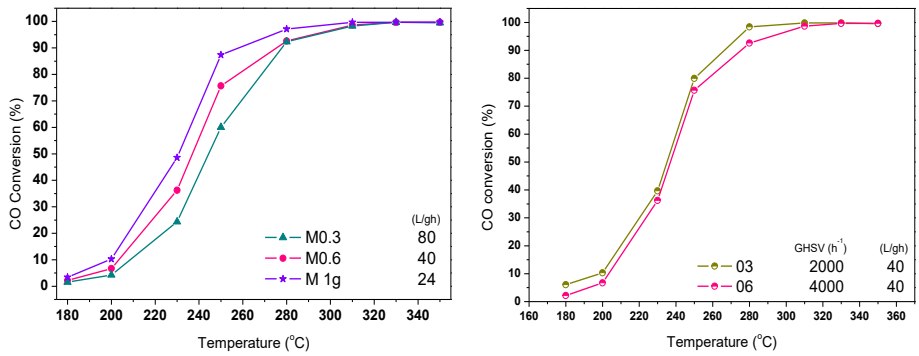

Figura R.11. Actividad catalítica en condiciones modelo de: a) M0.3, M0.6 y M1 a 4000h^{-1}; b) M0.3 y M0.6 a 40 L/gh

De hecho, en base a los bajos espesores de capa obtenidos, cabía esperar la ausencia de limitaciones de transferencias de masas. Por lo tanto, se puede

postular que, para los espesores de capa obtenidos, la actividad catalítica de los catalizadores estructurados no está significativamente limitada por los procesos difusionales del CO, lo cual permite obtener comportamientos catalíticos superiores cuanta más cantidad de catalizador se soporta en el micromonolito. De hecho, resultados similares en cuanto a la ausencia de limitaciones para tales espesores de capa catalítica han sido publicados recientemente por Laguna et al. [42] quienes demostraban que el comportamiento catalítico en microrreactores no estaba controlado por limitaciones difusionales para espesores de en torno a 10 μm. En la misma línea, Potemkin et al. [43] establecieron un límite sobre las 20 μm, para el cual los procesos difusionales no controlaban la velocidad de reacción. De manera general, Farrauto et al. [44] propusieron que los catalizadores de estructurados de WGS no estaban limitados por procesos de difusión en el poro.

Partiendo de los resultados anteriores, el efecto de la presencia de la capa buffer en el comportamiento catalítico de los sistemas estructurados puede ser directamente correlacionado con la química de los sistemas puesto que, en los micromonolitos estudiados, la adición de la capa buffer debajo de la capa de catalizador no debería afectar a las propiedades del transporte de masas ya que se mantienen bajos espesores de capa catalítica.

En la figura R.12 se muestra la actividad catalítica que presentaban los sistemas M0.3 y M0.3-B0.3, en función de la temperatura, cuando se ensayan a 4000 h^{-1} y a 2000 h^{-1} en condiciones modelo.

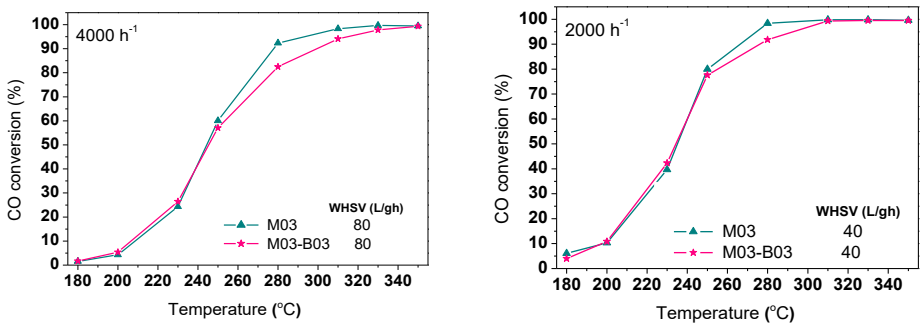

Figura R.12. Efecto de la capa buffer layer en la actividad catalítica en condiciones modelo: a) 4000 h^{-1}; b) 2000 h^{-1}

Por otra parte, M0.3 y M0.3-B0.3 se ensayaron en mezcla que simula la salida de un reactor de autoreformado, tras la adición de vapor de agua de manera que se favorezca la reacción de WGS (50% H_2, 7% CO, 9% CO_2, 30% H_2O, balanceado en N_2). En dichas condiciones, Figura R.13, el catalizador M0.3 disminuye su actividad catalítica desplazándose a mayores temperaturas. En esta figura, la actividad del M0.3 se compara con la obtenida por Germani et al. [45] para un catalizador 1.4%Pt/CeO_2/Al_2O_3 estructurado en un microrreactor operando a ~73 $L \cdot g^{-1} \cdot h^{-1}$ y empleando una alimentación similar a la anterior (32,2% H_2, 9,6% CO, 8,4% CO_2, 23% H_2O, balanceado en Ar). A pesar de las diferencias en cuanto al contenido de Pt, la relación L/gh y la composición de la mezcla reactiva ambos catalizadores estructurados

presentan similares conversiones de CO con la temperatura. De esta manera, podría asumirse que su misma ley de velocidad debería ajustar nuestros resultados experimentales si se consideran las distintas cargas de Pt en el factor pre-exponencial de la expresión de Arrhenius:

$$-r_{CO} = (1.5 \cdot 10^8) \times \left(e^{-\frac{86000}{RT}}\right) \times CO^{0.13} \times H_2O^{0.49} \times H_2^{-0.45} \times CO_2^{-0.12} \times \left(1 - \frac{H_2 \times CO_2}{K_{eq} \times CO \times H_2O}\right) \quad \textit{(Ecuación R.1)}$$

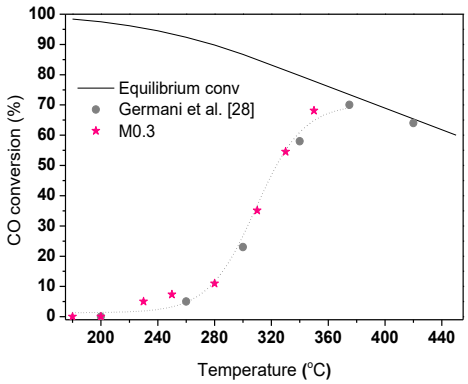

Figura R.13. Comparación de la actividad catalítica presentada por el monolito a 80 L/gh empleando una alimentación 50% H_2, 7% CO, 9% CO_2, 30% H_2O, balanceado en N_2 con los resultados presentados por Germani et al [28] para un microreactor que opera a 73 $L \cdot g^{-1} \cdot h^{-1}$ empleando una alimentación de composción 32,2% H_2, 9,6% CO, 8,4% CO_2, 23% H_2O, balanceada en Ar.

Sin embargo, la presencia de la capa buffer afecta claramente la actividad catalítica de los monolitos cuando se prueban en una mezcla reactiva típica de la salida de un reactor de autoreformado tras la adición de vapor de agua, Figura R.14.a. En estas condiciones, la presencia de la capa buffer consigue casi duplicar la actividad catalítica de los sistemas a 260 ºC. Considerando

que el catalizador era el mismo, dicha mejora debe ser adscrita sólo a la presencia de la capa buffer. Además, la presencia de la capa buffer prácticamente no afecta la actividad del catalizador en condiciones modelo. Por lo tanto, la variación en el comportamiento catalítico ha de relacionarse con la corriente reactiva en función de la presencia o no de la capa buffer de CeAl. La figura R.14.b compara las conversiones de CO observadas para M0.3 y M0.3-B0.3 con las calculadas asumiendo la ley cinética propuesta por Germani et al. [28]. Así, las conversiones observadas y calculadas parecen ajustar bastante bien en el caso del sistema M0.3 obteniéndose un ajuste lineal de pendiente 1.01±0.05. Sin embargo, el ajuste lineal del sistema M0.3-B0.3 presentaba una pendiente mayor (1.42±0.08) de acuerdo con las observadas mejoras catalíticas.

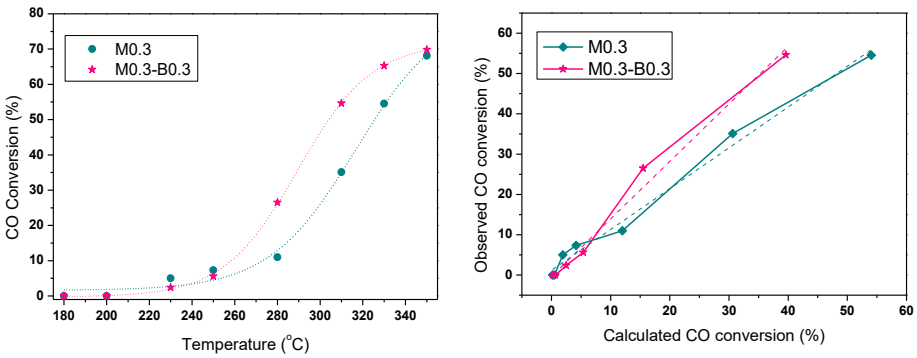

Figura R.14. a) Efecto de la capa buffer en la actividad catalítica de M0.3 y M0.3-B0.3 a 80 L·g^{-1}·h^{-1} empleando una alimentación compuesta por 50% H_2, 7% CO, 9% CO_2, 30% H_2O, balanceada en N_2; b) Comparación de la conversión observada y calculada según la ley cinética propuesta por Germani et al. [45]

Cuando se observan los órdenes de reacción propuestos en literatura para catalizadores de Pt/Al_2O_3 y/o Pt/CeO_2, las mayores diferencias se detectan cuando la corriente de alimentación no incluye CO_2 y H_2 [4,14]. En general, cuando se incluyen dichas especies los órdenes aparentes y las energías de activación son bastante similares a pesar de las diferencias en la naturaleza del soporte, el contenido de Pt y la composición de la mezcla reactiva. La principal diferencia entre los estudios se da en el orden de reacción aparente para el agua que varía entre 0.44-1.10. Obviamente, dichas diferencias deben ser atribuidas a la naturaleza del soporte y/o a la presencia de Re. Con respecto al CO_2, el orden de reacción aparente cercano a cero se explica por la débil interacción entre el CO_2 con la superficie de Pt [30]. Por su parte, las diferencias observadas para el orden de reacción aparente para el CO se deben a la disminución de la energía de enlace del CO absorbido en Pt conforme aumenta el grado de cubrimiento [46–49], lo cual también explica el orden negativo para el H_2: conforme aumenta el cubrimiento del CO, su energía de enlace disminuye favoreciendo la adsorción e inhibición de la reacción de WGS causada por las especies de H_2 [50]. Phatak et al. [14] propuso un orden de reacción para el H_2, (- 0.5 aprox.), afirmando que, una vez que la superficie está saturada, el H atómico dominará la superficie [14]. El incremento del grado de cubrimiento de la superficie por parte de las especies de H atómico, conlleva la inhibición de la reacción de WGS. Además, los diferentes órdenes aparentes de reacción calculados para el agua fueron asociados a diferentes mecanismos de reacción en función del soporte.

En el presente trabajo, no se pueden proponer distintos mecanismos de reacción ni distintas energías de activación puesto que el catalizador empleado es siempre el mismo. De acuerdo con los resultados observados, la velocidad de reacción del catalizador M0.3-B0.3 puede ajustarse de acuerdo a la ecuación R.1 cuando se ensaya en mezcla modelo. Sin embargo, en presencia de una corriente de reacción que simula la de salida de un reformador, la capa buffer altera el comportamiento catalítico del catalizador estructurado resultando en comportamientos catalíticos superiores. En este caso, los datos experimentales pueden ser ajustados con una ecuación cinética similar cuya única diferencia con la anterior es un orden de reacción aparente para el agua superior:

$$-r_{CO} = (1.6 \cdot 10^{8}) \times \left(e^{-\frac{86000}{RT}}\right) \times CO^{0.13} \times H_2O^{0.70} \times H_2^{-0.45} \times CO_2^{-0.12} \times \left(1 - \frac{H_2 \times CO_2}{K_{eq} \times CO \times H_2O}\right) \quad \text{(Ecuación R.2)}$$

El incremento del orden de reacción para el agua debe atribuirse a una mayor disponibilidad del soporte para activar el agua. Recientemente, Clay et al. [51] modelizó mediante DFT la cinética de un catalizador de Pt para WGS proponiendo un mecanismo con carboxilos como intermedios de reacción y afirmando que el paso limitante de velocidad era la etapa de disociación del agua. De acuerdo con su modelo, el paso limitante de velocidad es dependiente del grado de cubrimiento de la superficie por CO de tal forma que, para mayores presiones parciales de CO, el paso limitante de velocidad pasa a ser la formación del intermedio carboxilo. El cambio del paso limitante

de la velocidad de reacción hace referencia a la dependencia de los órdenes de reacción aparentes con respecto a las condiciones de reacción ya que estas determinarán el cubrimiento de la superficie en función de las presiones parciales superficiales. En consecuencia, un mayor cubrimiento de la superficie por especies de H_2 resultará en una inhibición de la formación de los productos de reacción formados por reacción de CO + OH.

Olimpiou et al. [3], que estudió catalizadores de Pt y Rh soportados sobre γ-Al_2O_3 empleando el método SSITKA, concluyó que los grupos hidroxilos lábiles así como las especies de H procedían de la molécula de agua y se encontraban principalmente sobre el soporte. Sin embargo, sólo una pequeña fracción de dichas especies son energéticamente capaces de difundir hasta el metal para dar H_2 [52,53].

Además, otros estudios DFT sostienen que la disociación de agua esta favorecida en óxidos de cerio parcialmente reducidos, con o sin Pt [54]. Más recientemente, Anarifard et al. llevó a cabo un estudio DFT sobre Pt/Cerio postulando que la disociación del agua se da principalmente en las vacantes de oxígeno a través de la transferencia de átomos de H a átomos de oxígeno circundantes del soporte [55]. Además, el papel de las vacantes de oxígeno se relacionó con una mayor capacidad para estabilizar fragmentos originados en la disociación del agua.

Así, la introducción de la capa buffer CeAl debe proporcionar un mayor número de sitios para la absorción de moléculas de agua. De hecho, la elevada

presión parcial del H_2 deberá resultar en una superficie de cerio parcialmente reducida favoreciéndose así, la disociación de las moléculas de agua y la estabilización de las especies disociadas en la capa buffer [52–56].

Además, una mayor concentración de vacantes de oxígeno conlleva densidades electrónicas superiores en torno a las partículas metálicas [13,19,57–59]. Dicha densidad electrónica debería inhibir la adsorción del H_2 debido a su carácter donador lo que conllevaría una mayor disponibilidad de sitios activos para la adsorción del CO a la vez que se disminuye su energía de adsorción en Pt. En la misma línea, Farrauto et al. [48] logró unas selectividades superiores para la reacción de PrOx a partir del a disminución de la fuerza de interacción H_2-metal. Sin embargo, este efecto es independiente de la presencia de la capa buffer de manera que no puede explicar por sí mismo la mejora catalítica observada.

Volviendo a la idea inicial, resulta evidente que la hipótesis basada en incrementar el número de moléculas de agua absorbidas de manera que puedan ser activadas conllevando mejores comportamientos catalíticos, ha sido alcanzada. En tales condiciones reductoras, incrementando la concentración de óxido de cerio mediante la incorporación de la capa buffer, se incrementa el número de vacantes de oxígeno de manera que se logran catalizadores estructurados con superiores comportamientos catalíticos. Sin embargo, el balance entre el carácter reductor y oxidante de la corriente de entrada controla la capacidad de mejora proporcionada por la capa buffer. Así,

si el carácter de la mezcla de alimentación es más oxidante, como en el caso de la mezcla modelo, las moléculas de agua pueden oxidar la capa buffer inhibiendo los beneficios proporcionados por la misma. No obstante, si el carácter reductor de la mezcla de reacción supera al oxidante, la capa buffer actúa como una reserva de grupos hidroxilos capaz de difundiros hasta los sitios activos metálicos a velocidades superiores que las de la reacción.

5. Rol de la capa buffer: importancia de la disociación de H_2O en WGS

Distintos sistemas estructurados fueron preparados estando todos ellos compuestos por dos capas diferenciadas: la capa buffer, justo encima del substrato metálico, y sobre esta, la capa de catalizador. En este estudio, la composición de la capa buffer fue modificada mientras que siempre se mantuvo la capa de catalizador constante. El papel de la capa buffer en la reacción de WGS fue directamente correlacionado con el agua.

La composición de las capas buffers fue seleccionada en función de la capacidad para activar agua de los distintos óxidos. Así, la alúmina no es capaz de disociar agua mientras que un CeO_2/Al_2O_3 sí que presenta dicha capacidad debido a las vacantes de O presentes en su red. Por último, un óxido de cerio dopado con Eu^{3+} debería ser presentar capacidades superiores para la activación de las moléculas de agua en base a una mayor concentración de vacantes provicadas tanto por la descompensación de carga como por la diferencia entre los tamaños de ambas especies.

Por último, se preparó un micromonolito constituido por una sola capa a partir de una mezcla física compuesta a su vez por el catalizador y por el buffer de cerio dopado con europio. La idea fue que si conseguíamos mejorar el contacto entre el buffer que activaba el agua y el sitio activo de Pt, se conseguirían mejores rendimientos catalíticos.

5.1. Preparación de los sistemas estructurados

La preparación y adecuación de los micromonolitos se realizó de la misma forma que en el apartado 4.1. Por otra parte, se necesitaron 4 sólidos iniciales Al_2O_3, CeO_2/Al_2O_3 y $Ce_{0.9}Eu_{0.1}O_2/Al_2O_3$. Ambos soportes basados en cerio estaban constituidos por un 20 p/p% de óxido de cerio (dopado o sin dopar) soportado sobre una γ-Al_2O_3 de alta superficie. Estos se sintetizaron por impregnación húmeda y de forma análoga a la descrita en el apartado 3.1. En el caso del Eu, el precursor usado fue $Eu(NO_3)_3 \cdot 5H_2O$ (Aldrich). Como catalizador se usó un Pt (2 p/p%)/CeO_2/Al_2O_3 siendo este soporte comercial (Puralox) y también se sintetizó como se describe en el apartado 2.1. La nomenclatura empleada para los Al_2O_3, CeO_2/Al_2O_3 y $Ce_{0.9}Eu_{0.1}O_2/Al_2O_3$ fue Al, CeAl y CeEuAl mientras que el catalizador se denominó Pt/CeAl. La mezcla física se llamó PMix y fue preparada mezclando CeEuAl y Pt/CeAl en proporción 1:1.

Todos los catalizadores se depositaron en los monolitos mediante el método washcoating y para la preparación de la suspensión se empleó la misma receta detallada en el apartado 4.1. En este estudio, se mantuvo constante la cantidad

de sólido depositado en todos los casos. Así, todos los catalizadores estructurados compuestos por dos capas contenían 0.3 g de buffer y sobre estos, 0.3 g de catalizador. Por su parte, el sistema estructurado sintentizado a partir de la mezcla física contenía 0.6g de PMix. Para denominar a las respectivas suspensiones, se empleó el prefijo "S_" seguido del nombre del correspondiente polvo inicial. Por ejemplo, a la suspensión formulada a partir del CeAl se la llamó S_CeAl.

La nomenclatura empleada para los catalizadores estructurados hacía referencia al buffer incorporado; de esta forma al monolito que contenía una capa de buffer basada en CeAl se le denominó M_CeAl mientras que al que contenía la PMix se le denominó P_Mix. Con el objetivo de esclarecer, en la Figura R.15 se presenta el conjunto de catalizadores estructurados de una forma esquemática.

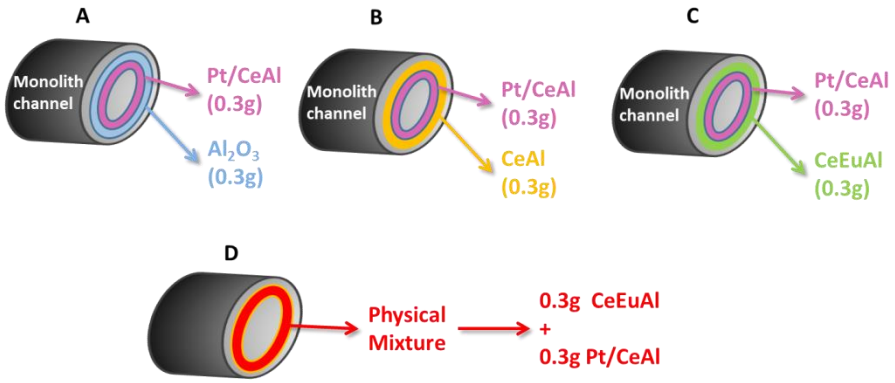

Figura R.15. Esquemáticamente, conjunto de catalizadores estructurados preparados en este apartado

5.2. Resultados y discusión

En la Figura R.16.a, se muestra la actividad catalítica del catalizador de Pt inicial comparado con su respectiva suspensión. Ambas muestras exhibieron similares comportamientos catalíticos indicando que no se habían producido cambios importantes en el catalizador durante el proceso de estructurado.

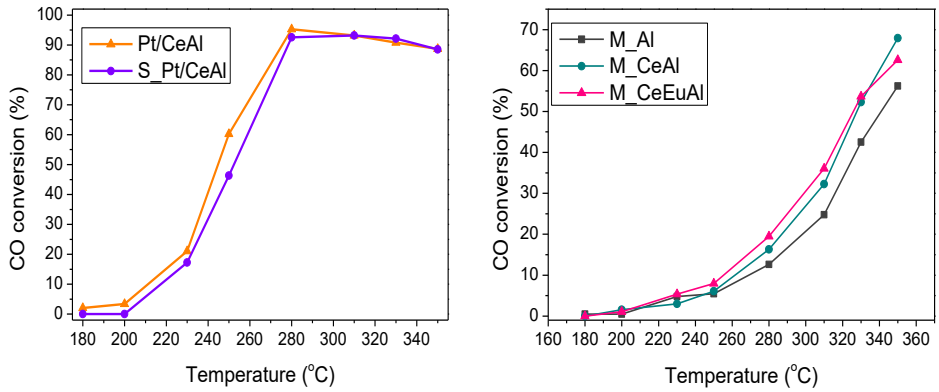

Figura R.16. Actividad catalítica obtenida para a) Pt/CeAl y S_Pt/CeAl a 6 L/gh; b) M_Al, M_CeAl and M_CeEuAl a 80 L/gh empleando para ambos una alimentación compuesta por 7% CO + 9% CO_2 + 50% H_2 + 30% H_2O

Por otra parte, en la Figura R.16.b se observa la actividad catalítica de los micromonolitos M_Al, M_CeAl and M_CeEuAl. Las diferencias en actividad catalíticas entre las muestras en polvo y los catalizadores estructurados deben atribuirse a las diferentes condiciones catalíticas en las que fueron testados, 6 L/gh y 80 L/gh, respectivamente.

Con el objetivo de determinar la contribución de la naturaleza de la capa buffer en función de la atmósfera de reacción, se analizó la variación de las

concentraciones relativas de cada componente en la corriente de alimentación (Figura R.17).

En este caso, la concentración del CO_2 fue disminuida del 9% al 3% con el objetivo de ampliar el rango de variación de los componentes. A partir de la composición inicial resultante, 7% CO + 3% CO_2 + 50% H_2 + 30% H_2O, se variaron las presiones parciales de cada componente. La Figura R.17 muestra los resultados obtenidos para esta serie de experimentos. Teniendo en cuenta que la reacción de WGS es un equilibrio, el incremento de la concentración de los productos de la reacción a la entrada del reactor deberá conllevar una disminución de la conversión de CO.

Especialmente para los buffer compuestos por óxido de cerio, la variación del % CO_2 no conllevó cambios importantes en las conversiones de CO observadas. Contrariamente, la incorporación de H_2 a la mezcla reactiva provocaba importantes disminuciones en las actividades catalíticas. Esto debe atribuirse tanto al desplazamiento del equilibrio termodinámico como a la competición entre las moléculas de CO e H_2 para ser adsorbidos en los sitios activos metálicos. Por su parte, el aumento del % CO también disminuía las conversiones de CO en todos los casos probablemente debido al mayor número de moléculas de CO que deben ser convertidas por el mismo número de centros activos de Pt. En general, se puede afirmar que todos los cambios observados en las variaciones de % CO, % CO_2 e % H_2 fueron similares en todos los sistemas estructurados analizados.

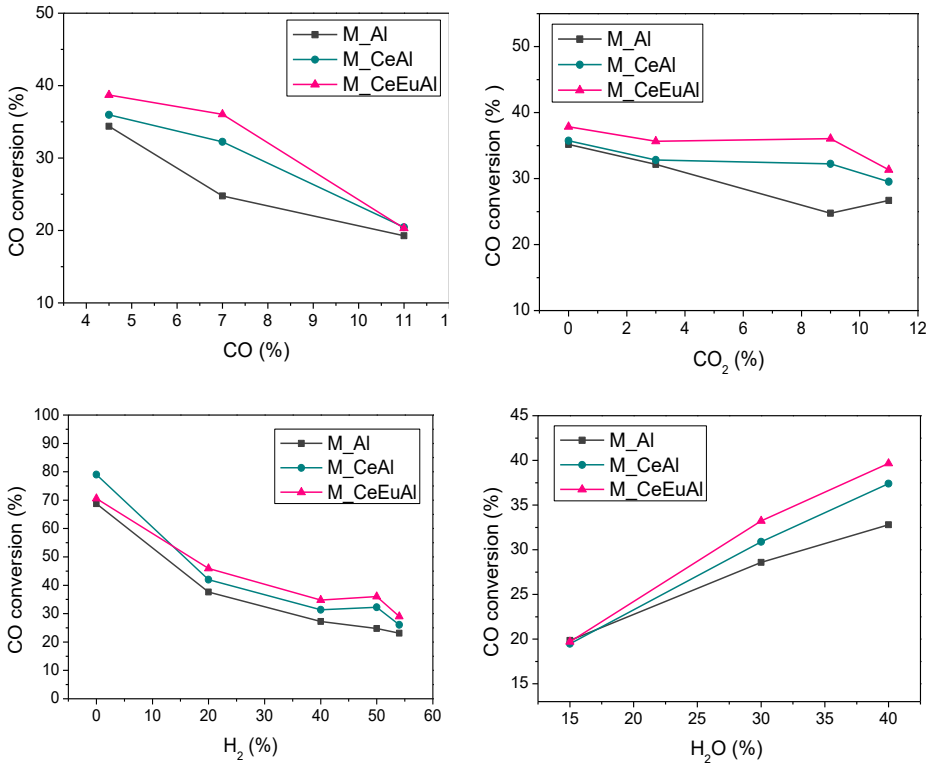

Figura R.17. Efecto sobre la actividad catalítica de los sistemas M_Al, M_CeAl and M_CeEuAl cuando se variaban las presiones parciales de: a) % CO; b) % CO_2; c) % H_2 y d) % H_2O

Sin embargo, la variación de la concentración de H_2O sí que conllevaba diferentes cambios en el comportamiento de los estructurados en función de la naturaleza de la capa buffer (Figura R.17.d). A bajas concentraciones de H_2O todos los micromonolitos alcanzaban las mismas conversiones de CO. El incremento de la presión parcial conllevaba mejores conversiones de CO para todos los sistemas lo cual, teniendo en cuenta que la reacción de WGS es un equilibrio, parece lógico. A pesar de esto, el grado de mejora observado en

función de la concentración de H_2O fue: M_CeEuAl > M_CeAl > M_Al. De acuerdo al hipótesis inicial, esto puede estar relacionado con el las diferentes capacidades para disociar agua de los distintos óxidos que componían las capas buffer. De hecho, la capacidad de mejora respondía directamente al número de vacantes de oxígeno contenido en cada uno de los óxidos.

Hasta este momento, las mejoras del comportamiento catalítico des sistemas estructurados se consigue mediante la incorporación de dos capas diferenciadas: la capa de catalizador y la capa buffer con capacidad de modular la actividad del catalizador en función de su capacidad para disociar moléculas de agua y de las condiciones de reacción. No obstante, cabría esperar que una mejora del contacto entre ambas capas, mezclándolas físicamente previa deposición, conllevara mejoras en la actividad catalítica del sistema. En la Figura R.18 se muestran la actividad catalítica del catalizador preparado a partir de la mezcla física comparado con todos los demás estructurados preparados.

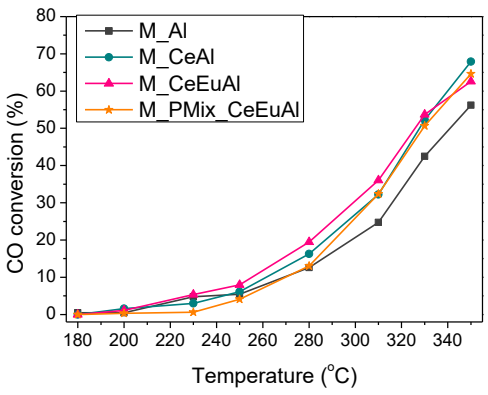

Figura R.18. Actividad catalítica presentada por M_Al, M_CeAl, M_CeEuAl and M_PMix_CeEuAl, empleando una corriente de alimentación 7%CO + 9%CO_2 + 30%H_2O + 50 % H_2 y 80 L/gh

Los resultados mostraron que el comportamiento catalítico de los sistemas estructurados no responde a nuestras expectativas, de manera que las conversiones de CO no fueron superiores en el caso del M_PMix_CeEuAl. Esto podría deberse a la inmersión de los centros activos metálicos en el seno la capa catalítica lo cual conlleva que no se mejore su comportamiento.

El efecto de la presión parcial del agua para estos sistemas se presenta en la Figura R.19.a. En tales condiciones, la muestra M_PMix_CeEuAl muestra superiores comportamientos catalíticos en comparación con el resto de muestras. De hecho, el aumento de la presión parcial de agua induce mayores mejoras en catalizador estructurado con la mezcla física que en los catalizados que contienen dos capas.

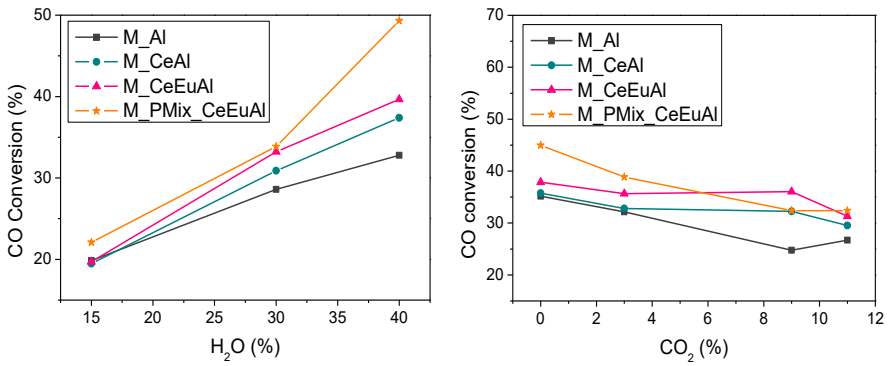

Figura R.19. Actividad catalítica obtenida para M_Al, M_CeAl, M_CeEuAl y M_PMix_CeEuAl cuando son variadas: a) % H_2O y b) % CO_2

Teniendo en cuenta que la única diferencia que existía entre el test que variaba las presiones parciales de agua y la actividad catalítica de la Figura R.18 es la % CO_2 introducida, el efecto del CO_2 fue analizado (Figura

R.19.b). Durante este experimento, se observó como la presencia de CO_2 afectaba en mayor medida al M_PMix_CeEuAl que al resto de los sistemas compuestos por dos capas lo cual se puede explicar a partir de efectos de desactivación por especies carbonáceas fuertemente unidas al Ce^{3+} de manera que se bloqueen los sitios activos del soporte capaces de activar el H_2O. Esto podría implicar que la configuración en dos capas también logra un efecto beneficioso en cuanto a los efectos de desactivación por especies carbonáceas. Resultados parecidos fueron presentados por Ruettinger et al. [60] quienes observaron, tras envejecer el catalizador, tonos más oscuros en las capas de catalizador externas atribuyéndolo a cantidades mayores de especies carbonáceas depositadas. De hecho, esto podría explicar que concentraciones superiores de CO_2 a la entrada del reactor conlleven disminuciones en las conversiones de CO más leves.

Con el fin de analizar los cambios observados relacionados con el agua en función de la naturaleza del buffer, se llevaron a cabo experimentos seguidos por IR en los que se incorporaban cantidades crecientes de agua sobre las muestras en polvo. Para los sistemas que contenían cerio, el crecimiento observado de las bandas atribuidas a OH e H asociados (3900 – 3400 cm^{-1}) debe ser directamente relacionado con una cierta capacidad para disociar agua. Además, las diferencias observadas en cuanto a las posiciones de las bandas fueron relacionadas con las distintas naturalezas de los óxidos, conllevando distintos entornos químicos y, por lo tanto, distintas frecuencias de vibración. Además, conforme se introducían mayores cantidades agua se

detectó el crecimiento de una banda a 1640 cm^{-1} adscrita a agua molecularmente absorbida

En la Figura R.20, se muestran los espectros obtenidos para las muestras cuando se había introducido cantidades similares agua ($3 \cdot 10^{-18}$ $\mu mol/nm^2$). En la región 3900 – 3400 cm^{-1}, se observan diversas bandas atribuidas a vibraciones de OH así como a especies de H [61,62]. En la región 2240 – 1320 cm^{-1}, la amplia banda que se observa en torno a 1600 cm^{-1} puede ser atribuida a agua molecularmente absorbida. Probablemente, esta banda está constituida por diversas contribuciones debido a los distintos entornos químicos en los que el agua está absorbida. Como puede observarse, la capacidad mostrada por los sólidos para disociar moléculas de agua así como para absorberla siguió la tendencia: CeEuAl > CeAl > Al.

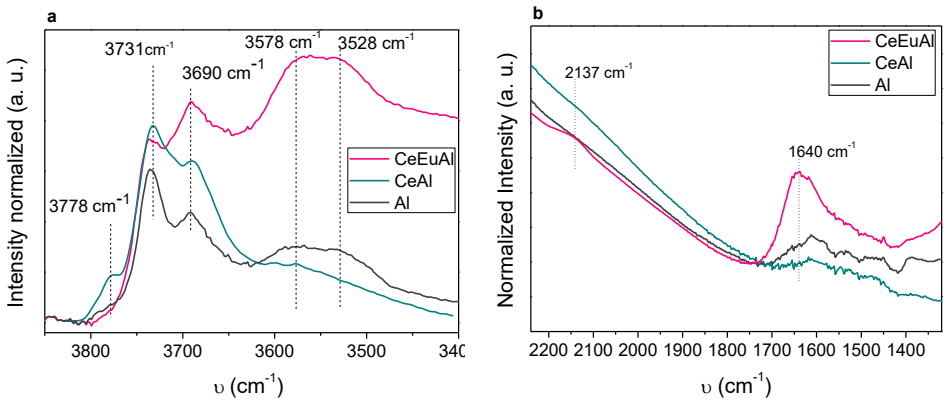

Figura R.20. Espectros FT-IR obtenidos para Al, CeAl and CeEuAl cuando $3 \cdot 10^{-18}$ $\mu mol/nm^2$ de agua fueron introducidos: a) 3900 – 3400 cm^{-1}; b) 2250 – 1320 cm^{-1}

Una vez saturadas, se desgasificaron las muestras sometiéndolas a vacío primario y secundario y, posteriormente, calentadas a 50, 100, 150 y 200ºC. En la Figura R.21, se observan los espectros de las muestras cuando fueron sometidos a 200 ºC. En comparación el CeAl, la muestra CeEuAl parecía ser capaz de mantener una mayor cantidad de agua absorbida como se intuye a partir de la mayor intensidad de las bandas atribuidas a agua molecularmente absorbida observada en ambas regiones.

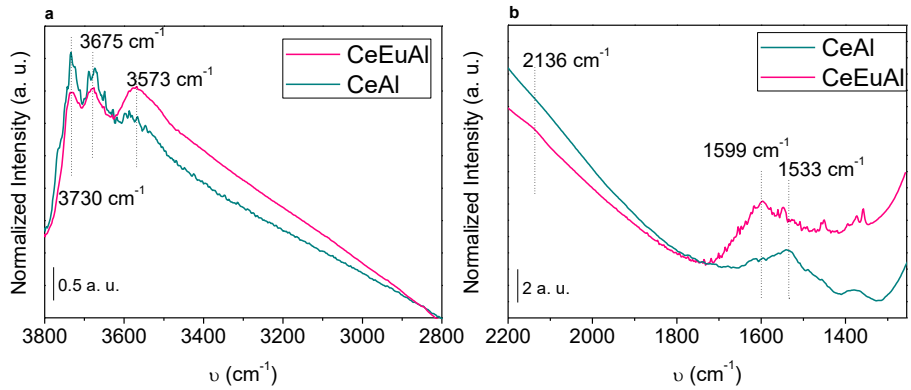

Figura R.21. Espectros FT-IR obtenidos para las muestras CeAl y CeEuAl durante la desorción de agua a T=200 ºC samples: a) rango 3900 – 3400 cm^{-1}; b) rango 2250 – 1320 cm^{-1}

Con el propósito de confirmar las observaciones en cuanto a la capacidad de retener especies de agua, tras absorber pequeñas cantidades de H_2O sobre las muestras S_Al, S_CeAl y S_CeEuAl(500 μL), se realizó una desorción a temperatura programada empleando una rampa de 5 ºC/min.

En la Figura R.22, se presentan los perfiles de m/z=18 normalizados por el área superficial de cada muestra. En todos los casos, se obtuvieron perfiles similares compuestos principalmente por dos procesos de desorción en función de la temperatura. El pico observado en torno a 350-600 ºC debe ser atribuido a procesos realacionados con el óxido de alúmina [63]. Por su parte, los procesos que se aprecian en torno a 120-350 ºC deben ser atribuidos al óxido de cerio y parecen estar constituidos al menos por dos procesos distintos situados a 120 ºC and 260 ºC, aproximadamente. De acuerdo con Thinon et al. [64] dichos procesos pueden ser relacionados, respectivamente, con procesos de desorción de agua molecular y disociativa. Ha de mencionarse que el segundo proceso de desorción podría deberse también a desorciones de agua molecularmente absorbida cuyas moléculas presentan fuertes interacciones a través de puentes de H.

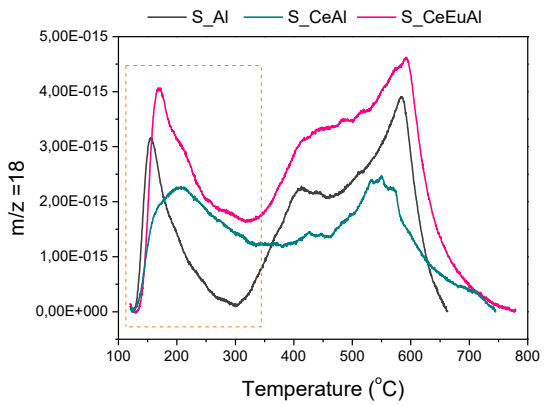

Figura R.22. Espectros FT-IR de las muestras Al, CeAl and CeEuAl obtenidos durante la adsorción de agua: a) 3900 – 3400 cm^{-1}; b) 2250 – 1320 cm^{-1}

Gráficamente, puede discernirse como la muestra S_Al perdía el agua a menores temperaturas si la comparamos con las muestras compuestas por cerio. Así, las diferencias observadas en este rango de temperatura dben ser exclusivamente al óxido de cerio. Además, el S_CeEuAl exhibe una mayor señal de agua a lo largo de todo el rango de desorción incluyendo a las temperaturas máximas en las cuales la reacción de WGS ha sido llevada a cabo. Esto implica que esta muestra parece ser capaz de mantener absorbidas mayores cantidades de agua.

Peden et al. [65] estudió las interacciones entre el agua y superficie oxidadas y reducidas de óxido de cerio concluyendo que las moléculas de agua se asociaban a sitios reducidos Ce^{3+}. Efectivamente, la muestra dopada con Eu presentaba mayores capacidades para disociar agua y para retenerla molecularmente absorbida lo cual se debe relacionar directamente con una mayor concentración de vacantes de oxígeno.

Dicha conclusión está de acuerdo con los resultados observados en los experimentos de FT-IR y debe ser relacionada directamente con la importancia del agua en la reacción de WGS así como con la hipótesis inicial.

Por lo tanto, se ha demostrado que la incorporación una capa buffer conlleva mejores comportamientos catalíticos debido a una modulación de la capacidad para disociar agua en función de la concentración de vacantes de oxígeno. Así mismo, dicha disociación parece estar relacionada con una capacidad superior de mantener absorbidas las especies de agua probablemente debido a unas

mayores densidades electrónicas generadas por mayores concentraciones de vacantes de oxígeno.

En conclusión, el estructurado de catalizadores compuestos por dos capas diferenciadas aparece como una propuesta interesante ya que consigue mejores comportamientos catalíticos, debido a procesos de disociación de agua favorecidos pero además, inhibe los efectos de desactivación provocados especies carbonáceas en este tipo de catalizadores.

6. Rol del metal noble en la reacción de WGS: Pt vs Au

El último capítulo pretende arrojar luz en cuanto al papel que juegan los metales nobles en la reacción de WGS a través de la comparación de mismos. Para ello este capítulo se subdivide en tres partes, en la primera una serie catalizadores fueron preparados, caracterizados y ensayados catalíticamente. En la segunda, se estructuraron catalizadores equivalentes de Au y Pt evaluándose el efecto del estructurado para cada uno de ellos así como la capacidad de realizar la reacción de WGS asistida por O_2. Por último, se llevó un estudio EXAFS-XANES que provee resultados tanto atendiendo a su estructura como a su dinámica.

Parte I: Catalizadores de Au y Pt en polvo sobre diferentes soportes para la reacción de WGS

Para este estudio, se soportó un 2 p/p% de Au y Pt sobre soportes basados en distintos óxidos siendo estos γ-Al_2O_3, CeO_2/Al_2O_3 and $Ce_{0.8}Fe_{0.2}O_2/Al_2O_3$. La

nomenclatura seleccionada para los soportes fue Al_2O_3, CeAl and CeFeAl. Para los catalizadores, se empleó una terminología análoga pero añadiéndose un prefijo que indicaba el metal. Por ejemplo, los catalizadores de Au y Pt preparados a partir del soporte CeAl, fueron denominados Au/CeAl y Pt/CeAl. Todos los catalizadores preparados presentaban propiedades texturales y composiciones químicas cercanas a las nominales.

Por su parte, la dispersión de los catalizadores de determino mediante HR-TEM. A pesar de que inicialmente ambos metales presentaban tamaños de partícula distintos, 4 nm y 2 nm para el Au y el Pt respectivamente, durante la reacción el Pt parecía sinterizar alcanzando tamaños de en torno a 4 nm según los resultados obtenidos por quimisorción de CO. Esto permitía analizar las atribuir las diferencias exhibidas entre los catalizadores, a la naturaleza del metal y/o su interacción con el soporte pero no a efectos estructurales relacionados con el tamaño de partícula.

En la Figura R.23, se muestra la actividad catalítica obtenida por estos catalizadores cuando fueron testados en condiciones modelo así como en condiciones reales. Los test de actividad catalítica muestran notables diferencias en función del metal noble y de la naturaleza del soporte. Así, la importancia del soporte parecía ser mucho mayor para el Au que para el Pt. De hecho, mientras que el Au/Al era prácticamente inactivo, el Pt/Al conseguía incluso alcanzar las conversiones de equilibrio lo cual se debe relacionar con su capacidad intrínseca para disociar el agua. A pesar de esto,

la presencia de un óxido reducible, como el cerio, que lleve a cabo dicha disociación resulta en mejoras significativas de su comportamiento catalítico.

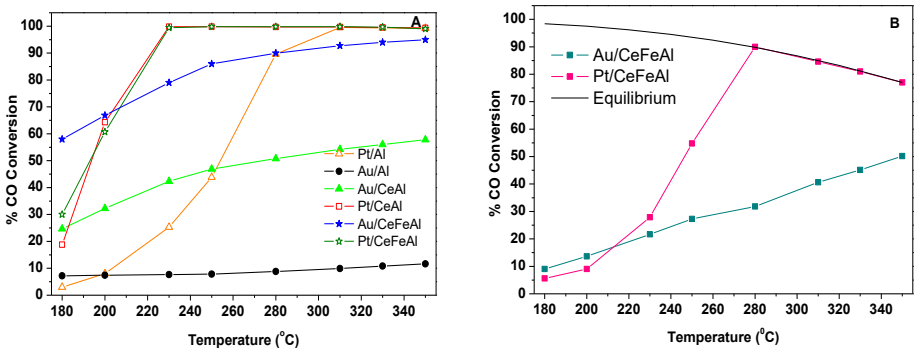

Figura R.23. Actividad catalítica exhibida por los catalizadores cuando se testan en a) Condiciones modelo y b) Condiciones reales

Por otra parte, el uso del CeFeAl conlleva significativas mejoras catalíticas en el caso del Au doblando casi las conversiones de CO en todo el rango de temperaturas. A pesar de que las diferencias entre el Pt/CeAl y el Pt/CeFeAl fueron bastante menos acusadas (observándose sólo leventemente en las temperaturas más bajas), los catalizadores Pt/CeFeAl y Au/CeFeAl fueron seleccionados y testados en condiciones reales (Figura R.23.b). En tales condiciones quedó la superioridad del Pt para trabajar en presencia de H_2 y CO_2 claramente demostrada.

Con el objetivo de dilucidar a qué se debían tales diferencias se caracterizaron las propiedades electrónicas de los catalizadores a partir de espectroscopía UV-Vis. La Tabla R.1 muestra lo valores obtenidos para la energía de band del óxido de cerio para todas las muestras. Con respecto a los soportes, la

disminución de la energía de band gap presentada por el soporte CeFeAl con respecto al CeAl se explica por la incorporación de niveles electrónicos aportados por el Fe entre la banda de conducción y la banda de valencia del óxido de cerio.

Tabla R.1. Energías de band gap calculadas

Sample	Direct band gap (eV)	Indirect band gap (eV)
CeAl	3.05	2.80
CeFeAl	2.93	2.45
Pt/CeAl	2.94	2.12
Au/CeAl	2.97	2.90
Pt/CeFeAl	2.79	2.26
Au/CeFeAl	2.11	1.50

Por su parte, los catalizadores de Au presentan en todos los casos valores de band gap menores que los exhibidos por los catalizadores de Pt. Esto puede explicarse en base a las estructura electrónica de ambos sistemas. La presencia de *metal induced gap states* (MIGS) es el resultado de la interacción del metal noble con la superficie del óxido de cerio. La interacción iónica entre los metales nobles cargados negativamente y los clusters de vacantes superficiales resulta en la sobreposición de los niveles de 5d del Pt con los 2p del O, mientras que los niveles 5d de Au caen entre los niveles del 2p del O y los 4f del Ce. Independientemente de la configuración de los estados energéticos de ambos sistemas, los electro extra procedentes de los metales nobles resultan en un transferencia electrónica de los conjuntos Ce(Fe)-

$O(V_O)$-Ce(Fe) hacia el metal noble siendo mayor la carga negativa en el Pt que en el Au.

Por lo tanto, el superior comportamiento catalítico observado en el caso del Pt/CeFeAl se relaciona directamente con las diferencias que ambos catalizadores presentaban en sus estructuras electrónicas viniendo esto relacionado en las distintas energías de band gap calculadas.

Parte II: Au/CeFeAl y Pt/CeFeAl estructurados en micromonolitos metálicos

Esta parte se focaliza en la aplicación de catalizadores de catalizadores estructurados de Au y Pt para la reacción de WGS con el objetivo superar las restricciones de volumen asociadas a los reactores convencionales de lecho catalítico para la reacción de WGS aprovechando las excelentes transferencias de calor y de masa porporcionadas por los micromonolitos metálicos. El efecto del proceso de estructurado se evalúa también a lo largo de esta parte. Por otra parte, se analizó el efecto de la adición de pequeñas cantidades de oxígeno que permitan paliar los efectos de desactivación por especies carbonáceas. Los resultados catalíticos se relacionaron directamente con la naturaleza del metal noble y con las condiciones de reacción. Con tal objetivo, los catalizadores, Pt/CeFeAl y Au/CeFeAl se prepararon y estructuraron mediante el método washcoating. Las suspensiones empleadas, secadas y calcinadas, fueron caracterizadas y testadas en WGS. La nomenclatura empleada para las suspensiones fue S_Pt/CeFeAl y

S_Au/CeFeAl. Por su parte, los catalizadores estructurados se denominaron M_Pt/CeFeAl y M_Au/CeFeAl.

En la Figura R.24, se presenta la actividad catalítica de los catalizadores iniciales y de las suspensiones correspondientes en mezcla modelo. Como puede observarse, el proceso de estructurado conlleva serias disminuciones en cuanto a la actividad catalítica en el caso del catalizador basado en Au. Esto puede atribuirse a cambios en el tamaño de las partículas de Au. Por su parte, el Pt parecía soportar bastante bien el método washcoating y prácticamente no se aprecian cambios significativos entre la actividad catalítica del catalizador inicial y su respectiva suspensión.

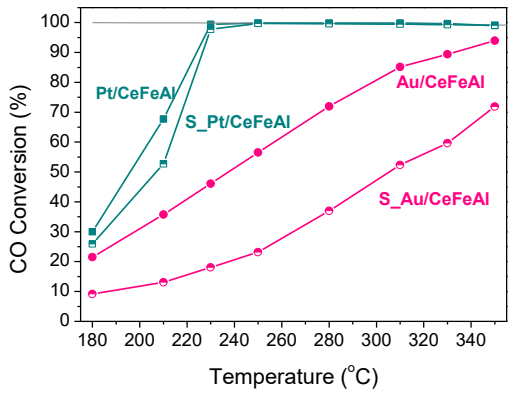

Figura R.24. Conversiones de CO obtenidas para las muestras en polvo en mezcla modelo y a 4000 h^{-1}

Por otra parte, también se ensayaron los catalizadores estructurados en condiciones modelo (Figura R.25). De acuerdo a lo esperado, el M_Pt/CeFeAl mostraba superiores comportamientos catalíticos en comparación con el

M_Au/CeFeAl. De hecho, el M_Au/CeFeAl presentaba pobres conversiones a lo largo de todo el rango de reacción.

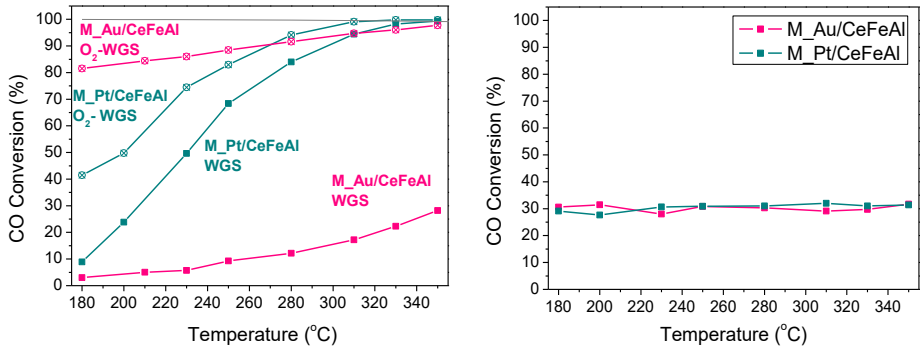

Figura R.25. CO conversions in obtained for the micromonolithic structures in: a) model and O_2-model; b) TOX

La incorporación a la corriente de reacción de pequeñas cantidades de oxígeno (O_2-WGS) suponía un importante aumento en cuanto a las conversiones obtenidas por ambos catalizadores. No obstante, el incremento de actividad catalítica mostrado por el M_Au/CeFeAl era, además de sorprendente, muy superior al exhibido por el M_Pt/CeFeAl para el cual la mejora disminuye conforme aumenta la temperatura de reacción.

Teniendo en cuenta que la reacción de oxidación de CO se puede dar de forma paralela y que, de hecho, los catalizadores de metales nobles son muy activo para este tipo de reacciones [66], se realizó un ensayo análogo pero en ausencia de agua sobre ambos catalizadores estructurados (Figura R.25.b). Ambos catalizadores presentaban conversiones análogas para la reacción de

oxidación de CO alcanzando el máximo de conversión permitido por la estequiometría de la alimentación durante todo el rango de temperaturas siendo este un 30 %.

El M_Pt/CeFeAl presenta un incremento máximo de conversión a 180 ºC que se corresponde exactamente con el posible incremento que se obtendría en el caso de que sí se dieran ambas reacciones de forma paralela. Similares resultados fueron obtenidos por Duprez et *al*. [67] quien afirmaba que el incremento de la actividad catalítica observado para catalizadores de Pt en reacciones de WGS asistidas por oxígeno se podía atribuir únicamente a dichas reacciones en paralelo.

Contrariamente, en el caso del catalizador M_Au/CeFeAl, el incremento de conversión observado para la reacción WGS asistida por oxígeno no se puede atribuir al hecho de que se den, de forma paralela, la reacción de WGS y reacción de oxidación de CO. Por lo tanto, el Au como metal noble sí que parece ser capaz de dar la reacción de WGS asistida por oxígeno. En literatura ha sido descrito que el efecto beneficioso de la incorporación de O_2 favorece la generación de grupos OH lo que favorecería la reacción de WGS [68,69].

Por otra parte, en el caso de los catalizadores de Au, la importancia vital del soporte ya ha sido demostrada. Así pues, el efecto beneficioso de la incorporación de oxígeno pudiera estar también relacionada con la inhibición de los efectos de desactivación del soporte tales como la sobrerreducción del soporte y/o el bloqueo de los centros activos para la disociación del agua del

soporte. De hecho, también ha sido reportado que la incorporación de oxígeno facilita la descomposición de las especies carbonáceas liberando los sitios activos que volverían a estar disponibles para la disociación de agua lo cual explicaría el incremento de conversión observado en la reacción de WGS [70].

En conclusión, la adición de O_2 a la reacción de WGS invierte la balanza en favor de los catalizadores de Au siendo este el único de los dos metales capaz de dar una reacción de WGS asistida por oxígeno.

A pesar de que la dilucidación del efecto de la adición de pequeñas cantidades de oxígeno a la reacción de WGS, esto se presenta como una interesante estrategia que potencia la reacción de WGS siendo especialmente atractiva cuando se combina con los micromonolitos metálicos debido a las importantes reducciones de volumen que permiten de manera que tales dispositivos puedan ser implementados en procesos de combustible basados en hidrógeno.

Parte III: Estudios *Operando* XANES-EXAFS sobre catalizadores basados en Au y Pt

En condiciones de reacción los catalizadores pueden llevar cabo cambios químicos que transformen, de una forma significativa su estructura con respecto a la que inicialmente presentaban [71]. Las técnicas de caracterización in *In situ/operando* aparecen como interesantes ya que

permiten análisis detallados de las propiedades estructurales, electrónicas y químicas de los catalizadores en condiciones de reacción. Por ello, se estudiaron catalizadores de Pt/CeAl y Au/CeAl mediante las técnicas XANES-EXAFS durante la reacción de WGS.

En la Figura R.26 se presentan los resultados extraídos de los espectros XANES para el catalizador de Pt cuando este es expuesto a CO e H_2 en rampa de temperatura. Este experimento se justifica debido al pretratamiento al que se somete a este catalizador antes de la reacción de WGS.

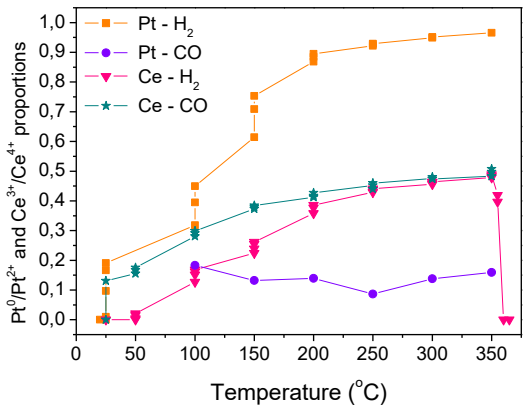

Figura R.26. Proporciones Ce^{3+}/Ce^{4+} y Pt^{0}/Pt^{2+} calculadas cuando el Pt/CeAl se expone a corrientes de CO e H_2

Mientras que el cerio se reducía aproximadamente de la misma forma en presencia de CO y de H_2 (Ce^{3+}/Ce^{4+} = 0.44), el Pt sólo se reducía en presencia de H_2 pero no de CO.

Además, los estados de oxidación a los que ambas especies llegaban durante la reducción en H_2 se mantenían aproximadamente constantes durante la reacción de WGS. Sin embargo, en el caso del Au, los estados de oxidación cambiaban bruscamente durante la reacción de WGS debido a la ausencia de pretratamiento para este catalizador. Los cambios en los estados de oxidación deben acarrear cambios estructurales en las especies que lo sufren. En la Figura R.27 se presentan los espectros EXAFS del cerio que se obtuvieron durante la reacción de WGS para cada uno de los catalizadores. Como puede discernirse, los espectros de cerio permanecen casi constantes con el aumento de temperatura mientras que en el caso del oro se pueden apreciar importantes variaciones con el aumento de la temperatura.

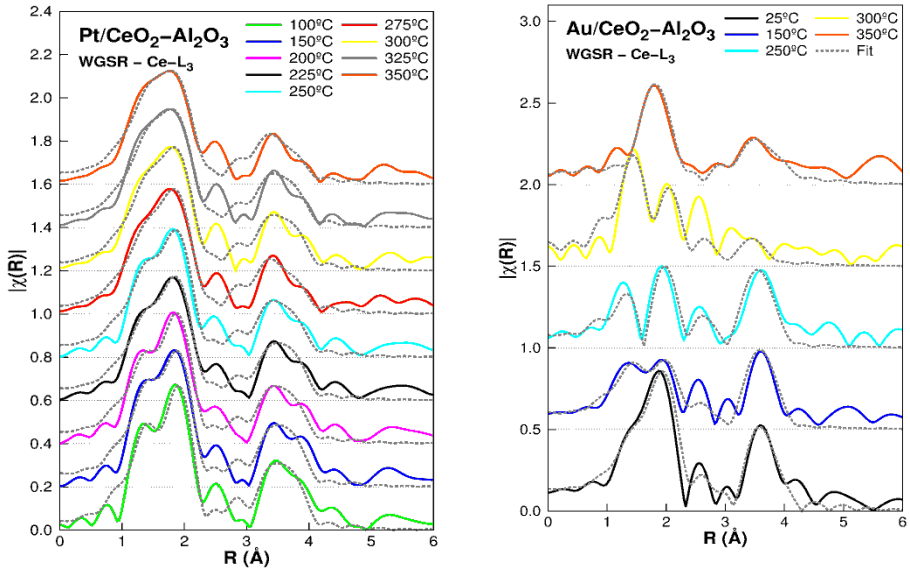

Figura R.27. Espectros EXAFS en el espacio R obtenidos para el Ce-L_3 cuando se calientan durante la reacción de WGS: a) Pt/CeAl; b) Au/CeAl

Por otra parte, para ambos catalizadores, se detectó una esfera de coordinación en torno a los ~2 Å que se corresponde con la interacción de grupos hidroxilos con la superficie del cerio. Sin embargo, dicha señal empieza a ser evidente a partir de 150 ºC volviendo a decrecer cuando se alcanzan los 300 ºC. Contrariamente, el catalizador de Pt mantiene la interacción Ce-OH durante todo el rango de temperaturas. Este comportamiento es consistente con el grado de oxidación presentado por el cerio en el XANES indicando que la adsorción y disociación del agua se da en las vacantes de oxígeno.

Por otra parte, atendiendo a los metales, los espectros EXAFS para el Pt-L_3 y Au-L_3 se presentan en la Figura R.28. En el caso del Pt, las oscilaciones EXAFS indicaban interacciones Pt-Pt cuyo número de coordinación parecía ser constante a lo largo de todo el rango de temperaturas. Sin embargo, a valores bajos de R (~1.5 Å) aparecen unas oscilaciones que disminuyen conforme aumenta la temperatura. Dichas oscilaciones pueden ser ajustadas como especies OH asociadas a los átomos de Pt indicando la disociación de agua en la superficie del metal incluso a elevadas temperaturas.

Además, el Pt parece crecer epitaxialmente constituyendo partículas de tres capas de la cuales los átomos de Pt situados en la capa inferior ocupando posiciones que inicialmente deberían estar ocupadas por oxígenos de la red del cerio. Además, se detectaron pequeñas variaciones del número de

coordinación Pt-Ce lo que sugiere cambios en las proporciones relativas del tamaño de las capas intermedia e inferior conforme aumenta la temperatura. Conviene mencionar que la temperatura a la cual se observaron dichos cambios coincide con la temperatura a la cual los catalizadores de Pt exhiben notables incrementos de conversión durante la reacción de WGS.

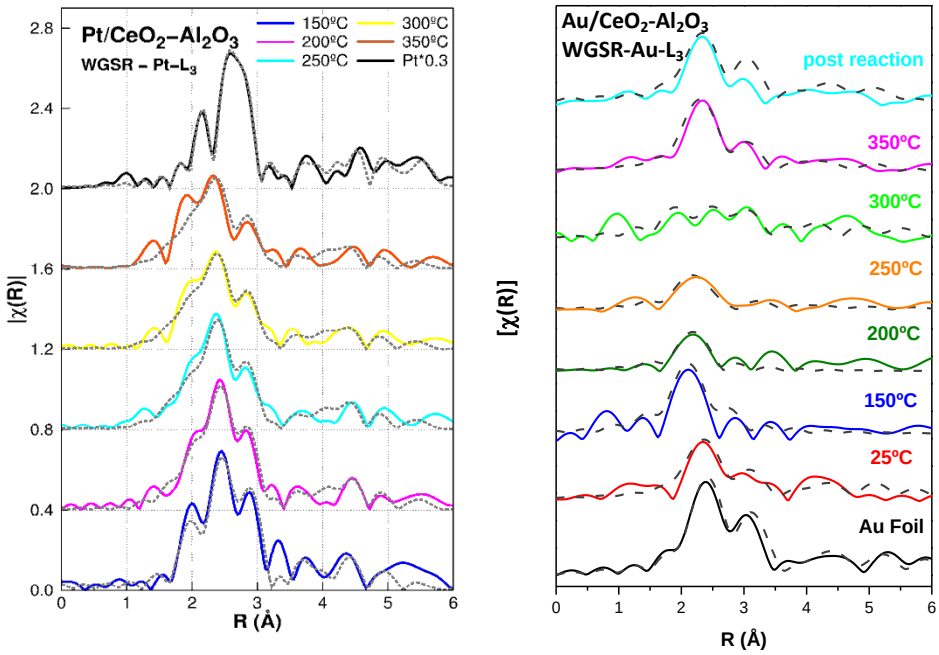

Figura R.28. Espectros EXAFS en el espacio R obtenidos durante la reacción de WGS: a) Pt-L_3 para el Pt/CeAl; b) Au-L_3 para el Au/CeAl

En cuanto a la dinámica del Au, la proporción Au superficial – Au bulk aumenta significativamente cuando la temperatura pasa de 25 ºC a 100 ºC lo cual sugiere una completa redispersión de las partículas de Au durante la reacción de WGS. Esta redispersión parecía ir acompañada de un incremento

de las señales de Au-Ce y Au-O lo que podría implicar que los atomos de Ay se sitúan en las vacantes de oxígeno de manera que queden rodeados de átomos de O

Los resultados obtenidos mediante la absorción de RX realizado en condiciones de *Operando* sobre catalizadores de Au y Pt soportados sobre CeO_2/Al_2O_3 permiten concluir que el incremento de actividad que experimentan los catalizadores de metales nobles en presencia de cerio se debe a la capacidad del óxido de cerio parcialmente reducido de absorber y disociar moléculas de agua. Teniendo en cuenta que la WGS es controlada por la velocidad de difusión del agua, la capacidad de mantener absorbidos los grupos hidroxilos en la interfase metal/soporte durante la reacción de WGS explicando los resultados catalíticos obtenidos en función del metal noble.

Referencias

[1] A.R. Dubrovskiy, E. V. Rebrov, S.A. Kuznetsov, J.C. Schouten, Catal. Today 147 (2009) 198.

[2] C. Ratnasamy, J.P. Wagner, Catal. Rev. 51 (2009) 325.

[3] G.G. Olympiou, C.M. Kalamaras, C.D. Zeinalipour-Yazdi, A.M. Efstathiou, Catal. Today 127 (2007) 304.

[4] D.C. Grenoble, M.M. Estadt, D.F. Ollis, J. Catal. 67 (1981) 90.

[5] S. Seong, A.B. Anderson, 3654 (1996) 11744.

[6] A. Martinez-Arias, J.M. Coronado, R. Cataluna, J.C. Conesa, J. Soria, J. Phys. Chem. B 102 (1998) 4357.

[7] S. Damyanova, J.M.C. Bueno, Appl. Catal. A Gen. 253 (2003) 135.

[8] A.P. Ferreira, J.C.S. Araújo, J.W.C. Liberatoria, S. Damyanova, D. Zanchetc, F.B. Noronha, J.M.C. Bueno, Stud. Surf. Sci. Catal. 167 (2007) 433.

[9] J.Z. Shyu, K. Otto, J. Catal. 115 (1989) 16.

[10] G. Dutta, U. V. Waghmare, T. Baidya, M.S. Hegde, K.R. Priolkar, P.R. Sarode, Chem. Mater. 18 (2006) 3249.

[11] C.I. Vignatti, M.S. Avila, C.R. Apesteguía, T.F. Garetto, Catal. Today 171 (2011) 297.

[12] G. Jacobs, S. Ricote, U.M. Graham, B.H. Davis, (2014).

[13] M. Gonzalez Castaño, T.R. Reina, S. Ivanova, M.A. Centeno, J.A. Odriozola, J. Catal. 314 (2014) 1.

[14] A.A. Phatak, N. Koryabkina, S. Rai, J.L. Ratts, W. Ruettinger, R.J. Farrauto, G.E. Blau, W.N. Delgass, F.H. Ribeiro, Catal. Today 123 (2007) 224.

[15] S.J. Tauster, S.C. Fung, R.L. Garten, J. Am. Chem. Soc. 100 (1978) 170.

[16] M. Gonzalez Castaño, T.R. Reina, S. Ivanova, M.A. Centeno, J.A. Odriozola, J. Catal. 314 (2014) 1.

[17] J. Kugai, J.T. Miller, N. Guo, C. Song, J. Catal. 277 (2011) 46.

[18] P.C.A. Brito, D.A.A. Santos, J.G.S. Duque, M.A. Macêdo, Phys. B Condens. Matter 405 (2010) 1821.

[19] C.T. Campbell, C.H.F. Peden, Science 309 (2005) 713.

[20] N. Acerbi, S. Golunski, S.C. Tsang, H. Daly, C. Hardacre, R. Smith, P. Collier, J. Phys. Chem. C 116 (2012) 13569.

[21] G. Avgouropoulos, T. Ioannides, J. Mol. Catal. A Chem. 296 (2008) 47.

[22] A.S. Reddy, C.Y. Chen, C.C. Chen, S.H. Chien, C.J. Lin, K.H. Lin, C.L. Chen, S.C. Chang, J. Mol. Catal. A Chem. 318 (2010) 60.

[23] T. Tabakova, L. Ilieva, I. Ivanov, R. Zanella, J.W. Sobczak, W. Lisowski, Z. Kaszkur, D. Andreeva, Appl. Catal. B Environ. 136-137 (2013) 70.

[24] T. Tabakova, V. Idakiev, D. Andreeva, I. Mitov, Appl. Catal. A Gen. 202 (2000) 91.

[25] T.R. Reina, S. Ivanova, J.J. Delgado, I. Ivanov, V. Idakiev, T. Tabakova, M.A. Centeno, J.A. Odriozola, ChemCatChem 6 (2014) 1401.

[26] O.H. Laguna, M.A. Centeno, M. Boutonnet, J.A. Odriozola, Appl. Catal. B Environ. 106 (2011) 621.

[27] S.Y. Choung, M. Ferrandon, T. Krause, 99 (2005) 257.

[28] W. Ruettinger, O. Ilinich, R.J. Farrauto, J. Power Sources 118 (2003) 61.

[29] X. Wang, R.J. Gorte, J.P. Wagner, J. Catal. 212 (2002) 225.

[30] Y. Nagai, K. Dohmae, Y. Ikeda, N. Takagi, T. Tanabe, N. Hara, G. Guilera, S. Pascarelli, M.A. Newton, O. Kuno, H. Jiang, (2008) 9303.

[31] P. Panagiotopoulou, J. Papavasiliou, G. Avgouropoulos, T. Ioannides, D.I. Kondarides, Chem. Eng. J. 134 (2007) 16.

[32] D. Pierre, W. Deng, M. Flytzani-Stephanopoulos, Top. Catal. 46 (2007) 363.

[33] J.M. Zalc, V. Sokolovskii, D.G. Löffler, J. Catal. 206 (2002) 169.

[34] R.J. Farrauto, Y. Liu, W. Ruettinger, O. Ilinich, L. Shore, T. Giroux, Catal. Rev. 49 (2007) 141.

[35] P. Avila, M. Montes, E.E. Miró, Chem. Eng. J. 109 (2005) 11.

[36] S. Ivanova, O.H. Laguna, M.Á. Centeno, A. Eleta, M. Montes, J.A. Odriozola, Renew. Hydrog. Technol. (2013) 225.

[37] V.G. Milt, S. Ivanova, O. Sanz, M.I. Domínguez, A. Corrales, J.A. Odriozola, M.A. Centeno, Appl. Surf. Sci. 270 (2013) 169.

[38] O. Sanz, L.M. Martínez T, F.J. Echave, M.I. Domínguez, M.A. Centeno, J.A. Odriozola, M. Montes, Chem. Eng. J. 151 (2009) 324.

[39] V. Meille, Appl. Catal. A Gen. 315 (2006) 1.

[40] Q. Fu, H. Saltsburg, M. Flytzani-Stephanopoulos, Science 301 (2003) 935.

[41] P.B. Weisz, J.S. Hicks, (1961).

[42] O.H. Laguna, M. González Castaño, M.A. Centeno, J.A. Odriozola, Chem. Eng. J. 275 (2015) 45.

[43] D.I. Potemkin, P.V. Snytnikov, V.D. Belyaev, V. a. Sobyanin, Chem. Eng. J. 176-177 (2011) 165.

[44] R.J. Farrauto, Y. Liu, W. Ruettinger, O. Ilinich, L. Shore, T. Giroux, Catal. Rev. 49 (2007) 141.

[45] G. Germani, P. Alphonse, M. Courty, Y. Schuurman, C. Mirodatos, Catal. Today 110 (2005) 114.

[46] X. Zheng, J. Mantzaras, R. Bombach, Combust. Flame 161 (2014) 332.

[47] S. Aranifard, S.C. Ammal, A. Heyden, J. Phys. Chem. C 116 (2012) 9029.

[48] X. Liu, O. Korotkikh, R. Farrauto, Appl. Catal. A Gen. 226 (2002) 293.

[49] L. Grabow, Y. Xu, M. Mavrikakis, Phys. Chem. Chem. Phys. 8 (2006) 3369.

[50] P. Thormählen, M. Skoglundh, E. Fridell, B. Andersson, J. Catal. 188 (1999) 300.

[51] J.P. Clay, J.P. Greeley, F.H. Ribeiro, W.N. Delgass, W.F. Schneider, J. Catal. 320 (2014) 106.

[52] D. Martin, D. Duprez, J. Phys. Chem. B 112 (2006) 4428.

[53] D. Duprez, Catal. Today 112 (2006) 17.

[54] Y. Lykhach, V. Johánek, H. a. Aleksandrov, S.M. Kozlov, M. Happel, T. Skála, P. St. Petkov, N. Tsud, G.N. Vayssilov, K.C. Prince, K.M.

Neyman, V. Matolín, J. Libuda, J. Phys. Chem. C 116 (2012) 12103.

[55] S. Aranifard, S.C. Ammal, A. Heyden, J. Phys. Chem. C 118 (2014) 6314.

[56] G. Jacobs, P.M. Patterson, L. Williams, E. Chenu, D. Sparks, G. Thomas, B.H. Davis, Appl. Catal. A Gen. 262 (2004) 177.

[57] S.M. Opalka, T.H. Vanderspurt, R. Radhakrishnan, Y. She, R.R. Willigan, J. Phys. Condens. Matter 20 (2008) 064237.

[58] F.W. Poulsen, M. Glerup, P. Holtappels, Solid State Ionics 135 (2000) 595.

[59] Z. V. Popović, Z.D. Dohčević-Mitrović, N. Paunović, M. Radović, Phys. Rev. B - Condens. Matter Mater. Phys. 85 (2012) 1.

[60] W. Ruettinger, X. Liu, R.J. Farrauto, Appl. Catal. B Environ. 65 (2006) 135.

[61] C. Li, Y. Sakata, T. Arai, K. Domen, K. Maruya, T. Onishi, J. Chem. Soc. Faraday Trans. 1 85 (1989) 1451.

[62] M.I. Zaki, M.A. Hasan, F.A. Al-Sagheer, L. Pasupulety, Colloids Surfaces A Physicochem. Eng. Asp. 190 (2001) 261.

[63] J.H. Kwak, R.J. Chimentao, C.H.F. Peden, J. Phys. Chem. C 111 (2007) 2661.

[64] O. Thinon, K. Rachedi, F. Diehl, P. Avenier, Y. Schuurman, Top. Catal. 52 (2009) 1940.

[65] M.A. Henderson, C.L. Perkins, M.H. Engelhard, S. Thevuthasan, C.H.F. Peden, Surf. Sci. 526 (2003) 1.

[66] O.H. Laguna, M.A. Centeno, G. Arzamendi, L.M. Gandía, F. Romero-Sarria, J.A. Odriozola, Catal. Today 157 (2010) 155.

[67] J. Barbier, D. Duprez, Appl. Catal. B Environ. 3 (1993) 61.

[68] T. Utaka, K. Sekizawa, K. Eguchi, Appl. Catal. A Gen. 194 (2000) 21.

[69] G.C. Chinchen, M.S. Spencer, K.C. Waugh, D.A. Whan, J. Chem. Soc. Faraday Trans. 1 83 (1987) 2193.

[70] T.R. Reina, S. Ivanova, V. Idakiev, J.J. Delgado, I. Ivanov, T. Tabakova, M.A. Centeno, J.A. Odriozola, Catal. Sci. Technol. 3 (2013) 779.

[71] T. Bunluesin, R.J. Gorte, G.W. Graham, Appl. Catal. B Environ. 15 (1998) 107.